frontiers | Research Topics

Artificial intelligence-based computer-aided diagnosis applications for brain disorders from medical imaging data, volume II

Edited by
Ahmed Shalaby, Fahmi Khalifa, Ahmed Soliman, Ahmed Refaey Hussein, Mohamed Abdelazim and Safa Elaskary

Published in
Frontiers in Neuroscience
Frontiers in Neuroinformatics

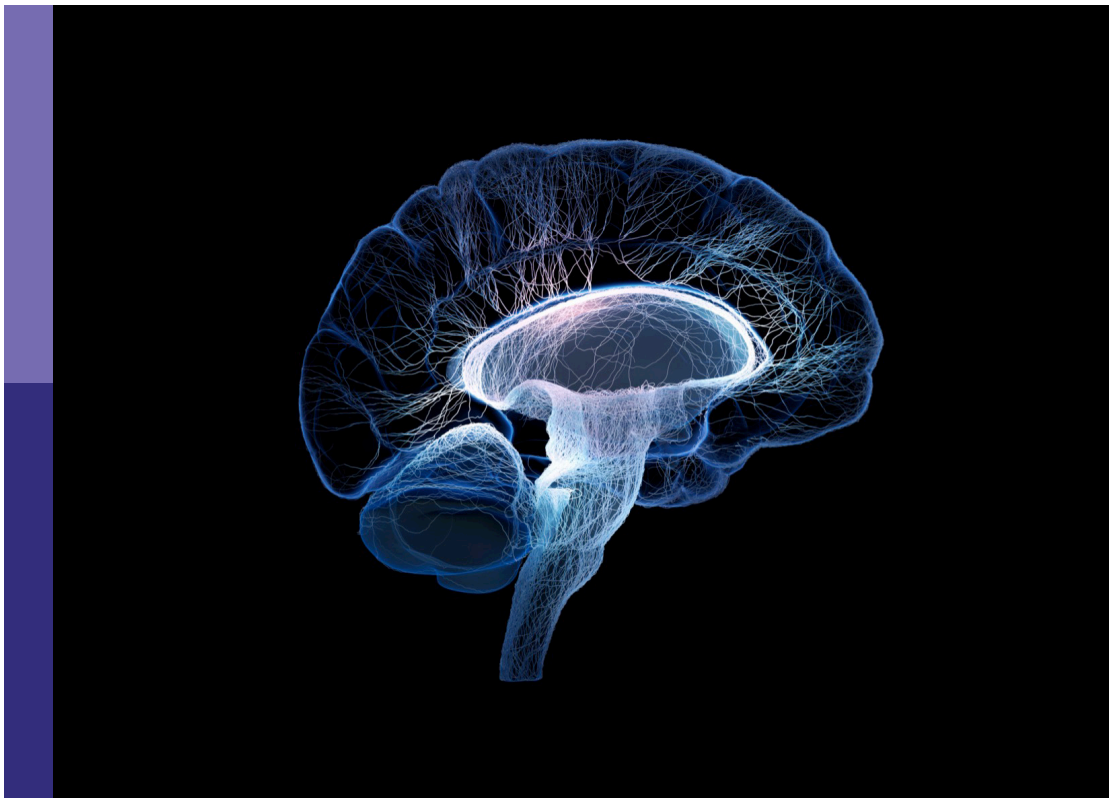

FRONTIERS EBOOK COPYRIGHT STATEMENT

The copyright in the text of individual articles in this ebook is the property of their respective authors or their respective institutions or funders. The copyright in graphics and images within each article may be subject to copyright of other parties. In both cases this is subject to a license granted to Frontiers.

The compilation of articles constituting this ebook is the property of Frontiers.

Each article within this ebook, and the ebook itself, are published under the most recent version of the Creative Commons CC-BY licence. The version current at the date of publication of this ebook is CC-BY 4.0. If the CC-BY licence is updated, the licence granted by Frontiers is automatically updated to the new version.

When exercising any right under the CC-BY licence, Frontiers must be attributed as the original publisher of the article or ebook, as applicable.

Authors have the responsibility of ensuring that any graphics or other materials which are the property of others may be included in the CC-BY licence, but this should be checked before relying on the CC-BY licence to reproduce those materials. Any copyright notices relating to those materials must be complied with.

Copyright and source acknowledgement notices may not be removed and must be displayed in any copy, derivative work or partial copy which includes the elements in question.

All copyright, and all rights therein, are protected by national and international copyright laws. The above represents a summary only. For further information please read Frontiers' Conditions for Website Use and Copyright Statement, and the applicable CC-BY licence.

ISSN 1664-8714
ISBN 978-2-8325-3100-6
DOI 10.3389/978-2-8325-3100-6

About Frontiers

Frontiers is more than just an open access publisher of scholarly articles: it is a pioneering approach to the world of academia, radically improving the way scholarly research is managed. The grand vision of Frontiers is a world where all people have an equal opportunity to seek, share and generate knowledge. Frontiers provides immediate and permanent online open access to all its publications, but this alone is not enough to realize our grand goals.

Frontiers journal series

The Frontiers journal series is a multi-tier and interdisciplinary set of open-access, online journals, promising a paradigm shift from the current review, selection and dissemination processes in academic publishing. All Frontiers journals are driven by researchers for researchers; therefore, they constitute a service to the scholarly community. At the same time, the *Frontiers journal series* operates on a revolutionary invention, the tiered publishing system, initially addressing specific communities of scholars, and gradually climbing up to broader public understanding, thus serving the interests of the lay society, too.

Dedication to quality

Each Frontiers article is a landmark of the highest quality, thanks to genuinely collaborative interactions between authors and review editors, who include some of the world's best academicians. Research must be certified by peers before entering a stream of knowledge that may eventually reach the public - and shape society; therefore, Frontiers only applies the most rigorous and unbiased reviews. Frontiers revolutionizes research publishing by freely delivering the most outstanding research, evaluated with no bias from both the academic and social point of view. By applying the most advanced information technologies, Frontiers is catapulting scholarly publishing into a new generation.

What are Frontiers Research Topics?

Frontiers Research Topics are very popular trademarks of the *Frontiers journals series*: they are collections of at least ten articles, all centered on a particular subject. With their unique mix of varied contributions from Original Research to Review Articles, Frontiers Research Topics unify the most influential researchers, the latest key findings and historical advances in a hot research area.

Find out more on how to host your own Frontiers Research Topic or contribute to one as an author by contacting the Frontiers editorial office: frontiersin.org/about/contact

Artificial intelligence-based computer-aided diagnosis applications for brain disorders from medical imaging data, volume II

Topic editors

Ahmed Shalaby — University of Texas Southwestern Medical Center, United States
Fahmi Khalifa — Morgan State University, United States
Ahmed Soliman — University of Louisville, United States
Ahmed Refaey Hussein — Manhattan College, United States
Mohamed Abdelazim — Mansoura University, Egypt
Safa Elaskary — King Abdulaziz University, Saudi Arabia

Citation

Shalaby, A., Khalifa, F., Soliman, A., Hussein, A. R., Abdelazim, M., Elaskary, S., eds. (2023). *Artificial intelligence-based computer-aided diagnosis applications for brain disorders from medical imaging data, volume II*. Lausanne: Frontiers Media SA. doi: 10.3389/978-2-8325-3100-6

Table of contents

05 Editorial: Artificial intelligence-based computer-aided diagnosis applications for brain disorders from medical imaging data, volume II
Fahmi Khalifa, Ahmed Shalaby, Ahmed Soliman, Safa Elaskary, Ahmed Refaey and Mohamed Abdelazim

10 Convolutional Neural Networks for Classification of T2DM Cognitive Impairment Based on Whole Brain Structural Features
Xin Tan, Jinjian Wu, Xiaomeng Ma, Shangyu Kang, Xiaomei Yue, Yawen Rao, Yifan Li, Haoming Huang, Yuna Chen, Wenjiao Lyu, Chunhong Qin, Mingrui Li, Yue Feng, Yi Liang and Shijun Qiu

18 A transfer learning approach for multiclass classification of Alzheimer's disease using MRI images
Rizwan Khan, Saeed Akbar, Atif Mehmood, Farah Shahid, Khushboo Munir, Naveed Ilyas, M. Asif and Zhonglong Zheng

31 Clinical features and FLAIR radiomics nomogram for predicting functional outcomes after thrombolysis in ischaemic stroke
Qingqing Xu, Yan Zhu, Xi Zhang, Dan Kong, Shaofeng Duan, Lili Guo, Xindao Yin, Liang Jiang, Zaiyi Liu and Wanqun Yang

43 Disrupted interhemispheric coordination of sensory-motor networks and insula in major depressive disorder
Chunguo Zhang, Huan Jing, Haohao Yan, Xiaoling Li, Jiaquan Liang, Qinqin Zhang, Wenting Liang, Yangpan Ou, Can Peng, Yang Yu, Weibin Wu, Guojun Xie and Wenbin Guo

54 Broad learning for early diagnosis of Alzheimer's disease using FDG-PET of the brain
Junwei Duan, Yang Liu, Huanhua Wu, Jing Wang, Long Chen and C. L. Philip Chen, for the Alzheimer's Disease Neuroimaging Initiative

64 Patterns of inflammation, microstructural alterations, and sodium accumulation define multiple sclerosis subtypes after 15 years from onset
Antonio Ricciardi, Francesco Grussu, Baris Kanber, Ferran Prados, Marios C. Yiannakas, Bhavana S. Solanky, Frank Riemer, Xavier Golay, Wallace Brownlee, Olga Ciccarelli, Daniel C. Alexander and Claudia A. M. Gandini Wheeler-Kingshott

75 EEG assessment of brain dysfunction for patients with chronic primary pain and depression under auditory oddball task
Yunzhe Li, Banghua Yang, Zuowei Wang, Ruyan Huang, Xi Lu, Xiaoying Bi and Shu Zhou

89 Using support vector machine to explore the difference of function connection between deficit and non-deficit schizophrenia based on gray matter volume
Wenjing Zhu, Zan Wang, Miao Yu, Xiangrong Zhang and Zhijun Zhang

100 Preoperative prediction of sonic hedgehog and group 4 molecular subtypes of pediatric medulloblastoma based on radiomics of multiparametric MRI combined with clinical parameters
Yuanlin Wang, Longlun Wang, Bin Qin, Xihong Hu, Wenjiao Xiao, Zanyong Tong, Shuang Li, Yang Jing, Lusheng Li and Yuting Zhang

109 Abnormal flow pattern of low wall shear stress and high oscillatory shear index in spontaneous vertebral artery dissection with vertebral artery hypoplasia
Jiajia Bao, Xinling Gan, Wentao Feng, Yanbo Li, Yue Qiu, Muke Zhou, Jian Guo and Li He

frontiers | Frontiers in Neuroscience

TYPE Editorial
PUBLISHED 12 July 2023
DOI 10.3389/fnins.2023.1241926

Check for updates

OPEN ACCESS

EDITED AND REVIEWED BY
Vince D. Calhoun,
Georgia State University, United States

*CORRESPONDENCE
Fahmi Khalifa
✉ fahmi.khalifa@morgan.edu

RECEIVED 17 June 2023
ACCEPTED 30 June 2023
PUBLISHED 12 July 2023

CITATION
Khalifa F, Shalaby A, Soliman A, Elaskary S, Refaey A and Abdelazim M (2023) Editorial: Artificial intelligence-based computer-aided diagnosis applications for brain disorders from medical imaging data, volume II.
Front. Neurosci. 17:1241926.
doi: 10.3389/fnins.2023.1241926

COPYRIGHT
© 2023 Khalifa, Shalaby, Soliman, Elaskary, Refaey and Abdelazim. This is an open-access article distributed under the terms of the Creative Commons Attribution License (CC BY). The use, distribution or reproduction in other forums is permitted, provided the original author(s) and the copyright owner(s) are credited and that the original publication in this journal is cited, in accordance with accepted academic practice. No use, distribution or reproduction is permitted which does not comply with these terms.

Editorial: Artificial intelligence-based computer-aided diagnosis applications for brain disorders from medical imaging data, volume II

Fahmi Khalifa[1]*, Ahmed Shalaby[2], Ahmed Soliman[3], Safa Elaskary[4], Ahmed Refaey[5] and Mohamed Abdelazim[6]

[1]Electrical and Computer Engineering, Morgan State University, Baltimore, MD, United States, [2]Lyda Hill Department of Bioinformatics, Southwestern Medical Center, University of Texas, Dallas, TX, United States, [3]Department of Computer Engineering, Faculty of Engineering, Mansoura University, Mansoura, Egypt, [4]Department of Biomedical Equipment and Technology, Applied Health Sciences, Pharos University, Alexandria, Egypt, [5]School of Engineering and Physical Sciences, University of Guelph, Guelph, ON, Canada, [6]Electronics and Communications Engineering, Mansoura University, Mansoura, Egypt

KEYWORDS

artificial intelligence, brain disorders, Electroencephalography (EEG), Alzheimer's disease, convolutional neural network (CNN), schizophrenia, multiple sclerosis, acute ischaemic stroke (AIS)

Editorial on the Research Topic
Artificial intelligence-based computer-aided diagnosis applications for brain disorders from medical imaging data, volume II

Artificial intelligence/Machine learning (ML) has recently received growing interest used to study of the etiology and mechanisms of several brain disorders by analyzing neuroimages and/or neuro signals, such as structural magnetic resonance imaging (MRI), functional MRI, and positron emission tomography (PET), Electroencephalography (EEG) signals, etc. Recent research work has achieved remarkable performance improvements to develop computer-aided diagnosis of many brain disorders. The latter include, autism, multiple sclerosis (MS), dementia, Alzheimer's disease (AD), gliomas, Schizophrenia, and Epilepsy.

Generally, manually processing of brain images/data is subjective, often time consuming, and chances of errors in the interpretation are not irrelevant (Segato et al., 2020). Thus, AI-based systems are growing fields for brain disorder analysis due to its capability to facilitate analyzing complex brain medical data to extract meaningful relationships in datasets, and reliable diagnostic cues for several clinical aims. For example, this can be used to eventually help physicians for more appropriate and precision medicine treatments.

Literature work utilizes variety of traditional ML or advanced end-to-end DL techniques to build CAD systems for brain data analysis. Both traditional and DL-based methods have shown significant performance in many brain applications. One of the limitations of traditional methods is, however; is that most of the learning techniques are often tailored to a specific application and usually need a lot of tuning and. On the other hand, CAD

systems exploiting DL combined with recent progress in neuroimaging technologies have demonstrated unprecedented performance. to predict or provide better diagnosis of brain diseases. However, they require long training time and most of the techniques are less interpretable, i.e., lack explanation explanations.

This Research Topic is a continuation of the first topic (Shalaby et al., 2023) focusing on recent scientific findings of research work utilizing AI/ML/DL methods for neuroimaging-based brain disorder analysis. The target audience for this topic includes engineering and medical researchers/professionals with the purpose to stimulate discussion on the AI system designs for brain disorders for disease diagnostic and prognostic. The topic consists of 10 accepted articles that deal with AI/ML algorithms to investigate different problems. A brief summary of each article is provided below.

A study by Tan et al. is conducted to investigate the cognitive impairment relation with type 2 diabetes mellitus (T2DM) in an effort to assist clinicians analyze and predict cognitive impairment early. The method used a 3D 11-layer convolutional neural network (CNN) and documented that he classifier could identify T2DM-related cognitive decline with a classification accuracy of 84.85% and achieved an area under the curve of 92.65%. The study concluded the importance of the study to objectively analyze and predict patients' cognitive impairment, which can provide treatments to the patients in the early stage. It is important to block or delay the development of dementia. Despite the demonstrated performance, the study had a small sample size, which necessitate using larger sample sizes in the future studies. Also, both functional and structure images should be used for better diagnosis and strong evidence of the reported conclusions.

Alzheimer's disease (AD) is an acute degenerative disease affecting the elderly population all over the world. Although the development of AD is irreversible, preventive measures in the presymptomatic stage of AD can effectively slow down deterioration. Additionally, the detection of disease at an early stage crucial to the clinical treatment. Khan et al. introduced as study that utilized transfer learning (TL) to classify various stages of AD using MRI images. The architecture is exploited the pre-trained VGG16 and 19 architectures with addition of a layer-wise transfer learning. Their model can distinguish between four groups normal controls and various stages of AD. The latter is stratified as early mild cognitive impairment (EMCI), late mild cognitive impairment (LMCI), and AD. Conducted experimental results demonstrated the superiority of the proposed approach. Additionally, the comparison with existing methods demonstrates that the proposed framework is superior in terms of accuracy and prediction. We achieved an accuracy of 97.89% for the proposed 4-way classification. The main limitation of the study is the number of images used for system evaluation and that the TL-based architecture requires resizing of the input images, which results in loss of texture information when scaling down.

Unlike Khan et al. and Duan et al. exploited fluorodeoxyglucose positron emission tomography (FDG-PET) in an AD study using ML. The study hypothesized the detection of the metabolism of glucose in patients' brains can help to identify changes related to AD before brain damage occurs. The authors introduced a broad network-based model to enhance the features of FDG-PET extracted via 2D CNN for early diagnosis of AD (BLADNet) through PET brain. BLADNet can search for information over a broad space through the addition of new BLS blocks without retraining of the whole network, thus improving the accuracy of AD classification. Experiments were conducted on a dataset containing 2,298 FDG-PET images of 1,045 subjects from the ADNI database and the reported results demonstrate the superiority of the BLADNet in EMCI and LMCI classification to those used in previous studies on early diagnosis of AD with FDG-PET. The reported results are encouraging and the model can be integrated into the clinical workflow as a powerful auxiliary diagnosis tool for reading PET imaging of patients with AD. However, the study has some limitations including the fact that many patients may have neurological diseases other than AD that can affect the prediction results. The model could not provide interpretable information for radiologists of patients gradually progressing from MCI to AD, despite that t-SNE dimension reduction documented that. Thus, validation in large cohort and a more general patient population should be conducted as the actual clinical prediction is much more complicated.

An ML-based pipeline is introduced by Ricciardi et al. in a retrospective study using quantitative MRI-derived features to correlate with multiple sclerosis (MS), severity. The authors produced a multi-modal set of quantitative MRI features encompassing relaxometry, microstructure, sodium ion concentration, and tissue volumetry. In an effort to use them improve the understanding of the underlying disease by better delineating its alteration patterns. Classical ML classifier, namely random forest (RF) was employed to discriminate between HC, CIS, relapsing remitting (RR) and secondary progressive (SP) MS patients. Additional evaluation for each classification task was dedicated to identifying the relative contribution of each MRI-derived tissue property to the classification task itself. The reported binary accuracies [99% (HC vs. SP) and 95% (CIS vs. SP); 82 (HC vs. RR) and 83% (CIS vs. RR); 76% (RR vs. SP), and 79% (HC vs. CIS)] offered specific insights for different classification tasks, highlighting the need for more research emphasizing the role of quantitative MRI in the lesions of early CIS and MS subjects to score risks of progression. Similar to Tan et al., the sample sized used in the evaluation is small (e.g., SP group has only 13 subjects) which also introduce bias in the classifier. Despite the study showed that different MRI features appear to be biophysically meaningful when discriminating CIS and clinically defined MS phenotypes, the authors emphasized on additional studies with larger sample size and histological evidence are required to substantiate these findings.

In as study for acute ischaemic stroke (AIS), Xu et al. investigated the potential of medical images-derived features to predict the clinical outcome of patients with AIS. Particularly, this retrospective study investigated and validate a radiomics nomogram for predicting AIS prognosis using diffusion-weighted imaging (DWI) and fluid-attenuated inversion recovery (FLAIR) images. The study cohort included 257 patients from three clinical centers. Their framework extracted radiomic features from

radiologist-defined regions of interest (ROIs) using ITK-SNAP[1] software. Then, two feature selection methods, minimum redundancy and maximum (mRMR) and the least absolute shrinkage and selection operator algorithm (LASSO) are used to select the candidate features. Experiments based on extracted radiomics either DWI or FLAIR, as well as DWI-FLAIR, were established. A radiomics nomogram with patient characteristics and radiomics signature was built using a multivariate logistic regression model. The presented quantitative results showed that FLAIR-derived radiomics have a similar performance with the DWI- DWI-FLAIR-derived radiomics–prediction performance AUCs of 0.922 (95% CI: 0.876–0.968), 0.875 (95% CI: 0.815–0.935), and 0.895 (95% CI: 0.840–0.950), respectively. The results document the ability of the non-invasive clinical-FLIAR radiomics nomogram in predicting ASI prognosis after thrombolysis, as step that could help clinicians plan rehabilitation for stroke patients. Despite the study demonstrated good calibration, and decision curve analysis confirmed the clinical value of this nomogram, the cohort sample size is relatively small, which may lead to overfitting, similar to Tan et al. and Ricciardi et al.. This had been compensated in part by that the study used patient data with different MRI scanners and other two clinical centers as two external validation sets. In addition, patients with lacunar infarction and posterior circulation stroke were excluded from the current study, which was justified for the need to ensure strict grouping and no bias in the radiomics results.

In literature, a few studies have explored the differences in functional connectivity (FC) between the different Schizophrenia by analyzing gray matter volume (GMV), which is a challenge research area due to the fact that the characteristics of brain networks are still unknown. Zhu et al. aimed in their work to study the alterations of FC between deficient schizophrenia (DS) and non-deficient schizophrenia (NDS) based on the ROI obtained by ML algorithms and differential GMV. They investigated and analyzed the relationships between the alterations and the clinical symptoms were analyzed. In addition, the thalamic FC imbalance in the two groups was further explored using resting-state fMRI scans. Investigation on a cohort of 85 subjects (16 DS, 31 NDS, and 38 HC) was conducted based on GMV image data and support vector machine (SVM) to classify DS and NDS. Clinical scales including the Brief Psychiatric Rating Scale (BPRS), the Scale for the Assessment of Negative Symptoms (SANS), and the Scale for the Assessment of Positive Symptoms (SAPS) were also used for further evaluation. Brain regions with high weight in the classification were used as seed points in whole-brain FC analysis and thalamic FC imbalance analysis. Finally, partial correlation analysis explored the relationships between altered FC and clinical scale in the two subtypes. The results obtained a relatively high SVM-based classification accuracies and authors concluded that the ROI from GMV highlighted the difference in FC between DS and NDS from the local to the brain network, which provides new information for exploring the neural physiopathology of the two subtypes of schizophrenic. The findings of this study corroborate the previous conclusion of the hypothesis that thalamocortical imbalance in both of the two subtypes of schizophrenia. In addition, the FC value of THA.R and SMN in the DS group was negatively correlated with the SANS score, but the FC value of THA.R and SMN in the NDS group was positively correlated with the SAPS score, which deepens the understanding of the pathological mechanism of the two subtypes of schizophrenia. However, all the reported results utilized only SVM-based ML with a small imbalanced groups and larger samples in the future are needed to confirm current findings. Finally, the study only included the right thalamus in the study of thalamocortical imbalance, which will make the attribution of thalamic FC imbalance analysis in the two subtypes of schizophrenia incomplete.

Li et al., proposed deep learning method for objective assessment of chronic primary pain using the EEG and PLI matrices and frequency band data of auditory stimulation state. The aim was to distinguish among chronic primary pain (CPP), depressive disorder (DD), and HC subjects. The study was conducted on a cohort 67 subjects (23 healthy subjects, 22 patients with depression, and 22 patients with CPP) under the auditory oddball paradigm. The results showed that the CNN classification model of EEG is better than that of PLI, with the highest accuracy of 85.01% in Gamma band in former and 79.64% in Theta band in later. The study concluded that the current approach may be a step toward an EEG-based auxiliary diagnosis of CPP. Namely, the authors suggest that the EEG of each frequency band may play a role in the pathophysiology of CPP. Third, the abnormal pattern of EEG activity in CPP patients may represent a potential new therapeutic target, such as intervention through non-invasive brain stimulation technology or neural feedback methods targeting Theta and Gamma oscillation and FPN networks. In particular, the emerging transcranial magnetic stimulation can modulate the oscillation and synchronization of neurons at specific frequencies, so it may be a promising method for pain modulation (Polanía et al., 2018). This study has several limitations that should be considered. Firstly, the sample size was relatively small with only 67 subjects, limiting the generalizability of the findings. A larger and more diverse sample would increase the reliability and applicability of the method. Secondly, the study focused on a specific experimental condition and population, using EEG and PLI data collected under the auditory oddball paradigm. It is important to validate the results in different conditions and on a broader range of subjects to ensure the method's generalizability. Lastly, the choice of specific features, such as EEG and PLI matrices and frequency band data, may introduce biases and overlook other relevant information.

A similar study to Li et al. for major depressive disorder (MDD) was conducted by Zhang et al. to investigate common and unique patterns of homotopic connectivity and their relationships with clinical characteristics in patients with MDD. Experiments were conducted on balanced cohort (42 MDD patients and 42 HCs), where a range of clinical variables were collected for group comparisons using correlation analysis, SVM, and voxel-mirrored homotopic connectivity (VMHC). In particular, exploratory eye movement (EEM), event-related potentials (ERPs) and resting-state functional magnetic resonance imaging (rs-fMRI) data were analyzed. The study showed that patients with MDD showed decreased VMHC in the insula, and increased VMHC in the cerebellum 8/vermis 8/vermis 9 and superior/middle occipital gyrus. SVM analysis using VMHC values in the cerebellum 8/vermis 8/vermis 9 and insula, or VMHC values in the

1 www.itksnap.org

superior/middle occipital gyrus and insula as inputs can distinguish HCs and patients with MDD with high accuracy, sensitivity, and specificity. The study conclusion was that decreased VMHC in the insula and increased VMHC values in the sensory-motor networks may be a distinctive neurobiological feature for patients with MDD, which could potentially serve as imaging markers to discriminate HCs and patients with MDD. In total, there are still some limitations in this study. Clearly, this is a small preliminary report that needs to be replicated. Second, the study focused on patients who did not take medicine at the time of the first episode, and patients who had relapsed and did not take medicine for at least 2 weeks. The dissemination of research findings may be constrained for patients who experience relapses since the impact of antidepressant medications and number of episodes on brain spontaneous activity cannot be entirely ruled out. Also, the patients were scanned at baseline only and no investigation of neuronal activity after treatment were done.

An integrative prediction model, constructed based on radiomics of multiparametric MRI and clinical parameters was proposed by Wang et al. for predicting Sonic Hedgehog (SHH) and Group 4 (G4) molecular subtypes of pediatric medulloblastoma (MB). In their study, 7,045 radiomic features were extracted from T1-weighted (T1), contrast-enhanced T1 (T1c), T2-weighted imaging (T2), T2 fluid-attenuated inversion recovery imaging (T2FLAIR), and apparent diffusion coefficient (ADC) maps, using variance thresholding, SelectKBest, and Least Absolute Shrinkage and Selection Operator (LASSO) regression algorithms. Then, features were filtered (17 optimal features) using LASSO regression, and a logistic regression (LR) algorithm and Delong test was used to compare the differences between different models. The analysis was conducted on a retrospective preoperative MRI images and clinical data of 95 patients with MB, (47 and 48 cases of SHH and G4 subtypes, respectively). The overall testing accuracies based on the area under curve (AUC) of receiver operator characteristic (ROC) were 0.751 (95% CI: 0.587–0.915) and 0.849 (95% CI: 0.695–1.000), with and without clinical parameters, respectively (Delong's test with $p = 0.0144$). Decision curves and nomogram further validate that the combined model can achieve net benefits in clinical work and thus can potentially provide a non-invasive clinical approach to predict SHH and G4 molecular subtypes of MB preoperatively. Despite the promising results of the combined model, the study cohort has a small number of cases and the WNT and G3 groups were not included in the study. Further, the results of this study lack external validation to better assess the generalizability of the model.

A retrospective study by Bao et al. is conducted to assess/quantify hemodynamic parameters using CT angiography (CTA) in spontaneous vertebral artery dissection (sVAD). The authors investigated that if sVAD might tend to develop in vertebral artery hypoplasia (VAH) with hemodynamic dysfunction. The geometries of 14 patients (28 vessels) were reconstructed using Mimics and Geomagic Studio software from CTA. ANSYS ICEM and ANSYS FLUENT were utilized for mesh generation, set boundary conditions, solve governing equations, and perform numerical simulations. Slices were obtained at the upstream area, dissection or midstream area and downstream area of each VA. The blood flow patterns were visualized through instantaneous streamline and pressure at peak systole and late diastole. The hemodynamic parameters included pressure, velocity, time-averaged blood flow, time-averaged wall shear stress (TAWSS), oscillatory shear index (OSI), endothelial cell action potential (ECAP), relative residence time (RRT) and time-averaged nitric oxide production rate (TARNO). The study results showed a significant focal increased velocity in the dissection area of steno-occlusive sVAD with VAH compared to other nondissected areas (0.910 m/s vs. 0.449 vs. 0.566, $p < 0.001$). Also, focal slow flow velocity was observed in the dissection area of aneurysmal dilatative sVAD with VAH according to velocity streamlines. Based on the rsults, the authors concluded that steno-occlusive sVAD with VAH patients had abnormal blood flow patterns of focal increased velocity, low time-averaged blood flow, low TAWSS, high OSI, high ECAP, high RRT and decreased TARNO. These results provide a good basis for further investigation of sVAD hemodynamics and support the applicability of the CFD method in testing the hemodynamic hypothesis of sVAD. In summary, this study has several limitations that should be considered. Firstly, it had a retrospective design, which relies on existing data and may be subject to bias or incomplete information. Prospective studies would offer more robust data collection. Secondly, the study had a small sample size of only 14 patients, which limits the statistical power and generalizability of the findings. Additionally, the numerical simulations performed using ANSYS ICEM and ANSYS FLUENT are subject to certain assumptions and limitations. The accuracy of the results depends on the accuracy of the models and boundary conditions used in the simulations.

In total, the collection comprises 10 comprehensive papers that tackle different but extremely relevant to AI-based CAD systems for brain disorders. The issue papers focus on development of better diagnostic tools to analyze medical images/signals from patients with various brain disorders. We extend our heartfelt gratitude to all the contributing authors who submitted their exceptional research work, as their contributions have enriched the content and breadth of this publication. Furthermore, the guest editors would also like to acknowledge the contribution of many experts who have participated in the review process to select candidate papers for publications by providing helpful and constructive feedback to the authors to improve the contents and presentations of their articles. Finally, we would like to extend our gratitude to the Editor-in-Chief and the publishing team for their unwavering support throughout the different stages of this Research Topic. Their valuable input, suggestions, comments, and feedback have been instrumental in ensuring the success of this endeavor.

In conclusion, we believe that this Research Topic will make a notable contribution to the scientific community by disseminating cutting-edge research and fostering collaboration among researchers and practitioners in the field of AI-based CAD systems for brain disorders.

Author contributions

All authors have participated in preparing the Research Topic, managing the peer review of the submitted

manuscripts, and contributing to the writing and review of the editorial.

Conflict of interest

The authors declare that the research was conducted in the absence of any commercial or financial relationships that could be construed as a potential conflict of interest.

Publisher's note

All claims expressed in this article are solely those of the authors and do not necessarily represent those of their affiliated organizations, or those of the publisher, the editors and the reviewers. Any product that may be evaluated in this article, or claim that may be made by its manufacturer, is not guaranteed or endorsed by the publisher.

References

Polanía, R., Nitsche, M. A., and Ruff, C. C. (2018). Studying and modifying brain function with non-invasive brain stimulation. *Nat. Neurosci.* 21, 174–187. doi: 10.1038/s41593-017-0054-4

Segato, A., Marzullo, A., Calimeri, F., and De Momi, E. (2020). Artificial intelligence for brain diseases: a systematic review. *APL Bioeng.* 4, 041503. doi: 10.1063/5.0011697

Shalaby, A., Soliman, A., Elaskary, S., Refaey, A., Abdelazim, M., and Khalifa, F. (2023). Editorial: Artificial intelligence based computer-aided diagnosis applications for brain disorders from medical imaging data. *Front. Neurosci.* 17, 998818. doi: 10.3389/fnins.2023.998818

frontiers | Frontiers in Neuroscience

ORIGINAL RESEARCH
published: 19 July 2022
doi: 10.3389/fnins.2022.926486

Convolutional Neural Networks for Classification of T2DM Cognitive Impairment Based on Whole Brain Structural Features

Xin Tan[1,2], Jinjian Wu[1], Xiaomeng Ma[1], Shangyu Kang[1], Xiaomei Yue[1], Yawen Rao[1], Yifan Li[1], Haoming Huang[2], Yuna Chen[2], Wenjiao Lyu[1], Chunhong Qin[2], Mingrui Li[1], Yue Feng[1], Yi Liang[2] and Shijun Qiu[2]**

[1] First Clinical Medical College, Guangzhou University of Chinese Medicine, Guangzhou, China, [2] Medical Imaging Center, First Affiliated Hospital of Guangzhou University of Chinese Medicine, Guangzhou, China

OPEN ACCESS

Edited by:
Ahmed Refaey,
Manhattan College, United States

Reviewed by:
Ziliang Zhu,
University of North Carolina at Chapel Hill, United States
Zhen Yuan,
University of Macau, China
Feng Liu,
Tianjin Medical University General Hospital, China
Ruiwang Huang,
South China Normal University, China

***Correspondence:**
Shijun Qiu
qiu-sj@163.com
Yi Liang
lysogood@126.com

Specialty section:
This article was submitted to Brain Imaging Methods, a section of the journal Frontiers in Neuroscience

Received: 22 April 2022
Accepted: 22 June 2022
Published: 19 July 2022

Citation:
Tan X, Wu J, Ma X, Kang S, Yue X, Rao Y, Li Y, Huang H, Chen Y, Lyu W, Qin C, Li M, Feng Y, Liang Y and Qiu S (2022) Convolutional Neural Networks for Classification of T2DM Cognitive Impairment Based on Whole Brain Structural Features. Front. Neurosci. 16:926486. doi: 10.3389/fnins.2022.926486

Purpose: Cognitive impairment is generally found in individuals with type 2 diabetes mellitus (T2DM). Although they may not have visible symptoms of cognitive impairment in the early stages of the disorder, they are considered to be at high risk. Therefore, the classification of these patients is important for preventing the progression of cognitive impairment.

Methods: In this study, a convolutional neural network was used to construct a model for classifying 107 T2DM patients with and without cognitive impairment based on T1-weighted structural MRI. The Montreal cognitive assessment score served as an index of the cognitive status of the patients.

Results: The classifier could identify T2DM-related cognitive decline with a classification accuracy of 84.85% and achieved an area under the curve of 92.65%.

Conclusions: The model can help clinicians analyze and predict cognitive impairment in patients and enable early treatment.

Keywords: type 2 diabetes mellitus, cognitive impairment, classification, convolutional neural networks, MRI

INTRODUCTION

Type 2 diabetes mellitus (T2DM) can disrupt the balance that the human brain constructs for regulating blood glucose levels, which causes insulin resistance and elevated blood glucose levels. This may result in an imbalance of energy supply in the brain tissue, which can lead to irreversible damage over long term. During this process, some patients with T2DM may experience various cognitive impairments (Srikanth et al., 2020; You et al., 2021), including memory, executive ability, and affective disorders; T2DM is associated with a higher risk of dementia. Previous studies have shown that T2DM is one of the main risk factors for Alzheimer's disease (AD) (Biessels and Despa, 2018). Some patients with T2DM do not present cognitive impairment (T2DM-noCI); however, they belong to high-risk groups. This stage is the best intervention period to prevent the progression of cognitive impairment. Therefore, a classification model is important for clinicians to provide early treatment.

Previous neuroimaging studies established that extensive structural damage occurred in patients with T2DM. Geijselaers et al. (2015) confirmed that cognitive impairment in T2DM is

associated with impaired brain structure and is closely related to the stability of blood glucose levels and insulin resistance. Espeland et al. (2013) conducted a 3–6-year follow-up study on patients with T2DM, and they established that the probability of gray matter volume decreasing gradually increased with time, and the cortex gradually became thinner. Vergoossen et al. (2020) demonstrated abnormal changes in the structure of the white matter in patients with T2DM, and these abnormalities were correlated with cognitive impairments. Espeland et al. (2016) established that patients with T2DM had increased white matter hyperintensities and decreased brain tissue volume. However, the adverse effects of the brain structure could be reduced after controlling body weight. Erus et al. (2015) revealed that lower gray matter volumes are associated with long-term T2DM, and intensive glycemic treatment could slow down this process. Yao et al. (2021) established that the gray matter volume decreased in the limbic system. Lee et al. (2018) proved that the brain volume of patients with T2DM decreased to different degrees in subjects with mild cognitive impairment and dementia, which was closely related to the decrease in cognitive function. Sanjari Moghaddam et al. (2019) established that the white matter microstructure of some brain regions, such as the frontal lobe, temporal lobe, parietal lobe, and cingulate gyrus, was damaged, which was closely related to the decrease in memory and attention, information processing ability, as well as executive ability. Based on the results of previous studies on the structural abnormalities of the brain in patients with T2DM, we used high-resolution three-dimensional T1-weighted imaging (3D-T1) to obtain brain structural images of patients and used them for image recognition training of the classification model.

In recent years, the use of machine learning methods, such as support vector machines (SVMs), k-nearest neighbors, random forests, and other ensemble classifiers, to analyze MRI images to predict the disease stage of patients has achieved good results (Segar et al., 2019; Aminian et al., 2020; Gou et al., 2021; Huang et al., 2021). However, these conventional machine learning methods have significant limitations (Yamanakkanavar et al., 2020). Before analyzing the features extracted from the brain regions and predicting the results of patient status, it is necessary for the machine learning methods to select the brain regions with significant abnormalities manually. Artificial extractions are based on existing clinical or experimental experience, and they might overlook some useful areas that have not been found at present. Moreover, when the number of layers of the neural network is increased, the conventional network encounters problems such as local optimization, overfitting, and gradient diffusion.

Deep-learning technology is a branch of machine learning that imitates the thinking of the human brain. It applies a back-propagation learning algorithm to learn the parameters of a deep neural network (Carin and Pencina, 2018) and has the ability to represent learning and input information filtering layer-by-layer, which can realize end-to-end supervised and unsupervised learning. A convolutional neural network (CNN) is a deep neural network with a convolution structure inspired by the receptive field mechanism in biology (Qiu et al., 2018, 2020; Wen et al., 2020). This is a deep learning model for image processing. The CNN has two advantages over other machine learning methods. First, in addition to the full connection layer and the output layer, the neurons in the CNN use partial connections, whereas those in the conventional neural networks are all connected. Second, the CNN shares weights among the neurons in the same layer to reduce the complexity of the network model. These characteristics make the CNN more suitable for image feature learning and expression, as compared to other deep learning methods. To date, this model has been used for every major breakthrough in the field of image recognition. The CNN and many models derived from it have been used in classification tasks of cognitive impairments and they have achieved excellent results. Therefore, we used the CNN to construct a classification model for cognitive impairment in patients with T2DM.

RESEARCH DESIGN AND METHODS

Participants

In this study, 107 participants (45 T2DM patients with cognitive impairment and 62 without) from the Endocrine Department in the first affiliated hospital of Guangzhou University of Traditional Chinese Medicine were enrolled. T2DM was defined according to the latest criteria published by the American Diabetes Association: HbA1c $\geq$ 6.5% (48 mmol/mol); fasting blood glucose $\geq$ 7.0 mmol/L (126 mg/dL); oral glucose tolerance test 2 h postprandial blood glucose $\geq$11.1 mmol/L (200 mg/dL); symptoms of hyperglycemia or hyperglycemic crises; and random blood glucose$\geq$11.1 mmol/L (200 mg/dL), without symptoms of hyperglycemia, and the standard of 1 to 3 items was reviewed. Participants were excluded if they had a history of psychiatric diseases; stroke; epilepsy; head trauma; brain surgery; cerebrovascular accidents; obvious cognitive impairment who find it difficult to cooperate with the cognitive scale test; or had severe liver, kidney, or heart disease (like coronary heart disease, heart failure); and rheumatoid- and thyroid-related diseases (especially hyperthyroidism). A transient ischemia attack in the past 2 years, alcohol or tobacco abuse, severe hypertension (systolic pressure $\geq$ 160 mmHg or systolic pressure $\geq$ 110 mmHg), and contraindications to MRI were also exclusion criteria, as were specific brain abnormalities on conventional MR scans. Moreover, the patients with T2DM were excluded if they had unstable blood glucose control, acute or chronic metabolic complications of clinical diabetes and severe hypoglycemia, or a history of ketoacidosis.

Medical History and Biometric Measurements

Medical history and medication use were recorded with a standardized questionnaire, and patients in this study were mainly treated with insulin and metformin. Systolic and diastolic blood pressure, biometric examinations, and body mass index (BMI) were measured. The biometric examinations, including those of averaged fasting glucose, HbA1c, fasting C-peptide, total cholesterol, triglycerides, and low density lipoprotein were measured with standard laboratory testing.

Data Augmentation

The sample size for the training dataset was 74. To design a better model and improve the generalization ability of the model, we used 3D random rotation for data augmentation. The steps are as follows. First, MR images were normalized *via* nonlinear transformation and picture size adjustment. Second, we obtained the center coordinates of rotation, that is, the center coordinates of the image. Third, the rotation matrix, rotation box, rotation landmarks, and image rotation were achieved. Finally, the sample number was amplified 10 times that of the original data.

Cognitive Assessment

All participants underwent a series of neuropsychological tests that evaluated general cognitive function, memory, attention, executive function, and visuospatial skills, including the Montreal Cognitive Assessment (MoCA, Beijing edition), the auditory verbal learning test, the trail-making test, Grooved pegboard test, digit-symbol test, and digital sequence test. MoCA scores served as an index of the cognitive status, which divided our T2DM patients into two groups, T2DM patients with cognitive impairment (T2DM-CI) group and T2DM-noCI group. Participants whose MoCA score was less than 26 were considered to have cognitive impairment. The AVLT contains three parts, including immediate tasks, 5-min tasks, and 20-min delayed recall tasks, which were used to assess short-term and delayed memory, and the digital sequence test was used as a simple method to assess immediate memory. The trail-making tests were mainly used to evaluate attention and psychomotor speed. All the tests took approximately 30 min to administer.

MRI Dataset Acquisition

MRI 3D-T1 was acquired as the brain structural images to classify T2DM patients with and without cognitive impairment. Model training, internal validation, and testing were performed on the dataset.

MR images were all acquired with a 3T Siemens Prisma with an 8-channel head coil. Conventional brain axial T1-weighted, T2-weighted, and FLAIR images were obtained for every subject to exclude organic disease. Subjects were instructed to keep their eyes closed but to remain awake and to keep their heads still during the scan. Head motion was controlled as much as possible using foam padding, and scanner noise was reduced using earplugs. Structural images were acquired with the following parameters: TR = 2,000 ms, TE = 2.6 ms, inversion time = 450 ms, flip angle = 12°, matrix = 256×256, field of view = 250 ×250 mm, and 256 continuous sagittal slices with 1-mm thickness. The voxel of 3D-T1 image in this study was 1 ×1 ×1mm.

Brain Extraction

Before extracting the brain tissues, MRI images were first converted from DICOM format into ANALYZE in a recursive routine using the Python language. The brain extraction tool (BET) in the FMRIB Software Library was used to extract the brain tissue. The BET algorithm is a common brain tissue extraction method based on a deformable lattice model. The algorithm has high robustness and accuracy, and is computationally fast, making it a good method for extracting the brain tissue. This method first calculated the gray-scale image of MRI brain images and estimated three values, including the gray threshold, the maximum value, and the maximum value for distinguishing the brain and other tissues. Thereafter, the algorithm estimated the focus of the brain tissue and obtained the initial brain tissue according to the gray values. Finally, the initial brain surface was constructed using a 3D triangle facet. Tangential and smoothing forces were built in every triangle facet, which caused the initial brain surface to maintain a fixed distance and smoothness and made the brain surface sufficiently smooth and stable.

Features Addition

We selected 21 features, including clinical data and neuropsychological test scores. The clinical data included HbA1c, fasting blood glucose, fasting insulin, systolic blood pressure, total cholesterol, triglycerides, low-density lipoprotein, fasting C-peptide, and BMI. Neuropsychological test scores included the auditory verbal learning test (immediate, 5 mins, delay, recall), the trail-making test, Grooved pegboard test, the Mini-Mental State Exam, digit-symbol test, and digital sequence test. The features above were then filled with null values and normalized to 0–1, and then merged with the 3D image as an additional layer.

CNN Construction and Training

We constructed an 11-layer 3D CNN. The steps for constructing the network mainly included image input, convolution, rectified linear unit, pooling, and image classification. The network structures are listed in **Table 1**. In the table, the size of the input layer was 64 × 64 × 11, wherein 64 × 64 refers to the size of pixels, and 11 refers to the number of channels, which was obtained by 3D scaling of 256 layer images. Starting from the second row, the number in the second column represents that corresponding to the third column. For instance, 11 in the second row refers to 11 convolution layers. Subsequently, the model was trained. We input the images and evaluated the network after each loop, and training was stopped. The network was updated after 10 iterations with no loss improvement. The samples were normalized samples with mean 0 and var = 1 before being passed to the net. Randomized samples were selected from the dataset during training. We used a fold cross-validation to verify the stability of the model. In this model, the precision, accuracy, recall, F1 score, and area under the curve (AUC) were calculated. The formulae are as follows.

$$\begin{aligned} \text{Precision} &= \text{TP}/(\text{TP}+\text{FP}) \\ \text{Recall} &= \text{TP}/(\text{TP}+\text{FN}) \\ \text{Accuracy} &= (\text{TP}+\text{TN})/(\text{TP}+\text{FP}+\text{TN}+\text{FN}) \\ \text{F1 score} &= \text{P x R}/2(\text{P}+\text{R}) \end{aligned}$$

(TP: true positive, FP: false positive, TN:true negative, FN: false negative, P: precision, R: recall).

RESULTS

Characteristics of Patients

A total of 107 participants were recruited for this study, included 45 T2DM-CI and 62 T2DM-noCI. The average age of all patients was 48.78 years, and 59.81% of patients were men (64 of 107). Moreover, the average MoCA score of the patients was 25.15 (**Table 2**). Brain structural MRI data of the 107 patients enrolled.

Deep Learning Network Training and Performance

In this study, 74 samples were the training set and 33 samples were designed as the test set. The training set and the test set were randomly assigned. The training set included 42 T2DM patients with cognitive impairments and 32 without. The test set included 15 T2DM patients with cognitive impairments and 18 without. Initially, only 3D-T1 images were used to construct the model. The accuracy of the model was 75.80 % and it achieved an AUC of 74.27%. After adding 21 clinical features, the accuracy of the model was 84.85% (**Figure 1A**) and it achieved an AUC of 92.65% (**Figure 1B**). On the other hand, the precision of this model was 86.67%, the recall was 81.25%, and F1 score was 83.87%. Ten-fold cross validation was done and its AUC was 0.79231.

After the final training, we obtained the training curve (**Figure 2**). The loss curves of the training dataset and the test dataset showed a downward trend, and the overall success rate of learning was on the rise.

TABLE 1 | The information on the 11-layer 3D CNN.

	Number of layers	Layer category
Layer 1	1	input
Layer 2	11	conv
Layer 3	11	batchNorm
Layer 4	17	conv
Layer 5	17	batchNorm
Layer 6	34	conv
Layer 7	34	batchNorm
Layer 8	1,024	fc
Layer 9	2	fc
Layer 10	2	softmax
Layer 11	2	output

The input layer (Layer 1) size was 64 × 64 × 11.

TABLE 2 | Characteristics of included T2DM studies.

Characteristics	T2DM patients (n = 107) (mean ± SD)
Age (year)	48.78 ± 9.24
Sex (male/female)	64/43
Education level	10.27 ± 4.09
HbA1c % (mmol/mol)	9.34 ± 2.45
BMI (kg/m2)	24.23 ± 2.80
MoCA	25.15 ± 3.61

SD, standard deviation; HbA1c, glycated hemoglobin; BMI, body mass index; MoCA, Montreal Cognitive Assessment.

DISCUSSION

In this study, we employed a deep learning method for the classification of T2DM patients with and without cognitive impairments based on MRI 3D-T1 brain structural images. After brain extraction, data augmentation, and selection of 21 features to help neural networks learn, CNN construction, and training, we constructed a model for classification. After testing the test set and performing model validation of the training set, the loss curves showed a downward trend, and the overall success rate of learning increased, which indicated that the model had good discrimination ability. The model achieved performance with an AUC of 0.9265. The accuracy of classification was 84.85%.

The Clinical Significance of the Model

Previous studies have shown that greater cognitive decline occurs among patients with T2DM, as compared to the general nondiabetic population of the same age; therefore, T2DM patients may present cognitive disorders at an earlier age. However, although the incidence rate of T2DM individuals affected by cognitive dysfunction has gradually increased, sufficient clinical attention has not been paid to the development of cognitive impairments in patients with T2DM. Currently, some cognitive tests, such as the MoCA scale, are widely used in the clinical diagnosis of cognitive impairment. Many previous neuroimaging studies have used the MoCA scale for grouping. The MoCA scale can achieve relatively good accuracy for multiple samples. Recognizing its important role, this study used the MoCA scale for grouping. However, for individuals, it may produce some bias, which is closely related to the tester's test level, test environment, and subject's cooperation. Our model aims to use images as a more objective method to diagnose T2DM cognitive impairment. A scanned image can more objectively show pathological characteristics and significantly reduce human bias than manual classification using a scale.

Since the cause of AD is irreversible (Yang et al., 2021) and there is no cure, the early diagnosis of AD is crucial for treatments to slow down the development of the disease. Various studies have confirmed that T2DM is one of the main risk factors for AD, and patients may experience various cognitive impairments, such as memory loss, executive ability reduction, and affective disorder. In contrast to the cognitive impairments in AD, most of the cognitive dysfunctions in patients with T2DM are reversible. Specifically, the best stage to implement preventive measures is when T2DM patients present no cognitive impairment. However, in the research of classification and prediction models of cognitive impairments, most of them focus on AD, specifically the evolution and prediction of mild cognitive impairment (MCI) in AD. Few studies have focused on T2DM-related cognitive disorders. Lin et al. (2018) studied and classified the features of brain MRI images in patients with MCI and AD using multi-dimensional MRI information to establish an AD prediction model. Zhu et al. (2021) proposed a temporally

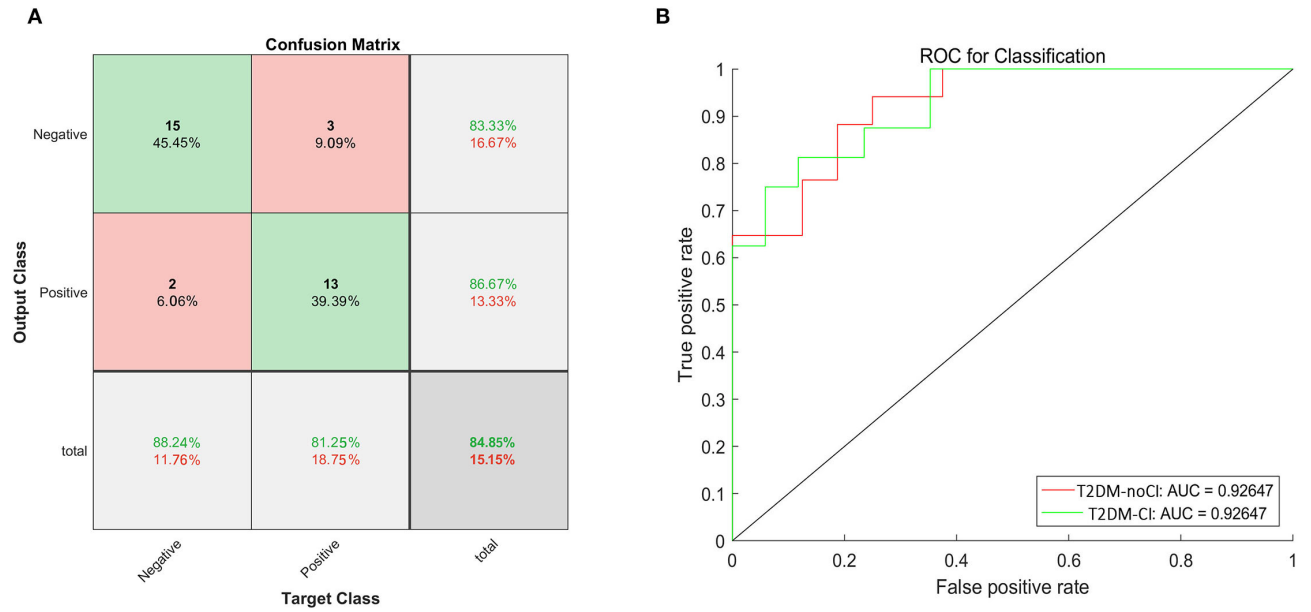

FIGURE 1 | The confusion matrix and the ROC curve of the test dataset. **(A)** The green boxes represent the true negative and positive rates, and the red boxes represent the false negative and positive rates. The dark gray boxes in the lower right corner represent the accuracy. The accuracy was 84.85%. **(B)** The ROC curve to classify cognition, the red line represented the ROC of T2DM-noCI, and the green line represented the ROC of T2DM-CI. The AUC was 92.65%.

structured SVM model to classify MCI and AD to achieve early detection and diagnosis. Hett et al. (2021) presented a novel graph-based grading framework to combine the features and a multiscale approach that enabled the analysis of alterations of whole-brain structures and classified MCI and AD with an AUC of 85%. Jin et al. (2020) used a deep learning model (3D attention network, 3DAN) to classify MCI and AD based on structural MRI; the model demonstrated good performance in predicting MCI subjects who will progress to AD with an accuracy of 72%. Jie et al. (2020) designed a wc-kernel-based CNN framework for learning the features of MCI and AD diagnosis using fMRI. These previous studies on cognitive impairment in AD can provide a methodological and theoretical basis for this study.

In this study, we combined imaging and clinical objective information and built a classification model using the CNN, which achieved performance with an AUC of 0.9265. The accuracy of classification was 84.85%. These results indicated that the model has good discrimination ability in classifying T2DM patients with and without cognitive impairments. It can help clinicians objectively analyze and predict the cognitive impairment of patients by combining imaging and clinical data, not by using neurological test scales alone, which may cause human error. In addition, according to the classification results, clinicians can treat patients at an early stage, as it is important to prevent the development of dementia and improve the quality of life of patients.

The Superiority of the Model

Before constructing the final model, we attempted to use 3D-T1 images only to construct the model. The accuracy rate reached 75.80%. As the sample size was not sufficiently large, the accuracy rate did not attain our expected goal; therefore, we added 21 clinical features to increase the stability of the model. Further research will expand the sample size, increase the accuracy of image diagnosis, and achieve an ideal classification effect. In day-to-day clinical work, doctors can make diagnoses using scanned images. The 21 clinical features included HbA1c, fasting blood glucose, fasting insulin, and systolic blood pressure. The selection of these clinical features was based on the degree to which they may affect T2DM or are closely related to the patient's cognition. For instance, the previous literature and our previous studies (Qin et al., 2019; Tan et al., 2019; Li et al., 2020) have confirmed that HbA1c is closely related to cognitive impairment in patients with T2DM. The higher the level of HbA1c, the more serious is the cognitive impairment of patients. In addition, cholesterol and triglycerides were confirmed to be related to a reduction in cognitive levels (Hakala et al., 2021). We did not consider diabetes duration as a clinical feature. As type 2 diabetes is a chronic disease with latent onset, we could not determine the exact onset time of disease in the patients. The onset time could be the time since the onset of the disease but not the real illness time. Moreover, the time of onset of type 2 diabetes can include the early asymptomatic stage. We believe that a sufficiently accurate estimation of the duration of diabetes cannot be achieved; therefore, we did not apply this index to the prediction model.

Few studies have been conducted on the classification of cognitive impairment in patients with T2DM. Most of these studies used conventional machine learning methods, such as the SVM classifier. Liu et al. (2019) marked whole-brain resting state functional connections (RSFCs) and used SVM

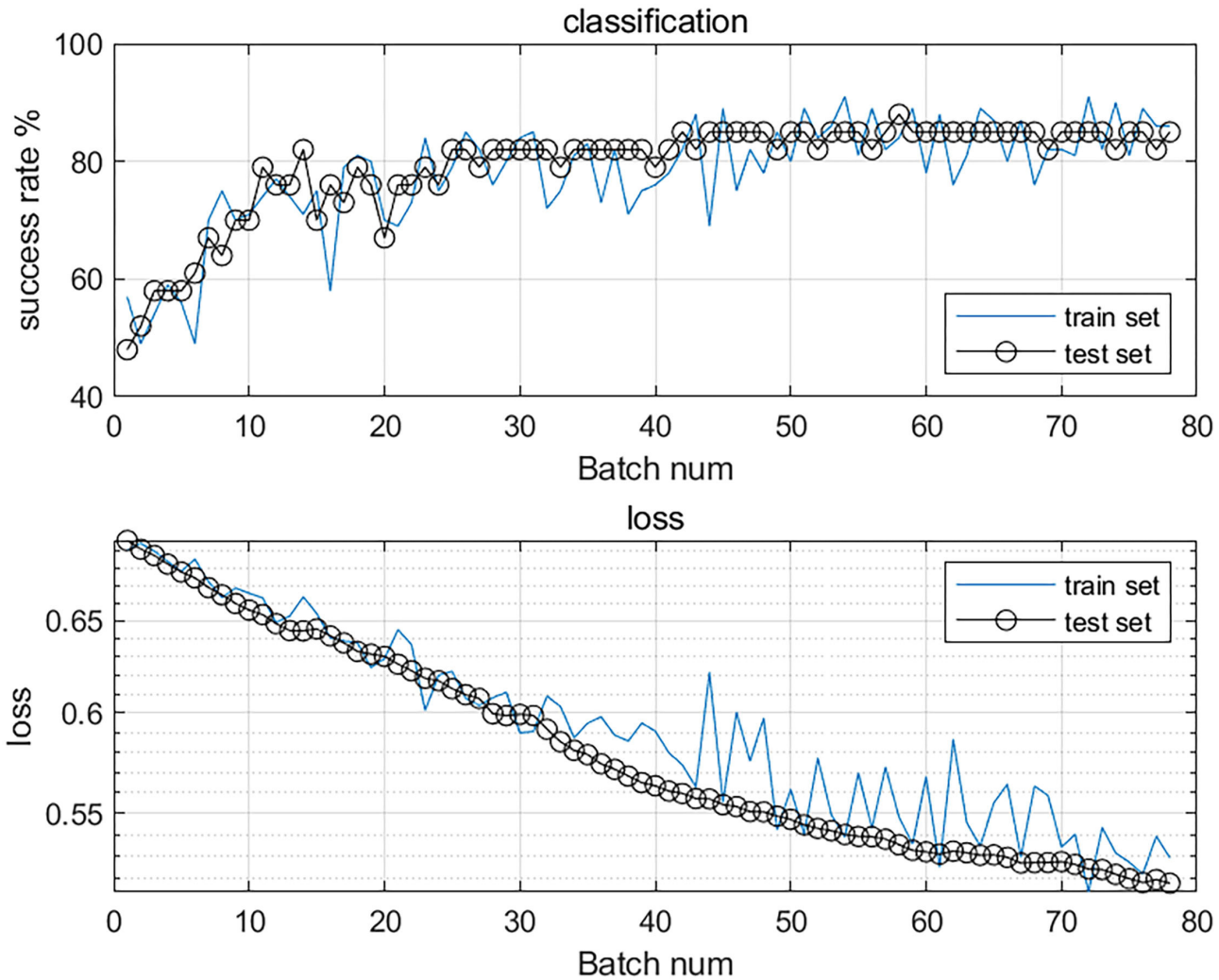

FIGURE 2 | The accuracy and loss value curves of the classification model. The top curve shows the overall success rate, the increasing success rate proves that its accuracy is improving. The bottom curve shows the loss curves of the training and test sets, the loss value is decreasing, which proves that the model is converging and has good stability.

to identify cognitive dysfunction in patients with T2DM. The SVM is one of the most common machine learning models. It can effectively distinguish features of different categories by constructing high-dimensional decision planes in feature space. It has an excellent performance in the case of small sample sizes and high dimensions; however, some of its disadvantages cannot be ignored. The extraction of image features is typically based on prior assumptions. Abnormal changes caused by T2DM might be overlooked because they are not considered in the assumptions, and some brain regions related to T2DM might not match the defined brain regions, resulting in a decline in the expression of the extracted regional features. Conversely, the features extracted by conventional machine learning methods rely on image preprocessing, such as strict registration and segmentation, and they need to go through various processing steps based on image denoising and normalization, which usually requires the guidance of experts in the field of brain science.

Deep learning is good at mining abstract-distributed feature representations from the original input data, and these representations have good generalization ability. Deep neural networks are the main forms at present, and CNN is one of the classic and widely used network structures. The CNN can effectively reduce the complexity of the network; reduce the number of training parameters; and make the model invariant to translation, distortion, as well as scaling. Thus, it has strong robustness as well as fault tolerance. Additionally, it is easy to train and optimize the network structure. It has significant advantages over shallow models in terms of feature extraction and model fitting. In this study, we used a 11-layer CNN to perform an automatic analysis of the whole-brain structure of patients with T2DM without extracting the relevant image features in advance, which reduced the experience difference. Moreover, we appropriately increased the depth of the network and added convolution layers, which extracted abstract

features and improved the accuracy of the classifier. Finally, a classification model of cognitive impairment in T2DM patients was constructed, and a good classification effect was achieved.

Our T2DM cognitive impairment classifier was a 3D-CNN model. 3D-CNN achieves the automatic classification of diagnostic images by capturing the anatomical shape changes of MRI on strictly registered MRI data, combining three 3D convolution layers with a two-layer fully connected network for global fine-tuning training (Dolz and Desrosiers, 2017). Most relative classification models used in previous studies were based on the 2D-CNN method. However, when using 2D images to study 3D neural images, the information between the 3D structures in the images is usually ignored. The 3D-CNN is more accurate in the feature extraction of spatial information, which means that the network has higher accuracy (Singh, 2020; Singh et al., 2020). In our CNN model, the features of the voxel model were extracted using convolution layers; the extracted features were integrated by pooling layers; and finally, the model was classified in the full connection layers.

CONCLUSION

In this study, we constructed a 3D 11-layer CNN model to classify T2DM patients with and without cognitive impairments. This model achieved performance with an AUC of 0.9265 and the accuracy of classification was 84.85%, which prompted to achieve a good classification effect. It can help clinicians objectively analyze and predict patients' cognitive impairment and provide treatments to the patients in the early stage. It is important to block or delay the development of dementia.

LIMITATION

The limitations of this study are as follows. First, the sample size of the current study may be relatively small, and future studies with larger sample sizes are required. Second, because our sample size was small, we could not group different ages, the degree of cognitive impairments, and drug treatments separately. In this study, we attempted to select patients with type 2 diabetes who are below 70 years, and the average age of our patients in this study was 48.78. However, the small sample size was unsuitable for further grouping. Further studies with larger samples can consider age grouping and have stricter control of drug use, which may make the model more objective. Third, brain structural images were used to construct a classification model. However, previous studies have shown that functional brain changes occur earlier than structural changes. Therefore, future studies using brain function images or multimodal MRI images of patients with T2DM to construct a classification model are necessary.

DATA AVAILABILITY STATEMENT

The raw data supporting the conclusions of this article will be made available by the authors, without undue reservation.

ETHICS STATEMENT

The studies involving human participants were reviewed and approved by the Ethics Committee of Guangzhou University of Traditional Chinese Medicine. The patients/participants provided their written informed consent to participate in this study.

AUTHOR CONTRIBUTIONS

JW, XM, SK, XY, YR, and HH collected the data. XT and SQ contributed to the study design, are the guarantors of this manuscript, had full access to all the data in the study, and took responsibility for the integrity of the data and the accuracy of the data analysis. XT wrote this manuscript. CQ, ML, YL, YC, WL, and YL performed the analysis. All authors contributed to the article and read and approved the final manuscript.

FUNDING

This work was supported by the grants from the Key International Cooperation Project of National Natural Science Foundation of China (81920108019) and the Medical Scientific Research Foundation of Guangdong Province (A2021182).

ACKNOWLEDGMENTS

The authors thank the staff of the Endocrine Department in the First Affiliated Hospital of Guangzhou University of Traditional Chinese Medicine for their important contributions.

SUPPLEMENTARY MATERIAL

The Supplementary Material for this article can be found online at: https://www.frontiersin.org/articles/10.3389/fnins.2022.926486/full#supplementary-material

REFERENCES

Aminian, A., Zajichek, A., Arterburn, D. E., Wolski, K. E., Brethauer, S. A., Schauer, P. R., et al. (2020). Predicting 10-year risk of end-organ complications of type 2 diabetes with and without metabolic surgery: a machine learning approach. *Diabetes Care.* 43, 852–859. doi: 10.2337/dc19-2057

Biessels G. J., and Despa F. (2018). Cognitive decline and dementia in diabetes mellitus: mechanisms and clinical implications. *Nat. Rev. Endocrinol.* 14, 591–604. doi: 10.1038/s41574-018-0048-7

Carin, L., and Pencina, M. J. (2018). On deep learning for medical image analysis. *JAMA.* 320, 1192–1193. doi: 10.1001/jama.2018.13316

Dolz, J., and Desrosiers, C. (2017). 3D fully convolutional networks for subcortical segmentation in MRI: a large-scale study. *Neuroimage.* 170, 456–470. doi: 10.1016/j.neuroimage.2017.04.039

Erus, G., Battapady, H., Zhang, T., Lovato, J., Miller, M. E., Williamson, J.D., et al. (2015). Spatial patterns of structural brain changes in type 2 diabetic patients and their longitudinal progression with intensive control of blood glucose. *Diabetes Care.* 38, 97–104. doi: 10.2337/dc14-1196

Espeland, M. A., Bryan, R. N., Goveas, J. S., Robinson, J. G., Siddiqui, M. S., Liu, S., et al. (2013). Influence of type 2 diabetes on brain volumes and changes in brain volumes: results from the women's health initiative magnetic resonance imaging studies. *Diabetes Care*. 36, 90–97. doi: 10.2337/dc12-0555

Espeland, M. A., Erickson, K., Neiberg, R. H., Jakicic, J. M., Wadden, T. A., Wing, R. R., et al. (2016). Brain and white matter hyperintensity volumes after 10 years of random assignment to lifestyle intervention. *Diabetes Care*. 39, 764–771. doi: 10.2337/dc15-2230

Geijselaers, S. L. C., Sep, S. J. S., Stehouwer, C. D. A., and Biessels, G. J. (2015). Glucose regulation, cognition, and brain MRI in type 2 diabetes: a systematic review. *Lancet Diabetes Endocrinol*. 3, 75–89. doi: 10.1016/S2213-8587(14)70148-2

Gou, W., Ling, C. W., He, Y., Jiang, Z., Fu, Y., Xu, F., et al. (2021). Interpretable machine learning framework reveals robust gut microbiome features associated with type 2 diabetes. *Diabetes Care*. 44, 358–366. doi: 10.2337/dc20-1536

Hakala, J.O., Pahkala, K., Juonala, M., Salo, P., Kähönen, M., Hutri-Kähönen, N., et al. (2021). Cardiovascular risk factor trajectories since childhood and cognitive performance in midlife: the cardiovascular risk in young finns study. *Circulation*. 143, 1949–1961. doi: 10.1161/CIRCULATIONAHA.120.052358

Hett, K., Ta, V. T., Oguz, I., Manjón, J. V., and Coupé, P. (2021). Multi-scale graph-based grading for Alzheimer's disease prediction. *Med. Image Anal*. 67, 101850. doi: 10.1016/j.media.2020.101850

Huang, Y., Sun, X., Jiang, H., Yu, S., Robins, C., Armstrong, M. J., et al. (2021). A machine learning approach to brain epigenetic analysis reveals kinases associated with Alzheimer's disease. *Nat. Commun*. 12, 4472. doi: 10.1038/s41467-021-24710-8

Jie, B., Liu, M., Lian, C., Shi, F., and Shen, D. (2020). Designing weighted correlation kernels in convolutional neural networks for functional connectivity based brain disease diagnosis. *Med. Image Anal*. 63, 101709. doi: 10.1016/j.media.2020.101709

Jin, D., Zhou, B., Han, Y., Ren, J., Han, T., Liu, B., et al. (2020). Generalizable, reproducible, and neuroscientifically interpretable imaging biomarkers for Alzheimer's disease. *Adv. Sci. (Weinh)*. 7, 2000675. doi: 10.1002/advs.202000675

Lee, A. K., Rawlings, A. M., Lee, C. J., Gross, A. L., Huang, E. S., Sharrett, A. R., et al. (2018). Severe hypoglycaemia, mild cognitive impairment, dementia and brain volumes in older adults with type 2 diabetes: the Atherosclerosis Risk in Communities (ARIC) cohort study. *Diabetologia*. 61, 1956–1965. doi: 10.1007/s00125-018-4668-1

Li, Y., Liang, Y., Tan, X., Chen, Y., Yang, J., Zeng, H., et al. (2020). Altered functional hubs and connectivity in type 2 diabetes mellitus without mild cognitive impairment. *Front. Neurol*. 11, 1016. doi: 10.3389/fneur.2020.01016

Lin, W., Tong, T., Gao, Q., Guo, D., Du, X., Yang, Y., et al. (2018). Convolutional neural networks-based MRI Image analysis for the Alzheimer's disease prediction from mild cognitive impairment. *Front. Neurosci*. 12, 777. doi: 10.3389/fnins.2018.00777

Liu, Z., Liu, J., Yuan, H., Liu, T., Cui, X., Tang, Z., et al. (2019). Identification of cognitive dysfunction in patients with T2DM using whole brain functional connectivity. *Genom. Proteom. Bioinform*. 17, 441–452. doi: 10.1016/j.gpb.2019.09.002

Qin, C., Liang, Y., Tan, X., Leng, X., Lin, H., Zeng, H., et al. (2019). Altered whole-brain functional topological organization and oognitive function in type 2 diabetes mellitus patients. *Front. Neurol*. 10, 599. doi: 10.3389/fneur.2019.00599

Qiu, S., Chang, G. H., Panagia, M,, Gopal, D. M., Au, R., and Kolachalama, V. B. (2018). Fusion of deep learning models of MRI scans, Mini-Mental State Examination, and logical memory test enhances diagnosis of mild cognitive impairment. *Alzheimer's Dementia*. 10, 737–49. doi: 10.1016/j.dadm.2018.08.013

Qiu, S., Joshi, P. S., Miller, M. I., Xue, C., Zhou, X., Karjadi, C., et al. (2020). Development and validation of an interpretable deep learning framework for Alzheimer's disease classification. *Brain*. 143, 1920–1933. doi: 10.1093/brain/awaa137

Sanjari Moghaddam, H., Ghazi Sherbaf, F., and Aarabi, M. H. (2019). Brain microstructural abnormalities in type 2 diabetes mellitus: a systematic review of diffusion tensor imaging studies. *Front. Neuroendocrinol*. 55, 100782. doi: 10.1016/j.yfrne.2019.100782

Segar, M. W., Vaduganathan, M., Pate,l K. V., McGuire, D. K., Butler, J., Fonarow, G. C., et al. (2019). Machine learning to predict the risk of incident heart failure hospitalization among patients with diabetes: the WATCH-DM risksScore. *Diabetes Care*. 42, 2298–2306. doi: 10.2337/dc19-0587

Singh, A. (2020). Deep learning 3D structures. *Nat. Methods*. 17, 249. doi: 10.1038/s41592-020-0779-y

Singh, S. P., Wang, L., Gupta, S., Goli, H., Padmanabhan, P., and Gulyás, B. (2020). 3D deep learning on medical images: a review. *Sensors (Basel)*. 20, 5097. doi: 10.3390/s20185097

Srikanth, V., Sinclair, A. J., Hill-Briggs, F., Moran, C., and Biessels, G. J. (2020). Type 2 diabetes and cognitive dysfunction-towards effective management of both comorbidities. *Lancet Diabetes Endocrinol*. 8, 535–545. doi: 10.1016/S2213-8587(20)30118-2

Tan, X., Liang, Y., Zeng, H., Qin, C., Li, Y., Yang, J., et al. (2019). Altered functional connectivity of the posterior cingulate cortex in type 2 diabetes with cognitive impairment. *Brain Imaging Behav*. 13, 1699–1707. doi: 10.1007/s11682-018-0017-8

Vergoossen, L. W., Schram, M. T., de Jong, J. J., Stehouwer, C. D., Schaper, N. C., Henry, R. M., et al. (2020). White matter connectivity abnormalities in prediabetes and type 2 diabetes: the maastricht study. *Diabetes Care*. 43, 201–208. doi: 10.2337/dc19-0762

Wen, J., Thibeau-Sutre, E., Diaz-Melo, M., Samper-González, J., Routier, A., Bottani, S., et al. (2020). Convolutional neural networks for classification of Alzheimer's disease: Overview and reproducible evaluation. *Med. Image Anal*. 63, 101694. doi: 10.1016/j.media.2020.101694

Yamanakkanavar, N., Choi, J. Y., and Lee, B. (2020). MRI segmentation and classification of human brain using deep learning for diagnosis of Alzheimer's disease: a survey. *Sensors (Basel)*. 20, 3243. doi: 10.3390/s20113243

Yang, P., Zhou, F., Ni, D., Xu, Y., Chen, S., Wang, T., et al. (2021). Fused sparse network learning for longitudinal analysis of mild cognitive impairment. *IEEE Trans. Cybern*. 51, 233–246. doi: 10.1109/TCYB.2019.2940526

Yao, L., Yang, C., Zhang, W., Li, S., Li, Q., Chen, L., et al. (2021). A multimodal meta-analysis of regional structural and functional brain alterations in type 2 diabetes. *Front. Neuroendocrin*. 62, 100915. doi: 10.1016/j.yfrne.2021.100915

You, Y., Liu, Z., Chen, Y., Xu, Y., Qin, J., Guo, S., et al. (2021). The prevalence of mild cognitive impairment in type 2 diabetes mellitus patients: a systematic review and meta-analysis. *Acta Diabetol*. 58, 671–685. doi: 10.1007/s00592-020-01648-9

Zhu, Y., Kim, M., Zhu, X., Kaufer, D., and Wu, G. (2021). Long range early diagnosis of Alzheimer's disease using longitudinal MR imaging data. *Med. Image Anal*. 67, 101825. doi: 10.1016/j.media.2020.101825

Conflict of Interest: The authors declare that the research was conducted in the absence of any commercial or financial relationships that could be construed as a potential conflict of interest.

The reviewer FL declared a past co-authorship with the author SQ to the handling editor.

Publisher's Note: All claims expressed in this article are solely those of the authors and do not necessarily represent those of their affiliated organizations, or those of the publisher, the editors and the reviewers. Any product that may be evaluated in this article, or claim that may be made by its manufacturer, is not guaranteed or endorsed by the publisher.

Copyright © 2022 Tan, Wu, Ma, Kang, Yue, Rao, Li, Huang, Chen, Lyu, Qin, Li, Feng, Liang and Qiu. This is an open-access article distributed under the terms of the Creative Commons Attribution License (CC BY). The use, distribution or reproduction in other forums is permitted, provided the original author(s) and the copyright owner(s) are credited and that the original publication in this journal is cited, in accordance with accepted academic practice. No use, distribution or reproduction is permitted which does not comply with these terms.

frontiers | Frontiers in Neuroscience

TYPE Original Research
PUBLISHED 09 January 2023
DOI 10.3389/fnins.2022.1050777

Check for updates

OPEN ACCESS

EDITED BY
Fahmi Khalifa,
Mansoura University, Egypt

REVIEWED BY
Nuwan Madusanka,
Inje University, South Korea
Subrata Bhattacharjee,
Inje University, South Korea

*CORRESPONDENCE
Rizwan Khan
✉ imrizvankhan@gmail.com

SPECIALTY SECTION
This article was submitted to Brain Imaging Methods, a section of the journal Frontiers in Neuroscience

RECEIVED 22 September 2022
ACCEPTED 05 December 2022
PUBLISHED 09 January 2023

CITATION
Khan R, Akbar S, Mehmood A, Shahid F, Munir K, Ilyas N, Asif M and Zheng Z (2023) A transfer learning approach for multiclass classification of Alzheimer's disease using MRI images. *Front. Neurosci.* 16:1050777. doi: 10.3389/fnins.2022.1050777

COPYRIGHT
© 2023 Khan, Akbar, Mehmood, Shahid, Munir, Ilyas, Asif and Zheng. This is an open-access article distributed under the terms of the Creative Commons Attribution License (CC BY). The use, distribution or reproduction in other forums is permitted, provided the original author(s) and the copyright owner(s) are credited and that the original publication in this journal is cited, in accordance with accepted academic practice. No use, distribution or reproduction is permitted which does not comply with these terms.

A transfer learning approach for multiclass classification of Alzheimer's disease using MRI images

Rizwan Khan[1]*, Saeed Akbar[2], Atif Mehmood[3,4], Farah Shahid[5], Khushboo Munir[6], Naveed Ilyas[7], M. Asif[8] and Zhonglong Zheng[1,9]

[1]Department of Computer Science and Mathematics, Zhejiang Normal University, Jinhua, China, [2]School of Computer Science, Huazhong University of Science and Technology, Wuhan, China, [3]Division of Biomedical Imaging, Department of Biomedical Engineering and Health Systems, KTH Royal Institute of Technology, Stockholm, Sweden, [4]Department of Computer Science, National University of Modern Languages, Islamabad, Pakistan, [5]Department of Computer Science, University of Agriculture, Sub Campus Burewala-Vehari, Faisalabad, Pakistan, [6]Department of Radiology and Diagnostic Imaging, University of Alberta, Edmonton, AB, Canada, [7]Department of Physics, Khalifa University of Science and Technology, Abu Dhabi, United Arab Emirates, [8]Department of Radiology, Emory Brain Health Center-Neurosurgery, School of Medicine, Emory University, Atlanta, GA, United States, [9]Key Laboratory of Intelligent Education Technology and Application of Zhejiang Province, Zhejiang Normal University, Jinhua, China

Alzheimer's is an acute degenerative disease affecting the elderly population all over the world. The detection of disease at an early stage in the absence of a large-scale annotated dataset is crucial to the clinical treatment for the prevention and early detection of Alzheimer's disease (AD). In this study, we propose a transfer learning base approach to classify various stages of AD. The proposed model can distinguish between normal control (NC), early mild cognitive impairment (EMCI), late mild cognitive impairment (LMCI), and AD. In this regard, we apply tissue segmentation to extract the gray matter from the MRI scans obtained from the Alzheimer's Disease National Initiative (ADNI) database. We utilize this gray matter to tune the pre-trained VGG architecture while freezing the features of the ImageNet database. It is achieved through the addition of a layer with step-wise freezing of the existing blocks in the network. It not only assists transfer learning but also contributes to learning new features efficiently. Extensive experiments are conducted and results demonstrate the superiority of the proposed approach.

KEYWORDS

Alzheimer's disease, multiclass classification, deep learning, MRI, early diagnosis of AD

1. Introduction

Alzheimer's is one of the most crucial causes of dementia all over the world. Several neurological illnesses, including dementia, afflict a sizable portion of the global population. Patients with Alzheimer show more clear symptoms after the age of 60. However, in some cases, as a result of some gene abnormalities, the symptoms may start to show up at a young age (30–50). Alzheimer's gives rise to functional and structural changes in the brain (Hampel et al., 2021). The progression of Alzheimer's disease (AD) from normal control (NC) spans over a number of years with some intermediate stages ranging from the development of early mild cognitive impairment (EMCI) to late mild cognitive impairment (LMCI). These changes can be observed through MRI images and blood plasma spectroscopy (Pan et al., 2020; Palmer et al., 2021).

Visualizing the MRI scans can somehow allow the physicians to detect the contraction of the gray matter. However, it is a complex process to detect these changes manually. Machine learning-based techniques for the classifications, such as support vector machines (SVMs), artificial neural networks (ANNs), and deep learning-based convolutional neural networks (CNNs), remained very useful in the detection of these minor tissue-level changes (Mehmood et al., 2021). It is important to note that SVM and ANN give local and global optimization-based solutions. However, deep learning-based CNNs consider the feature extraction and learning in the model itself and are considered to be more useful in medical image analysis (Pan et al., 2020; Cheng et al., 2022). But these methods are data-hungry and demand large-scale training datasets to learn the task (i.e., classification in this case) from scratch (Chen et al., 2022; Khan et al., 2022).

Recent advancements in imaging technology, including computerized axial tomography (CT), magnetic resonance images (MRI), and positron emission tomography (PET) (Masdeu et al., 2005; Han et al., 2022) images, have revolutionized the detection of Alzheimer's. Due to ionization effects and cost and computational complexity, gathering a large-scale data set for a particular task is very challenging. The 3D MRI images produced through high-dimensional diagnostic equipment contain several images in a single voxel. These voxels can help to diagnose Alzheimer's at an early stage (Zhang et al., 2019).

A deep Siamese convolution neural network (SCNN) for the multiclass classification of AD is proposed by Mehmood et al. (2020). A natural image-based network to represent neuroimaging data (NIBR-Net) is another significant approach in the target domain, based on a sparse autoencoder (Gupta et al., 2013), where the network learns from a set of bases from natural images with the help of convolution to extract features from the Alzheimer's Disease Neuroimaging Initiative (ADNI) dataset. This method selects the useful features in a single hierarchy while iteratively filtering the undesirable features. Considering the multiple classes of Alzheimer a deep learning-based multiclass classifier is proposed by Farooq et al. (2017). Apart from this, several computer-aided techniques have been suggested for diagnosing AD, especially in the case of severe dementia (Petot and Friedland, 2004; Acharya et al., 2021). Similarly, the issue of the imbalance of class data is handled by Murugan et al. (2021) with the help of a deep DEMNET by using the pre-processed dataset.

Training a neural network with a small-scale dataset (i.e., MRIs) with a higher prediction rate and a higher accuracy is a great challenge. In this study, we propose to utilize the pre-trained VGG16 and VGG19 models to predict NC, EMCI, LMCI, and AD. We extract the gray matter (GM) from the brain MRIs because using entire voxels or raw data directly to train neural networks also presents data management. We applied skull striping and tissue segmentation operations to segregate the full brain MRIs. Considering the data-hungry nature of the neural networks, we proposed to apply data augmentation to the extracted GM slices. It also resolves the challenges of overfitting, which is often aroused due to the unavailability of large-scale dataset. In addition, we step-wise freeze the blocks and add layers to transfer the features for accurate predictions on four classes of the input data, i.e., NC, EMCI, LMCI, and AD. Thus, we resolve the challenges of prospective fluctuations and imbalanced data size and class variation problems. The overall experimental evaluations and comparison with several state-of-the-art approaches demonstrate that the proposed transfer learning method outperformed the extant techniques, making it more suitable for future interactive Alzheimer's applications.

2. Related work

The fundamental causes of Alzheimer's are still unknown, and it is believed to be genetic (Adami et al., 2018). Alzheimer's affects a number of social cognitive capacities and results in several neurological conditions that are memory-related (Ramzan et al., 2020). According to an estimate, by the year 2050, 131.5 million individuals will be globally affected by Alzheimer's disease (AD) (Prince et al., 2015). It will become the top cause of death for older people as the number of patients grows daily. High-dimensional data from imaging modalities like MRI, fMRI, PET, amyloid-PET, diffusion tensor imaging, and neurological tests are essential parts of the existing strategies for the diagnosis (Tanveer et al., 2020; Afzal et al., 2021). However, differentiating between the patterns with radiological readings is still quite a difficult task due to the complexity of the minute patterns. As a result, it is difficult to establish an early diagnosis of Alzheimer's. Recently, several deep learning and machine learning-based techniques to enhance picture quality have been presented (Khan et al., 2019; Alenezi and Santosh,

2021). Additionally, the feature extraction- and classification-based approaches can be regularly employed to create prediction models for applications based on intelligent and expert systems (Mehmood et al., 2021; Shams et al., 2021; El-Hasnony et al., 2022).

The progression of Alzheimer's took several years, ranging from NC to MCI and AD. The development of MCI is also considered as early and late MCI (Sperling et al., 2011; Huang et al., 2018). It is imperative to diagnose the disease at an early stage, which is only possible through an accurate classification of various stages of disease (Khan et al., 2022). The recent developments in machine learning and deep learning-based methods can significantly contribute to the target domain (Tanveer et al., 2020). The extraction of the feature and identification of these features based on these techniques can ease the burden on the healthcare system (Razzak et al., 2022). The main objective of the binary class and multi-class classification is to distinguish the features of normal images from impaired images to detect the stage of the disease. Support vector machines (SVM), K-nearest neighbors (KNNs), fuzzy learning, decision trees, random forests, and dimensionality reduction algorithms, like principal component analysis, are readily used methods in traditional machine learning research (Vecchio et al., 2020). The feature extraction through CNNs and deployment of CNNs have revolutionized the whole process (Bi et al., 2020; Liang and Gu, 2021) and can yield acceptable results for the early detection of AD. CNN-based methods can adeptly learn the input images' features to identify a particular disease stage. Hao et al. (2020) suggested a multi-modal framework to extract neurological information from the MRIs in order to classify the various phases of dementia. In order to classify AD, NC, and MCI, Tong et al. developed a multimodal classification framework based on MRI, FDG, and PET scans (Tong et al., 2017). Other recent approaches for the classification of Alzheimer's (Tajbakhsh et al., 2016; Jain et al., 2019; Khan et al., 2019, 2022) can somehow resolve the challenges and some other tries to introduce some transfer learning based approaches (Afzal et al., 2021; Mehmood et al., 2021). However, it is still challenging to extract accurate features to distinguish the images and diagnose the disease at an early stage.

Considering the MRIs, a multi-modal framework is proposed to extract neurological features for the classification of various stages of dementia (Hao et al., 2020). Tong et al. proposed a multimodal classification for AD based on MRI, FDG, and PET images to classify AD, NC, and MCI. A multi-modal learning-based network (Liu et al., 2014) based on PET, and MRI images, a multi-modal stack-net (Shi et al., 2017), and a similarity matrix-based method are proposed by Zhu et al. (2014) based PET, CSF, and MRI biomarkers to distinguish various stages of AD. Some methods rely on the extraction of 2D slices, and some others utilize the whole voxel to distinguish several categories of disease (Payan and Montana, 2015; Islam and Zhang, 2018). A 3D deeply supervised adaptable convolutional neural network (CNN-3D) is proposed by Hosseini-Asl et al. (2018) to predict AD without relying on skull striping with generic feature learning through bio-markers. However, the data management challenges are still complex when handling medical images. In the case of the target problem gathering, a large-scale dataset is a great challenge as compared to ordinary computer vision and image processing tasks as we know that deep learning-based models are data-hungry and demand a large-scale dataset. Therefore, transfer learning approaches (Aderghal et al., 2018; Li et al., 2018; Basaia et al., 2019) are preferred, which utilize the weights from the pretrained models on the large scale datasets such as ImageNet (Mehmood et al., 2021).

To categorize the various stages of the disease with transfer learning, a deep Siamese convolution neural network (SCNN) for the multiclass classification of AD is proposed by Mehmood et al. (2020). A natural image-based network to represent neuroimaging data (NIBR-Net) is another significant approach in the target domain, based on sparse autoencoder (Gupta et al., 2013), where the network learns from a set of bases from natural images with the help of convolution to extract features from the ADNI dataset. A sparse multi-tasking deep learning-based method is proposed by Suk et al. (2016) with a feature adaptive weighting system. This method selects the useful features in a single hierarchy while iteratively filtering the undesirable features. Considering the multiple classes of Alzheimer, a deep learning-based multiclass classifier is proposed by Farooq et al. (2017). Apart from this, several computer-aided techniques have been suggested for diagnosing AD, especially in the case of severe dementia (Petot and Friedland, 2004). These models can assist the physicians in combination with computer-aided intelligent and expert systems (Jo et al., 2019) In this article, we proposed a multi-class classification network by using transfer learning through VGG architecture. We applied a step-wise block freezing strategy to the VGG-16 and VGG-19 models with some additional layers. The proposed method achieves higher accuracy and is capable of working with a small-scale dataset. The overall experimental evaluations demonstrate the superiority of the proposed method as compared to the state-of-the-art approaches.

3. The proposed methodology

In this study, we proposed a transfer learning-based multi-class classification for the early diagnosis of AD. The patients' data in this study was obtained from the ADNI database. We gathered 315-T1 weighted MRI images of four classes: NC, EMCI, LMCI, and AD. The processing overview of these images is shown in Figure 1. We extracted the gray matter through these 3D voxels and utilize these GM slices to train VGG architectures, as shown in Figure 2. We utilized the weights

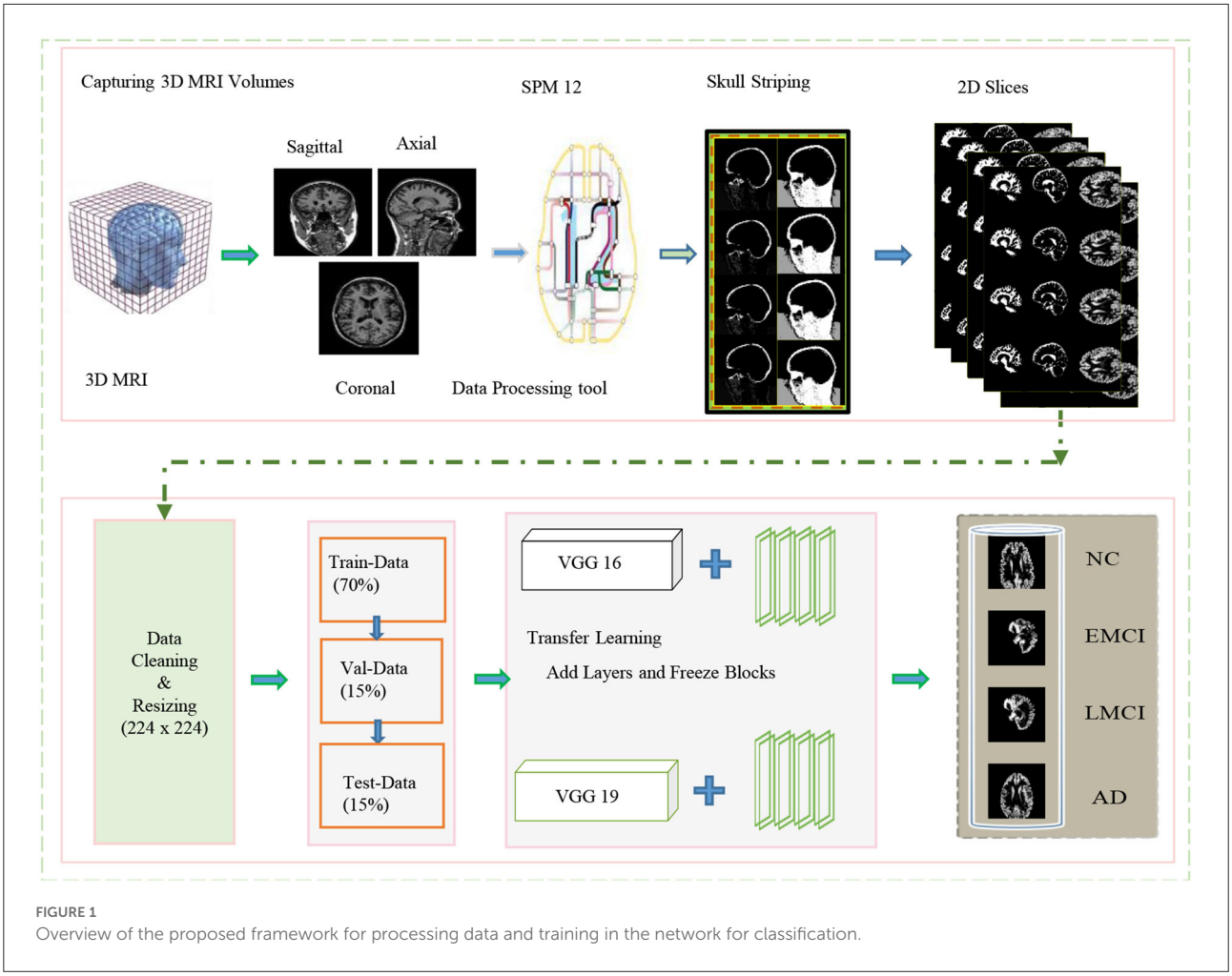

FIGURE 1
Overview of the proposed framework for processing data and training in the network for classification.

from the pre-trained network on ImageNet and adopted a layer-wise transfer learning while step-wise freezing the blocks. The proposed framework successfully classifies various stages of AD and yields significant results by using only a small-scale dataset.

3.1. Datasets and pre-processing on data

The magnetic resonance imaging technology is continually being improved and developed by researchers, and it has revolutionized the way neurological disorders are discovered and diagnosed. Whereas, the inconsistent intensity scale of the image makes it difficult to visualize and evaluate the data manually (Lundervold and Lundervold, 2019). It is essential to provide the correct information during learning if learning-based technologies are to produce accurate predictions. Thus, data preprocessing is a crucial step to manage to increase the contrast and pixel intensity. We applied several pre-processing operations on the available MRI scans of several patients obtained from the ADNI data repository. The specification of the dataset utilized in this work is shown in Table 1. A different number of subjects are selected to handle the class imbalance problem. We mainly exclude the opening and closing slices of the MRI due to the limited information contained in these slices. Images (i.e., 3D MRI scans) obtained from ADNI are available in neuroimaging informatics technology initiative (NIFTI) format. We pre-process these images by utilizing the statistical parametric mapping tool (SPM12) for the tissue-wise segmentation of the input into gray matter, white matter, and cerebrospinal fluid (CSF). We perform several operations (i.e., skull striping, registration, normalization, and segmentation) to extract the 2D-MRI PNG images from the available MRI scans.

In this study, we focused only on the gray-matter slices to detect the memory loss changes in early AD detection. We consider the ICBM space template for affine regularization and a bias regularization of $1e^{-}3$ with a full bias width at half maximum of 60 mm cutoff. Once these prepossessing operations are complete, we resize all the images to a size of 224×224. These images are suitable for training and testing and analogous to the size of ImageNet. The subjects involved in this dataset

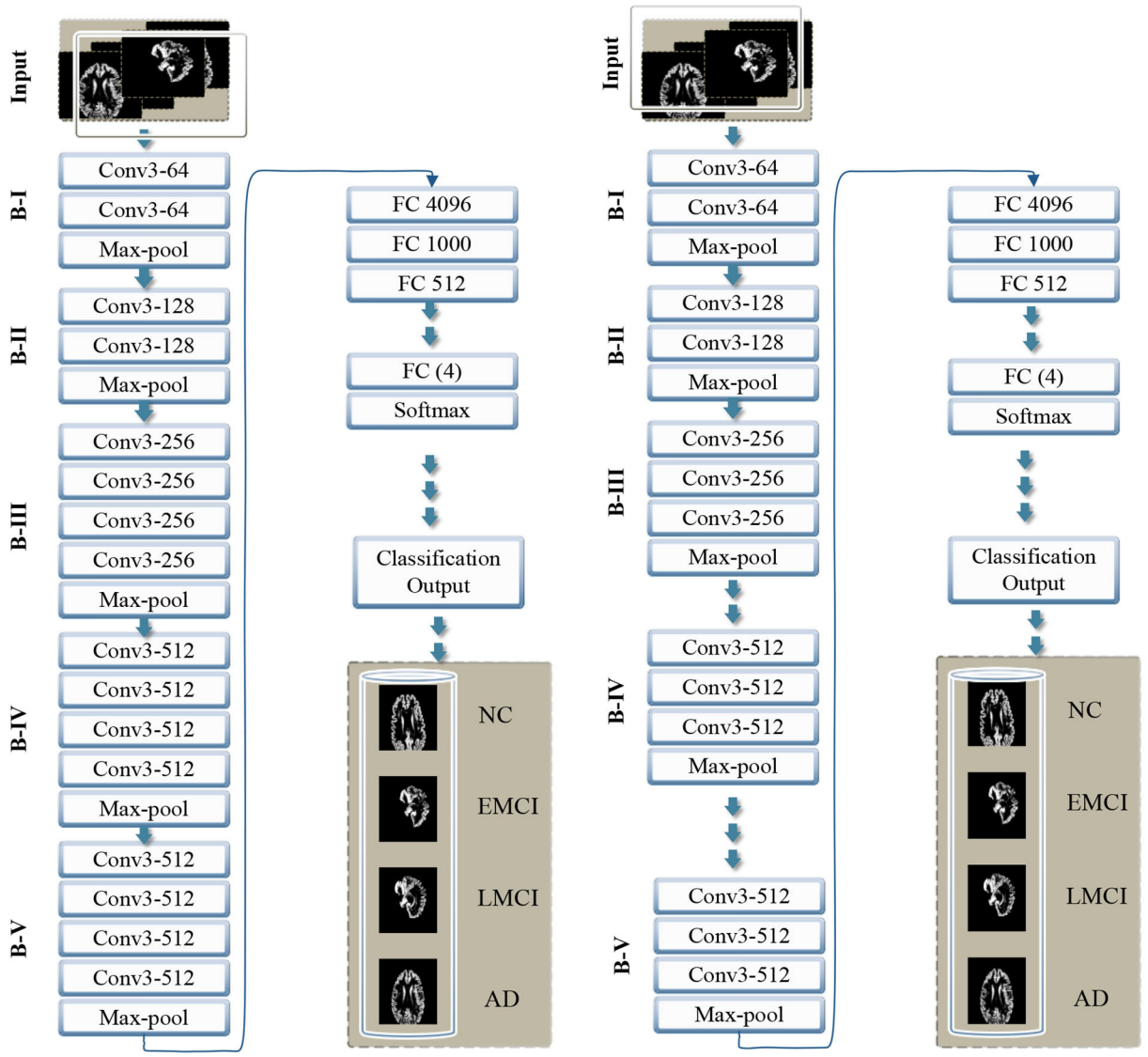

FIGURE 2
Overview of the proposed framework with step-wise block (B) representation as B-I to B-V. The left side shows VGG 16, and the right side shows the VGG 19 model with the proposed layer-wise transfer learning in both networks, blocks are frozen from B-I to B-V alternatively.

TABLE 1 Sample size of the dataset with specifications and number of subjects utilized for each class.

Type	Subjects	Age	MMSE	Slices
NC	75	73 ± 8.5	26.5 ± 1.4	4637
EMCI	75	74 ± 7.7	29.5 ± 1.2	1882
LMCI	80	72 ± 7.9	28.5 ± 1.6	4558
AD	85	75 ± 9.5	24.5 ± 1.9	3349

are scanned with respect to different durations of visits of the patients. Every scan is a different subject and contains the GM, WM, and CSF slices; of which, GM slices are fed to the network to interpret the usable information extracted through MRI volumes. In this regard, we split our dataset into training (70%), testing (15%), and validation data (15%).

4. Neural networks and transfer learning framework

Convolutional neural networks perform convolutional operations to extract the features from the input data. These features are learned during the training process. Later on, the network's prediction behavior determines the network's

learning quality. In artificial intelligence (AI), CNNs are distinguished from the other type of networks due to the superior performance of these networks in the multiple-image processing and visualization domains. The main type of layers in these networks are convolutional layers. These are the first layers that extract the features which are pooled with pooling layers. Finally, the fully connected layers are applied. Considering the recent advancements in AI and neural networks for feature extraction and associated task, we employed VGG 19 and VGG 16 architecture with a transfer learning approach for the target problem.

Transfer learning is a method for developing a predictive model for a separate but related problem that can then be utilized partially or entirely to speed up training and ultimately enhance the model's performance for the problem. It involves applying a previously trained model to new problems. Transfer learning-based techniques are now very popular in the field of medical image processing. Considering the advantages of automatic feature extraction and identification with the help of a pre-trained model have proved to be very useful in the target domain. Using a pre-trained model saves the time and effort of building a new model from scratch. It is also difficult to train a substantially large-scale network without amassing millions of annotated images. Therefore, using the pre-trained weights of a network with precise tuning on fresh data is a distinct and advantageous approach. Two models adopted in this study for transfer learning are pre-trained on the ImageNet database comprising millions of images.

The existing models, for example, Inception-Net with 23.62 million parameters, Xception-Net with 22.85 million, and ResNet with 23 million parameters, can also be used for transfer learning. However, considering the importance of the target problem, we selected VGG architecture with 138 million parameters. Feature transfer can be problematic in particular circumstances, such as when the datasets are small or imbalanced. Because transfer learning will not be effective if the final classification layer's characteristics are insufficient to distinguish the classes for a particular problem. Thus if the datasets are not comparable, the feature will hardly be transferred. We present transfer learning results in two categories, i.e., VGG 16 and VGG 19. Thus in each case, we propose to freeze some of the blocks in the network while freezing some fully connected layers.

5. VGG model with proposed transfer learning and experimental evaluations

The pretrained VGG-16 and VGG-19 models utilized in this study are trained on the ImageNet database. We consider freezing the weights and leveraging a pretrained convolutional base. We also include fully connected classification layers to transform the network for our multi-class classification task. The first layer in the model learn feature extraction. The initial layers learn to extract the generic features, and the final layers learn the target-oriented features. We added the new fully connected dense layers and performed several experiments with the rectified linear unit (ReLU) activation function. The main objective of the activation function is to induce non-linearity in the data. It can be expressed for an input value (v) as below.

$$ReLU(v) = max(0, v) \tag{1}$$

$$ReLU(x) = \begin{cases} 0, \text{ if v } < 0 \\ \text{x, if v} \geq 0 \end{cases} \tag{2}$$

The final layers in both of the models (i.e., VGG 16 and VGG 19) use the Softmax function. The number of neurons is reduced to 4 due to four classes (i.e., NC, EMCI, LMCI, and AD) in the target problem. The softmax function is the generalization of logistic regression, which is utilized in the classification of mutually exclusive classes. It converts the values to a normalized probability distribution of input for user display. Therefore, it is utilized at the final layer of the network and expressed as σ for input vector v_i and standard exponential e followed by a normalization factor with a summation $\sum$ at the bottom for the K number of classes in the multiclass classifier.

$$\sigma(\overrightarrow{v})i = \frac{e^{v_i}}{\sum_{j=1}^{k} e^{v_j}} \tag{3}$$

The loss function utilized in this regard is categorical cross-entropy loss which exponentially penalizes error in the probability prediction. The target problem involves predictions for more than one class, i.e., NC, EMCI, LMCI, and AD, and involves 4 labels. Therefore, loss function for the network also varies accordingly, and we consider categorical cross-entropy loss for these multiple-class classification problems. The categorical cross-entropy loss with p_i probabilities for i^{th} labels with truth values t_i, for the N number of classes is expressed as $\mathcal{L}_{CrE}$.

$$\mathcal{L}_{CrE} = \sum_{N=1}^{n} \sum_{i=1}^{n(size)} t_i log(p_i) \tag{4}$$

Our goal is to reduce the loss as much as possible. In each case, the cross-entropy for the i number of classes was estimated for the dementia's d_i, where $i = 1....5$ in this case. The probability of the output y for each class can be estimated for dementia, where the cross-entropy for each category NC, EMCI, LMCI, and AD is CE_{NC}, CE_{EMCI}, CE_{LMCI}, and CE_{AD}, respectively.

5.1. Experiments and evaluation metrics

We categorize our experiments based on VGG 16 and VGG 19 models. In each category, we perform several experiments. The overall performance is measured in terms of confusion matrices (Deng et al., 2016) where true positives (TP), true negatives (TN), false positives (FP), and false negatives (FN) give an overview of the accuracy, specificity, sensitivity, and precision. We also measure f1-score in addition to accuracy, specificity, sensitivity, and precision. Each column in the confusion matrix is a visual tool to understand the predicted score, where columns and rows show the true and predicted labels, respectively.

5.2. Evaluation metrics

In order to evaluate the performance of the proposed framework, the confusion matrix consists of TP, FP, TN, and FN. Thus, an overview of the confusion matrix gives a comprehensive overview of the F1-score, specificity (Sp), sensitivity (Se), accuracy (Ac), and precision (Pr) value because all of these metrics follow TP, TN, FP, and FN. Witten and Frank (2002). The mathematical expressions below depict this relationship explicitly.

5.2.1. Positive predictive value

The positive predictive value is called the precision and shows the portion of real positive cases.

$$Pr = \frac{TP}{TP + FP} \tag{5}$$

5.2.2. Sensitivity

Sensitivity is the recall value that shows the actual positive and the correctly predicted portion of values. This metric reflects correctly anticipated cases and depicts the coverage of real positive cases, also termed the true positive rate (TPR).

$$Se = \frac{TP}{TP + FN} \tag{6}$$

5.2.3. Specificity

Specificity is associated with the likelihood of a negative test rate in the absence of the condition and is considered a true negative rate.

$$Sp = \frac{TN}{TN + FP} \tag{7}$$

5.2.4. Accuracy

Classification accuracy is a statistical measurement that evaluates the performance of a classification model by dividing the number of correct predictions by the total number of predictions.

$$Ac = \frac{TP + TN}{TP + FN + TN + FP} \tag{8}$$

5.2.5. F1 measurement

The F-Metric is a method for combining accuracy and recall into a single measure that encompasses both and is widely utilized in classification tasks.

$$F1 - Measure = \frac{TP}{TP + \frac{1}{2}(FP + FN)} \tag{9}$$

In addition, we also present graphical and numeric results in terms of accuracy for each class.

5.3. Experimental settings and results

Experimental results for precision, accuracy, and F1 score of VGG 16 and VGG 19 (with and without data augmentation) are presented in the Table 2. In this table, we show the results for NC, EMCI, LMCI, and AD, respectively. The overall performance of the network with and without data augmentation is also shown in this table. The average accuracy of VGG 16 with and without data augmentation for all four classes is 96.39%. Similarly, the average accuracy of the VGG 19 with and without data augmentation for all four classes is 96.81%. This comparison demonstrates that VGG 19 performs slightly better than VGG 16. We also demonstrate the fact with the help of box plots shown in Figure 3. The results are shown for VGG 16 and VGG 19 with data augmentation (WDA) and without data augmentation (WODA).

The proposed framework's overall performance is much better compared to the existing methods. To demonstrate the fact we present the comparison of the proposed method with several state-of-the-art approaches. The results of this comparison are shown in Table 3. In addition, we also compare the performance of the proposed framework with other state-of-the-art models, including DenseNet, Inception ResNet V2, AlexNet, Inception V3, ResNet101, and ResNet50. The results for comparison of these methods with the proposed framework are shown in Table 4. This table shows that the proposed framework (i.e., VGG19+ALFB, VGG16+ALFB) outperformed the other models. To demonstrate the performance of our method with respect to the existing state-of-the-art approaches, we provide a comprehensive comparison with several methods. The competitor approaches include a deep sparse multi-task learning for feature selection in the diagnosis of AD (DSMAD-Net) (Suk et al., 2016), CNN-expedited (Wang et al., 2017)

TABLE 2 The comparison of the evaluation metrics in terms of precision, accuracy, and F1 score for VGG16 and VGG19 with and without data augmentation.

Model	VGG16 (Without DA)			VGG16 (With DA)		
Metrics	Precision	Accuracy	F1 Score	Precision	Accuracy	F1 Score
NC	91.71	99.20	95.30	97.65	99.40	98.51
EMCI	99.60	90.07	93.61	99.22	91.13	95
LMCI	96.06	99.85	97.91	96.46	99.70	96.02
AD	99.38	93.52	96.36	99.56	98.27	98.91
Model	VGG16 (Without DA)			VGG16 (With DA)		
Metrics	Precision	Accuracy	F1 Score	Precision	Accuracy	F1 Score
NC	97.65	97.41	96.82	97.27	99.80	98.51
EMCI	99.22	86.52	92.43	100	99.09	99.54
LMCI	96.46	99.41	97.91	98.41	100	99.19
AD	99.56	97.26	98.39	99.85	97.98	98.90

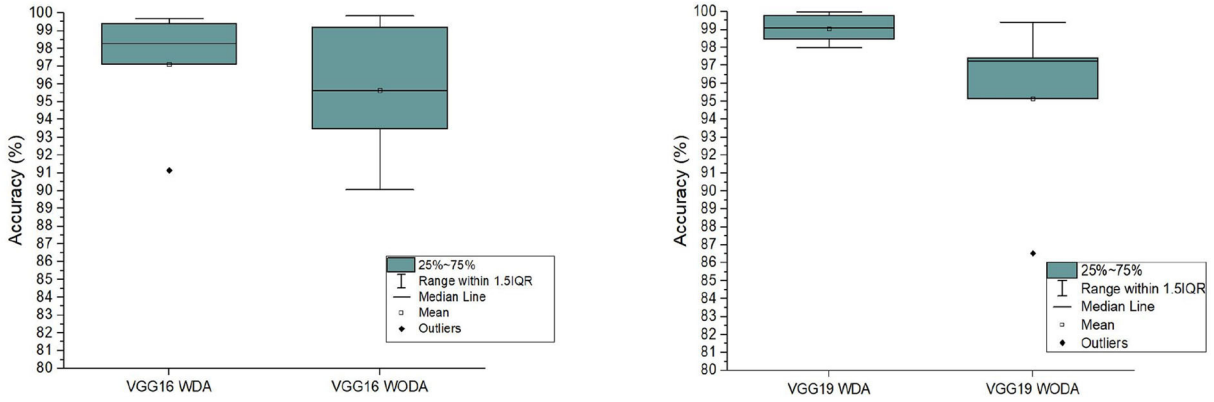

FIGURE 3
The comparison of the accuracy of the proposed frameworks with data augmentation (WDA) and without data augmentation (WODA).

classification of AD on imaging modalities (CAIM) (Aderghal et al., 2018), a transfer learning approach for the early diagnosis of AD on MRI image (TLEDA-Net) (Mehmood et al., 2021), multi-domain transfer learning (TL), a matrix similarity-based method (Zhu et al., 2014), multimodal learning (Liu et al., 2014), multimodal stacked Net (Shi et al., 2017), shape-attributes of brain structures as biomarkers for AD (SABS-AD) (Glozman et al., 2017), detecting AD on small dataset (Li et al., 2018), multimodal neuroimaging feature learning with multimodal stacked deep polynomial networks for diagnosis of AD (MMSPN-AD) (Basaia et al., 2019), multimodal classification of AD diagnosis (MMC-AD) (Tong et al., 2017), predicting AD with a 3D neural network (3D-CNN-PAD) (Payan and Montana, 2015), natural image bases to represent neuroimaging data (NIBR-Net) (Gupta et al., 2013), a differential diagnosis strategy (Sørensen et al., 2017), a transfer learning bases method (Naz et al., 2022), a convolutional neural networks-based MRI image analysis for the AD prediction from MCI (Lin et al., 2018), and a novel end-to-end hybrid network for AD detection using 3D CNN and 3D CLSTM (Xia et al., 2020). We performed several experiments, while the freezing pre-trained base and step-wise tested the performance for several blocks in VGG 16 and VGG 19. We include additional layers (ADL) and perform experiments with a block-freezing strategy. We independently present the results of the effects of the proposed changes on VGG16 and VGG19.

The results for the training loss and test accuracy with additional layers and frozen blocks in the VGG16 model is shown in Figure 4. The resulting confusion matrices to evaluate the network's performance in terms of true and predicted labels are shown in Figure 5. The confusion matrices are shown for (Figure 5A) without data augmentation and

TABLE 3 Comparison of the accuracy of the various state-of-the-art approaches with the proposed work.

References	Methods	Modalities	Distinction	Data	Accuracy (%)
Tong et al. (2017)	MMC-AD	MRI, FDG-PET	AD, NC, MCI	ADNI	72.9
Wang et al. (2017)	CNN-Expedited	MRI	NC, MCI	OASIS	90.6
Payan and Montana (2015)	3D-CNN-PAD	MRI	NC, MCI, AD	ADNI	85.3
Gupta et al. (2013)	NIBR-Net	MRI	NC, MCI, AD	ADNI	78.2
Cheng et al. (2017)	Multi-Domain TL	MRI	NC, MCI	ADNI	94.7
Sørensen et al. (2017)	Differential Diagnosis	sMRI+Volumetry HS+CT	MCI & AD	ADNI & AIBL	62.7
Zhu et al. (2014)	Matrix-Similarity	MRI+PET, CSF	MCI converter, MCI-NC, AD	ADNI	72.6
Liu et al. (2014)	Multimodal learning	MRI+PET	AD, NC, MCI	ADNI	53.8
Suk et al. (2016)	DSMAD-Net	MRI+PET	NC, MCI, AD	ADNI	62.9
Shi et al. (2017)	Multimodal Stacked Net	MRI+PET	AD,NC, cMCI/MCI	ADNI	57.0
Glozman et al. (2017)	SABS-AD, Transfer-Learning (ImageNet)	MRI	AD, MCI, NC	ADNI	83.5
Aderghal et al. (2018)	CAIM, Transfer-Learning	MRI	AD, MCI, NC (2-way classification)	ADNI	72.91
Li et al. (2018)	Transfer-Learning	MRI	AD,NC	ADNI	84
Shi et al. (2017)	MMSPN-AD, Transfer-Learning	MRI	AD,NC, MCI	ADNI	75.1
Lin et al. (2018)	CNN	MRI	MCI to AD conversion	ADNI	88.79
Xia et al. (2020)	3D CLSTM, CNN	MRI	AD,NC, MCI	ADNI	94.19
Mehmood et al. (2021)	TLEDA-Net	MRI	AD, MCI, LMCI, NC 2 way classification	ADNI	83.64
Naz et al. (2022)	Transfer learning (Avg on Vgg-19)	MRI	AD, MCI, NC 2 way classification	ADNI	98.12
VGG 19+ALFB (Ours)	Transfer-Learning (VGG16+ALFB)	MRI	NC, EMCI, LMCI, AD (4-way classification)	ADNI	98.47
VGG 16+ALFB (Ours)	Transfer-Learning (VGG16+ALFB)	MRI	NC, EMCI, LMCI, AD (4-way classification)	ADNI	97.12

TABLE 4 Comparison of the proposed architectures with adding layer and freezing blocks (ALFB) in VGG16 and VGG-19, with the existing state-of-the-art architectures in terms of accuracy.

Networks	Accuracy	Networks	Accuracy
DenseNet	92.70	Inception V3	88.33
Inception ResNetV2	85.82	ResNet101	91.56
AlexNet	89.33	ResNet50	93.98
VGG-19+ALFB (Ours)	98.47	VGG-16+ALFB (Ours)	97.12

(Figure 5B) with data augmentation. The comparison of the accuracy is shown in Table 2 for corresponding confusion matrices, the data augmentation slightly improves the network performance.

Similarly, for the VGG 19 model, we show the results for the training loss and testing accuracy in Figure 6, whereas the corresponding confusion matrices are shown in Figure 7. The comparison of the confusion matrices and the accuracy in Table 2 demonstrate that VGG 19 performs slightly better than VGG 16. Comparing the confusion matrices for both networks depicts that the data augmentation slightly improves the overall performance of the networks during transfer learning. In Table 2 we present the results for the specificity, sensitivity, and f1-score for VGG-16 and VGG19 with additional layers and freezing blocks. It depicts the performance and overall efficiency of the proposed method. To improve the robustness and fully-fine tune the model, we propose to increase the data size with data augmentation. It proved to be useful because gathering a large-scale dataset in the target domain is a great challenge. In comparison, the network-based methods are heavily dependent on large-scale datasets. The data augmentation improves the data's size significantly and resolves the challenges of class imbalance and over-fitting.

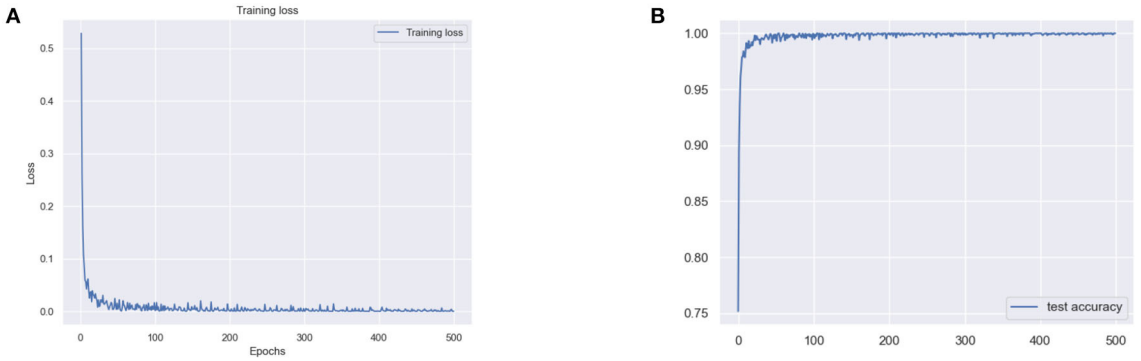

FIGURE 4
(A) Training loss and **(B)** test accuracy of the VGG 16 model with additional layer and freezing the block.

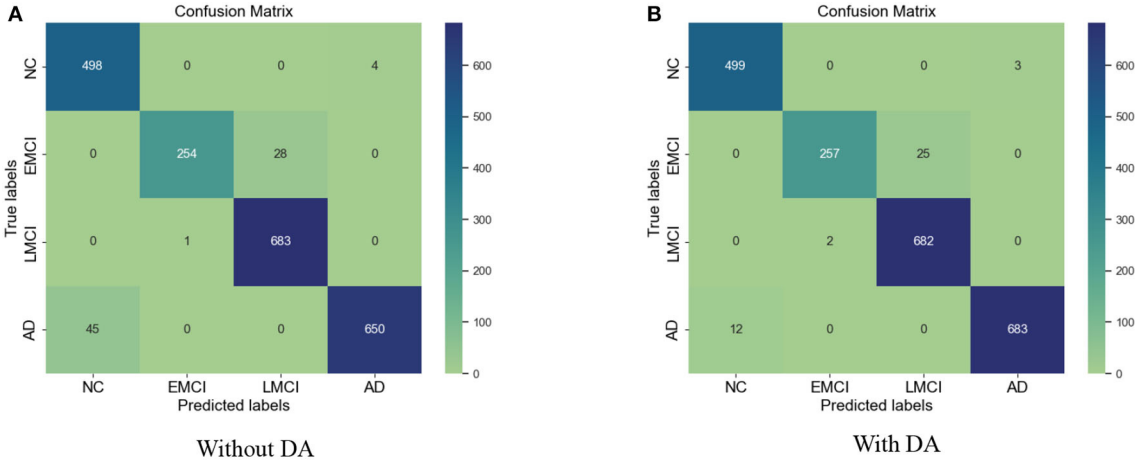

FIGURE 5
(A) Confusion matrix without augmentation. **(B)** Confusion matrix with augmentation for the VGG 16.

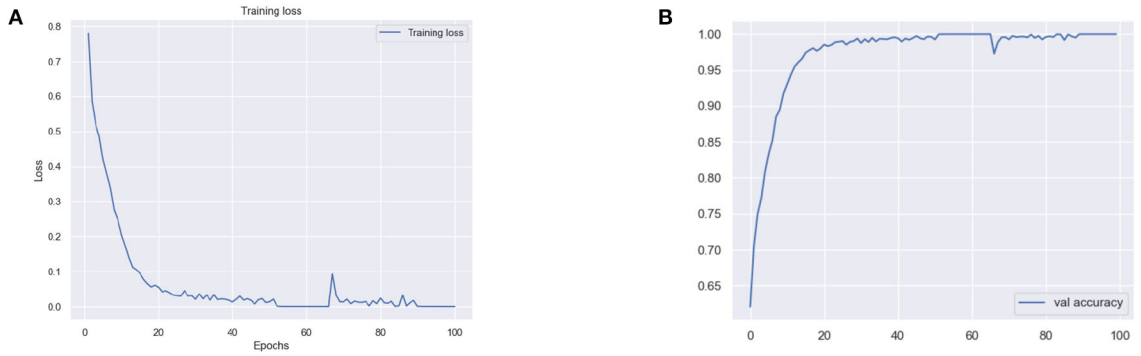

FIGURE 6
(A) Training loss and **(B)** validation (val) accuracy of the VGG 19 model with additional layer and freezing the blocks.

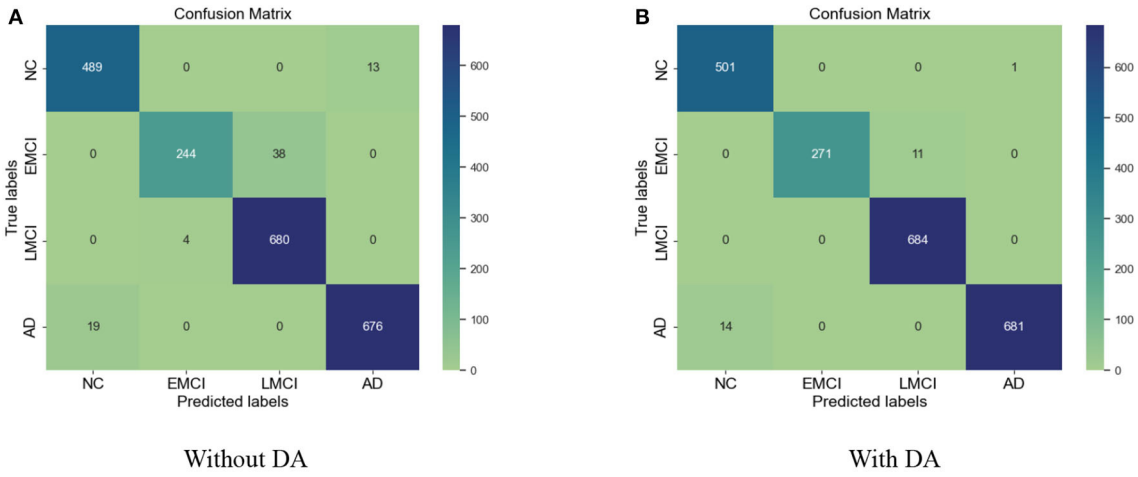

FIGURE 7
(A) Confusion matrix without data augmentation (DA). **(B)** Confusion matrix with DA for VGG 19.

6. Conclusion

This study presents a transfer learning-based approach to diagnose various stages of AD. We intend to automate the detection of various stages of Alzheimer's to ease the burden on the healthcare system. We use the pre-trained VGG architectures, i.e., VGG 16 and VGG 19, and propose a layer-wise transfer learning while adding layers and step-wise freezing the blocks in the pre-trained architecture. We leverage the pre-trained convolutional base, fine-tune the model for our 4-way classification on MRI images, and obtain state-of-the-art results in the target domain. The proposed layer-wise transfer learning significantly improves the framework's performance, where we also resolve the challenges of class imbalance and small data samples. The comparison with existing methods demonstrates that the proposed framework is superior in terms of accuracy and prediction. We achieved an accuracy of 97.89% for the proposed 4-way classification.

Data availability statement

The original contributions presented in the study are included in the article/supplementary material, further inquiries can be directed to the corresponding author.

Author contributions

RK contributes to the conceptualization, methodology, data curation, and writing of the original draft preparation with software and validation process. All authors also conceived in the process and approved the manuscript for submission.

Funding

This work was funded by the National Natural Science Foundation of China (NSFC62272419 and 11871438), the Natural Science Foundation of Zhejiang Province ZJNSFLZ22F020010, and Zhejiang Normal University Research Fund ZC304022915.

Acknowledgments

Data collection and sharing for this project was funded by the ADNI database (National Institutes of Health Grant U01 AG024904) and Department of Defense (DOD) ADNI (award number W81XWH-12-2-0012). ADNI is funded by the National Institute on Aging, the National Institute of Biomedical Imaging and Bioengineering, and through generous contributions from the following: AbbVie, Alzheimer's Association; Alzheimer's Drug Discovery Foundation; Araclon Biotech; BioClinica, Inc.; Biogen; Bristol-Myers Squibb Company; CereSpir, Inc.; Cogstate; Eisai Inc.; Elan Pharmaceuticals, Inc.; Eli Lilly and Company; EuroImmun; F. Hoffmann-La Roche Ltd. and its affiliated company Genentech, Inc.; Fujirebio; GE Healthcare; IXICO Ltd.; Janssen Alzheimer Immunotherapy Research & Development, LLC.; Johnson & Johnson Pharmaceutical Research & Development LLC.; Lumosity; Lundbeck; Merck & Co., Inc.; Meso Scale Diagnostics, LLC.; NeuroRx Research; Neurotrack Technologies; Novartis Pharmaceuticals Corporation; Pfizer Inc.; Piramal Imaging; Servier; Takeda Pharmaceutical Company; and Transition Therapeutics. The Canadian Institutes of Health Research is providing funds to support ADNI clinical sites in Canada.

Private sector contributions are facilitated by the Foundation for the National Institutes of Health (www.fnih.org). The grantee organization is the Northern California Institute for Research and Education, and the study is coordinated by the Alzheimer's Therapeutic Research Institute at the University of Southern California. ADNI data are disseminated by the Laboratory for Neuro Imaging at the University of Southern California. Data used in the preparation of this article were obtained from the ADNI database (http://adni.loni.usc.edu/). As such, the investigators within the ADNI contributed to the design and implementation of ADNI and/or provided data but did not participate in the analysis or writing of this report. A complete listing of ADNI investigators can be found at: http://adni.loni.usc.edu/wp-content/uploads/how_to_apply/ADNI_Acknowledgement_List.pdf.

Conflict of interest

The authors declare that the research was conducted in the absence of any commercial or financial relationships that could be construed as a potential conflict of interest.

Publisher's note

All claims expressed in this article are solely those of the authors and do not necessarily represent those of their affiliated organizations, or those of the publisher, the editors and the reviewers. Any product that may be evaluated in this article, or claim that may be made by its manufacturer, is not guaranteed or endorsed by the publisher.

References

Acharya, H., Mehta, R., and Singh, D. K. (2021). "Alzheimer disease classification using transfer learning," in *2021 5th International Conference on Computing Methodologies and Communication (ICCMC)* (Erode: IEEE), 1503–1508.

Adami, R., Pagano, J., Colombo, M., Platonova, N., Recchia, D., Chiaramonte, R., et al. (2018). Reduction of movement in neurological diseases: effects on neural stem cells characteristics. *Front. Neurosci.* 12, 336. doi: 10.3389/fnins.2018.00336

Aderghal, K., Khvostikov, A., Krylov, A., Benois-Pineau, J., Afdel, K., and Catheline, G. (2018). "Classification of Alzheimer disease on imaging modalities with deep cnns using cross-modal transfer learning," in *2018 IEEE 31st International Symposium on Computer-Based Medical Systems (CBMS)* (Karlstad: IEEE), 345–350.

Afzal, S., Maqsood, M., Khan, U., Mehmood, I., Nawaz, H., Aadil, F., et al. (2021). Alzheimer disease detection techniques and methods: a review. *Int. J. Interact. Multimedia Artif. Intell.* 6, 5. doi: 10.9781/ijimai.2021.04.005

Alenezi, F. S., and Santosh, K. C. (2021). Geometric regularized hopfield neural network for medical image enhancement. *Int. J. Biomed. Imaging* 2021, 6664569. doi: 10.1155/2021/6664569

Basaia, S., Agosta, F., Wagner, L., Canu, E., Magnani, G., Santangelo, R., et al. (2019). Automated classification of Alzheimer's disease and mild cognitive impairment using a single mri and deep neural networks. *Neuroimage Clin.* 21, 101645. doi: 10.1016/j.nicl.2018.101645

Bi, X., Li, S., Xiao, B., Li, Y., Wang, G., and Ma, X. (2020). Computer aided Alzheimer's disease diagnosis by an unsupervised deep learning technology. *Neurocomputing* 392, 296–304. doi: 10.1016/j.neucom.2018.11.111

Chen, Z., Wang, Z., Zhao, M., Zhao, Q., Liang, X., Li, J., et al. (2022). A new classification network for diagnosing Alzheimer's disease in class-imbalance mri datasets. *Front. Neurosci.* 16, 807085. doi: 10.3389/fnins.2022.807085

Cheng, B., Liu, M., Shen, D., Li, Z., and Zhang, D. (2017). Multi-domain transfer learning for early diagnosis of Alzheimer's disease. *Neuroinformatics* 15, 115–132. doi: 10.1007/s12021-016-9318-5

Cheng, D., Chen, C., Yanyan, M., You, P., Huang, X., Gai, J., et al. (2022). Self-supervised learning for modal transfer of brain imaging. *Front. Neurosci.* 16, 920981. doi: 10.3389/fnins.2022.920981

Deng, X., Liu, Q., Deng, Y., and Mahadevan, S. (2016). An improved method to construct basic probability assignment based on the confusion matrix for classification problem. *Inf. Sci.* 340, 250–261. doi: 10.1016/j.ins.2016.01.033

El-Hasnony, I. M., Elzeki, O. M., Alshehri, A., and Salem, H. (2022). Multi-label active learning-based machine learning model for heart disease prediction. *Sensors* 22, 1184. doi: 10.3390/s22031184

Farooq, A., Anwar, S., Awais, M., and Rehman, S. (2017). "A deep cnn based multi-class classification of Alzheimer's disease using MRI," in *2017 IEEE International Conference on Imaging Systems and Techniques (IST)* (Beijing: IEEE), 1–6.

Glozman, T., Solomon, J., Pestilli, F., Guibas, L., Initiative, A. D. N., et al. (2017). Shape-attributes of brain structures as biomarkers for Alzheimer's disease. *J. Alzheimers Dis.* 56, 287–295. doi: 10.3233/JAD-160900

Gupta, A., Ayhan, M., and Maida, A. (2013). "Natural image bases to represent neuroimaging data," in *International Conference on machiNE Learning* (PMLR), 987–994.

Hampel, H., Cummings, J., Blennow, K., Gao, P., Jack, C. R., and Vergallo, A. (2021). Developing the atx (n) classification for use across the Alzheimer disease continuum. *Nat. Rev. Neurol.* 17, 580–589. doi: 10.1038/s41582-021-00520-w

Han, H., Li, X., Gan, J. Q., Yu, H., Wang, H., Initiative, A. D. N., et al. (2022). Biomarkers derived from alterations in overlapping community structure of resting-state brain functional networks for detecting Alzheimer's disease. *Neuroscience* 484, 38–52. doi: 10.1016/j.neuroscience.2021.12.031

Hao, X., Bao, Y., Guo, Y., Yu, M., Zhang, D., Risacher, S. L., et al. (2020). Multi-modal neuroimaging feature selection with consistent metric constraint for diagnosis of Alzheimer's disease. *Med. Image Anal.* 60, 101625. doi: 10.1016/j.media.2019.101625

Hosseini-Asl, E., Ghazal, M., Mahmoud, A. H., Aslantas, A., Shalaby, A. M., Casanova, M. F., et al. (2018). Alzheimer's disease diagnostics by a 3d deeply supervised adaptable convolutional network. *Front. Biosci.* 23, 584–596. doi: 10.2741/4606

Huang, J., Chen, S., Hu, L., Niu, H., Sun, Q., Li, W., et al. (2018). Mitoferrin-1 is involved in the progression of Alzheimer's disease through targeting mitochondrial iron metabolism in a caenorhabditis elegans model of Alzheimer's disease. *Neuroscience* 385, 90–101. doi: 10.1016/j.neuroscience.2018.06.011

Islam, J., and Zhang, Y. (2018). Brain mri analysis for Alzheimer's disease diagnosis using an ensemble system of deep convolutional neural networks. *Brain Inform.* 5, 1–14. doi: 10.1186/s40708-018-0080-3

Jain, R., Jain, N., Aggarwal, A., and Hemanth, D. J. (2019). Convolutional neural network based Alzheimer's disease classification from magnetic resonance brain images. *Cogn. Syst. Res.* 57, 147–159. doi: 10.1016/j.cogsys.2018.12.015

Jo, T., Nho, K., and Saykin, A. J. (2019). Deep learning in Alzheimer's disease: diagnostic classification and prognostic prediction using neuroimaging data. *Front. Aging Neurosci.* 11, 220. doi: 10.3389/fnagi.2019.00220

Khan, N. M., Abraham, N., and Hon, M. (2019). Transfer learning with intelligent training data selection for prediction of Alzheimer's disease. *IEEE Access* 7, 72726–72735. doi: 10.1109/ACCESS.2019.2920448

Khan, R., Qaisar, Z. H., Mehmood, A., Ali, G., Alkhalifah, T., Alturise, F., et al. (2022). A practical multiclass classification network for the diagnosis of Alzheimer's disease. *Appl. Sci.* 12, 6507. doi: 10.3390/app12136507

Li, W., Zhao, Y., Chen, X., Xiao, Y., and Qin, Y. (2018). Detecting Alzheimer's disease on small dataset: a knowledge transfer perspective. *IEEE J. Biomed. Health Inform*. 23, 1234–1242. doi: 10.1109/JBHI.2018.2839771

Liang, S., and Gu, Y. (2021). Computer-aided diagnosis of Alzheimer's disease through weak supervision deep learning framework with attention mechanism. *Sensors* 21, 220. doi: 10.3390/s21010220

Lin, W., Tong, T., Gao, Q., Guo, D., Du, X., Yang, Y., et al. (2018). Convolutional neural networks-based mri image analysis for the Alzheimer's disease prediction from mild cognitive impairment. *Front. Neurosci*. 12, 777. doi: 10.3389/fnins.2018.00777

Liu, S., Liu, S., Cai, W., Che, H., Pujol, S., Kikinis, R., et al. (2014). Multimodal neuroimaging feature learning for multiclass diagnosis of Alzheimer's disease. *IEEE Trans. Biomed. Eng*. 62, 1132–1140. doi: 10.1109/TBME.2014.2372011

Lundervold, A. S., and Lundervold, A. (2019). An overview of deep learning in medical imaging focusing on mri. *Zeitschrift für Medizinische Physik* 29, 102–127. doi: 10.1016/j.zemedi.2018.11.002

Masdeu, J. C., Zubieta, J. L., and Arbizu, J. (2005). Neuroimaging as a marker of the onset and progression of Alzheimer's disease. *J. Neurol Sci*. 236, 55–64. doi: 10.1016/j.jns.2005.05.001

Mehmood, A., Maqsood, M., Bashir, M., and Shuyuan, Y. (2020). A deep siamese convolution neural network for multi-class classification of Alzheimer disease. *Brain Sci*. 10. doi: 10.3390/brainsci10020084

Mehmood, A., Yang, S., Feng, Z., Wang, M., Ahmad, A. S., Khan, R., et al. (2021). A transfer learning approach for early diagnosis of Alzheimer's disease on mri images. *Neuroscience* 460, 43–52. doi: 10.1016/j.neuroscience.2021.01.002

Murugan, S., Venkatesan, C., Sumithra, M., Gao, X.-Z., Elakkiya, B., Akila, M., et al. (2021). Demnet: a deep learning model for early diagnosis of Alzheimer diseases and dementia from mr images. *IEEE Access* 9, 90319–90329. doi: 10.1109/ACCESS.2021.3090474

Naz, S., Ashraf, A., and Zaib, A. (2022). Transfer learning using freeze features for Alzheimer neurological disorder detection using adni dataset. *Multimedia Syst*. 28, 85–94. doi: 10.1007/s00530-021-00797-3

Palmer, W. C., Park, S. M., and Levendovszky, S. R. (2021). Brain state transition analysis using ultra-fast fmri differentiates MCI from cognitively normal controls. *Front. Neurosci*. 16, 975305. doi: 10.3389/fnins.2022.975305

Pan, D., Zeng, A., Jia, L., Huang, Y., Frizzell, T., and Song, X. (2020). Early detection of Alzheimer's disease using magnetic resonance imaging: a novel approach combining convolutional neural networks and ensemble learning. *Front. Neurosci*. 14, 259. doi: 10.3389/fnins.2020.00259

Payan, A., and Montana, G. (2015). Predicting Alzheimer's disease - a neuroimaging study with 3d convolutional neural networks. *ArXiv*, abs/1502.02506. doi: 10.48550/arXiv.1502.02506

Petot, G. J., and Friedland, R. P. (2004). Lipids, diet and Alzheimer disease: an extended summary. *J. Neurol Sci*. 226, 31–33. doi: 10.1016/j.jns.2004.09.007

Prince, M. J., Wimo, A., Guerchet, M., Ali, G.-C., Wu, Y.-T., and Prina, M. A. (2015). *World Alzheimer Report 2015 - The Global Impact of Dementia: An Analysis of Prevalence, Incidence, Cost and Trends*. Available online at: https://www.alzint.org/u/WorldAlzheimerReport2015.pdf

Ramzan, F., Khan, M. U. G., Rehmat, A., Iqbal, S., Saba, T., Rehman, A., et al. (2020). A deep learning approach for automated diagnosis and multi-class classification of Alzheimer's disease stages using resting-state fmri and residual neural networks. *J. Med. Syst*. 44, 1–16. doi: 10.1007/s10916-019-1475-2

Razzak, I., Naz, S., Ashraf, A., Khalifa, F., Bouadjenek, M. R., and Mumtaz, S. (2022). Mutliresolutional ensemble partialnet forAlzheimer detection using magnetic resonance imaging data. *Int. J. Intell. Syst*. 37, 6613–6630. doi: 10.1002/int.22856

Shams, M. Y., Elzeki, O. M., Abouelmagd, L. M., Hassanien, A. E., Abd Elfattah, M., and Salem, H. (2021). Hana: a healthy artificial nutrition analysis model during covid-19 pandemic. *Comput. Biol. Med*. 135, 104606. doi: 10.1016/j.compbiomed.2021.104606

Shi, J., Zheng, X., Li, Y., Zhang, Q., and Ying, S. (2017). Multimodal neuroimaging feature learning with multimodal stacked deep polynomial networks for diagnosis of Alzheimer's disease. *IEEE J. Biomed. Health Inform*. 22, 173–183. doi: 10.1109/JBHI.2017.2655720

Sørensen, L., Igel, C., Pai, A., Balas, I., Anker, C., Lillholm, M., et al. (2017). Differential diagnosis of mild cognitive impairment and Alzheimer's disease using structural mri cortical thickness, hippocampal shape, hippocampal texture, and volumetry. *Neuroimage Clin*. 13, 470–482. doi: 10.1016/j.nicl.2016.11.025

Sperling, R. A., Aisen, P. S., Beckett, L. A., Bennett, D. A., Craft, S., Fagan, A. M., et al. (2011). Toward defining the preclinical stages of Alzheimer's disease: recommendations from the national institute on aging-Alzheimer's association workgroups on diagnostic guidelines for Alzheimer's disease. *Alzheimers Dement*. 7, 280–292. doi: 10.1016/j.jalz.2011.03.003

Suk, H.-I., Lee, S.-W., and Shen, D. (2016). Deep sparse multi-task learning for feature selection in Alzheimer's disease diagnosis. *Brain Struct. Funct*. 221, 2569–2587. doi: 10.1007/s00429-015-1059-y

Tajbakhsh, N., Shin, J. Y., Gurudu, S. R., Hurst, R. T., Kendall, C. B., Gotway, M. B., et al. (2016). Convolutional neural networks for medical image analysis: full training or fine tuning? *IEEE Trans. Med. Imaging* 35, 1299–1312. doi: 10.1109/TMI.2016.2535302

Tanveer, M., Richhariya, B., Khan, R. U., Rashid, A. H., Khanna, P., Prasad, M., et al. (2020). Machine learning techniques for the diagnosis of Alzheimer's disease: a review. *ACM Trans. Multimedia Comput. Commun. Appl*. 16, 1–35. doi: 10.1145/3344998

Tong, T., Gray, K., Gao, Q., Chen, L., Rueckert, D., Initiative, A. D. N., et al. (2017). Multi-modal classification of Alzheimer's disease using nonlinear graph fusion. *Pattern Recognit*. 63, 171–181. doi: 10.1016/j.patcog.2016.10.009

Vecchio, F., Miraglia, F., Alù, F., Menna, M., Judica, E., Cotelli, M. S., et al. (2020). Classification of Alzheimer's disease with respect to physiological aging with innovative eeg biomarkers in a machine learning implementation. *J. Alzheimers Dis*. 75, 1253–1261. doi: 10.3233/JAD-200171

Wang, S., Shen, Y., Chen, W., Xiao, T., and Hu, J. (2017). "Automatic recognition of mild cognitive impairment from MRI images using expedited convolutional neural networks," in *International Conference on Artificial Neural Networks* (Springer), 373–380.

Witten, I. H., and Frank, E. (2002). Data mining: practical machine learning tools and techniques with java implementations. *ACM Sigmod Rec*. 31, 76–77. doi: 10.1145/507338.507355

Xia, Z., Yue, G., Xu, Y., Feng, C., Yang, M., Wang, T., et al. (2020). "A novel end-to-end hybrid network for Alzheimer's disease detection using 3D CNN and 3D CLSTM," in *2020 IEEE 17th International Symposium on Biomedical Imaging (ISBI)* (Iowa City, IA: IEEE), 1–4.

Zhang, F., Tian, S., Chen, S., Ma, Y., Li, X., and Guo, X. (2019). Voxel-based morphometry: improving the diagnosis of Alzheimer's disease based on an extreme learning machine method from the adni cohort. *Neuroscience* 414, 273–279. doi: 10.1016/j.neuroscience.2019.05.014

Zhu, X., Suk, H.-I., and Shen, D. (2014). A novel matrix-similarity based loss function for joint regression and classification in ad diagnosis. *Neuroimage* 100, 91–105. doi: 10.1016/j.neuroimage.2014.05.078

frontiers | Frontiers in Neuroscience

TYPE Original Research
PUBLISHED 22 February 2023
DOI 10.3389/fnins.2023.1063391

Check for updates

OPEN ACCESS

EDITED BY
Ahmed Shalaby,
University of Louisville, United States

REVIEWED BY
Constantin-Cristian Topriceanu,
University College London, United Kingdom
Na Li,
Shandong Cancer Hospital, China

*CORRESPONDENCE
Lili Guo
✉ guolili163@163.com

SPECIALTY SECTION
This article was submitted to Brain Imaging Methods, a section of the journal Frontiers in Neuroscience

RECEIVED 07 October 2022
ACCEPTED 13 January 2023
PUBLISHED 22 February 2023

CITATION
Xu Q, Zhu Y, Zhang X, Kong D, Duan S, Guo L, Yin X, Jiang L, Liu Z and Yang W (2023) Clinical features and FLAIR radiomics nomogram for predicting functional outcomes after thrombolysis in ischaemic stroke. *Front. Neurosci.* 17:1063391. doi: 10.3389/fnins.2023.1063391

COPYRIGHT
© 2023 Xu, Zhu, Zhang, Kong, Duan, Guo, Yin, Jiang, Liu and Yang. This is an open-access article distributed under the terms of the Creative Commons Attribution License (CC BY). The use, distribution or reproduction in other forums is permitted, provided the original author(s) and the copyright owner(s) are credited and that the original publication in this journal is cited, in accordance with accepted academic practice. No use, distribution or reproduction is permitted which does not comply with these terms.

Clinical features and FLAIR radiomics nomogram for predicting functional outcomes after thrombolysis in ischaemic stroke

Qingqing Xu[1], Yan Zhu[1], Xi Zhang[1], Dan Kong[1], Shaofeng Duan[2], Lili Guo[1]*, Xindao Yin[3], Liang Jiang[3], Zaiyi Liu[4] and Wanqun Yang[4]

[1]Department of Radiology, The Affiliated Huaian No. 1 People's Hospital of Nanjing Medical University, Huaian, China, [2]GE HealthCare, Shanghai, China, [3]Department of Radiology, Nanjing Medical University Affiliated Nanjing Hospital, Nanjing, China, [4]Department of Radiology, Guangdong Academy of Medical Sciences, Guangdong Provincial People's Hospital, Guangzhou, China

Objective: We explored whether radiomics features extracted from diffusion-weighted imaging (DWI) and fluid-attenuated inversion recovery (FLAIR) images can predict the clinical outcome of patients with acute ischaemic stroke. This study was conducted to investigate and validate a radiomics nomogram for predicting acute ischaemic stroke prognosis.

Methods: A total of 257 patients with acute ischaemic stroke from three clinical centres were retrospectively assessed from February 2019 to July 2022. According to the modified Rankin scale (mRS) at 3 months, the patients were divided into a favourable outcome group (mRS of 0–2) and an unfavourable outcome group (mRS of 3–6). The high-throughput features from the regions of interest (ROIs) within the radiologist-drawn contour by AK software were extracted. We used two feature selection methods, minimum redundancy and maximum (mRMR) and the least absolute shrinkage and selection operator algorithm (LASSO), to select the features. Three radiomics models (DWI, FLAIR, and DWI-FLAIR) were established. A radiomics nomogram with patient characteristics and radiomics signature was built using a multivariate logistic regression model. The performance of the nomogram was evaluated in the test and validation sets. Ultimately, decision curve analysis was implemented to assess the clinical value of the nomogram.

Results: The FLAIR, DWI, and DWI-FLAIR radiomics model exhibited good prediction performance, with area under the curve (AUCs) of 0.922 (95% CI: 0.876–0.968), 0.875 (95% CI: 0.815–0.935), and 0.895 (95% CI: 0.840–0.950). The radiomics nomogram with clinical characteristics including the overall cerebral small vessel disease (CSVD) burden score, hemorrhagic transformation (HT) and admission National Institutes of Health Stroke Scale score (NIHSS) score and the FLAIR Radscore presented good discriminatory potential in the training set (AUC = 0.94; 95% CI: 0.90–0.98) and test set (AUC = 0.94; 95% CI: 0.87–1), which was validated in the validation set 1 (AUC = 0.95; 95% CI: 0.88–1) and

validation set 2 (AUC = 0.90; 95% CI: 0.768–1). In addition, it demonstrated good calibration, and decision curve analysis confirmed the clinical value of this nomogram.

Conclusion: This non-invasive clinical-FLIAR radiomics nomogram shows good performance in predicting ischaemic stroke prognosis after thrombolysis.

KEYWORDS

acute ischaemic stroke, diffusion-weighted imaging, outcome, radiomics, nomogram

1. Introduction

Stroke is the second leading cause of death and disability worldwide and the leading cause of death in China (GBD 2019 Stroke Collaborators., 2021). Ischaemic stroke (IS) accounts for 60–80% of all strokes and places a great burden on society due to its high mortality and disability rate (Cao et al., 2021). Recombinant tissue plasminogen activator alteplase (RT-PA) is the most effective drug for the treatment of acute ischaemic stroke. Although the majority of patients experience remission within the next 24 to 72 h, a significant number of patients continue to have dysfunction after thrombolytic therapy. Acute ischaemic stroke has a certain probability of hemorrhagic transformation (HT). Patients receiving intravenous thrombolytic therapy have an increased risk of hemorrhagic transformation, which may reduce or offset the benefit of thrombolytic therapy. Therefore, it is necessary to evaluate the basic clinical data of patients after they enter the emergency department to ensure the safety and effectiveness of intravenous thrombolysis. Cerebral small vessel disease (CSVD) refers to a series of pathological, imaging and clinical syndromes caused by various causes of cerebral arterioles, arterioles, venules, and capillaries (Wardlaw et al., 2013). In China, AIS caused by CSVD accounts for 25–50% (Huang, 2015). Most CSVD patients have an insidious onset and varied clinical manifestations. The presence and severity of symptoms depend on the location, degree and number of lesions. MRI findings can be used as a means to identify CSVD, mainly including residual small subcortical infarct (RSSI), cerebral microbleeds (CMB), white matter hyperintensities (WMH), perivascular spaces (PVS) and brain atrophy. This study retrospectively included the general clinical data and MRI findings of CSVD in patients with acute cerebral infarction undergoing intravenous thrombolysis who were followed up for 90 days. The purpose of this study was to analyse the correlation between the overall CSVD burden and the long-term prognosis of acute ischaemic stroke patients undergoing intravenous thrombolysis. Radiomics is a novel developed data analysis technique that can transform medical images into high-throughput quantitative features, assess the heterogeneity of diseased tissue, and reflect the physiological and pathological status and has been applied to the prediction of clinical outcomes. At present, radiomics has a promising application prospect in stroke, including the diagnosis of stroke (Peter et al., 2017),early prediction of clinical outcome (Wen et al., 2020) and evaluation of medium and long term prognosis (Tang et al., 2020; Quan et al., 2021; Wang et al., 2021; Zhou et al., 2022). Wen et al. (2020) developed a model based on radiological features extracted from computed tomography non-contrast computed tomography (NCCT) and computed tomography angiography (CTA) to predict the development of malignant acute middle cerebral Artery Infarction (mMCAi) in patients with cerebral infarction. Several recent studies have shown that the clinical-radiomics model extracted from diffusion-weighted imaging (DWI), fluid attenuated inversion recovery (FLAIR) or apparent diffusion coefficient (ADC) achieved satisfactory performance in predicting AIS outcomes (Tang et al., 2020; Quan et al., 2021; Wang et al., 2021; Zhou et al., 2022). Most patients with ischaemic stroke receive only routine sequences, including DWI, ADC and FLAIR. DWI can accurately describe the tissue spread and reflect the microstructure of the lesions, and the FLAIR sequence has a higher resolution and can provide more useful information. However, ADC represents the mean value of infarcts. Currently, no studies to date have combined radiomics and the CSVD burden score to predict the prognosis of AIS patients. Therefore, the purpose of this study was to explore the predictive value of DWI and FLAIR-based radiomics combined with the CSVD burden score in ischaemic stroke and to create a method that can be used in the management strategy of ischaemic stroke. Finally, an independent external validation set was used to validate the performance of the radiomics nomogram.

2. Subjects and methods

2.1. Subjects

A total of 257 patients from three clinical centres with acute infarction diagnosed by DWI after thrombolysis from February 2019 to July 2022 were retrospectively enrolled. Then, 166 patients from our hospital with a Siemens MR scanner were assigned to the training and test sets, and 41 patients from our hospital with a Philips MR scanner were assigned to the external validation set1 and 50 patients from other two clinical centres were assigned to external validation set 2. Distribution diagram of enrolled subjects in training set, test set, and external validation sets was showed in **Figure 1**. The inclusion criteria were as follows: (1) the time interval from onset to MR examination was ≤72 h; and (2) the patient had no old cerebral infarction and could live independently before the infarction. The exclusion criteria were as follows: (1) previous intracerebral haemorrhage, brain trauma, previous neurological disease, and severe artefacts on DWI or FLAIR images. (2) Lacunar cerebral infarct (≤ 10 mm). (3) Acute infarction of the posterior circulation. This study was a retrospective study and was approved by the ethics committee of our hospital. The requirement for informed consent was waived. Authors confirm that all methods

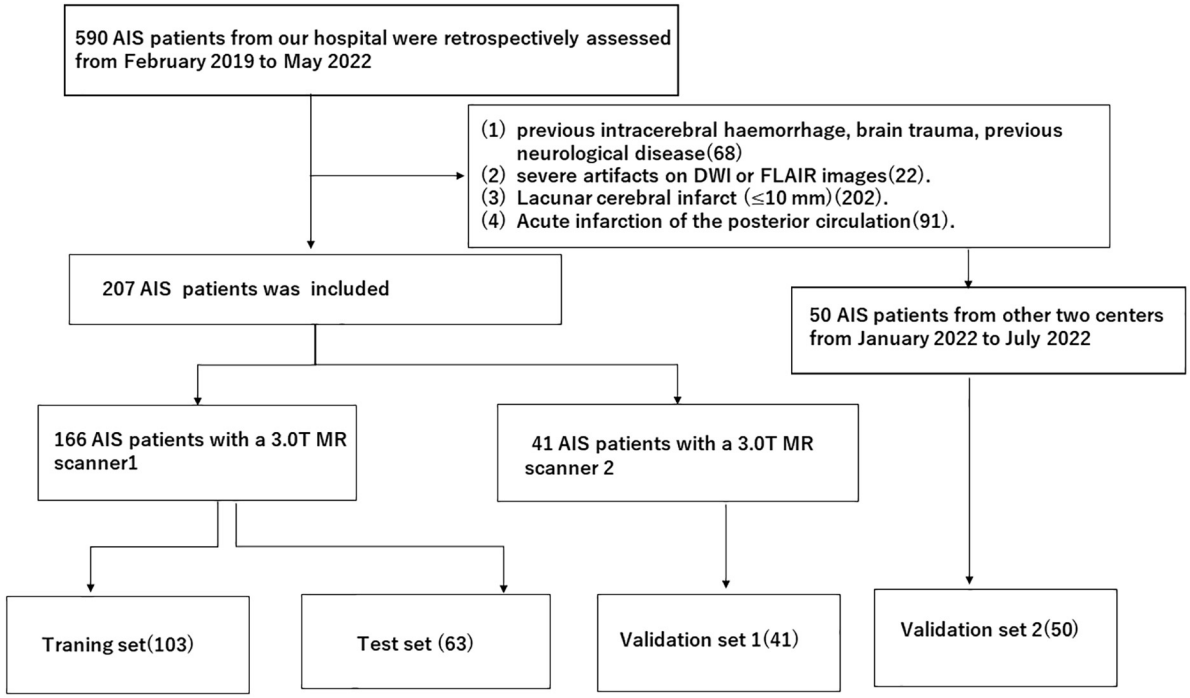

FIGURE 1
Distribution diagram of enrolled subjects in training set, test set and external validation sets.

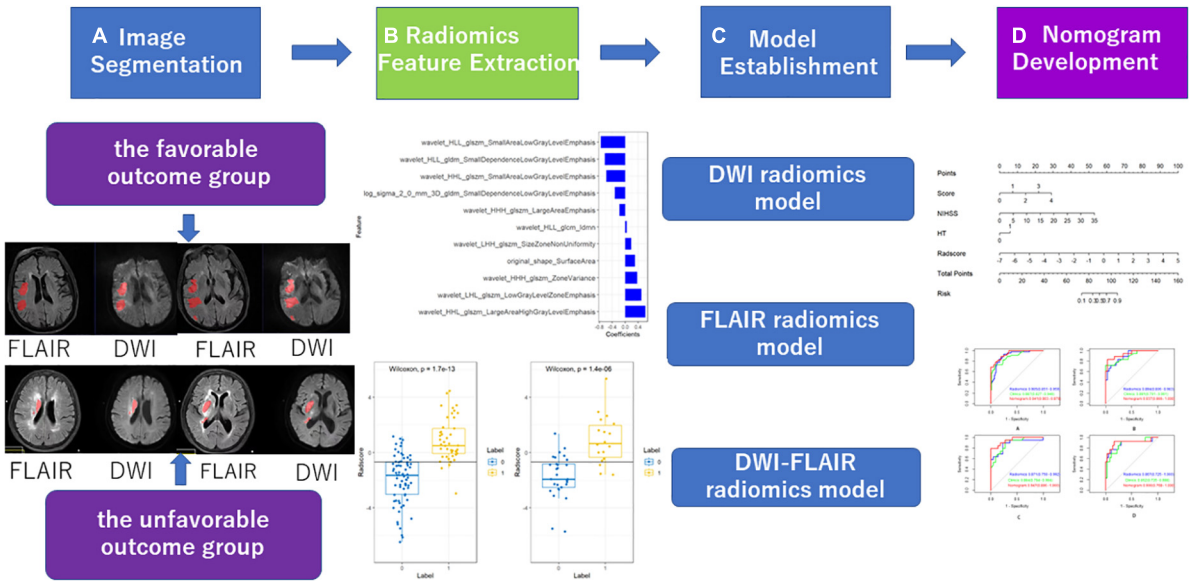

FIGURE 2
Workflow of radiomics analysis of the experiment.

were carried out in accordance with institutional guidelines and regulations.

2.2. Methods

2.2.1. DWI and FLAIR examination

A total of 166 acute ischaemic stroke patients underwent MRI examination with a 3.0T MR scanner (Siemens, Verio, Germany). The MRI protocol included axial FLAIR and DWI. The imaging protocol parameters were as follows: FLAIR [TR 9000 ms, TE 100 ms, inversion time (TI) 2500 ms], visual field (FOV) 220 × 220, matrix 256 × 256, DWI (TR 6700 ms, TE 100 ms), FOV 220 × 220, matrix 192 × 192, B value 1000 s/mm^2. Forty-one patients underwent MRI examination with a 3.0T MR scanner (Philips, Ingenia 3.0cx, Netherlands). The MRI protocol included the imaging protocol parameters were as follows: FLAIR (TR 9000 ms, TE 137 ms, TI 2500 ms), visual

TABLE 1 Patient features in the training sets and test sets.

Variable		The training sets			The test sets		
	Level	The favourable outcome group (*n* = 73)	The unfavourable outcome group (*n* = 45)	*P*-value	The favourable outcome group (*n* = 30)	The unfavourable outcome group (*n* = 18)	*P*-value
The overall CSVD burden score	0	5 (6.8)	0 (0)	0.068	3 (10)	0 (0)	
	1	31 (42.5)	12 (26.7)		10 (33.3)	3 (16.7)	
	2	28 (38.4)	23 (51.1)		13 (43.3)	9 (50)	
	3	9 (12.3)	9 (20.0)		4 (13.3)	5 (27.8)	
	4	0 (0.0)	1 (2.2)		0 (0)	1 (5.6)	0.200
HT	No	67 (91.8)	27 (60.0)	$<1^{e-04}$	27 (90)	13 (72.2)	
	Yes	6 (8.2)	18 (40.0)		3 (10)	5 (27.8)	0.230
Sex	Female	27 (37.0)	13 (28.9)		14 (46.7)	8 (44.4)	
	Male	46 (63.0)	32 (71.1)	0.482	16 (53.3)	10 (55.6)	1.00
Hypertension	No	21 (28.8)	14 (31.1)	0.787	6 (20)	5 (27.8)	0.535
	Yes	52 (71.2)	31 (68.9)		24 (80)	13 (72.2)	
Diabetes	No	56 (76.7)	35 (77.8)	0.894	23 (76.7)	13 (16.2)	0.731
	Yes	17 (23.3)	10 (22.2)		7 (23.3)	5 (83.8)	
Hyperlipemia	No	62 (84.9)	41 (91.1)	0.487	28 (93.3)	17 (94.4)	1.000
	Yes	11 (15.1)	4 (8.9)		2 (6.7)	1 (5.6)	
Coronary heart disease	No	67 (91.8)	41 (91.1)	1.000	27 (90)	17 (94.4)	1.000
	Yes	6 (8.2)	4 (8.9)		3 (10)	1 (5.6)	
Atrial fibrillation	No	56 (76.7)	31 (68.9)	0.348	26 (86.7)	11 (61.1)	0.092
	Yes	17 (23.3)	14 (31.1)		4 (13.3)	7 (38.9)	
Smoking	No	59 (80.8)	36 (80)	0.913	24 (80)	15 (83.3)	1.000
	Yes	14 (19.2)	9 (20)		6 (20)	3 (16.7)	
Drink	No	68 (89)	42 (93.3)	1.000	30 (100)	17 (94.4)	0.375
	Yes	5 (11)	3 (6.7)		0 (0)	1 (5.6)	
Age, mean (SD)		64.6 (12.6)	66.1 (11.3)	0.529	66.7 (13)	67.5 (14.5)	0.843
DP, mean (SD)		148 (21.6)	147.2 (15.4)	0.847	150 (20.2)	155.1 (19.2)	0.391
SP, mean (SD)		85.2 (13.4)	87 (11.1)	0.431	84 (13.4)	87.4 (12.7)	0.382
Admission NIHSS, mean (SD)		8.1 (3.7)	15.8 (6)	$<1^{e-04}$	8.2 (3.4)	17.3 (6.4)	<1e-04
Radscore, median (IQR)		−1.6 (−3.0, −0.7)	0.5 (−0.1, 1.7)	$<1^{e-04}$	−1.9 (−2.6, −0.8)	−0.7 (−3.0, 2.0)	<1e−04

DP, diastolic blood pressure; SP, systolic pressure; IQR, interquartile range; NIHSS, National Institutes of Health Stroke Scale; HT, hemorrhagic transformation.

field (FOV) 230 × 186 × 125, matrix 328 × 174 × 21, DWI (TR 2585 ms, TE 81 ms), FOV 220 × 220 × 125, matrix 136 × 110 × 21, B value 1000 s/mm^2. Thirty-six patients underwent MRI examination with a 3.0T MR scanner (Philips, Achieva Tx3.0, Netherlands). The imaging protocol parameters were as follows: FLAIR (TR 11000 ms, TE 125 ms, TI 2800 ms), visual field (FOV) 210 × 210 × 118, matrix 140 × 109, DWI (TR 2245 ms, TE 90 ms), FOV 220 × 220 × 125, matrix 136 × 110 × 21, B value 1000 s/mm^2. Fourteen patients underwent MRI examination with a 3.0T MR scanner (Philips, Ingenia 3.0cx, Netherlands). The MRI protocol included FLAIR axial, DWI axial scans. The imaging protocol parameters were as follows: FLAIR (TR 9000 ms, TE 120 ms, TI 2600 ms), visual field (FOV) 230 × 230, matrix 356 × 151, DWI (TR 2501 ms, TE 98 ms), FOV 230 × 230, matrix 152 × 122, B value 1000 s/mm^2.

2.2.2. Clinical data

The demographic and clinical data included sex, age, systolic blood pressure (SP), diastolic blood pressure (DP), MRI CSVD burden score, HT, baseline NIHSS score on admission and mRS score at 90 days. The MRI CSVD burden score was performed according to the scale established by Staals, with a total score of 0–4, and the brain damage caused by CSVD was greater if the score was higher (Staals et al., 2014). One point was recorded for each of the following: (1) any lacune; (2) periventricular WMHs (Fazekas score 2 or 3); (3) any CMB; and (4) moderate to severe (grade 2–4) PVS in the basal ganglia. We calculated an overall CSVD burden score ranging from 0 to 4 with the above 4 imaging markers, and all the scores were

TABLE 2 Population characteristics of patients with AIS in the training and test sets.

Variable	Level	Training (n = 118)	Test (n = 48)	P-value
The overall CSVD burden score	0	5 (4.2)	3 (6.2)	0.752
	1	43 (36.4)	13 (27.1)	
	2	51 (43.2)	22 (45.8)	
	3	18 (15.3)	9 (18.8)	
	4	1 (0.8)	1 (2.1)	
HT	No	94 (79.7)	40 (83.3)	0.744
	Yes	24 (20.3)	8 (16.7)	
Sex	Female	40 (33.9)	22 (45.8)	
	Male	78 (66.1)	26 (54.2)	0.206
Hypertension	No	35 (29.7)	11 (22.9)	0.379
	Yes	83 (70.3)	37 (77.1)	
Diabetes	No	91 (77.1)	36 (75)	0.770
	Yes	27 (22.9)	12 (25)	
Hyperlipemia	No	103 (87.2)	45 (93.8)	0.348
	Yes	15 (12.8)	3 (6.2)	
Coronary heart disease	No	108 (91.5)	44 (91.7)	1.000
	Yes	10 (8.5)	4 (8.3)	
Atrial fibrillation	No	87 (73.7)	37 (77.1)	0.652
	Yes	31 (26.3)	11 (22.9)	
Smoking	No	95 (80.5)	39 (81.2)	0.913
	Yes	23 (19.5)	9 (18.8)	
Drink	No	110 (93.2)	47 (97.9)	0.405
	Yes	8 (6.8)	1 (2.1)	
Age, mean (SD)		65.2 (12.1)	67 (13.4)	0.393
DP, mean (SD)		147.7 (19.4)	151.9 (19.8)	0.203
SP, mean (SD)		85.9 (12.6)	85.2 (13.1)	0.772
Admission NIHSS, mean (SD)		11 (6)	11.6 (6.4)	0.592
Radscore, median (IQR)		−0.7 (−2.2, 0.4)	−0.9 (−2.2, 0.3)	0.842

DP, diastolic blood pressure; SP, systolic pressure; IQR: interquartile range; NIHSS, National Institutes of Health Stroke Scale; HT, hemorrhagic transformation.

assessed by 2 experienced neuroradiologists. The Fazekas scale was used to evaluate the sum of perivascular WMHs and deep WMHs, and the score ranged from 0 to 6. The PVS score was selected from the basal ganglia and central semioval region, and a 4-point scale was used to grade the severity of PVS (Wenli et al., 2021).

2.2.3. Image segmentation and data analysis

2.2.3.1. ROI segmentation and high-throughput feature extraction

Two experienced radiologists (Dr. A, Dr. B) manually segmented lesions on DWI using ITK-SNAP[1] software and then duplicated the region of interest (ROI) on DWI to the corresponding FLAIR sequence. Fifty patients were randomly selected and segmented by doctors with 5 years and 10 years of experience in neuroimaging diagnosis. The doctors with 5 years of experience segmented the data twice with an interval of 2 weeks between segmentations. A physician with 10 years of experience segmented the data once. The correlation coefficient (ICC) was used to test the intraobserver and intergroup ROI consistency (ICC > 0.75 indicates good agreement). High-throughput features were extracted according to the ROI of each case, including first-order features, shape features, and texture features.

2.2.3.2. Establishment and evaluation of the models

In this study, a feature variable dataset was composed of 166 cases segmented by physicians with 5 years of experience, and the dataset was randomly divided into a training set and a test set at a ratio of 6:4. The data of the training set were used for feature screening and constructing the prediction model, and the data of the test set were used to verify the effect of the model internally. The area under the curve (AUC), sensitivity, specificity and accuracy of the receiver operating characteristic (ROC) curve were used to evaluate the validity and reliability of the prediction model for acute ischaemic stroke after thrombolysis. Features with good repeatability and stability were used to establish the Radscore. The Radscore was calculated by linear fusion of selected features. The calibration curve was used to evaluate the prediction effect of the model. The decision

1 www.itksnap.org

10.3389/fnins.2023.1063391

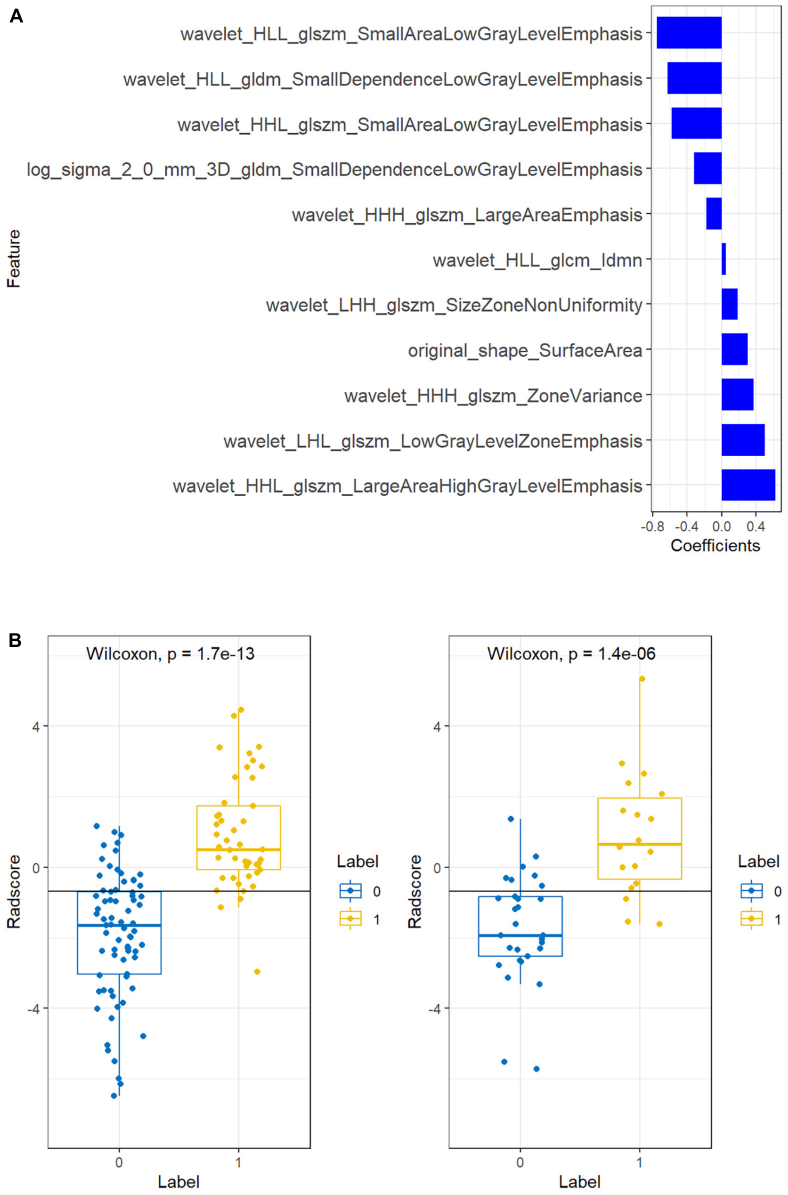

FIGURE 3
Feature coefficients **(A)** and radiomics scores **(B)**.

TABLE 3 The clinical model of multivariate regression results.

Variable	OR	CI.95	*P*-value
The overall CSVD burden score	1.96	(0.99; 3.86)	0.053
Admission NIHSS	1.37	(1.21; 1.56)	$<1e^{-04}$
HT	2.87	(0.77; 10.72)	0.118

curve was used to evaluate the potential clinical net benefit of the prediction model.

2.2.4. Statistical methods

SPSS 20.0 was used for statistical analysis, the independent sample *t* test was used for the ages of patients in the two groups, and the $\chi 2$ test was used for sex distribution differences. A *P* value < 0.05 was considered as a statistically significant difference. All statistical analyses were performed with R software, version 3.4.0. The "DescTools" package was used for ICC calculation, and the "Caret" package was used for data grouping, Spearman correlation analysis and calibration analysis. The "glmnet" package was used for LASSO regression analysis and to construct the Radscore. The "pROC" package was used to plot ROC curves and calculate the characteristics and sensitivity of the models.

3. Results

3.1. General patient information

The study flowchart included image segmentation, feature extraction, model establishment, and nomogram (Figure 2). A total of 166 patients from our hospital with acute ischaemic stroke were

TABLE 4 The nomogram model of multivariate regression results.

Variable	OR	CI.95	*P*-value
The overall CSVD burden score	2.70	(1.11; 6.60)	0.029
Admission NIHSS	1.23	(1.05; 1.44)	0.008
HT	2.24	(0.45; 11.01)	0.322
Radscore	3.13	(1.73; 5.67)	0.000

divided into two groups. The favourable outcome group comprised 103 cases (62 males and 41 females) and 63 cases (42 males and 21 females) in the unfavourable outcome group. The clinical data (the overall CSVD burden score, HT, age, sex, SP, DP, admission NIHSS score) and imaging characteristics of the training set and the test set were analysed by the chi-square test, and logistic regression analysis was performed with $P < 0.1$ as the inclusion criterion. In the training set, the overall CSVD burden score, HT, admission NIHSS score and Radscore were statistically significant (Table 1), while in the test set, the NIHSS score and Radscore were significantly different ($P < 0.1$), and there was no significant difference in outcome distribution between the two sets (Table 2).

3.2. Extraction and selection of radiomic features and establishment of radiomic signatures

The intraobserver and interobserver ICC values were 0.89 and 0.81, respectively, suggesting good consistency. The segmentation dataset of all images for subsequent feature extraction and screening and the model establishment was composed of the data after the first segmentation by the doctor with 5 years of experience. The AUC value of the FLAIR radiomics model in evaluating the prognosis of thrombolysis in acute ischaemic stroke was 0.922 (95% CI: 0.876–0.968), which was higher than that of the DWI radiomics model (AUC = 0.875, 95% CI: 0.815–0.935) and DWI-FLAIR radiomics model (AUC = 0.895, 95% CI: 0.840–0.950), although there was no significant difference between the three models. Based on the FLAIR radiomics model, we first performed mRMR to remove redundant and irrelevant features and retained 30 features and then performed LASSO dimensionality reduction processing to finally screen 11 features with non-zero coefficients, including 1 shape feature and 10 texture features. The parameters and coefficients of each feature are shown in Figure 3A. Subsequently, the radiomics label radiomics score (RAD-score) (Figure 3B) was established to reflect the distribution of the good prognosis group and poor prognosis group in the training group and the test group.

Figure 3A shows the feature parameters of the FLAIR radiomics model. Figure 3B shows the Radscore of the FLAIR radiomics model for the training group and test group. The blue bar below baseline 0 indicates patients with poor prognosis prediction, while the yellow bar above baseline 0 indicates patients with good prognosis prediction. The cross part represents the model prediction error, and the overall prediction effect is good.

3.3. Development of the radiomics nomogram

Multivariate logistic regression analysis showed that the overall CSVD burden score (OR = 1.96, 95% CI: 0.99∼3.86), HT (OR = 1.37, 95% CI: 1.21∼1.56) and NIHSS score (OR = 2.87, 95% CI: 0.77∼10.72) were independent predictors of prognosis in patients with acute ischaemic stroke after thrombolysis (Table 3). Finally, the overall CSVD burden score (OR = 2.7, 95% CI: 1.11∼6.60), HT (OR = 2.24, 95% CI: 0.45∼11.01), NIHSS score (OR = 1.23, 95% CI: 1.05∼1.44) and Radscore (OR = 3.13, 95% CI: 1.73∼5.67) were selected in the training set to create a radiomics nomogram (Table 4 and Figure 4). The prognosis of the training and test sets after thrombolytic therapy for predicting AIS was evaluated by calibration curves (Figure 5). Hosmer-Lemeshow test showed

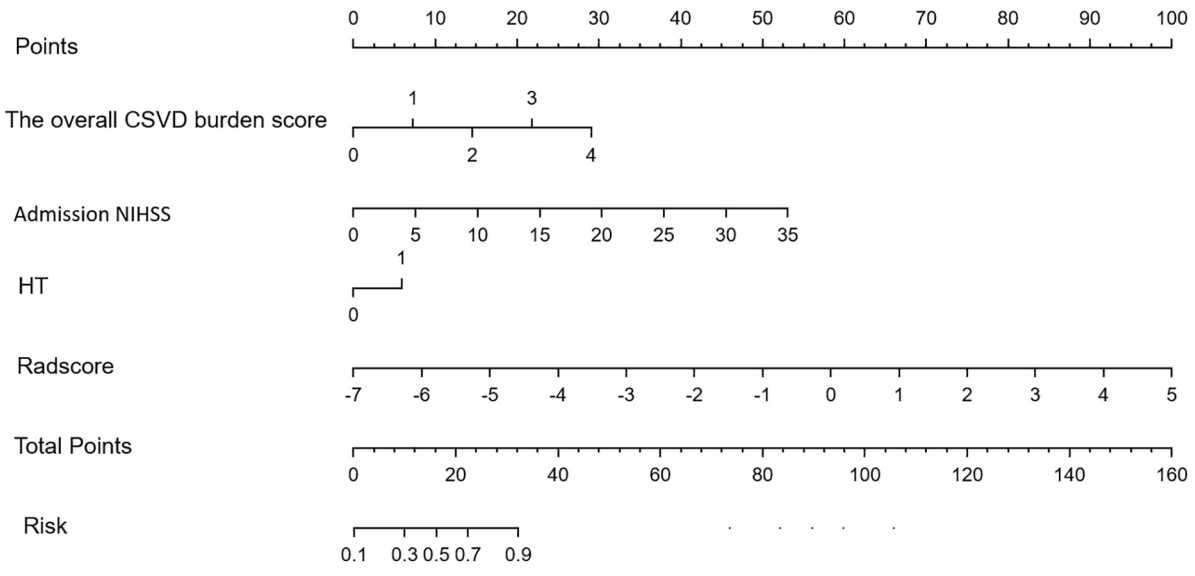

FIGURE 4
Radiomics nomogram for predicting the clinical functional outcome of ischaemic stroke.

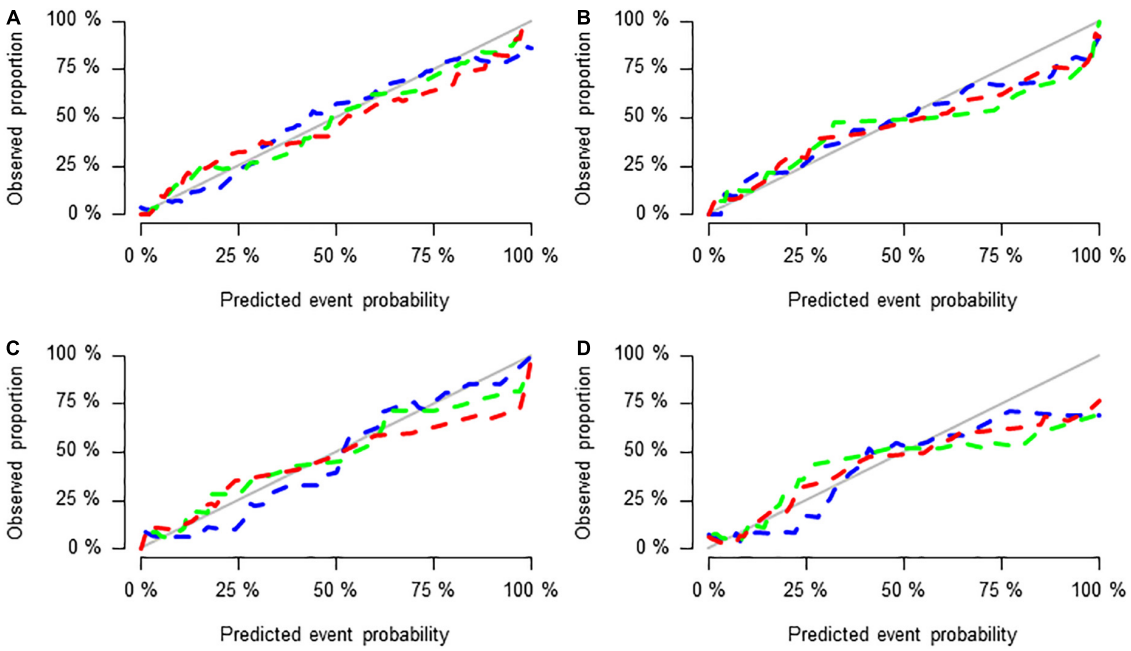

FIGURE 5
Calibration curves of the three groups of models in the training set **(A)**, test set **(B)**, validation set 1 **(C)**, and validation set 2 **(D)**.

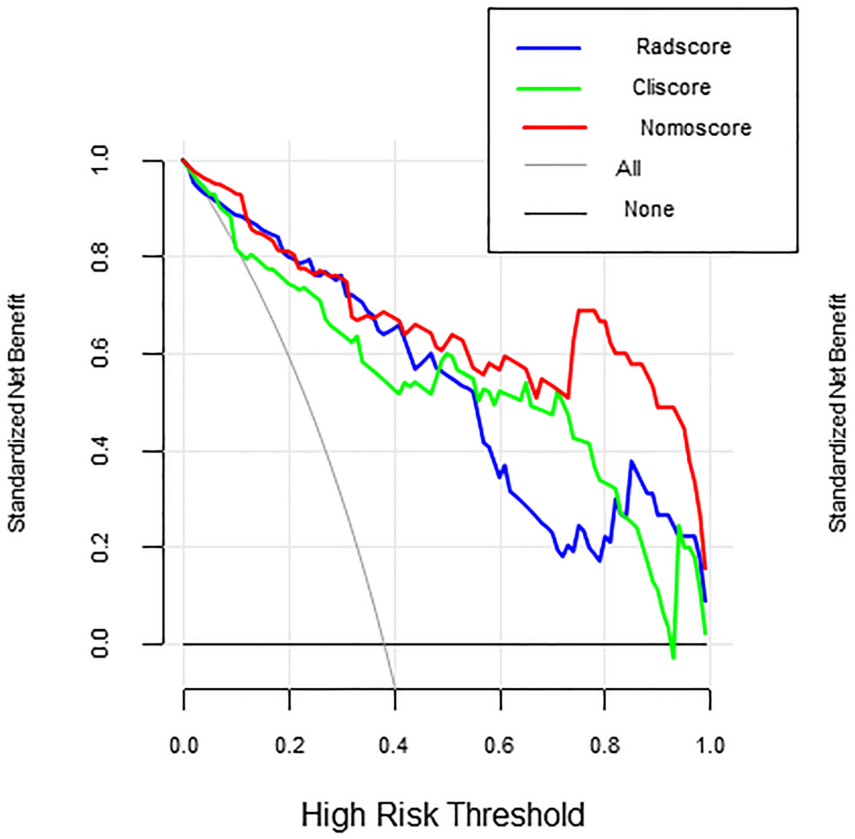

FIGURE 6
Decision curves.

good calibration in the training data set (P = 0.17) and the test set (P = 0.62), indicating high accuracy of the prediction model. Decision curves (Figure 6) were used to evaluate the clinical utility of the combined clinical-radiomics prediction model. DCA demonstrated that if the threshold probability was greater than 0.4 in clinical decision making, the nomogram is superior to the

TABLE 5 The prediction results of the three models in the training and test sets.

Model	Accuracy	Accuracy lower	Accuracy upper	Sensitivity	Specificity	Pos. pred. value	Neg. pred. value
FLAIR radiomics (Train)	0.822	0.741	0.886	0.933	0.753	0.700	0.948
FLAIR radiomics (Test)	0.792	0.650	0.895	0.833	0.767	0.682	0.885
Clinics (Train)	0.847	0.770	0.907	0.733	0.918	0.846	0.848
Clinics (Test)	0.854	0.722	0.939	0.722	0.933	0.867	0.848
Nomogram (Train)	0.839	0.760	0.900	0.889	0.808	0.741	0.922
Nomogram (Test)	0.854	0.722	0.939	0.789	0.897	0.833	0.867

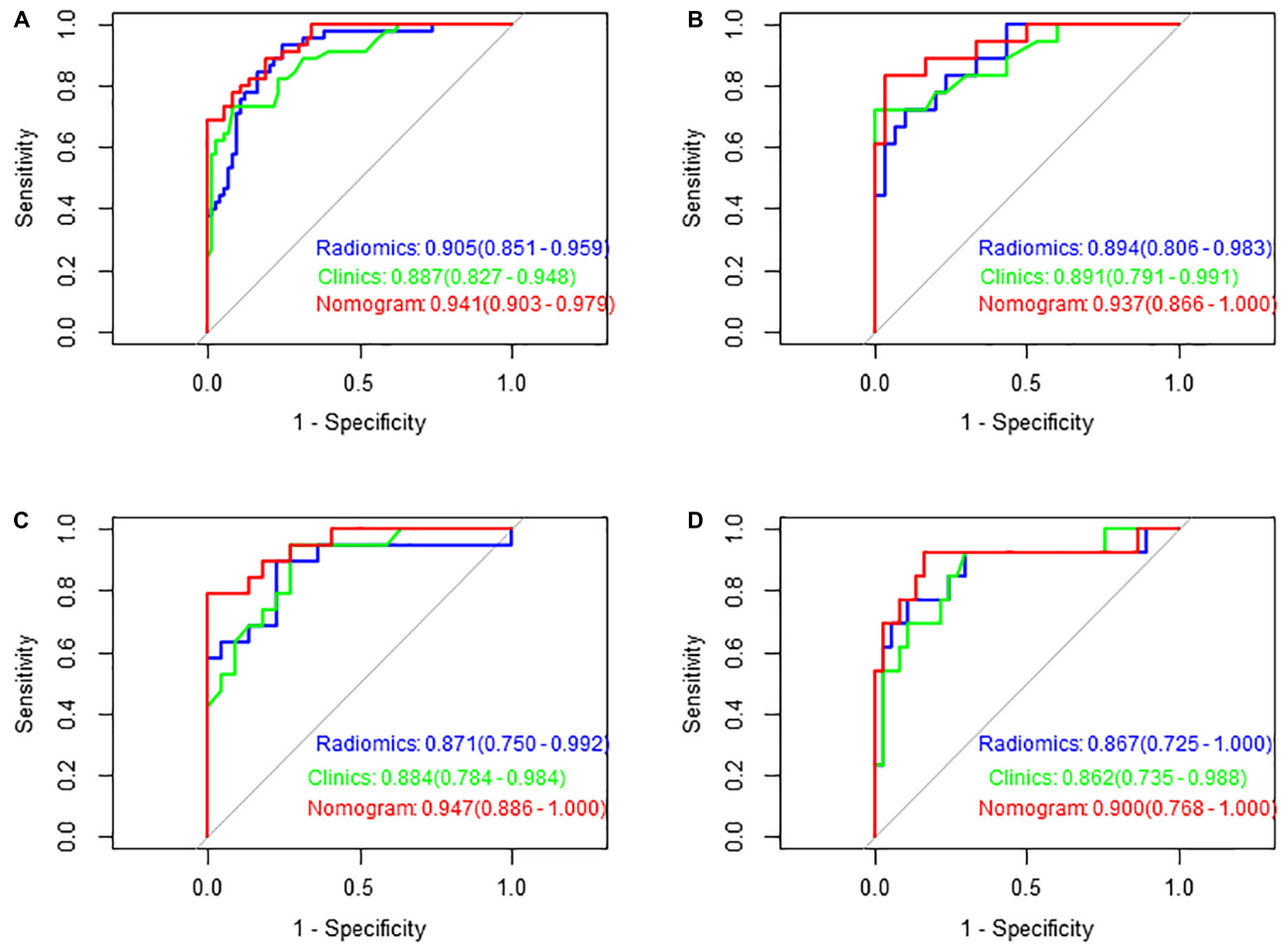

FIGURE 7
Receiver operating characteristic (ROC) curves of the three models in predicting the clinical functional outcomes of ischaemic stroke in the training set **(A)**, test set **(B)**, validation set 1 **(C)**, and validation set 2 **(D)**.

FLAIR radiomics and the clinical model. The sensitivity, specificity, accuracy, negative predictive value and positive predictive value of FLAIR radiomics, clinical features and clinical-FLAIR radiomics in predicting the prognosis of acute ischaemic stroke after thrombolytic therapy in the training set and the test set are shown in Table 5. ROC curves were used to evaluate the efficacy of the three models (clinical, radiomics, and clinical-radiomics models) in predicting the prognosis of AIS after thrombolysis in the training set and the test set. Among them, the clinical-radiomics model (radiomics nomogram) had the highest prediction efficacy, and the AUCs of the training set and the test set were 0.94 (95% CI: 0.90–0.98) and 0.94 (95% CI: 0.87–1), respectively, which was validated in the independent validation set1 (AUC = 0.95; 95% CI 0.88–1) and validation set 2 (AUC = 0.90; 95% CI 0.768–1) (Figure 7). DeLong test was used to compare the nomogram ROC curve with clinical model in both training set (Z = 2.4278, P = 0.01519) and test set (Z = 1.4023, P = 0.1608).

The overall CSVD burden score, Admission NIHSS, HT and Radscore are vertically corresponding to the "points" in the first row. Finally, these "points" are added together to obtain the "total points"

in the last row as the poor prognosis risk score, and the probability of poor prognosis of each stroke patient can be obtained.

Figures 5A–D shows the calibration curves of the three groups of models in the training set, test set and validation set 1 and validation set 2, reflecting the potential clinical net benefits of the models. The horizontal axis shows the nomogram predicting the prognosis of acute ischaemic stroke, and the vertical axis shows the actual prognosis of acute ischaemic stroke. The prediction efficacy is better if the solid line is closer to the grey line.

In **Figure 6** decision curves show the decision curves of the three groups of models in the training set, reflecting the prediction efficiency of the models. The horizontal axis represents the threshold probability, the vertical axis represents the net benefit, and the solid lines represent the benefit curves of the models. DCA demonstrated that if the threshold probability was greater than 0.4 in clinical decision making, the nomogram is superior to the FLAIR radiomics and the clinical model.

Figures 7A–D shows the ROC curves of FLAIR radiomics, the clinical model, and the nomogram in the training set, test set, and validation set 1 and validation set 2, reflecting the comprehensive comparison of sensitivity and specificity among the three models. The AUC values of the test group were 0.89, 0.89, and 0.94, respectively.

4. Discussion

Stroke is a serious threat to human health worldwide. Early diagnosis and prognosis assessment are crucial for the management of AIS. The prognosis of acute ischaemic stroke is different due to differences in cerebrovascular reserve, collateral circulation and risk factors (Yang et al., 2013). DWI shows lesions within a short time (a few hours) after onset (Chalela et al., 2007), which represents the core of ischaemic stroke. Many studies have shown that the volume of stroke is correlated with clinical functional outcome (Jiang et al., 2020). In addition, the boundary between the core area and the penumbra is clear, which is easy to identify and delineate, and the consistency is good. FLAIR images have high resolution, long scanning time, and relatively more image information. Quan G et al. showed that radiomics features extracted from FLAIR and ADC can be used as biomarkers for predicting adverse clinical outcomes of AIS and can also improve the predictive performance when added to the combined model (Quan et al., 2021). The overall CSVD burden score is independently related to the severity of neurological deficits and the clinical outcome of AIS. Liu et al. (2019) showed that the overall CVSD burden score is a reliable predictor of poor prognosis of AIS after IV RT-PA treatment. In this study, ROIs were collected three times for each patient, and the correlation coefficient (ICC) was used to test the consistency of ROIs within and between observer groups, which ensured the reproducibility of extracted radiomics features. Radiomics has been used to evaluate the prognosis and treatment of ischaemic stroke (Wang et al., 2020). In this study, 201 patients with acute ischaemic stroke were enrolled to explore the value of radiomics based on DWI and FLAIR combined with the overall CSVD burden score in predicting the prognosis of ischaemic stroke and to create a method that can be used in the management strategy of ischaemic stroke. Our study showed that the AUC value of the FLAIR model in estimating clinical outcomes of acute ischaemic stroke after thrombolysis was 0.922, 95% CI: 0.876–0.968, which was higher than that of the DWI model (AUC = 0.875, 95% CI: 0.815–0.935) and DWI-FLAIR model (AUC = 0.895, 95% CI: 0.840–0.950). Tanriverdi et al. (2016) found that the increase in FLAIR hyperintensity in ischaemic tissue indicated a good prognosis of patients after intravenous thrombolytic therapy. Tang et al. (2020) showed that radiomics features could be used as prognostic biomarkers based on penumbral quantification and developed a radiomics nomogram to predict the prognosis of thrombolysis in patients with AIS, the AUC of the radiomics nomogram predicting favourable clinical outcome reached 0.886 (95% CI 0.809–0.963) on day 7 and 0.777 (95% CI 0.666–0.888) at 3 months. However, their model was constructed from the radiomic features extracted from PWI and DWI. In clinical practice, most patients with ischaemic stroke receive only routine test sequences. Wang et al. (2021) developed a clinical radiomics nomogram based on DWI, which showed good performance in predicting the prognosis of ischaemic stroke in the training cohort [AUC = 0.80; 95% confidence interval (CI) 0.75–0.86], which was validated in the validation cohort (AUC = 0.73; 95% CI 0.63–0.82). However, their study only included DWI sequences and studied all AIS patients, while we only collected patients who could receive thrombolytic therapy. Our model fitted well and the AUC value of FLAIR model was higher than that of DWI and DWI-FLAIR model, although there were no significant differences between the three models. We finally select FLAIR model to establish Normogram to solve the clinical problem, because radiomics is more dependent on image resolution and heterogeneity, and FLAIR sequence resolution shows more information than DWI sequence. However, the combination of DWI and the FLAIR radiomics model did not improve the evaluation performance, which may be caused by the mutual interference of the extracted radiomics features.

In this study, a total of 11 features related to the prognosis of ischaemic stroke after thrombolysis were screened by a FLAIR radiomics model, including 1 shape feature and 10 texture features. The small area low grey level emphasis (SALGLE), zone variance (ZV), large area high grey level emphasis (LAHGLE), large area emphasis (LAE), size zone non-uniformity (SZN), small dependence low grey level emphasis (SDLGLE) and so on are of great significance for the prognosis of patients with acute ischaemic stroke. SALGLE measures the proportion of small and dark areas of the image. LAHGLE measures the proportion of areas with brighter and larger dimensions. ZV is the change in the measured volume. LAE measures the distribution of large focal areas, and if the value is larger, the texture is coarser. SZN measures changes in the volume of the size region in the image. SDLGLE measures the strong correlation with the dispersion of the darker parts of the image. Among the 11 features, SALGLE and LAHGLE had the greatest relative weights. All of these features reflect the heterogeneity of infarcts and if the value is higher and the prognosis of stroke is poor.

The poor prognosis of stroke patients is related to many factors, such as age, blood pressure, previous neurological disorder, admission NIHSS score, collateral circulation, white matter hyperintensity, cerebral microbleeds and so on. This study showed that the overall CSVD burden score, HT, and admission NIHSS score were associated with ischaemic stroke prognosis. CSVD is a chronic disease of the whole brain, and the imaging findings are often more severe than the clinical manifestations. CSVD imaging markers include lacunes, WMHs, CMBs, and PVSs, which often coexist. Overall, these imaging markers may reflect an overall status of the distal small artery or arteriole bed, and a moderate-to-severe overall CSVD burden may represent an overall more vulnerable

cerebral microcirculation (Arba et al., 2016). Therefore, the overall CSVD burden score may be more suitable for evaluating the overall effect of CSVD on the brain. The benefits and risks of intravenous thrombolysis in patients with CSVD should be individually evaluated to reduce the incidence of cerebral haemorrhage and poor prognosis after thrombolysis in ischaemic stroke. Tian et al. (2022) showed that the status of CSVD and infarction number predicted recurrent stroke in patients with acute minor stroke and TIA. Chen et al. (2020) believe that CSVD is associated with more disability and bleeding events, may represent different vascular lesions, and plays different roles in the outcome of stroke. Studies have shown that the overall CVSD score is a reliable predictor of adverse AIS outcome after IV RT-PA treatment, and CSVD is associated with endothelial dysfunction and blood−brain barrier leakage, which may lead to a larger stroke volume and a worse prognosis after intravenous thrombolytic therapy after stroke (Arba et al., 2019). As a common imaging marker of CSVD, WMHs can affect the prognosis of stroke through various mechanisms. In the hyperacute phase of ischaemic stroke, WMH may affect the infarct volume and is related to the increase in infarct area, thus affecting the prognosis (Helenius et al., 2017). The clinical outcome of AIS after thrombolysis is related not only to vascular recanalisation and collateral circulation but also to the increase in vascular bed resistance and the decrease in cerebral blood flow regulation function after cerebral small vessel disease. In the acute phase of IS, this regulatory dysfunction leads to further reduction of cerebral perfusion and collateral circulation dysfunction, resulting in the expansion of ischaemic penumbra and increased risk of poor prognosis. Lacunes account for approximately a quarter of the total number of ischaemic strokes. The overall CSVD burden score in this study can correct the limitations of individual imaging biomarkers, and the radiomics nomogram can predict the risk of poor outcome after RT-PA treatment, especially in patients with two or more severe CSVD imaging markers, and more accurately predict the outcome of intravenous thrombolysis in ischaemic stroke. Our study show the radiomics nomogram presented good discriminatory potential in the training set (AUC = 0.94; 95% CI: 0.90–0.98) and test set (AUC = 0.94; 95% CI: 0.87–1), which was validated in the validation set 1 (AUC = 0.95; 95% CI 0.88–1) and validation set 2 (AUC = 0.90; 95% CI 0.768–1). DeLong test was used to compare the nomogram ROC curve with clinical model in both training set (Z = 2.4278, P = 0.01519) and test set (Z = 1.4023, P = 0.1608), and the difference was not statistically significant in the test set. However, it demonstrated good calibration, and decision curve analysis confirmed the clinical value of this nomogram. DCA demonstrated that if the threshold probability was greater than 0.4 in clinical decision making, the nomogram is superior to the FLAIR radiomics and the clinical model.

There were also some limitations in this study. Firstly, the sample size is relatively small, which may lead to overfitting. So, our study also used patient data with different MRI scanners and other two clinical centres as two external validation sets, and the repeatability and consistency were good. Secondly, this study is a retrospective study, therefore our results obtained from the consecutive AIS patients to reduce the choice of selection bias. Finally, patients with lacunar infarction and posterior circulation stroke were excluded from our study. Lacunar infarction has a small lesion and a slight neurological defect, and the prognosis is generally good. Posterior circulation stroke accounts for about 20% of ischaemic stroke, and is generally more serious than anterior circulation stroke, with higher disability rate and mortality. In order to ensure strict grouping and no bias in the radiomics results, lacunar infarction and posterior circulation infarction were excluded from this experiment. At present, we are following up the patients with posterior circulation infarction, and we plan to further study them with radiomics.

In conclusion, this study shows that the FLAIR radiomics model have a similar performance with the DWI radiomics model and DWI-FLAIR radiomics model. Clinical combination with the FLAIR radiomics nomogram shows good performance in predicting the prognosis of ischaemic stroke after thrombolysis, this could help clinicians plan rehabilitation for stroke patients.

Data availability statement

The raw data supporting the conclusions of this article will be made available by the authors, without undue reservation.

Ethics statement

Written informed consent was obtained from the individual(s) for the publication of any potentially identifiable images or data included in this article.

Author contributions

QX and LG contributed to the conception of the study. QX and SD performed the data analyses. QX wrote the manuscript. LG contributed to the revision of the article. YZ, XZ, and DK helped perform the analysis with constructive discussions. XY, LJ, ZL, and WY contributed to the article data from other two clinical centers as external validation set. All authors contributed to the article and approved the submitted version.

Funding

This study was supported by grants from the Postdoctoral Research Program of Jiangsu Province under project (No. 2019K278) to LG.

Acknowledgments

We thank all members of the Department of Radiology of the Affiliated Huai'an First People's Hospital of Nanjing Medical University for helpful discussions and invaluable help in manuscript preparation.

Conflict of interest

SD was employed by GE HealthCare.

The remaining authors declare that the research was conducted in the absence of any commercial or financial relationships that could be construed as a potential conflict of interest.

Publisher's note

All claims expressed in this article are solely those of the authors and do not necessarily represent those of their affiliated organizations, or those of the publisher, the editors and the reviewers. Any product that may be evaluated in this article, or claim that may be made by its manufacturer, is not guaranteed or endorsed by the publisher.

References

Arba, F., Giannini, A., Piccardi, B., Biagini, S., Palumbo, V., Giusti, B., et al. (2019). Small vessel disease and biomarkers of endothelial dysfunction after ischaemic stroke. *Eur. Stroke J.* 4, 119–126.

Arba, F., Palumbo, V., Boulanger, J., Pracucci, G., Inzitari, D., Buchan, A. M., et al. (2016). Leukoaraiosis and lacunes are associated with poor clinical outcomes in ischemic stroke patients treated with intravenous thrombolysis. *Int. J. Stroke* 11, 62–67. doi: 10.1177/1747493015607517

Cao, J., Eshak, E. S., Liu, K., Arafa, A., Sheerah, H., Yu, C., et al. (2021). Age-period-cohort analysis of stroke mortality attributable to high systolic blood pressure in China and Japan. *Sci. Rep.* 11:19083. doi: 10.1038/s41598-021-98072-y

Chalela, J. A., Kidwell, C. S., Nentwich, L. M., Luby, M., Butman, J. A., Demchuk, A. M., et al. (2007). Magnetic resonance imaging and computed tomography in emergency assessment of patients with suspected acute stroke: a prospective comparison. *Lancet* 369, 293–298.

Chen, H., Pan, Y., Zong, L., Jing, J., Meng, X., Xu, Y., et al. (2020). Cerebral small vessel disease or intracranial large vessel atherosclerosis may carry different risk for future strokes. *Stroke Vasc. Neurol.* 5, 128–137.

GBD 2019 Stroke Collaborators. (2021). Global, regional, and national burden of stroke and its risk factors, 1990-2019: a systematic analysis for the Global Burden of Disease Study 2019. *Lancet Neurol.* 20, 795–820.

Helenius, J., Mayasi, Y., and Henninger, N. (2017). White matter hyperintensity lesion burden is associated with the infarct volume and 90-day outcome in small subcortical infarcts. *Acta Neurol. Scand.* 135, 585–592. doi: 10.1111/ane.12670

Huang, Y. N. (2015). Chinese consensus on diagnosis and treatment of cerebral small vessel diseases. *Chin. J. Neurol.* 48, 838–844.

Jiang, L., Peng, M., Chen, H., Geng, W., Zhao, B., Yin, X., et al. (2020). Diffusion-weighted imaging (DWI) ischemic volume is related to FLAIR hyperintensity-DWI mismatch and functional outcome after endovascular therapy. *Quant. Imaging Med. Surg.* 10, 356–367. doi: 10.21037/qims.2019.12.05

Liu, X., Li, T., Diao, S., Cai, X., Kong, Y., Zhang, L., et al. (2019). The global burden of cerebral small vessel disease related to neurological deficit severity and clinical outcomes of acute ischemic stroke after IV rt-PA treatment. *Neurol. Sci.* 40, 1157–1166. doi: 10.1007/s10072-019-03790-x

Peter, R., Korfiatis, P., Blezek, D., Beitia, A. O., Stepan-Buksakowska, I., Horinek, D., et al. (2017). A quantitative symmetry-based analysis of hyperacute ischemic stroke lesions in noncontrast computed tomography. *Med. Phys.* 44, 192–199. doi: 10.1002/mp.12015

Quan, G., Ban, R., Ren, J., Liu, Y., Wang, W., Dai, S., et al. (2021). FLAIR and ADC image-based radiomics features as predictive biomarkers of unfavorable outcome in patients with acute ischemic stroke. *Front. Neurosci.* 15:730879. doi: 10.3389/fnins.2021.730879

Staals, J., Makin, S. D., Doubal, F. N., Dennis, M. S., and Wardlaw, J. M. (2014). Stroke subtype, vascular risk factors, and total MRI brain small-vessel disease burden. *Neurology* 83, 1228–1234.

Tang, T., Jiao, Y., Cui, Y., Zhao, D., Zhang, Y., Wang, Z., et al. (2020). Penumbra-based radiomics signature as prognostic biomarkers for thrombolysis of acute ischemic stroke patients: a multicenter cohort study. *J. Neurol.* 267, 1454–1463. doi: 10.1007/s00415-020-09713-7

Tanriverdi, Z., Gocmen, R., Oguz, K. K., Topcuoglu, M. A., and Arsava, E. M. (2016). Elevations in tissue fluid-attenuated inversion recovery signal are related to good functional outcome after thrombolytic treatment. *J. Stroke Cerebrovasc. Dis.* 25, 480–483. doi: 10.1016/j.jstrokecerebrovasdis.2015.10.024

Tian, Y., Pan, Y., Yan, H., Meng, X., Zhao, X., Liu, L., et al. (2022). Coexistent cerebral small vessel disease and multiple infarctions predict recurrent stroke. *Neurol Sci.* 43, 4863–4874. doi: 10.1007/s10072-022-06027-6

Wang, H., Lin, J., Zheng, L., Zhao, J., Song, B., and Dai, Y. (2020). Texture analysis based on ADC maps and T2-FLAIR images for the assessment of the severity and prognosis of ischaemic stroke. *Clin. Imaging* 67, 152–159. doi: 10.1016/j.clinimag.2020.06.013

Wang, H., Sun, Y., Ge, Y., Wu, P., Lin, J., Zhao, J., et al. (2021). A clinical-radiomics nomogram for functional outcome predictions in ischemic stroke. *Neurol Ther.* 10, 819–832. doi: 10.1007/s40120-021-00263-2

Wardlaw, J. M., Smith, E. E., Biessels, G. J., Cordonnier, C., Fazekas, F., Frayne, R., et al. (2013). Neuroimaging standards for research into small vessel disease and its contribution to ageing and neurodegeneration. *Lancet Neurol.* 12, 822–838.

Wen, X., Li, Y., He, X., Xu, Y., Shu, Z., Hu, X., et al. (2020). Prediction of malignant acute middle cerebral artery infarction via computed tomography radiomics. *Front. Neurosci.* 14:708. doi: 10.3389/fnins.2020.00708

Wenli, H., Lei, Y., and Xuan, T. L. (2021). Chinese expert consensus on diagnosis and treatment of cerebral small vessel disease 2021. *Chin. J. Stroke* 16, 716–726. doi: 10.3760/cma.j.cn112138-20201218-01028

Yang, G., Wang, Y., Zeng, Y., Gao, G. F., Liang, X., Zhou, M., et al. (2013). Rapid health transition in China, 1990-2010: findings from the Global Burden of Disease Study 2010. *Lancet* 381, 1987–2015. doi: 10.1016/S0140-6736(13)61097-1

Zhou, Y., Wu, D., Yan, S., Xie, Y., Zhang, S., Lv, W., et al. (2022). Feasibility of a clinical-radiomics model to predict the outcomes of acute ischemic stroke. *Korean J. Radiol.* 23, 811–820. doi: 10.3348/kjr.2022.0160

frontiers | Frontiers in Neuroscience

TYPE Original Research
PUBLISHED 07 March 2023
DOI 10.3389/fnins.2023.1135337

Check for updates

OPEN ACCESS

EDITED BY
Ahmed Shalaby,
University of Texas Southwestern Medical Center, United States

REVIEWED BY
Shouliang Qi,
Northeastern University, China
Marco Atzori,
Autonomous University of San Luis Potosí, Mexico

*CORRESPONDENCE
Guojun Xie
✉ xiegjfs@126.com
Wenbin Guo
✉ guowenbin76@csu.edu.cn

†These authors have contributed equally to this work

SPECIALTY SECTION
This article was submitted to Brain Imaging Methods, a section of the journal Frontiers in Neuroscience

RECEIVED 31 December 2022
ACCEPTED 22 February 2023
PUBLISHED 07 March 2023

CITATION
Zhang C, Jing H, Yan H, Li X, Liang J, Zhang Q, Liang W, Ou Y, Peng C, Yu Y, Wu W, Xie G and Guo W (2023) Disrupted interhemispheric coordination of sensory-motor networks and insula in major depressive disorder. *Front. Neurosci.* 17:1135337. doi: 10.3389/fnins.2023.1135337

COPYRIGHT
© 2023 Zhang, Jing, Yan, Li, Liang, Zhang, Liang, Ou, Peng, Yu, Wu, Xie and Guo. This is an open-access article distributed under the terms of the Creative Commons Attribution License (CC BY). The use, distribution or reproduction in other forums is permitted, provided the original author(s) and the copyright owner(s) are credited and that the original publication in this journal is cited, in accordance with accepted academic practice. No use, distribution or reproduction is permitted which does not comply with these terms.

Disrupted interhemispheric coordination of sensory-motor networks and insula in major depressive disorder

Chunguo Zhang[1†], Huan Jing[1†], Haohao Yan[2†], Xiaoling Li[1], Jiaquan Liang[1], Qinqin Zhang[1], Wenting Liang[1], Yangpan Ou[2], Can Peng[1], Yang Yu[1], Weibin Wu[1], Guojun Xie[1*] and Wenbin Guo[2*]

[1]Department of Psychiatry, The Third People's Hospital of Foshan, Foshan, Guangdong, China, [2]Department of Psychiatry, National Clinical Research Center for Mental Disorders, The Second Xiangya Hospital of Central South University, Changsha, Hunan, China

Objective: Prior researches have identified distinct differences in neuroimaging characteristics between healthy controls (HCs) and patients with major depressive disorder (MDD). However, the correlations between homotopic connectivity and clinical characteristics in patients with MDD have yet to be fully understood. The present study aimed to investigate common and unique patterns of homotopic connectivity and their relationships with clinical characteristics in patients with MDD.

Methods: We recruited 42 patients diagnosed with MDD and 42 HCs. We collected a range of clinical variables, as well as exploratory eye movement (EEM), event-related potentials (ERPs) and resting-state functional magnetic resonance imaging (rs-fMRI) data. The data were analyzed using correlation analysis, support vector machine (SVM), and voxel-mirrored homotopic connectivity (VMHC).

Results: Compared with HCs, patients with MDD showed decreased VMHC in the insula, and increased VMHC in the cerebellum 8/vermis 8/vermis 9 and superior/middle occipital gyrus. SVM analysis using VMHC values in the cerebellum 8/vermis 8/vermis 9 and insula, or VMHC values in the superior/middle occipital gyrus and insula as inputs can distinguish HCs and patients with MDD with high accuracy, sensitivity, and specificity.

Conclusion: The study demonstrated that decreased VMHC in the insula and increased VMHC values in the sensory-motor networks may be a distinctive neurobiological feature for patients with MDD, which could potentially serve as imaging markers to discriminate HCs and patients with MDD.

KEYWORDS

major depressive disorder, voxel-mirrored homotopic connectivity, support vector machine, magnetic resonance imaging, brain

1. Introduction

Major depressive disorder (MDD), a prevalent mental illness, is the foremost cause of disability worldwide (CONVERGE consortium, 2015; Yang et al., 2020). Furthermore, it is a complicated emotional disorder characterized by abnormal clinical symptoms, including cognitive disorders (such as feelings of excessive guilt or worthlessness), autonomic dysfunction (such as changes in appetite or sleep patterns), abnormal psychomotor activities (such as excitement or retardation), and elevated risk of suicide (Lou et al., 2019). Approximately 12% of the global population is affected by MDD, while the lifetime occurrence of MDD in the United States surpasses 20% (Hasin et al., 2018; Hayley et al., 2021; Fries et al., 2022). The incidence of MDD has risen since the outbreak of COVID-19 (COVID-19 Mental Disorders Collaborators, 2021). Approximately 25–50% of those with MDD exhibit deficiencies in one or more cognitive domains, which are considered key features of the condition (Liu et al., 2022).

Researches have demonstrated that MDD is a heritable and heterogeneous disorder (Andersson et al., 2019; Kendall et al., 2021; Nguyen et al., 2022), and its clinical features are associated with brain regions that exhibit anatomical differences. Multiple neuroimaging studies have attempted to identify the neurobiology of MDD and distinguished several neuroimaging characteristics between healthy controls (HCs) and patients with MDD. Zhang et al. (2022) found that, in comparison to HCs, patients with MDD exhibited decreased functional connectivity (FC) between the emotional subregion of the anterior cingulate cortex (ACC) and the hippocampus, thalamus, insula, angular gyrus, and posterior cingulate cortex. On the other hand, other studies reported increased connectivity between the hippocampus and the ACC and reduced connectivity between the insula and the ACC in patients with MDD (Krug et al., 2022). Functional brain imaging studies revealed significant changes in the FC in the cerebellum-neocortex and cerebellum-basal ganglia circuits in patients with MDD (Dai et al., 2022). Additionally, an increased long-range positive FC (lpFC) in the left inferior parietal lobule was found to distinguish HCs and patients with MDD (Dziedzic et al., 2022). Given that the architecture of the connectome affects the effectiveness and velocity of information transport, including regions such as anterior and middle cingulate cortex, medial occipital areas, superior frontal areas, post- and precentral gyrus, parahippocampal gyrus, and precuneus, the balance of intra-hemispheric and inter-hemispheric connectivity plays a crucial role in brain function (Krupnik et al., 2021).

Studies have demonstrated that communication between the left and right hemispheres of the human brain is a crucial aspect of both cognitive and emotional processing (Compton et al., 2005; Toro et al., 2008). Ran et al. (2020) showed that anatomical abnormalities in the corpus callosum in patients with MDD may result from caused by imbalanced inter-hemispheric communication. Concurrently, a magnetic resonance imaging (MRI) study indicated that the deterioration of inter-hemispheric FC is related to the severity of clinical depression and treatment outcomes of patients with MDD (Kozel et al., 2011; Zheng et al., 2022). Additionally, patients with MDD had notably higher overall average (static) functional connectivity (sFC), but lower variability of functional connectivity (vFC) within networks (Demirtas et al., 2016). As per the research by Liu et al. (2021) inter-hemispheric homotopic connection in particular regions could be serve as a potential biomarker to distinguish patients with MDD from HCs. Reduced inter-hemispheric coordination in the posterior default-mode network and visual regions was also revealed between HCs and patients with MDD (Guo et al., 2018).

Voxel-mirrored homotopic connectivity (VMHC) is a technique used to calculate resting-state FC between voxels in a hemisphere and their corresponding mirror regions in the opposite hemisphere (Jia et al., 2020; Fan et al., 2022). VMHC can be utilized to determine the intensity of functional connections between brain regions in both hemispheres that are located at the same position (Zuo et al., 2010; Jin et al., 2021). Several studies have concluded that the mechanism behind VMHC deficiency may be linked to extensive abnormalities in white matter integrity, dysfunction in local gray matter structure, and the mode of pathway reorganization (Yuan et al., 2012; Ding et al., 2015). Moreover, this method can be used to evaluate the relationship between time series dependent on blood oxygen levels, and to demonstrate how information is exchanged between the two hemispheres of the brain (Wei et al., 2018). Some clinical studies have demonstrated altered homotopic FC by measuring VMHC in patients with MDD (Lai and Wu, 2014; Hou et al., 2016). Support vector machine (SVM) is a specialized form of supervised machine learning that multivariable pattern recognition technology that is applied to predict psychosis based on neuroanatomical indicators (Shan et al., 2021). SVM can effectively identify a set of information and features from different brain regions, which can be used to classify patients and HC using neuroimaging data [such as functional magnetic resonance imaging (fMRI) data] (Steardo et al., 2020), making the classification results more convincing. Numerous studies have employed VMHC and SVM methods to study brain disorders, providing possible evidence for the discovery of biological markers in neuroimaging (Chen et al., 2021; Chu et al., 2022; Wu et al., 2022). However, it is still unclear whether abnormal VMHC can be used as an underlying brain imaging symbol to discriminate HCs from MDD using the SVM analysis.

In this study, our objective was to apply the VMHC method to identify the inter-hemispheric functional interaction during resting state in individuals with MDD. This study investigated whether abnormal VMHC might be utilized as a potential marker in patients with MDD by combining VMHC values with cognitive tests, exploratory eye movement (EEM), event-related potentials (ERPs), and other markers. We hypothesized that patients with MDD would exhibit reduced VMHC, which could serve as a potential imaging marker to differentiate between HCs and patients with MDD. In addition, we proposed that aberrant VMHC would be associated with clinical variables in MDD.

2. Materials and methods

2.1. Participants

Patients with MDD were recruited from Foshan Third People's Hospital. This study included 32 first-episode patients and 10 recurrent patients with MDD. Forty-two HCs matched for sex and years of education were recruited from the community. The

Diagnostic and Statistical Manual of Mental Disorders-5 (DSM-5) patient version is used to determine the diagnosis of MDD. For recurrent patients, the use of antidepressants was suspended for at least 2 weeks by themselves. The anxiety and depressive symptoms, social function, personality characteristics, coping style, social support, and psychological cognitive function of the subjects were measured by Hamilton Anxiety Scale (HAMA), Hamilton Depression Scale (HAMD), Social Disability Screening Schedule (SDSS), Eysenck Personality Questionnaire (EPQ), Simplified Coping Style Questionnaire (SCSQ), Social Support Scale (SSS), Wisconsin Card Sorting Test (WCST), and Repeatable Battery for the Assessment of Neuropsychological Status (RBANS). All participants were right-handed and ranged in age from 18 to 60 years old. The exclusion standards for all subjects were as follows: (1) a history of severe physical sickness or alcohol or drug abuse; (2) significant physical impairment, preventing completion of the follow-up study; and (3) the presence of mental retardation, dementia, and severe cognitive impairment in addition to other serious psychiatric problems.

The study was approved by the Research Ethics Committee of the Third People's Hospital of Foshan, and a written informed consent was obtained from all participants.

2.2. Event-related potentials (ERP) data acquisition

Event-related potential data were collected using a Japanese Kohden MEB-9402C myoelectric evoked potentiometer. Participants were instructed to sit comfortably and make an effort to concentrate. The electrode placement followed the 10/20 standard by the International Electroencephalogram Association. The ground was put in the center of the hand FPz. The right ear M2 point served as the recording electrode. The central Cz point served as the reference electrode. The electrode impedance was set to 5K, and the filter was 0.2–20 Hz. The analysis duration was 1000 ms. The stimulation is carried out in the traditional "Oddball" auditory stimulation mode, with a frequency of 1 times/s, a duration of 10 ms, and a sensitivity of 5 μV. The detection was accomplished by triggering and activating two systems, which were band-pass filtered 200 times with the low-frequency filter and the high-frequency filters. The settings for the non-target stimulus were set to 80% probability, 70 dB intensity, and 1000 Hz frequency, while the parameters for the target stimulus were set to 20% probability, 90 dB intensity, and 2000 Hz frequency. The two frequencies were randomly interspersed, and each scenario was repeated twice before the average value was calculated. The subject was presented with a target stimulus and the non-target stimulus was not utilized as a response. If a test subject had less than 80% hits, the test was considered invalid. The latencies of the N100, P200, N200, and P300 waves were recorded separately.

2.3. Exploratory eye movement (EEM) data acquisition

The EEM data was collected using a Shanghai-made Dekang DEM-2000 eye movement detector. The participants were instructed to sit comfortably in a chair and focus on a small screen in front of them. The angle of eyes movement from the left to the right side of the screen was 33°, and the distance between their eyes and the screen was 25 cm. The participants were instructed to pay close attention as the initial S-shaped pattern (S) was displayed on the screen for 15 s. Within this time, the device automatically captured the gaze positions and recorded the number of eye fixations (NEF). After that, the second and third S-shaped patterns (S2, S3), which were slightly different from the first image, were displayed on the screen. Every pattern lasted 15 s. When prompted with the question, "What is the difference between the two patterns," the participants were instructed to pay close attention before responding with, "There is no difference." The responsive seeking score was calculated from the gaze points in seven locations (only one point was considered in each region) for a period of 5 s (RSS). The device can automatically record the eye movement's trajectory, the data are automatically processed by the computer, and the entire procedure may be replayed for later use. A gaze point in EEM analysis is defined as an eye's gaze time that exceeds 200 ms on specific spot (the eyeball is moving within 2°). This is defined as the total number of gaze points in 15 s when the eye fixes on the S-pattern. The RSS score is broken down into seven S2 or S3 regions, and the instrument counts the NEF areas for a total of 5 s. No matter how often, the subject's attention on a certain place is worth one point. The maximum RSS score for each picture is thus 7, and for S2 and S3, the maximum RSS overall score is 14. NEF 30 and/or RSS 4 were used as the criterion for abnormality.

2.4. Measures

Hamilton Depression Scale (17 items) was used to assess depressive severity. A higher score indicates a more severe level of depressive symptoms (Bagby et al., 2004). The level of anxiety symptoms was evaluated using the HAMA. This scale consists of 14 items, each with a score ranging from 0 to 4. A higher score indicates a greater severity of anxiety symptoms. The SDSS is a 10-item scale that was clinician-administered to assess the level of functional impairment. A three-point Likert scale (0–2) was used to rate each item. A higher score indicates a greater level of functional impairment (Yan et al., 2022). Factor analysis of the EPQ scale revealed three orthogonal dimensions, leading to the proposed of four basic factors to determine personality: Extraversion (E), Neuroticism (N), Psychoticism (P), and Lie (L). These three dimensions reflect individuals' varying tendencies and levels of performance, resulting in different personality characteristics (Smith and Ellingson, 2002). The SCSQ is developed based on the characteristics of Chinese population. The questionnaire consists of 20 items, each rated on a four-point Likert scale with scores ranging from 0 to 3, and pertains to different coping strategies for handling everyday events (Cai et al., 2021). The SSS was used to evaluate social support. A total of 10 components and 3 dimensions made up the scale (i.e., subjective support, objective support, and support utilization). Scores under 20 indicate poor social support, between 20 and 30, moderate social support, and over 30, satisfied social support (Li and Shou, 2021). The

WCST is a card-matching task commonly used to evaluate cognitive flexibility and broader aspects of executive function in both research and clinical settings (Miles et al., 2021). The RBANS is a brief neurocognitive assessment tool that provides standardized measures of attention, language, memory, and visuospatial/constructional abilities (Faust et al., 2017).

2.5. Imaging data acquisition

Images were collected using a GE 3.0 T scanner (GE 3.0 T Signa Pioneer). The subjects were instructed to remain still, close their eyes, and stay awake. Soft earplugs and foam pads were employed to mitigate the effects of scanner noise and head movements during the imaging process. Scan parameters were repetition time/echo time = 2000/30 ms, 36 slices, 64 × 64 matrix, flip angle 90°, field of view 24 cm, slice thickness 4 mm, no gap, 250 volumes (500 s).

2.6. Data pre-processing

Data Processing Assistant for Resting-State fMRI (DPARSF) software was used to preprocess resting-state data in MATLAB. The slice timing and head motion in the images were corrected. To ensure the quality of the imaging data, the maximum x, y, or z displacement and angular motion for all subjects should have no more than 2 and 2°mm, respectively. The functional images were then resampled to 3 mm × 3 mm × 3 mm and normalized (Chao-Gan and Yu-Feng, 2010). An isotropic Gaussian kernel was used to smooth the processed images (fullwidth at half-maximum: 8 mm). Additionally, a linear trend removal and band-pass filtering (0.01–0.08 Hz) were processed (Song et al., 2011). Next, linear regression was used to remove a number of spurious covariates and their temporal derivatives from the data. These variables comprised the signal from a ventricular region of interest (ROI), the signal from a region centered in the white matter, and 24 head motion parameters determined *via* rigid body correction (Fox et al., 2005).

2.7. VMHC analysis

The REST software is used to examine VMHC (Song et al., 2011). In a brief, VMHC maps were created by computing Pearson correlations (Fisher z-transformed) between a given voxel and a mirrored voxel in the opposing hemisphere. The specifics of the VMHC analysis have been previously described in the literature (Zuo et al., 2010).

2.8. Statistical analysis

Data analysis in this study was conducted by using SPSS version 25.0. The chi-square test was used to examine the gender differences between the two groups. Two sample *t*-tests were employed to compare continuous variables such as age, years of education, and clinical scales. The significance level was set at $p < 0.05$.

The image data was analyzed using the DPARSF software. Two sample *t*-tests were conducted on each VMHC map to compare the groups. Then multiple comparison correction was performed based on the Gaussian random field (GRF) theory ($p < 0.001$ for voxel-level significance and $p < 0.05$ for cluster-level significance). Age, gender, education, and mean framewise displacement were used as covariates to minimize the potential influence of these variables.

For the correlation analyses, the mean VMHC values in aberrant brain areas with substantial differences between depressed patients and HCs were retrieved. The correlations between VMHC levels and clinical factors in patients with MDD were investigated using Pearson or Spearman correlation analyses. The significance level was set at $p < 0.05$ (corrected according to the Bonferroni's correction).

2.9. SVM analysis

The SVM analysis was used to determine the ability of VMHC values extracted from abnormal brain regions to differentiate between HCs and patients with MDD by utilizing the LIBSVM software[1] in MATLAB. The "leave one-out" method was used in the study.

3. Results

3.1. Demographic and clinical data

A total of 46 patients with MDD and 44 HCs were included in this study. However, due to significant head movement, the data of two HCs and four patients were excluded. As a result, the final imaging analysis included 42 patients with MDD and 42 HCs. Detailed demographic and medical information about the individuals can be found in **Supplementary Table 1**. The age difference between patients and HCs was significant ($p = 0.01$), and there was no significant difference between gender and years of education. There were significant differences in HAMA ($p < 0.001$), HAMD ($p < 0.001$), Neuroticism (N) ($p < 0.001$), Lie (L) ($p < 0.001$), Extraversion (E) ($p = 0.003$), SDSS ($p < 0.001$), SCSQ subscale scores ($p < 0.001$, $p = 0.001$), SSS ($p < 0.001$), NEF ($p < 0.001$), RSS ($p = 0.025$), N200 ($p = 0.038$), and P300 ($p = 0.012$) between the two groups. There was no significant difference between the two groups in SCSQ total scores, WCST, RBANS, N100, and P200.

3.2. VMHC analysis in depressed patients and HCs

Our results showed that in the patients with MDD, the VMHC values of the superior/middle occipital gyrus and cerebellum 8/vermis 8/vermis 9 increased compared to HCs, while the VMHC values of the insula decreased. The specific details can be found in **Table 1** and **Figure 1**.

1 http://www.csie.ntu.edu.tw/~cjlin/libsvm/

TABLE 1 Regions with abnormal VMHC values in patients with MDD.

Cluster location	Peak (MNI)			Number of voxels	*T*-value
	x	y	z		
Cerebellum 8/Vermis 8/Vermis 9	±6	−57	−30	126	4.3385
Superior/middle occipital gyrus	±12	−102	12	40	4.5177
Insula	±39	18	−3	44	−2.8516

MDD, major depressive disorder; MNI, Montreal Neurological Institute; VMHC, voxel-mirrored homotopic connectivity.

3.3. SVM analysis

According to abnormal VMHC values in various brain areas and the combination of these clusters, **Figure 2A** illustrates the effectiveness of differentiating patients with MDD from HCs. The sensitivity, specificity, and accuracy of the differentiation using the VMHC values in the cerebellum 8/vermis 8/vermis 9 and insula were 80.95, 83.33, and 82.14%, respectively (**Figure 2B**). From VMHC values in the superior/middle occipital gyrus and insula, the sensitivity was 78.57%, the specificity was 85.71%, and the accuracy was 82.14% (**Figure 2C**). In addition, the receiver operating curve (ROC) of applying abnormal VMHC to distinguish patients with MDD from HCs shown in **Supplementary Figure 1**, and the accuracy, sensitivity, and specificity of classification with ROC and SVM shown in **Supplementary Table 2**. ROC curve can only analyze a single brain region, while VMHC combined with SVM can analyze two brain regions. This is also an advantage of SVM, which takes into account the spatial and temporal distribution of the brain.

3.4. Correlation analysis result

Pearson/Spearman correlation analyses revealed the following correlations: (1) the VMHC values in the superior/middle occipital gyrus and SDSS total score ($r = -0.441$, $p = 0.003$, df = 41); (2) the VMHC values in the superior/middle occipital gyrus and the scores of Active Coping ($r = 0.332$, $p = 0.032$, df = 41); (3) the VMHC values in the superior/middle occipital gyrus and RSS2 ($r = 0.443$, $p = 0.018$, df = 27); and (4) the VMHC values in the insula and RP ($r = -0.341$, $p = 0.027$, df = 41) (**Figure 3**).

4. Discussion

In this study, decreased VMHC in the insula and increased VMHC values in the sensory-motor networks may be distinctive neurobiological feature for patients with MDD, which could serve as potential imaging markers to differentiate HCs and patients with MDD. In addition, we found correlations between abnormal VMHC values and clinical/cognitive parameters in MDD. The aberrant VMHC values were further demonstrated to be promising imaging indicators of MDD by using the SVM analysis.

Event-related potential is a mature method to understand brain function in cognitive process, which is expected to make greater contribution to the identification, prediction (Tsai and Liang, 2021), treatment and prevention of mental disorders (Hajcak et al., 2019), and P300 is a typical indicator of neurophysiological ERP (Wada et al., 2019). Our research results show that there are obvious differences between patients with MDD and HCs on the cognitive level, which is consistent with a previous study (Wang et al., 2023). This may be caused by the depression of the patients and the decrease of attention to external events. The number of fixations (NEF) and response search score (RSS) in EEM are related to mental state, active attention and cognitive function (Ross et al., 2000). The neural basis of EEM has been clearly explained by a research (Lencer and Trillenberg, 2008). Studies have proved that compared with the HC group, the eye movements of patients with MDD are abnormal (Wang Y. et al., 2022). At the same time, the combination of P300 and eye movement data can improve the accuracy of auxiliary diagnosis of depression (Diao et al., 2022). ERP and EEM combined with other psychological scale data, we can see that there are obvious differences between patients with MDD and HCs.

The insula, surrounded by cortical gyrus, white matter, and basal ganglia structures (Dziedzic et al., 2022), is a center of integration for emotional, visceromotor, autonomic, and interoceptive information. Its diverse functional roles may be due to its strong connections to a broad network of cortical and subcortical regions (Wang R. et al., 2022). Studies have shown that removal of the insular lobe may disrup autonomic nerve function and alter an individual's experience of emotions (Lacuey et al., 2019; Motomura et al., 2019). Processing input from many functioning systems involves an essential integration role for the insular cortex (Starr et al., 2009; Morita et al., 2014; Allen et al., 2016; Berret et al., 2019; Choi et al., 2022). Guo et al. (2015) found that compared with HCs, the insula of the front-limbic circuit, hate circuit, and visual regions of the patients with MDD showed decreased FC. At the same time, FC between the insula and ACC was also reduced (Krug et al., 2022). Patients with MDD showed abnormal FC between the insular subdivisions to the superior temporal sulcus, inferior prefrontal gyrus, amygdala, and posterior parietal cortex (Peng et al., 2018). Multiple studies on patients with MDD have revealed that, in comparison to HCs, their connectivity in insular lobes was reduced (Veer et al., 2010; Sliz and Hayley, 2012; Avery et al., 2014; Penner et al., 2016; Yin et al., 2018). The insula plays a key role in emotional regulation, conscious arousal, and consciousness. The decrease of insular connectivity may reflect the important regulation of negative or arousal stimuli. The decreased connectivity in the insula of patients with MDD may indicate an alteration in their perception of visceral responses and subjective sensory states (Critchley et al., 2004). Consistent with these results, we discovered that VMHC in the insula was significantly lower in patients with MDD compared to HCs, further supporting the insular crucial function in the neurological process underlying MDD. We speculate that the decrease of VMHC in the insula may be an indicator related to the emotional state of patients with MDD.

The cerebellum, located in the posterior fossa, is commonly known to control movement. However, recent studies show that it also plays a significant role in cognition and emotion (Rabellino et al., 2018; Habas, 2021; Su et al., 2021). In this study, compared with HCs, VMHC of the cerebellum 8/vermis 8/vermis 9 in patients with MDD was significantly increased. This increase in FC is often interpreted as a sign of dedifferentiation or compensatory

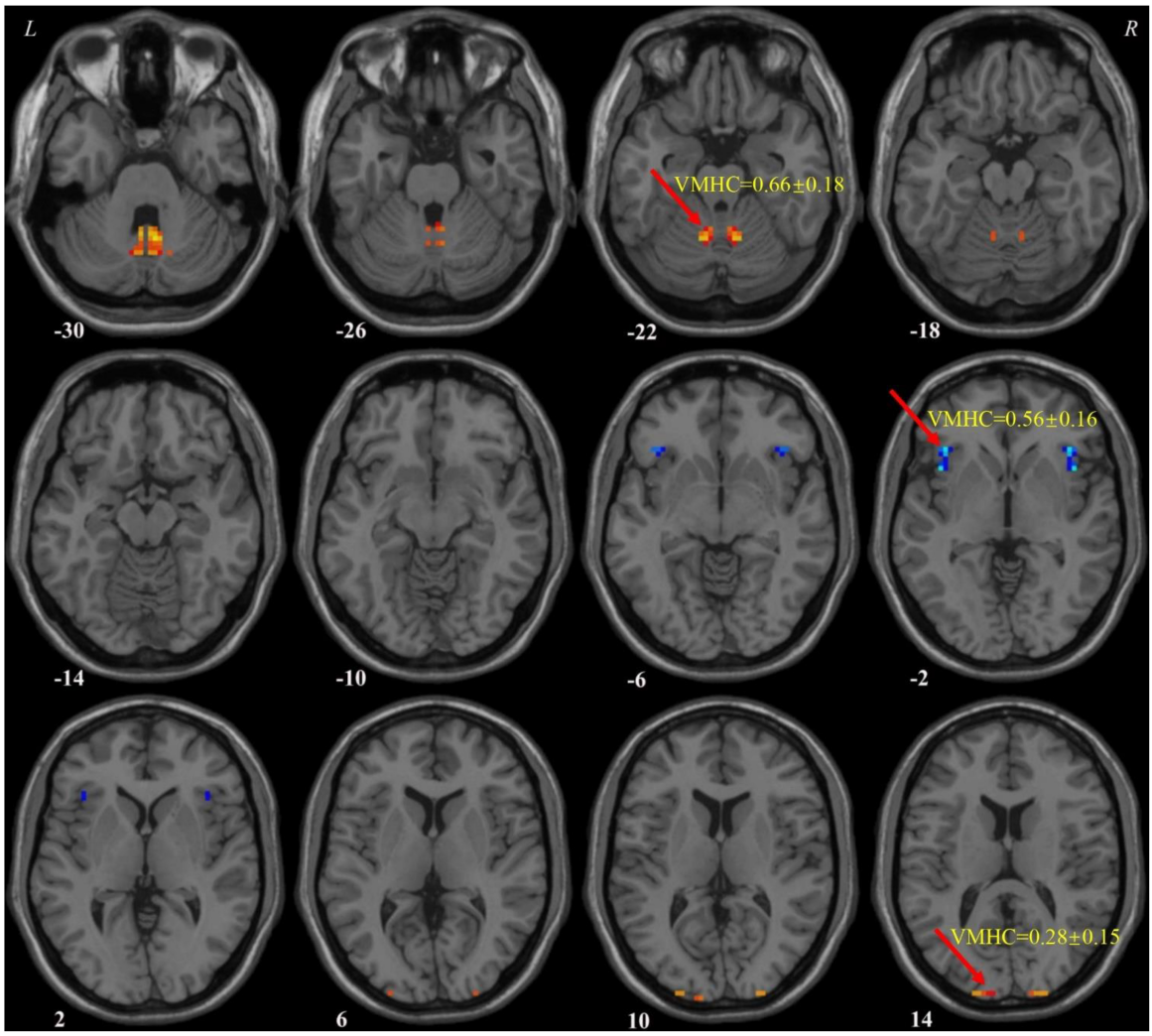

FIGURE 1
Voxel-mirrored homotopic connectivity (VMHC) values of abnormal regions in patients with MDD. MDD, major depressive disorder; VMHC, voxel-mirrored homotopic connectivity.

redistribution (Cabeza et al., 2002; Grady et al., 2005; Pagen et al., 2020). Inflammatory cytokines (i.e., tumor necrosis factor and interleukin 6) can activate astrocytes and show hyperfunction (increased blood flow and metabolism) (Guo et al., 2013a). Regional hyperfunction may encourage an increase in FC and regional activity (Liu et al., 2015; Wang et al., 2016). Studies have shown that patients with MDD with MDD experience a significant increase in communication between the cerebellum and the cerebellar-anterior default mode network (Ding et al., 2022). In comparison to HCs, our previous study found a marked decrease in the FC between the cerebellum and cerebral cortex in individuals with both treatment-sensitive and treatment-resistant depression (Guo et al., 2013b). Another study showed that the cerebellar-cerebral dynamic FC of patients with MDD was lower than that of HCs (Zhu et al., 2020). This is because MDD is a multidimensional disease related to emotion, cognition, memory, etc., some special default normal functions of HCs may become dysfunctional in MDD patients, such as the VMHC of the cerebellum 8/vermis 8/vermis 9 in this study.

The findings of this study showed a significant increase in the VMHC value of the superior/medium occipital gyrus. The occipital lobe, located at the back of the cerebral hemisphere, is primarily utilized for processing visual information, and communicating with the cerebral cortex. It plays a crucial role in how facial emotions are perceived and processed (Teng et al., 2018; Li and Wang, 2021). Patients with MDD may experience aberrant cognitive processes, such as attention deficit disorder and motor delay (Yu et al., 2017). The results of this study provide additional evidence to clarify the judgment of MDD.

Support vector machine has been widely used for classify mental illnesses. The FC signal as a potential diagnostic index requires that the sensitivity or specificity of SVM be higher than 0.6 (Guo et al., 2011; Shan et al., 2021). The previous SVM analysis showed that using SVM to classify the neuroimaging biomarkers of MDD resulted in a diagnostic accuracy is 98.96% (Song et al., 2022). Compared with a study by Song et al. (2022), our study found that patients with MDD had VMHC abnormalities in extensive brain regions. At this point, the two studies are consistent. Different

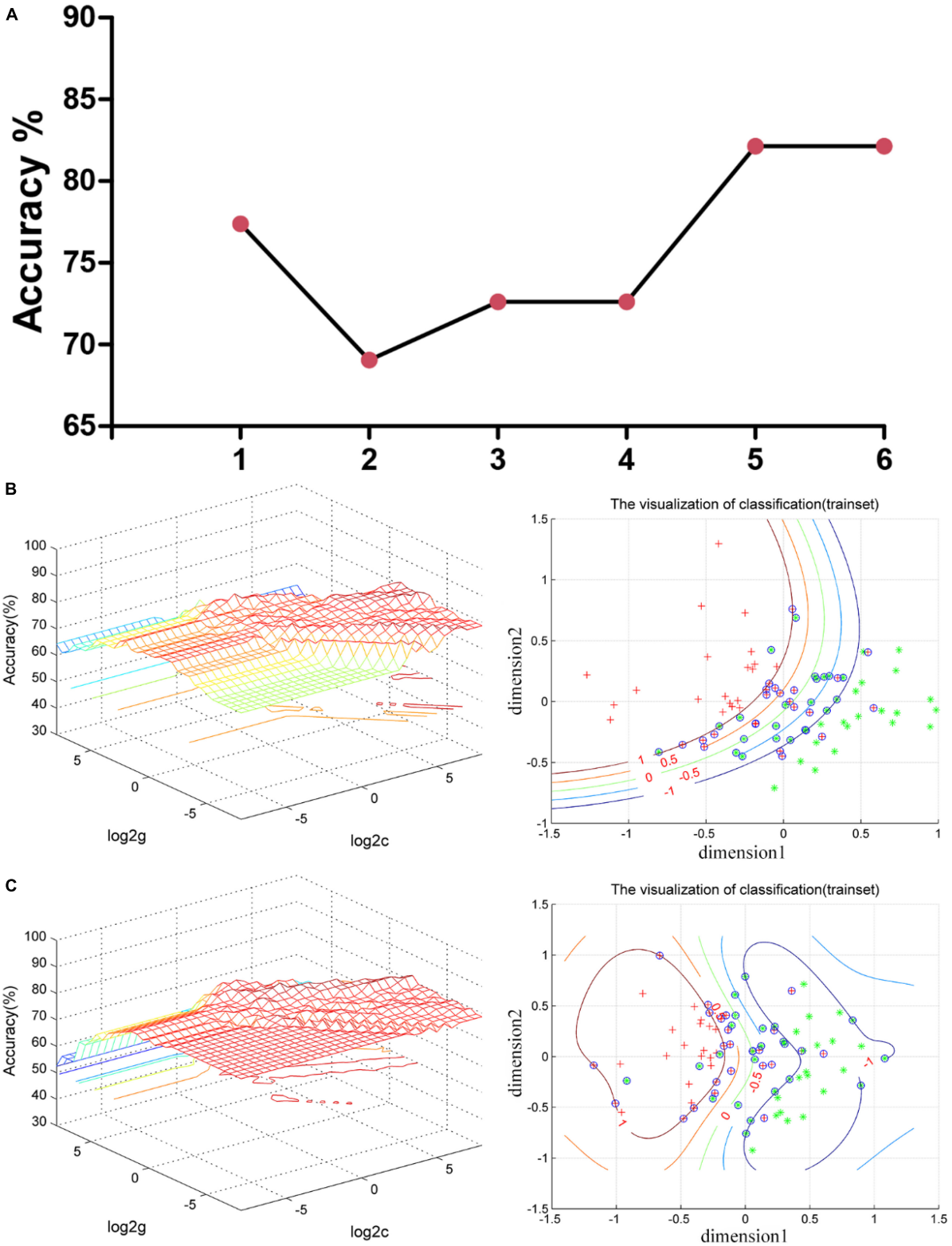

FIGURE 2
Support vector machine (SVM) results. **(A)** The accuracy of classification of six SVM analyses. One represents the VMHC values in the cerebellum 8/vermis 8/vermis 9; 2 represents the VMHC values in the superior/middle occipital gyrus; 3 represents the VMHC values in the insula; 4 represents the combination of the VMHC values in the cerebellum 8/vermis 8/vermis 9 and superior/middle occipital gyrus; 5 represents the combination of the VMHC values in the cerebellum 8/vermis 8/vermis 9 and insula; and 6 represents the combination of the VMHC values in the superior/middle occipital gyrus and insula. **(B)** SVM analysis applied the combination of the VMHC values in the cerebellum 8/vermis 8/vermis 9 and insula. Sensitivity = 80.95%, specificity = 83.33%, and accuracy = 82.14%. In the left part, the red cross represents patient with MDD, and the green asterisk represents healthy controls. The blue circle represents support vector. **(C)** SVM analysis applied the combination of the VMHC values in the superior/middle occipital gyrus and insula. Sensitivity = 78.57%, specificity = 85.71%, and accuracy = 82.14%. In the left part, the red cross represents patient with MDD, and the green asterisk represents healthy controls. The blue circle represents support vector. SVM, support vector machines; VMHC, voxel-mirrored homotopic connectivity; MDD, major depressive disorder.

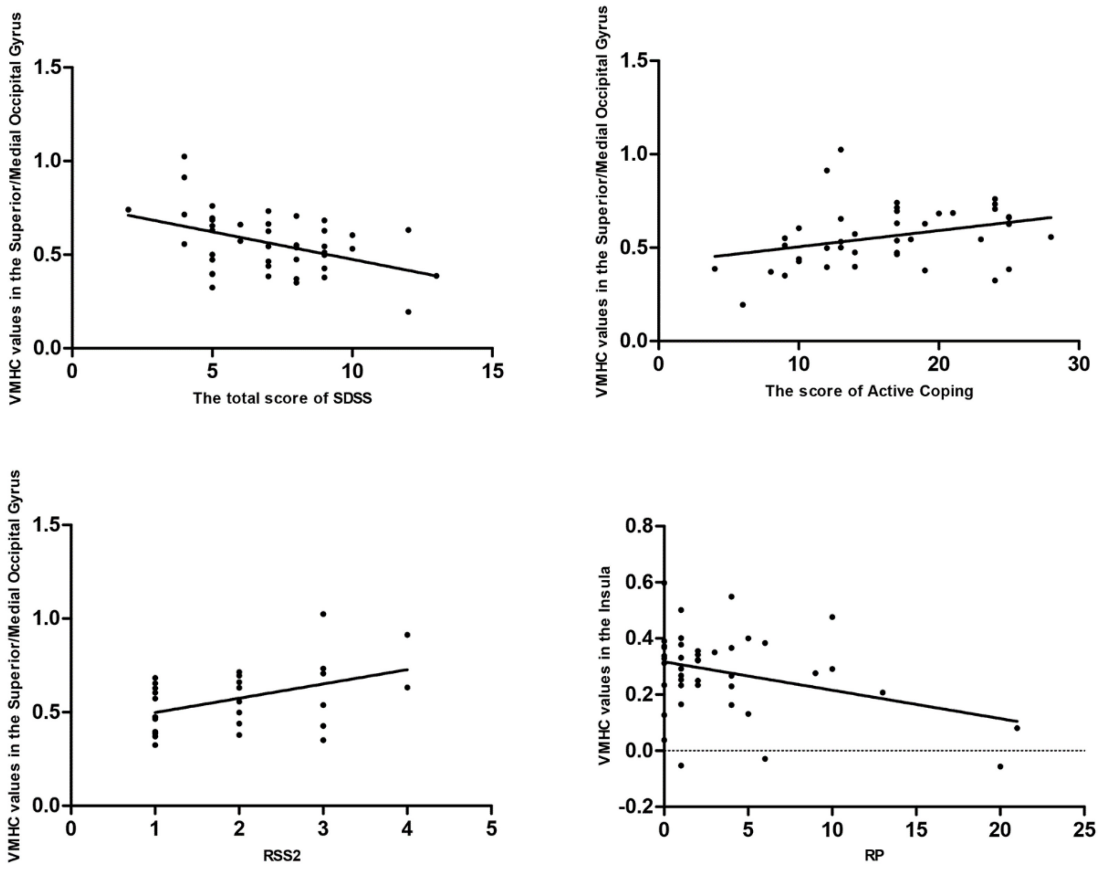

FIGURE 3
Pearson/Spearman correlations. Correlations were found as follows: (1) The VMHC values in the superior/middle occipital gyrus and the SDSS total scores ($r = -0.441$, $p = 0.003$, df = 41); (2) the VMHC values in the superior/middle occipital gyrus and the scores of Active Coping ($r = 0.332$, $p = 0.032$, df = 41); (3) the VMHC values in the superior/middle occipital gyrus and RSS2 ($r = 0.443$, $p = 0.018$, df = 27); and (4) the VMHC values in the insula and RP ($r = -0.341$, $p = 0.027$, df = 41). VMHC, voxel-mirrored homotopic connectivity; SDSS, social function defect screening scale; RSS2, responsive search score 2; RP, responses answer.

from Song et al. (2022) research, our research found abnormal VMHC in the insula and the sensory-motor networks. At the same time, we verify the difference between patients with MDD and HCs by measuring clinical data (such as ERP, EEM, and so on), which makes the study more convincing. The current SVM results show that the VMHC values of the insula, cerebellum 8/vermis 8/vermis 9 and superior/medium organic gyrus are greater than 0.78 in the sensitivity, accuracy, and specificity of distinguishing patients with MDD from HCs. Therefore, the VMHC values of the insula, cerebellum 8/vermis 8/vermis 9 and superior/medium organic gyrus may be used as potential imaging markers for MDD.

There are still some limitations in this study. First, the area under curve (AUC) of this study was impressive. But clearly, this is a small preliminary report that needs to be replicated. Second, we recruited patients who did not take medicine at the time of the first episode, and patients who had relapsed and did not take medicine for at least 2 weeks. The dissemination of research findings may be constrained for patients who experience relapses since the impact of antidepressant medications and number of episodes on brain spontaneous activity cannot be entirely ruled out. Finally, we only scanned the patients at baseline, so we did not know the alterations of spontaneous neuronal activity after treatment.

5. Conclusion

In conclusion, the study's comparison of VMHC alterations in HCs and patients with MDD was groundbreaking. Our research results show that decreased VMHC in the insula and increased VMHC values in the sensory-motor networks may be a distinctive neurobiological feature for patients with MDD, which might be served as potential imaging markers to discriminate HCs and Patients with MDD.

Data availability statement

The original contributions presented in this study are included in the article/**Supplementary material**, further inquiries can be directed to the corresponding authors.

Ethics statement

This study was approved by the Ethics Committee of the Third People's Hospital of Foshan (FSSY-LS202001).

The patients/participants provided their written informed consent to participate in this study.

Author contributions

CZ, HJ, and HY: writing—original draft, writing—review and editing, methodology, and software. XL, JL, QZ, WL, YO, CP, YY, and WW: validation, investigation, and resources. GX and WG: supervision, project administration, and funding acquisition. All authors contributed to the article and approved the submitted version.

Funding

This study was supported by grants from the "The 14th Five-Year" Medical High-level Key Medical Specialty Development Project of Foshan (Grant No. FSGSP145069), the Project of Foshan Science and Technology Bureau (Grant No. 2020001005608), and National Natural Science Foundation of China (Grant No. 82171508).

Conflict of interest

The authors declare that the research was conducted in the absence of any commercial or financial relationships that could be construed as a potential conflict of interest.

Publisher's note

All claims expressed in this article are solely those of the authors and do not necessarily represent those of their affiliated organizations, or those of the publisher, the editors and the reviewers. Any product that may be evaluated in this article, or claim that may be made by its manufacturer, is not guaranteed or endorsed by the publisher.

Supplementary material

The Supplementary Material for this article can be found online at: https://www.frontiersin.org/articles/10.3389/fnins.2023.1135337/full#supplementary-material

References

Allen, M., Fardo, F., Dietz, M. J., Hillebrandt, H., Friston, K. J., Rees, G., et al. (2016). Anterior insula coordinates hierarchical processing of tactile mismatch responses. *Neuroimage* 127, 34–43. doi: 10.1016/j.neuroimage.2015.11.030

Andersson, E., Crowley, J. J., Lindefors, N., Ljotsson, B., Hedman-Lagerlof, E., Boberg, J., et al. (2019). Genetics of response to cognitive behavior therapy in adults with major depression: a preliminary report. *Mol. Psychiatry* 24, 484–490. doi: 10.1038/s41380-018-0289-9

Avery, J. A., Drevets, W. C., Moseman, S. E., Bodurka, J., Barcalow, J. C., and Simmons, W. K. (2014). Major depressive disorder is associated with abnormal interoceptive activity and functional connectivity in the insula. *Biol. Psychiatry* 76, 258–266. doi: 10.1016/j.biopsych.2013.11.027

Bagby, R. M., Ryder, A. G., Schuller, D. R., and Marshall, M. B. (2004). The hamilton depression rating scale: has the gold standard become a lead weight? *Am. J. Psychiatry* 161, 2163–2177. doi: 10.1176/appi.ajp.161.12.2163

Berret, E., Kintscher, M., Palchaudhuri, S., Tang, W., Osypenko, D., Kochubey, O., et al. (2019). Insular cortex processes aversive somatosensory information and is crucial for threat learning. *Science* 364:eaaw0474. doi: 10.1126/science.aaw0474

Cabeza, R., Anderson, N. D., Locantore, J. K., and McIntosh, A. R. (2002). Aging gracefully: compensatory brain activity in high-performing older adults. *NeuroImage* 17, 1394–1402. doi: 10.1006/nimg.2002.1280

Cai, Z., Zheng, S., Huang, Y., Au, W. W., Qiu, Z., and Wu, K. (2021). The interactive effects of cognition on coping styles among Chinese during the COVID-19 pandemic. *Int. J. Environ. Res. Public Health* 18:3148. doi: 10.3390/ijerph18063148

Chao-Gan, Y., and Yu-Feng, Z. (2010). DPARSF: a MATLAB toolbox for "Pipeline" data analysis of resting-state fMRI. *Front. Syst. Neurosci.* 4:13. doi: 10.3389/fnsys.2010.00013

Chen, W., Hu, H., Wu, Q., Chen, L., Zhou, J., Chen, H. H., et al. (2021). Altered static and dynamic interhemispheric resting-state functional connectivity in patients with thyroid-associated ophthalmopathy. *Front. Neurosci.* 15:799916. doi: 10.3389/fnins.2021.799916

Choi, S., Kim, K., Kwon, M., Bai, S. J., Cha, M., and Lee, B. H. (2022). Modulation of neuropathic pain by glial regulation in the insular cortex of rats. *Front. Mol. Neurosci.* 15:815945. doi: 10.3389/fnmol.2022.815945

Chu, Y., Wu, J., Wang, D., Huang, J., Li, W., Zhang, S., et al. (2022). Altered voxel-mirrored homotopic connectivity in right temporal lobe epilepsy as measured using resting-state fMRI and support vector machine analyses. *Front. Psychiatry* 13:958294. doi: 10.3389/fpsyt.2022.958294

Compton, R. J., Feigenson, K., and Widick, P. (2005). Take it to the bridge: an interhemispheric processing advantage for emotional faces. *Brain Res. Cogn. Brain Res.* 24, 66–72. doi: 10.1016/j.cogbrainres.2004.12.002

CONVERGE consortium (2015). Sparse whole-genome sequencing identifies two loci for major depressive disorder. *Nature* 523, 588–591. doi: 10.1038/nature14659

COVID-19 Mental Disorders Collaborators (2021). Global prevalence and burden of depressive and anxiety disorders in 204 countries and territories in 2020 due to the COVID-19 pandemic. *Lancet* 398, 1700–1712. doi: 10.1016/S0140-6736(21)02143-7

Critchley, H. D., Wiens, S., Rotshtein, P., Ohman, A., and Dolan, R. J. (2004). Neural systems supporting interoceptive awareness. *Nat. Neurosci.* 7, 189–195. doi: 10.1038/nn1176

Dai, P., Zhou, X., Xiong, T., Ou, Y., Chen, Z., Zou, B., et al. (2022). Altered effective connectivity among the cerebellum and cerebrum in patients with major depressive disorder using multisite resting-state fMRI. *Cerebellum* [Epub ahead of print]. doi: 10.1007/s12311-022-01454-9

Demirtas, M., Tornador, C., Falcon, C., Lopez-Sola, M., Hernandez-Ribas, R., Pujol, J., et al. (2016). Dynamic functional connectivity reveals altered variability in functional connectivity among patients with major depressive disorder. *Hum. Brain Mapp.* 37, 2918–2930. doi: 10.1002/hbm.23215

Diao, Y., Geng, M., Fu, Y., Wang, H., Liu, C., Gu, J., et al. (2022). A combination of P300 and eye movement data improves the accuracy of auxiliary diagnoses of depression. *J. Affect. Disord.* 297, 386–395. doi: 10.1016/j.jad.2021.10.028

Ding, W., Cao, W., Wang, Y., Sun, Y., Chen, X., Zhou, Y., et al. (2015). Altered functional connectivity in patients with subcortical vascular cognitive impairment–A resting-state functional magnetic resonance imaging study. *PLoS One* 10:e0138180. doi: 10.1371/journal.pone.0138180

Ding, Y., Ou, Y., Yan, H., Fu, X., Yan, M., Li, H., et al. (2022). Disrupted cerebellar-default mode network functional connectivity in major depressive disorder with gastrointestinal symptoms. *Front. Cell Neurosci.* 16:833592. doi: 10.3389/fncel.2022.833592

Dziedzic, T. A., Bala, A., and Marchel, A. (2022). Anatomical aspects of the insula, opercula and peri-insular white matter for a transcortical approach to insular glioma resection. *Neurosurg. Rev.* 45, 793–806. doi: 10.1007/s10143-021-01602-5

Fan, B., Wu, P., Zhou, X., Chen, Z., Pang, L., Shi, K., et al. (2022). Aberrant resting-state interhemispheric functional connectivity in patients with anti-N-methyl-D-aspartate receptor encephalitis. *Neuroradiology* 64, 2021–2030. doi: 10.1007/s00234-022-02983-0

Faust, K., Nelson, B. D., Sarapas, C., and Pliskin, N. H. (2017). Depression and performance on the repeatable battery for the assessment of neuropsychological status. *Appl. Neuropsychol. Adult.* 24, 350–356. doi: 10.1080/23279095.2016.1185426

Fox, M. D., Snyder, A. Z., Vincent, J. L., Corbetta, M., Van Essen, D. C., and Raichle, M. E. (2005). The human brain is intrinsically organized into dynamic, anticorrelated functional networks. *Proc. Natl. Acad. Sci. U.S.A.* 102, 9673–9678. doi: 10.1073/pnas.0504136102

Fries, G. R., Saldana, V. A., Finnstein, J., and Rein, T. (2022). Molecular pathways of major depressive disorder converge on the synapse. *Mol. Psychiatry* 28, 284–297. doi: 10.1038/s41380-022-01806-1

Grady, C. L., McIntosh, A. R., and Craik, F. I. (2005). Task-related activity in prefrontal cortex and its relation to recognition memory performance in young and old adults. *Neuropsychologia* 43, 1466–1481. doi: 10.1016/j.neuropsychologia.2004.12.016

Guo, W., Cui, X., Liu, F., Chen, J., Xie, G., Wu, R., et al. (2018). Decreased interhemispheric coordination in the posterior default-mode network and visual regions as trait alterations in first-episode, drug-naive major depressive disorder. *Brain Imaging Behav.* 12, 1251–1258. doi: 10.1007/s11682-017-9794-8

Guo, W., Liu, F., Liu, J., Yu, L., Zhang, Z., Zhang, J., et al. (2013a). Is there a cerebellar compensatory effort in first-episode, treatment-naive major depressive disorder at rest? *Prog. Neuropsychopharmacol. Biol. Psychiatry* 46, 13–18. doi: 10.1016/j.pnpbp.2013.06.009

Guo, W., Liu, F., Xue, Z., Gao, K., Liu, Z., Xiao, C., et al. (2013b). Abnormal resting-state cerebellar-cerebral functional connectivity in treatment-resistant depression and treatment sensitive depression. *Prog. Neuropsychopharmacol. Biol. Psychiatry* 44, 51–57. doi: 10.1016/j.pnpbp.2013.01.010

Guo, W., Liu, F., Xiao, C., Zhang, Z., Liu, J., Yu, M., et al. (2015). Decreased insular connectivity in drug-naive major depressive disorder at rest. *J. Affect. Disord.* 179, 31–37. doi: 10.1016/j.jad.2015.03.028

Guo, W. B., Liu, F., Xue, Z. M., Yu, Y., Ma, C. Q., Tan, C. L., et al. (2011). Abnormal neural activities in first-episode, treatment-naive, short-illness-duration, and treatment-response patients with major depressive disorder: a resting-state fMRI study. *J. Affect. Disord.* 135, 326–331. doi: 10.1016/j.jad.2011.06.048

Habas, C. (2021). Functional connectivity of the cognitive cerebellum. *Front. Syst. Neurosci.* 15:642225. doi: 10.3389/fnsys.2021.642225

Hajcak, G., Klawohn, J., and Meyer, A. (2019). The utility of event-related potentials in clinical psychology. *Annu. Rev. Clin. Psychol.* 15, 71–95. doi: 10.1146/annurev-clinpsy-050718-095457

Hasin, D. S., Sarvet, A. L., Meyers, J. L., Saha, T. D., Ruan, W. J., Stohl, M., et al. (2018). Epidemiology of adult DSM-5 major depressive disorder and its specifiers in the United States. *JAMA Psychiatry* 75, 336–346. doi: 10.1001/jamapsychiatry.2017.4602

Hayley, S., Hakim, A. M., and Albert, P. R. (2021). Depression, dementia and immune dysregulation. *Brain* 144, 746–760. doi: 10.1093/brain/awaa405

Hou, Z., Song, X., Jiang, W., Yue, Y., Yin, Y., Zhang, Y., et al. (2016). Prognostic value of imbalanced interhemispheric functional coordination in early therapeutic efficacy in major depressive disorder. *Psychiatry Res. Neuroimaging* 255, 1–8. doi: 10.1016/j.pscychresns.2016.07.011

Jia, C., Ou, Y., Chen, Y., Li, P., Lv, D., Yang, R., et al. (2020). Decreased resting-state interhemispheric functional connectivity in medication-free obsessive-compulsive disorder. *Front. Psychiatry* 11:559729. doi: 10.3389/fpsyt.2020.559729

Jin, C., Qi, S., Teng, Y., Li, C., Yao, Y., Ruan, X., et al. (2021). Integrating structural and functional interhemispheric brain connectivity of gait freezing in Parkinson's disease. *Front. Neurol.* 12:609866. doi: 10.3389/fneur.2021.609866

Kendall, K. M., Van Assche, E., Andlauer, T. F. M., Choi, K. W., Luykx, J. J., Schulte, E. C., et al. (2021). The genetic basis of major depression. *Psychol. Med.* 51, 2217–2230. doi: 10.1017/S0033291721000441

Kozel, F. A., Rao, U., Lu, H., Nakonezny, P. A., Grannemann, B., McGregor, T., et al. (2011). Functional connectivity of brain structures correlates with treatment outcome in major depressive disorder. *Front. Psychiatry* 2:7. doi: 10.3389/fpsyt.2011.00007

Krug, S., Muller, T., Kayali, O., Leichter, E., Peschel, S. K. V., Jahn, N., et al. (2022). Altered functional connectivity in common resting-state networks in patients with major depressive disorder: a resting-state functional connectivity study. *J. Psychiatr Res.* 155, 33–41. doi: 10.1016/j.jpsychires.2022.07.040

Krupnik, R., Yovel, Y., and Assaf, Y. (2021). Inner hemispheric and interhemispheric connectivity balance in the human brain. *J. Neurosci.* 41, 8351–8361. doi: 10.1523/JNEUROSCI.1074-21.2021

Lacuey, N., Garg, V., Bangert, B., Hampson, J. P., Miller, J., and Lhatoo, S. (2019). Insular resection may lead to autonomic function changes. *Epilepsy Behav.* 97, 260–264. doi: 10.1016/j.yebeh.2019.04.035

Lai, C. H., and Wu, Y. T. (2014). Decreased inter-hemispheric connectivity in anterior sub-network of default mode network and cerebellum: significant findings in major depressive disorder. *Int. J. Neuropsychopharmacol.* 17, 1935–1942. doi: 10.1017/S1461145714000947

Lencer, R., and Trillenberg, P. (2008). Neurophysiology and neuroanatomy of smooth pursuit in humans. *Brain Cogn.* 68, 219–228. doi: 10.1016/j.bandc.2008.08.013

Li, N., and Shou, J. (2021). Risk factors for the frequent attendance of older patients at community health service centers in China: a cross-sectional study based on stratified sampling. *BMC Fam. Pract.* 22:221. doi: 10.1186/s12875-021-01575-w

Li, X., and Wang, J. (2021). Abnormal neural activities in adults and youths with major depressive disorder during emotional processing: a meta-analysis. *Brain Imaging Behav.* 15, 1134–1154. doi: 10.1007/s11682-020-00299-2

Liu, F., Zhu, C., Wang, Y., Guo, W., Li, M., Wang, W., et al. (2015). Disrupted cortical hubs in functional brain networks in social anxiety disorder. *Clin. Neurophysiol.* 126, 1711–1716. doi: 10.1016/j.clinph.2014.11.014

Liu, S., Tong, Y., Wang, X., Yu, X., and Xu, Y. (2022). Baseline cognitive functioning can predict the trajectory of acute treatment in first-episode major depressive disorder. *Eur. Arch. Psychiatry Clin. Neurosci.* [Epub ahead of print]. doi: 10.1007/s00406-022-01475-9

Liu, Y., Ou, Y., Zhao, J., and Guo, W. (2021). Abnormal interhemispheric homotopic functional connectivity is correlated with gastrointestinal symptoms in patients with major depressive disorder. *J. Psychiatr. Res.* 144, 234–240. doi: 10.1016/j.jpsychires.2021.10.016

Lou, Y., Lei, Y., Mei, Y., Leppanen, P. H. T., and Li, H. (2019). Review of abnormal self-knowledge in major depressive disorder. *Front. Psychiatry* 10:130. doi: 10.3389/fpsyt.2019.00130

Miles, S., Howlett, C. A., Berryman, C., Nedeljkovic, M., Moseley, G. L., and Phillipou, A. (2021). Considerations for using the wisconsin card sorting test to assess cognitive flexibility. *Behav. Res. Methods* 53, 2083–2091. doi: 10.3758/s13428-021-01551-3

Morita, T., Tanabe, H. C., Sasaki, A. T., Shimada, K., Kakigi, R., and Sadato, N. (2014). The anterior insular and anterior cingulate cortices in emotional processing for self-face recognition. *Soc. Cogn. Affect. Neurosci.* 9, 570–579. doi: 10.1093/scan/nst011

Motomura, K., Terasawa, Y., Natsume, A., Wakabayashi, T., and Umeda, S. (2019). Anterior insular cortex stimulation and its effects on emotion recognition. *Brain Stimul.* 224, 2167–2181. doi: 10.1016/j.brs.2018.12.898

Nguyen, T.-D., Harder, A., Xiong, Y., Kowalec, K., Hägg, S., Cai, N., et al. (2022). Genetic heterogeneity and subtypes of major depression. *Mol. Psychiatry* 27, 1667–1675. doi: 10.1038/s41380-021-01413-6

Pagen, L. H. G., van de Ven, V. G., Gronenschild, E., Priovoulos, N., Verhey, F. R. J., and Jacobs, H. I. L. (2020). Contributions of cerebro-cerebellar default mode connectivity patterns to memory performance in mild cognitive impairment. *J. Alzheimers Dis.* 75, 633–647. doi: 10.3233/JAD-191127

Peng, X., Lin, P., Wu, X., Gong, R., Yang, R., and Wang, J. (2018). Insular subdivisions functional connectivity dysfunction within major depressive disorder. *J. Affect. Disord.* 227, 280–288. doi: 10.1016/j.jad.2017.11.018

Penner, J., Ford, K. A., Taylor, R., Schaefer, B., Theberge, J., Neufeld, R. W., et al. (2016). Medial prefrontal and anterior insular connectivity in early schizophrenia and major depressive disorder: a resting functional mri evaluation of large-scale brain network models. *Front. Hum. Neurosci.* 10:132. doi: 10.3389/fnhum.2016.00132

Rabellino, D., Densmore, M., Theberge, J., McKinnon, M. C., and Lanius, R. A. (2018). The cerebellum after trauma: resting-state functional connectivity of the cerebellum in posttraumatic stress disorder and its dissociative subtype. *Hum. Brain Mapp.* 39, 3354–3374. doi: 10.1002/hbm.24081

Ran, S., Zuo, Z., Li, C., Yin, X., Qu, W., Tang, Q., et al. (2020). Atrophic corpus callosum associated with altered functional asymmetry in major depressive disorder. *Neuropsychiatr. Dis. Treat.* 16, 1473–1482. doi: 10.2147/NDT.S245078

Ross, R. G., Harris, J. G., Olincy, A., and Radant, A. (2000). Eye movement task measures inhibition and spatial working memory in adults with schizophrenia, ADHD, and a normal comparison group. *Psychiatry Res.* 95, 35–42. doi: 10.1016/S0165-1781(00)00153-0

Shan, X., Cui, X., Liu, F., Li, H., Huang, R., Tang, Y., et al. (2021). Shared and distinct homotopic connectivity changes in melancholic and non-melancholic depression. *J. Affect. Disord.* 287, 268–275. doi: 10.1016/j.jad.2021.03.038

Sliz, D., and Hayley, S. (2012). Major depressive disorder and alterations in insular cortical activity: a review of current functional magnetic imaging research. *Front. Hum. Neurosci.* 6:323. doi: 10.3389/fnhum.2012.00323

Smith, D. B., and Ellingson, J. E. (2002). Substance versus style: a new look at social desirability in motivating contexts. *J. Appl. Psychol.* 87, 211–219. doi: 10.1037/0021-9010.87.2.211

Song, X. W., Dong, Z. Y., Long, X. Y., Li, S. F., Zuo, X. N., Zhu, C. Z., et al. (2011). REST: a toolkit for resting-state functional magnetic resonance imaging data processing. *PLoS One* 6:e25031. doi: 10.1371/journal.pone.0025031

Song, Y., Huang, C., Zhong, Y., Wang, X., and Tao, G. (2022). Abnormal reginal homogeneity in left anterior cingulum cortex and precentral gyrus as a potential neuroimaging biomarker for first-episode major depressive disorder. *Front. Psychiatry* 13:924431. doi: 10.3389/fpsyt.2022.924431

Starr, C. J., Sawaki, L., Wittenberg, G. F., Burdette, J. H., Oshiro, Y., Quevedo, A. S., et al. (2009). Roles of the insular cortex in the modulation of pain: insights from brain lesions. *J. Neurosci.* 29, 2684–2694. doi: 10.1523/JNEUROSCI.5173-08.2009

Steardo, L. Jr., Carbone, E. A., de Filippis, R., Pisanu, C., Segura-Garcia, C., Squassina, A., et al. (2020). Application of support vector machine on fMRI data as

biomarkers in schizophrenia diagnosis: a systematic review. *Front. Psychiatry* 11:588. doi: 10.3389/fpsyt.2020.00588

Su, L. D., Xu, F. X., Wang, X. T., Cai, X. Y., and Shen, Y. (2021). Cerebellar dysfunction, cerebro-cerebellar connectivity and autism spectrum disorders. *Neuroscience* 462, 320–327. doi: 10.1016/j.neuroscience.2020.05.028

Teng, C., Zhou, J., Ma, H., Tan, Y., Wu, X., Guan, C., et al. (2018). Abnormal resting state activity of left middle occipital gyrus and its functional connectivity in female patients with major depressive disorder. *BMC Psychiatry* 18:370. doi: 10.1186/s12888-018-1955-9

Toro, R., Fox, P. T., and Paus, T. (2008). Functional coactivation map of the human brain. *Cereb. Cortex* 18, 2553–2559. doi: 10.1093/cercor/bhn014

Tsai, C.-C., and Liang, W.-K. (2021). Event-related components are structurally represented by intrinsic event-related potentials. *Sci. Rep.* 11:5670. doi: 10.1038/s41598-021-85235-0

Veer, I. M., Beckmann, C. F., van Tol, M. J., Ferrarini, L., Milles, J., Veltman, D. J., et al. (2010). Whole brain resting-state analysis reveals decreased functional connectivity in major depression. *Front. Syst. Neurosci.* 4:41. doi: 10.3389/fnsys.2010.00041

Wada, M., Kurose, S., Miyazaki, T., Nakajima, S., Masuda, F., Mimura, Y., et al. (2019). The P300 event-related potential in bipolar disorder: a systematic review and meta-analysis. *J. Affect. Disord.* 256, 234–249. doi: 10.1016/j.jad.2019.06.010

Wang, H., Guo, W., Liu, F., Chen, J., Wu, R., Zhang, Z., et al. (2016). Clinical significance of increased cerebellar default-mode network connectivity in resting-state patients with drug-naive somatization disorder. *Medicine* 95:e4043. doi: 10.1097/MD.0000000000004043

Wang, R., Mo, F., Shen, Y., Song, Y., Cai, H., and Zhu, J. (2022). Functional connectivity gradients of the insula to different cerebral systems. *Hum. Brain Mapp.* 44, 790–800. doi: 10.1002/hbm.26099

Wang, Y., Li, C., Liu, X., Peng, D., Wu, Y., and Fang, Y. (2023). P300 event-related potentials in patients with different subtypes of depressive disorders. *Front. Psychiatry* 13:1021365. doi: 10.3389/fpsyt.2022.1021365

Wang, Y., Lyu, H. L., Tian, X. H., Lang, B., Wang, X. Y., St Clair, D., et al. (2022). The similar eye movement dysfunction between major depressive disorder, bipolar depression and bipolar mania. *World J. Biol. Psychiatry* 23, 689–702. doi: 10.1080/15622975.2022.2025616

Wei, J., Wei, S., Yang, R., Yang, L., Yin, Q., Li, H., et al. (2018). Voxel-mirrored homotopic connectivity of resting-state functional magnetic resonance imaging in blepharospasm. *Front. Psychol.* 9:1620. doi: 10.3389/fpsyg.2018.01620

Wu, J., Wu, J., Guo, R., Chu, L., Li, J., Zhang, S., et al. (2022). The decreased connectivity in middle temporal gyrus can be used as a potential neuroimaging biomarker for left temporal lobe epilepsy. *Front. Psychiatry* 13:972939. doi: 10.3389/fpsyt.2022.972939

Yan, H., Shan, X., Li, H., Liu, F., and Guo, W. (2022). Abnormal spontaneous neural activity in hippocampal-cortical system of patients with obsessive-compulsive disorder and its potential for diagnosis and prediction of early treatment response. *Front. Cell Neurosci.* 16:906534. doi: 10.3389/fncel.2022.906534

Yang, J., Zheng, P., Li, Y., Wu, J., Tan, X., Zhou, J., et al. (2020). Landscapes of bacterial and metabolic signatures and their interaction in major depressive disorders. *Sci. Adv.* 6:eaba8555. doi: 10.1126/sciadv.aba8555

Yin, Z., Chang, M., Wei, S., Jiang, X., Zhou, Y., Cui, L., et al. (2018). Decreased functional connectivity in insular subregions in depressive episodes of bipolar disorder and major depressive disorder. *Front. Neurosci.* 12:842. doi: 10.3389/fnins.2018.00842

Yu, H. L., Liu, W. B., Wang, T., Huang, P. Y., Jie, L. Y., Sun, J. Z., et al. (2017). Difference in resting-state fractional amplitude of low-frequency fluctuation between bipolar depression and unipolar depression patients. *Eur. Rev. Med. Pharmacol. Sci.* 21, 1541–1550.

Yuan, K., Qin, W., Liu, P., Zhao, L., Yu, D., Zhao, L., et al. (2012). Reduced fractional anisotropy of corpus callosum modulates inter-hemispheric resting state functional connectivity in migraine patients without aura. *PLoS One* 7:e45476. doi: 10.1371/journal.pone.0045476

Zhang, Q., Wu, J., Pei, C., Ma, M., Dong, Y., Gao, M., et al. (2022). Altered functional connectivity in emotional subregions of the anterior cingulate cortex in young and middle-aged patients with major depressive disorder: a resting-state fMRI study. *Biol. Psychol.* 175:108426. doi: 10.1016/j.biopsycho.2022.108426

Zheng, G., Yingli, Z., Shengli, C., Zhifeng, Z., Bo, P., Gangqiang, H., et al. (2022). Aberrant inter-hemispheric connectivity in patients with recurrent major depressive disorder: a multimodal MRI study. *Front. Neurol.* 13:852330. doi: 10.3389/fneur.2022.852330

Zhu, D. M., Yang, Y., Zhang, Y., Wang, C., Wang, Y., Zhang, C., et al. (2020). Cerebellar-cerebral dynamic functional connectivity alterations in major depressive disorder. *J. Affect. Disord.* 275, 319–328. doi: 10.1016/j.jad.2020.06.062

Zuo, X. N., Kelly, C., Di Martino, A., Mennes, M., Margulies, D. S., Bangaru, S., et al. (2010). Growing together and growing apart: regional and sex differences in the lifespan developmental trajectories of functional homotopy. *J. Neurosci.* 30, 15034–15043. doi: 10.1523/JNEUROSCI.2612-10.2010

frontiers | Frontiers in Neuroscience

TYPE Original Research
PUBLISHED 13 March 2023
DOI 10.3389/fnins.2023.1137567

Check for updates

OPEN ACCESS

EDITED BY
Ahmed Shalaby,
University of Texas Southwestern Medical Center, United States

REVIEWED BY
Peixin Lu,
Wuhan University, China
Hamed Ghaffari,
Iran University of Medical Sciences, Iran

*CORRESPONDENCE
Junwei Duan
✉ jwduan@jnu.edu.cn
Jing Wang
✉ wj_adr@163.com

SPECIALTY SECTION
This article was submitted to Brain Imaging Methods, a section of the journal Frontiers in Neuroscience

RECEIVED 04 January 2023
ACCEPTED 13 February 2023
PUBLISHED 13 March 2023

CITATION
Duan J, Liu Y, Wu H, Wang J, Chen L and Chen CLP (2023) Broad learning for early diagnosis of Alzheimer's disease using FDG-PET of the brain. *Front. Neurosci.* 17:1137567. doi: 10.3389/fnins.2023.1137567

COPYRIGHT
© 2023 Duan, Liu, Wu, Wang, Chen and Chen. This is an open-access article distributed under the terms of the Creative Commons Attribution License (CC BY). The use, distribution or reproduction in other forums is permitted, provided the original author(s) and the copyright owner(s) are credited and that the original publication in this journal is cited, in accordance with accepted academic practice. No use, distribution or reproduction is permitted which does not comply with these terms.

Broad learning for early diagnosis of Alzheimer's disease using FDG-PET of the brain

Junwei Duan[1,2]*, Yang Liu[1], Huanhua Wu[3], Jing Wang[4]*, Long Chen[5] and C. L. Philip Chen[6], for the Alzheimer's Disease Neuroimaging Initiative

[1]College of Information Science and Technology, Jinan University, Guangzhou, China, [2]Guangdong Provincial Key Laboratory of Traditional Chinese Medicine Informatization, Jinan University, Guangzhou, China, [3]Department of Nuclear Medicine and PET/CT-MRI Centre, The First Affiliated Hospital of Jinan University, Guangzhou, China, [4]School of Computer Science, Guangdong Polytechnic Normal University, Guangzhou, China, [5]Department of Computer and Information Science, Faculty of Science and Technology, University of Macau, Taipa, Macau SAR, China, [6]School of Computer Science and Engineering, South China University of Technology, Guangzhou, China

Alzheimer's disease (AD) is a progressive neurodegenerative disease, and the development of AD is irreversible. However, preventive measures in the presymptomatic stage of AD can effectively slow down deterioration. Fluorodeoxyglucose positron emission tomography (FDG-PET) can detect the metabolism of glucose in patients' brains, which can help to identify changes related to AD before brain damage occurs. Machine learning is useful for early diagnosis of patients with AD using FDG-PET, but it requires a sufficiently large dataset, and it is easy for overfitting to occur in small datasets. Previous studies using machine learning for early diagnosis with FDG-PET have either involved the extraction of elaborately handcrafted features or validation on a small dataset, and few studies have explored the refined classification of early mild cognitive impairment (EMCI) and late mild cognitive impairment (LMCI). This article presents a broad network-based model for early diagnosis of AD (BLADNet) through PET imaging of the brain; this method employs a novel broad neural network to enhance the features of FDG-PET extracted *via* 2D CNN. BLADNet can search for information over a broad space through the addition of new BLS blocks without retraining of the whole network, thus improving the accuracy of AD classification. Experiments conducted on a dataset containing 2,298 FDG-PET images of 1,045 subjects from the ADNI database demonstrate that our methods are superior to those used in previous studies on early diagnosis of AD with FDG-PET. In particular, our methods achieved state-of-the-art results in EMCI and LMCI classification with FDG-PET.

KEYWORDS

Alzheimer's disease, PET, broad learning system, neural network, computer-aided diagnosis

1. Introduction

Alzheimer's disease (AD) cannot be diagnosed until obvious symptoms appear in the patient, but studies have found that patients with AD show abnormalities in regional metabolism before brain structure changes occur (Jagust et al., 2006). Fluorine 18 (18F) fluorodeoxyglucose (FDG) positron emission tomography (PET) is a non-invasive nuclear medicine imaging technique that can indicate the metabolic activity of tissues and organs (Marcus et al., 2014; Bouter et al., 2019; Levin et al., 2021). FDG-PET may detect

the onset of certain diseases earlier than other imaging tests (Brown et al., 2014). FDG-PET is regarded as an effective biomarker for earlier diagnosis of AD (Chételat et al., 2020). The onset of Alzheimer's disease is insidious and slow, and it can be divided into three stages: cognitively normal (CN), mild cognitive impairment (MCI), and Alzheimer's disease (AD). Patients with AD tend to show hypometabolism on 18F-FDG-PET scan in the regions of the posterior cingulate, parietotemporal cortices, and frontal lobes, while patients with MCI often show posterior cingulate and parietotemporal hypometabolism with variable frontal lobe involvement (Mosconi et al., 2008; Kobylecki et al., 2015). However, the difference between the two stages in FDG-PET is difficult to distinguish with the naked eye or through pattern recognition-based decisions made *via* qualitative readings. Because the disease involves a wide continuous spectrum, from normal cognition to MCI to AD, MCI can also be subdivided into early MCI (EMCI) and late MCI (LMCI) (Jessen et al., 2014).

Machine learning approaches can effectively extract features that are difficult to find with the naked eye and can outperform professional clinicians in certain imaging diagnosis problems (Zhang et al., 2020). A number of studies have already experimented with unsupervised learning (Suk and Shen, 2013), adversarial learning (Baydargil et al., 2021), and multi-scale learning (Lu et al., 2018) techniques in AD-related PET image analysis. These methods have achieved good results in classification of CN, MCI, and AD, but few studies have explored the refined classification of early EMCI and late LMCI.

Currently, deep learning-based approaches have been applied in early diagnosis of AD (Suk and Shen, 2013; Lu et al., 2018). Nevertheless, there are still many issues remaining in deep learning, such as gradient explosion and vanishing gradients, which limit the depth in terms of number of layers in the network or its fitting ability; some researchers have proposed residual learning (He et al., 2016) as a way to alleviate this problem. The broad learning system (BLS) is one kind of neural network without deep structure. BLS provides better fitting ability by increasing the number of network nodes horizontally and obtains solutions *via* pseudoinverse, with no need for an iterative backpropagation process. However, BLS obtains a feature representation of input data through random projection, which may result in too much redundant information that could influence the performance of the BLS model. Some researchers have experimented with variations of BLS that use other models as feature extractors in the feature mapping layer (Feng and Chen, 2018; Du et al., 2020; Jara-Maldonado et al., 2022; Wu and Duan, 2022). In this article, we propose a novel BLS-based method, in which we use grouped convolution layers to extract the features from slice groups in the first stage, and then these features are fed into a broad learning model for further feature enhancement.

This study proposes a machine learning model based on BLS to predict the clinical diagnosis in patients using 18F-FDG-PET of the brain. We attempted to predict patients' classifications as AD, MCI, or CN, and (within the category of MCI) as EMCI or LMCI. The hypothesis was that the broad learning-based model would be able to detect regional metabolic abnormalities caused by pathology, which are difficult to observe on clinical review, and improve the accuracy of individual diagnosis.

2. Materials and methods

2.1. Data acquisition

Data used in the preparation of this article were obtained from the Alzheimer's Disease Neuroimaging Initiative (ADNI) database (adni.loni.usc.edu). ADNI was launched in 2003 as a public–private partnership, led by Principal Investigator Michael W. Weiner, MD. The primary goal of ADNI has been to test whether serial magnetic resonance imaging (MRI), PET, other biological markers, and clinical and neuropsychological assessment can be combined to measure the progression of MCI and early AD.

In our study, we analyzed a total of 2,298 FDG-PET imaging studies of 1,045 patients obtained from ADNI. The datasets contained images of subjects of different ages. In ADNI 1, the subjects were grouped into three classes: CN, MCI, and AD. However, in ADNI 2/GO, the MCI stage was subdivided into EMCI and LMCI. To be classified as CN, subjects must have no memory complaints and be non-demented. To be classified as having MCI, subjects must have a Mini-Mental State Examination (MMSE) score between 24 and 30; the activities of daily living must be preserved, and dementia must be absent. Finally, to be classified as having AD, subjects must be clinically diagnosed as such, with an MMSE score between 20 and 26 (Jack Jr et al., 2008). Demographic information on our dataset is presented in Table 1. A total of 80% of the data (1,851 imaging studies, 598 patients) were used for model training. The remaining 20% (447 imaging studies; no repeat studies of the same subjects in the test set) were used for model testing, from which an additional test set (74 imaging studies for AD vs. MCI vs. CN classification and 45 imaging studies for EMCI vs. LMCI classification) was selected for validation by professional radiologists.

2.2. Data processing

For the purpose of eliminating differences between images acquired from various systems, FDG-PET images in ADNI have undergone a series of preprocessing steps, intensity normalization, and conversion to a uniform isotropic resolution of 8 mm full width at half maximum. We selected the processed images from ADNI; our method does not require any specific pre-defined ROI or VOI as traditional machine learning methods do. All 3D images were resampled to a size of 160 × 160 × 96; we treated the images as a series of 2D slices and removed slices with all-zero intensity on both sides, then divided the image into four groups of slices at equal intervals, with each group containing 23 slices. All processing steps were conducted in Python (version 3.8) using the packages scipy (http://www.scipy.org) and numpy (https://numpy.org/). Figure 1 shows a single slice, viewed on three planes.

2.3. Model development

Despite the good learning ability of deep neural networks, they are easy to overfit on small datasets and their training is also

TABLE 1 Demographics of datasets.

			Average age*	
Clinical diagnosis	No. of Patients	No. of imaging studies	Men	Women
AD	297	541	76.47 ± 7.57 (56–92)	75.11 ± 7.63 (55–92)
MCI	196	616	77.79 ± 7.01 (57–92)	74.82 ± 7.95 (57–96)
CN	242	627	77.12 ± 5.41 (62–91)	76.93 ± 6.37 (60–96)
Total	735	1,784	77.18 ± 6.75 (56–92)	75.76 ± 7.31 (55–96)
EMCI	152	265	73.89 ± 6.85 (56–90)	72.40 ± 8.40 (55–92)
LMCI	158	249	74.70 ± 7.37 (56–94)	71.80 ± 7.80 (55–91)
Total	310	514	74.27 ± 7.10 (56–94)	72.09 ± 8.11 (55–91)

AD, Alzheimer's disease; MCI, mild cognitive impairment; CN, cognitively normal.
*Data in parentheses are the range.

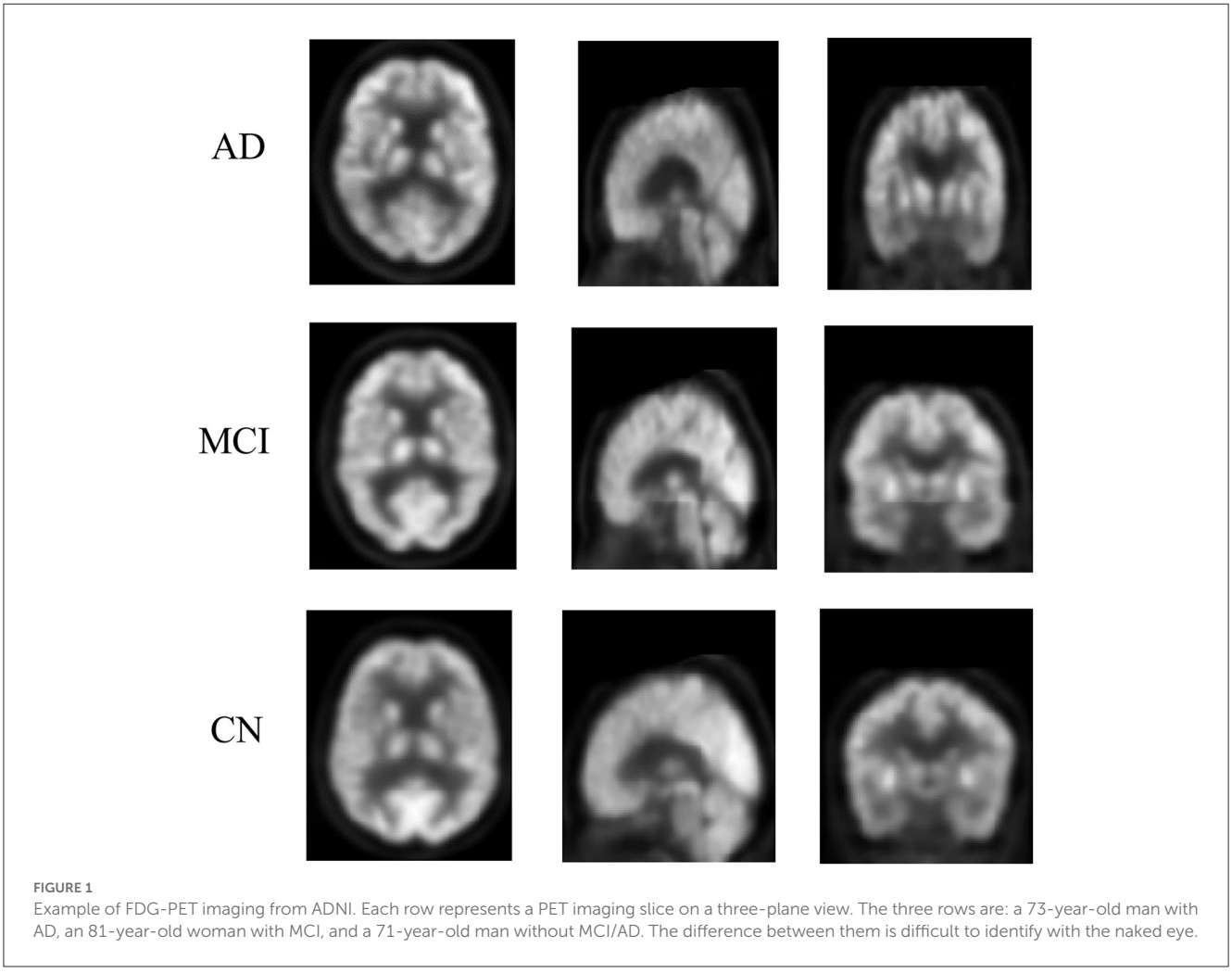

FIGURE 1
Example of FDG-PET imaging from ADNI. Each row represents a PET imaging slice on a three-plane view. The three rows are: a 73-year-old man with AD, an 81-year-old woman with MCI, and a 71-year-old man without MCI/AD. The difference between them is difficult to identify with the naked eye.

time-consuming. The BLS is a lightweight network with a broad structure proposed by Chen and Liu (2017). The inspiration for its design comes from a random vector functional link neural network (RVFLLNN) (Pao and Takefuji, 1992; Chu et al., 2019; Gong et al., 2021). It can obtain a globally optimal solution using a ridge regression algorithm during training. without an

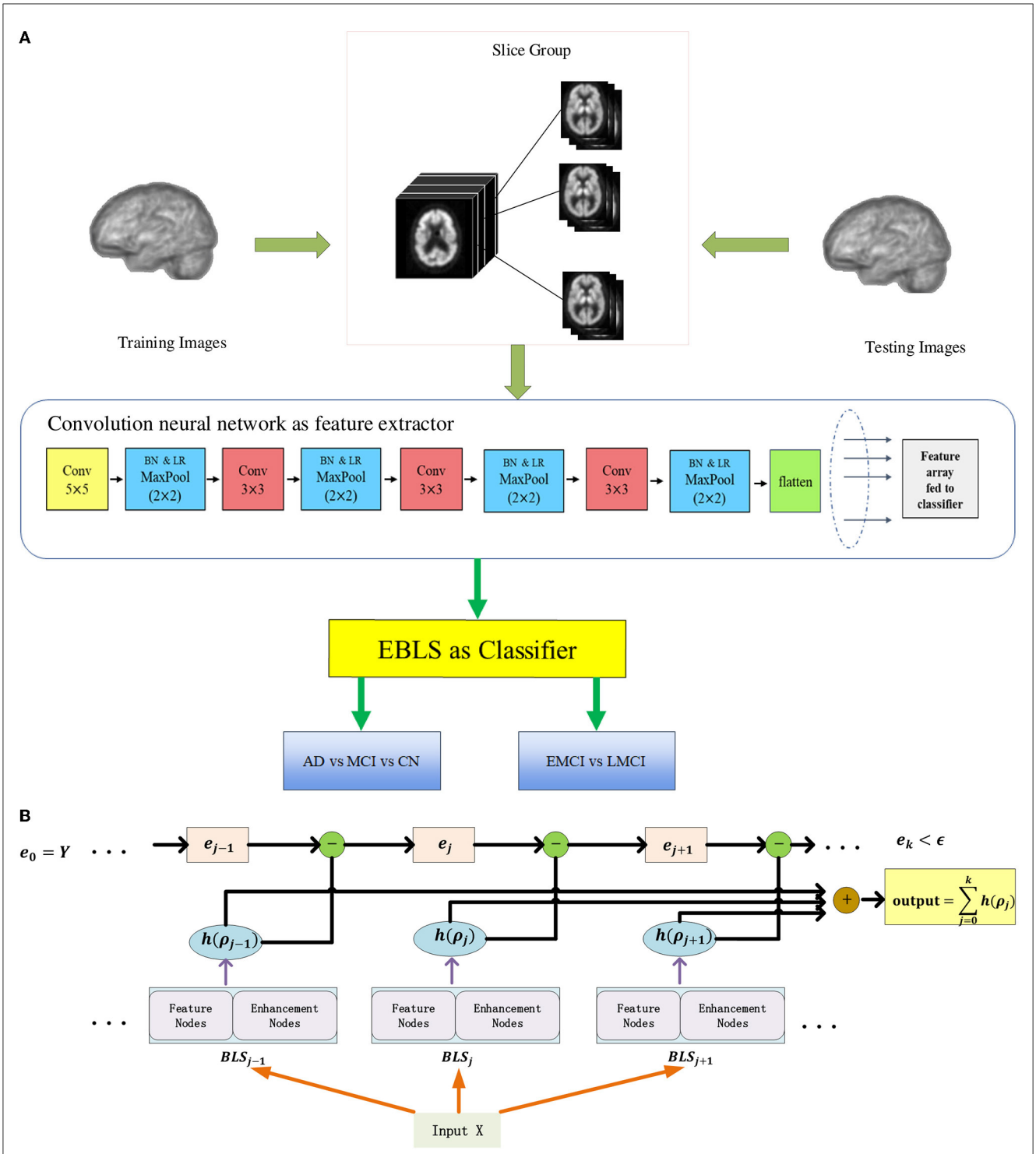

FIGURE 2
Each 3D image is decomposed into groups of 2D slices at equal intervals. In the first stage, deep convolutional features are extracted from each group by 2D CNN. In the second stage, all features from each slice group are concatenated to form a compact feature vector, and fed to EBLS for final prediction. **(A)** The overall architecture of BLADNet. **(B)** The detailed structure of EBLS.

iterative backpropagation process, meaning that its training is fast and efficient. The detailed description of the BLS is illustrated in the Supplementary material. Based on the BLS, we propose a broad network-based model for early diagnosis of AD (BLADNet) through PET imaging of the brain.

Figure 2 illustrates the overall architecture of BLADNet. The framework consists of two stages. In the first stage, we use a 2D CNN for automated feature learning from each group of slices rather than directly using a 3D CNN, which reduces the number of parameters to be learned. In the second stage, the features extracted from each group in the previous step are concatenated to form a compact sequence feature; then, the Extreme Broad Learning System (EBLS), based on a broad neural network, is used to enhance the features from 2D CNN and carry out the

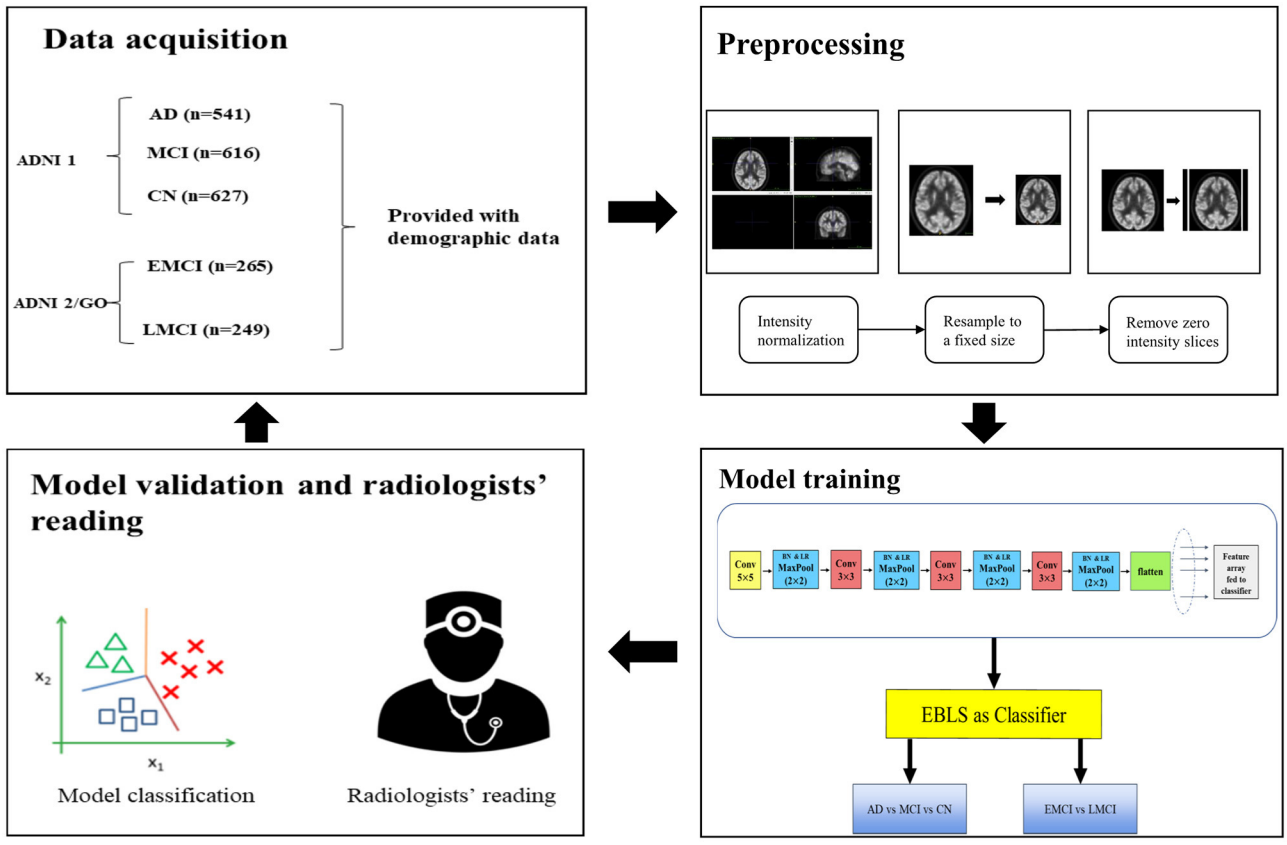

FIGURE 3
Main steps of the experiment. The data set was split into training and test sets at a ratio of 8:2. In the validation step, the radiologists were provided with demographic information to aid their readings.

final classification. A detailed description of the EBLS is provided in the Supplementary material[1]. Our model was developed in Python using the packages numpy and pytorch (https://pytorch.org/, version 1.7.1). All experiments were conducted using a computer with a Linux operating system (Ubuntu 18.04). The computer was equipped with a CPU (Intel(R) Core (TM) i9-9980XE, 3.00 GHz), 64 GB of DDR4 SDRAM, and GPU (GeForce RTX 3080) with CUDA Version 11.2 and cuDNN Version 9.1.85.

2.4. Model evaluation and statistical analysis

We performed the experiments of AD vs. MCI vs. CN classification as in previous studies on data from ADNI 1, and also performed additional experiments of refined classification between EMCI and LMCI on data from ADNI 2/GO. All data were randomly shuffled before being spli into the training set and test set. In all experiments, we used 80% of the samples for training and 20% of the samples for testing. In the experiment, we regard each category as positive samples respectively, the rest as negative samples, and then calculate metrics. We used accuracy, sensitivity, and specificity as metrics to evaluate classification performance. All metrics were calculated under a default threshold value of 0.5. We also plotted the ROC curve of all experiments and calculated the corresponding AUC.

Two board-certified professional radiologists working in a department of brain imaging and nuclear medicine (radiologist 1: HLZ, with 8 years of experience in brain imaging reading for AD diagnosis; radiologist 2: HHW, with 6 years of experience in brain imaging reading for AD diagnosis) were asked to give their diagnostic impressions of a dataset that was not used for model training. For each case, the radiologists were provided with the patient's age, gender, and MMSE score as additional information for validation. To validate the performance of the proposed model and the professional readings of radiologists, we compared the performance of our proposed model with that of the radiologists' interpretations. The main steps of the experiment are shown in Figure 3.

3. Experimental results

3.1. Results of model training

The prediction results of the broad network-based model are shown in Table 2. For classification of AD, MCI, and CN samples,

1 The code of EBLS model (https://github.com/YangLiuuuu/Extreme-Broad-Learning-System).

TABLE 2 Comparison of performance between our model and radiology readers in prediction of AD, MCI, and CN.

Our method on ADNI test set	Sensitivity (%)*	Specificity (%)*	Precision (%)*	F1 score (%)	No. of imaging studies
AD	92.16 (94/102)	97.56 (240/246)	94.00 (94/100)	93.06	102
MCI	89.34 (109/122)	95.58 (216/226)	91.60 (109/119)	90.46	122
CN	95.16 (118/124)	95.09 (213/224)	91.47 (118/129)	93.28	124
Radiologist 1					
AD	51.85 (14/27)	57.45 (27/47)	41.76 (14/34)	45.9	27
MCI	29.41 (5/17)	80.70 (46/57)	31.25 (5/16)	30.3	17
CN	46.67 (14/30)	77.27 (34/44)	58.33 (14/24)	51.85	30
Radiologist 2					
AD	37.04 (10/27)	72.34 (34/47)	43.48 (10/23)	40	27
MCI	35.29 (6/17)	63.16 (36/57)	22.22 (6/27)	27.27	17
CN	46.67 (14/30)	77.27 (34/44)	58.33 (14/24)	51.85	30

AD, Alzheimer's disease; MCI, mild cognitive impairment; CN, cognitively normal.
*Data in parentheses are raw data used to calculate the percentage.

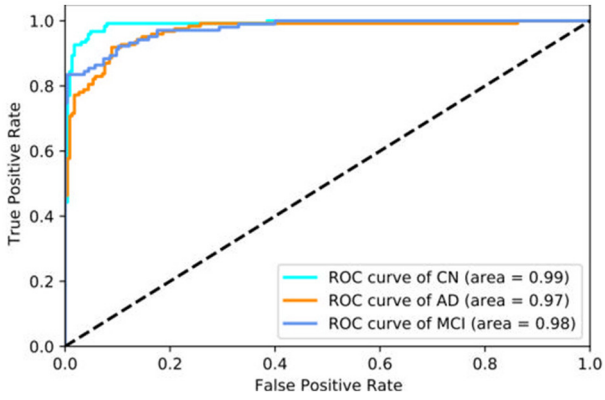

FIGURE 4
ROC curve of our method tested on the ADNI data set. The ROC curve labeled AD represents the model's performance in distinguishing AD vs. all other classes, the other curves represent the equivalent objective. The AUC is larger for CN than for the other classes, which indicates that our model can distinguish healthy subjects from patients with AD/MCI more successfully than other classifications.

sensitivity was 92.16 (94 of 102), 89.34 (109 of 122), and 95.16% (118 of 124), respectively; specificity was 97.56 (240 of 246), 95.58 (216 of 226), and 95.09% (213 of 224), respectively; and precision was 94.00 (94 of 100), 91.60 (109 of 119), and 91.47% (118 of 129), respectively. The ROC curves of our model, trained on 80% of the ADNI data and tested on the remaining 20%, are shown in Figure 4. The AUC in prediction of AD, MCI, and CN was 0.97, 0.98, and 0.99, respectively. The AUC for CN was the highest, indicating that our model can distinguish healthy subjects from patients with AD/MCI.

The results for EMCI and LMCI prediction are shown in Table 3. In this experiment, we treated LMCI as the positive class and EMCI as the negative class. Sensitivity was 81.63% (40 of 49) and specificity was 85.19% (46 of 54). Similar to the AD vs. MCI vs. CN experiment, the specificity of the model was much higher than the sensitivity, indicating that our model was better than radiologists at identifying healthy subjects.

3.2. Model interpretation: t-SNE plot

We used the t-SNE algorithm to reduce the dimensionality of the features extracted from the convolutional network and projected them into a two-dimensional space for visualization. As shown in Figure 5A, for the AD vs. MCI vs. CN experiment, there were obvious boundaries between the three categories. Moreover, only a few samples from other categories were scattered within the CN category, indicating that the model has a better screening ability for healthy cases than for patients. Similarly, as shown in Figure 5B, for EMCI and LMCI classification, the model divided the samples very successfully into two clusters. Although a few cases were mixed in the junction of the two clusters, which indicates that there is a transition stage from EMCI to LMCI, our model could distinguish the two stages well.

3.3. Comparison of model predictions with state-of-the-art methods

Recently, a substantial amount of work has been carried out exploring the application of machine learning approaches to AD prediction using brain imaging. Most of these studies have used structural imaging of the brain, with few studies using functional imaging, specifically 18F-FDG-PET. Some researchers have attempted to analyze 18F-FDG-PET for AD predictions, but these studies have yielded limited success (Liu et al., 2018; Lu et al., 2018; Pan et al., 2018; Ding et al., 2019; Huang et al., 2019; Hamdi et al., 2022). Tables 4, 5 summarize state-of-the-art deep learning methods for prediction of AD using 18F-FDG-PET imaging. Most

TABLE 3 Comparison of performance between our model and radiology readers in prediction of EMCI and LMCI.

	Sensitivity (%)*	Specificity (%)*	Precision (%)*	F1 score (%)	No. of imaging studies
Our method on test set 2	81.63 (40/49)	85.19 (46/54)	83.33 (40/48)	82.47	103
Radiologist 1	84.00 (21/25)	25.00 (5/20)	58.33 (21/36)	68.85	45
Radiologist 2	76.00 (19/25)	30.00 (6/20)	58.33 (19/33)	65.52	45

EMCI, early mild cognitive impairment; LMCI, late mild cognitive impairment.
*Data in parentheses are raw data used to calculate the percentage.

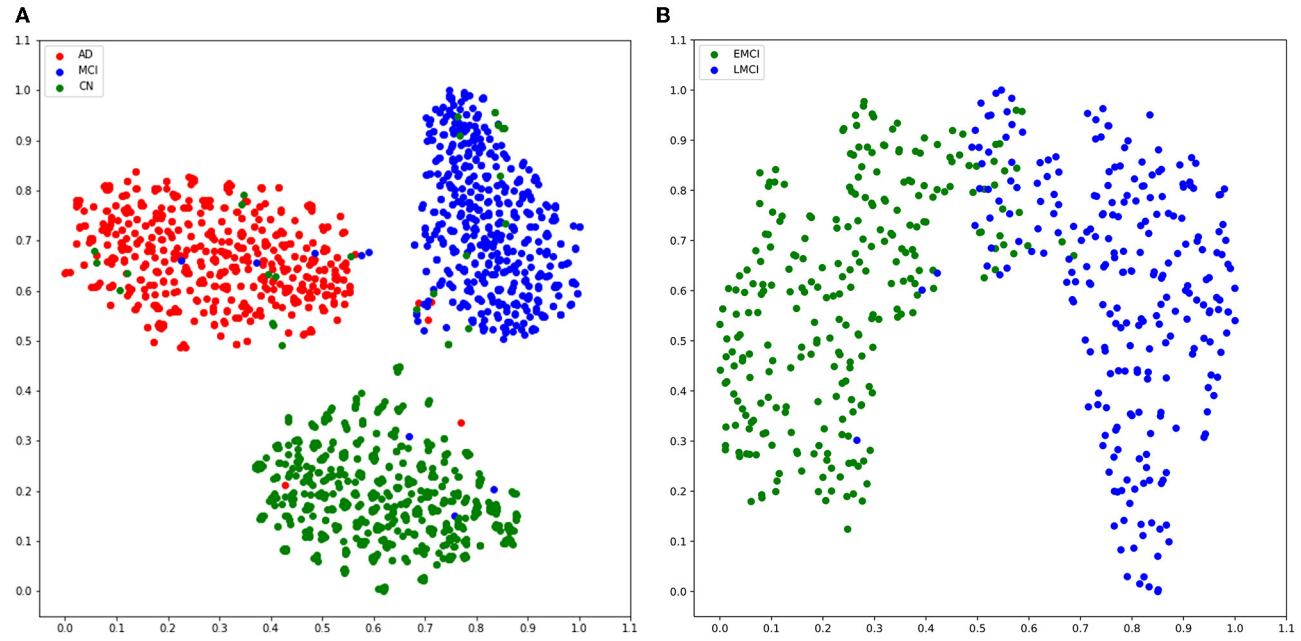

FIGURE 5
Scatter plot of all data after dimension reduction by t-SNE. **(A)** Visualization of dimension reduction for AD, MCI, and CN. **(B)** Visualization of dimension reduction for EMCI and LMCI.

of the methods investigated can only discriminate AD from CN or MCI from CN, while our method can classify patients at different stages of AD with higher sensitivity and specificity. In addition, compared with these methods, we used a larger test set in our experiments, which demonstrates the superior generalization ability of our method.

3.4. Comparison of model predictions with professional radiologists

As shown in Table 2, two radiologists gave their interpretations of a test set. For radiologist 1, the sensitivity results for MCI, AD, and CN were 51.85 (14 of 27), 29.41 (5 of 17), and 46.67% (14 of 30), respectively; the specificity results were 57.45 (27 of 47), 80.70 (46 of 57), and 77.27% (34 of 44), respectively; and the precision results were 41.76 (14 of 34), 34.25 (5 of 16), and 58.33% (14 of 24), respectively. For radiologist 2, sensitivity for MCI, AD, and CN was 37.04 (10 of 27), 35.29 (6 of 17), and 46.67% (14 of 30), respectively; specificity was 72.34 (34 of 47), 63.16 (36 of 57), and 77.27% (34 of 44), respectively; and precision was 43.48 (10 of 23), 22.22 (6 of 27), and 58.33% (14 of 24), respectively. It can be observed that the prediction results of our proposed model were better than those of the radiologist, which indicates that the model was able to find lesions that were difficult to observe with the naked eye. It is also worth noting that although the two radiologists obtained the same results in their evaluations of healthy cases, patients with MCI and AD were difficult to evaluate.

Table 3 reports reader performance on prediction of EMCI vs. LMCI. For radiologist 1, the results in terms of sensitivity, specificity, and precision were 84.00 (21 of 25), 25.00 (5 of 20), and 58.33% (21 of 36), respectively. For radiologist 2, the results were 76.00 (19 of 25), 30.00 (6 of 20), and 58.33% (19 of 33), respectively. Although radiologists had higher sensitivity in this scenario, their specificity was very low; this is because radiologists tend to predict cases as LMCI. In contrast, our model was able to achieve high specificity under high sensitivity.

4. Discussion

With the aging of the population, the number of patients with AD is continuously increasing. However, research on a cure for AD has been slow, and the focus of research has shifted to the early diagnosis of AD, so that early prevention measures can delay the progression of the disease. However, early identification of patients

TABLE 4 Summary of state-of-the-art methods for prediction of Alzheimer's disease (AD) using 18F-FDG-PET imaging.

References	Summary of method	Dataset specifications	Sensitivity	Specificity	AUC*
Ding et al. (2019)	Inception V3 network pre-trained on ImageNet	484 AD, 861 MCI, 764 non-AD/MCI scans from ADNI	AD 81%	94%	0.92
			MCI 54%	68%	0.63
			Non-AD/MCI 59%	75%	0.73
Huang et al. (2019)	3D VGG network	647 AD, 731 CN, 767 MCI 18F-FDG-PET scans from ADNI	AD vs. CN 90.24%	87.77%	0.9269
Lu et al. (2018)	A multiscale deep neural network	226 AD and 304 18F-FDG-PET scans from ADNI	AD vs. CN 91.54%	95.06%	NA
Liu et al. (2018)	A combination of 2D CNN and RNN	93 AD, 146 MCI, 100 CN scans from ADNI	AD vs. CN 91.4%	91%	0.953
			MCI vs. CN 78.1%	80%	0.839
Hamdi et al. (2022)	A 2D CNN network	220 AD, 635 CN FDG-PET scans from ADNI	AD vs. CN 94%	96%	0.95
Pan et al. (2018)	SVM	94 AD, 88 MCI, 90 CN subjects from ADNI	AD vs. CN 92.78%	91.38%	0.9598
			MCI vs. CN 84.20%	82.83%	0.8893
Current study	A broad learning-based network	541 AD, 616 MCI, 627 FDG-PET imaging studies from ADNI	AD 92.16%	97.56%	0.97
			MCI 89.34%	95.58%	0.98
			Non-AD/MCI 95.16%	95.09%	0.99

We report sensitivity, specificity, and area under the curve (AUC) for all these methods.
AD, Alzheimer's disease; MCI, mild cognitive impairment; CN, cognitively normal.
*A value of NA indicates that this result is not reported in the literature.

TABLE 5 Comparison of performance between our model and other existing methods in prediction of EMCI and LMCI.

References	Sensitivity (%)*	Specificity (%)*	F1 score (%)*	Dataset specifications
Singh et al. (2017)	64.82%	NA	0.6844	178 EMCI, 158 LMCI
Nozadi et al. (2018)	72.50%	79.20%	NA	164 EMCI, 189 LMCI
Forouzannezhad et al. (2020)	61.50%	64.3%	NA	296 EMCI, 193 LMCI
Ours	81.63%	85.19%	82.47%	265 EMCI, 249 LMCI

EMCI, early mild cognitive impairment, LMCI, late mild cognitive impairment.
*A value of NA indicates that this result is not reported in the literature.

at the prodromal stage of AD is still a challenging problem. The broad neural network-based model can identify patients with AD at different stages with high sensitivity and specificity. In addition, in identifying patients at the EMCI or LMCI stage, the proposed model is able to achieve high sensitivity under high specificity; notably, it outperformed professional radiologist readers, achieving higher sensitivity and specificity.

Previous research has studied the specific pattern of hypometabolism that can be observed in FDG-PET of patients with AD. Bilateral temporo-parietal hypometabolism has been found to be a dominant pattern related to clinically confirmed AD (Hoffman et al., 2000). Other studies have demonstrated that, as the disease progresses, FDG uptake is reduced, especially in the frontal, parietal, and lateral temporal lobes (Ossenkoppele et al., 2012). However, FDG-PET is not a definitive imaging biomarker for AD and MCI. Substantial previous efforts have been devoted to attempts to develop computer-aided methods of diagnosis of AD *via* other modalities, but few studies have been conducted involving attempts to applying machine learning approaches to classify patients with AD by FDG-PET alone. Previous attempts to identify MCI have resulted in limited sensitivity (81% for AD, 54% for MCI) and specificity (Ding et al., 2019). In addition to prediction of AD, our model performs refined classification of EMCI vs. LMCI, achieving sensitivity of 81.63% and specificity of 85.19% in doing so. Compared to previous studies, the key advantages of our model are as follows. First, due to the incremental learning ability of BLS, our model can be dynamically updated without retraining from scratch if new imaging studies are added; our EBLS model can further extend the incremental learning ability of BLS by adding new BLS blocks dynamically. In addition, our model exhibits better performance in the identification of the early stage of AD, which is of great significance for the diagnosis of AD, because early identification of AD facilitates early intervention in the progression of the disease. There are also some limitations to our model in that the training needs to be completed in two stages, and the process is complicated. In addition, training a convolution layer from scratch for the first time is still time-consuming work, and the BLS model in the second stage depends on the quality of feature extraction in the convolution layer.

Because of deep structure, deep learning models are very good at capturing abstract and intrinsic features of images. However, the problems existing in deep learning models, such as gradient explosion and vanishing gradients, usually limit the possibility of deepening the networks of deep learning models indefinitely.

BLS can solve this problem in a different way, providing good universal approximation ability with a flat structure. The universal approximation ability of BLS has been proven by Chen et al. (2018). Our proposed method utilizes a convolution layer as a feature extractor to provide deep space features for BLS, and our proposed EBLS model can enhance the features in broad space before computing the final output. The comparison in the section above demonstrates that our method achieves better performance than state-of-the-art deep learning methods, which demonstrates the role of broad learning in feature enhancement. In addition, compared to other studies that have only used dozens of images, our model was trained and validated on a large dataset containing thousands of images and achieves better performance, which indicates that our method has better generalizability. However, in real clinical scenarios, the reasons for hypometabolism observed in FDG-PET may be more complicated. For instance, other types of dementia, such as dementia with Lewy bodies (DLB) or frontotemporal dementia (FTD), may also cause pathological changes similar to AD. Further studies that verify this method on more complex data may in future provide more reliable clinical aids for diagnosis of AD.

Our study also has limitations. First, although the machine learning method has achieved very good results in the validation with the ADNI data set, actual clinical prediction is much more complicated. For instance, many patients may have neurological diseases other than AD, which will affect the prediction results. We will continue our investigation and apply our model to a more general patient population in the future. Second, the algorithm can learn features that are difficult to see with the naked eye (which means that its predictions can differ from experts' interpretations), and t-SNE dimension reduction also shows the gradual progression of patients from MCI to AD, but the model cannot provide interpretable information for radiologists.

5. Conclusion

In conclusion, in our study we have developed a novel broad network-based model for prediction of AD diagnosis using 18F-FDG-PET of the brain. The proposed broad learning-based model was able to achieve high accuracy, sensitivity, and specificity on the validation set and outperformed professional radiologist readers in predicting AD based on FDG-PET. Moreover, the proposed model can be integrated into the clinical workflow as a powerful auxiliary diagnosis tool for reading PET imaging of patients with AD.

Data availability statement

Publicly available datasets were analyzed in this study. This data can be found here: https://adni.loni.usc.edu.

Ethics statement

Ethical approval was not provided for this study on human participants because the data used in this research was obtained from public available dataset. The patients/participants provided their written informed consent to participate in this study.

Author contributions

JD: conceptualization, methodology, validation, visualization, writing—original draft, writing—review and editing, supervision, project administration, and funding acquisition. YL: data curation, methodology, software, validation, and writing—original draft. HW: validation and software. JW: supervision and project administration. LC: visualization and writing—review and editing. CC: conceptualization, resources, and supervision. All authors contributed to the article and approved the submitted version.

Funding

Data used in preparation of this article were obtained from the Alzheimer's Disease Neuroimaging Initiative (ADNI) database (http://adni.loni.usc.edu). As such, the investigators within the ADNI contributed to the design and implementation of ADNI and/or provided data but did not participate in analysis or writing of this report. A complete listing of ADNI investigators can be found at: http://adni.loni.usc.edu/wp-content/uploads/how_to_apply/ADNI_Acknowledgement_List.pdf. This work was supported in part by Guangdong Basic and Applied Basic Research Foundation under Grant 2021A1515011999, in part by the National Key Research and Development Program of China under Grant 2018YFC2002500, and in part by Guangdong Provincial Key Laboratory of Traditional Chinese Medicine Informatization under Grant 2021B1212040007.

Conflict of interest

The authors declare that the research was conducted in the absence of any commercial or financial relationships that could be construed as a potential conflict of interest.

Publisher's note

All claims expressed in this article are solely those of the authors and do not necessarily represent those of their affiliated organizations, or those of the publisher, the editors and the reviewers. Any product that may be evaluated in this article, or claim that may be made by its manufacturer, is not guaranteed or endorsed by the publisher.

Supplementary material

The Supplementary Material for this article can be found online at: https://www.frontiersin.org/articles/10.3389/fnins.2023.1137567/full#supplementary-material

References

Baydargil, H. B., Park, J. S., and Kang, D. Y. (2021). Anomaly analysis of Alzheimer's disease in PET images using an unsupervised adversarial deep learning model. *Appl. Sci.* 11, 2187. doi: 10.3390/app11052187

Bouter, C., Henniges, P., Franke, T. N., Irwin, C., Sahlmann, C. O., Sichler, M. E., et al. (2019). 18F-FDG-PET detects drastic changes in brain metabolism in the Tg4–42 model of Alzheimer's disease. *Front. Aging Neurosci.* 10, 425. doi: 10.3389/fnagi.2018.00425

Brown, R. K., Bohnen, N. I., Wong, K. K., Minoshima, S., and Frey, K. A. (2014). Brain PET in suspected dementia: patterns of altered FDG metabolism. *Radiographics* 34, 684–701. doi: 10.1148/rg.343135065

Chen, C. P., and Liu, Z. (2017). Broad learning system: an effective and efficient incremental learning system without the need for deep architecture. *IEEE Trans. Neural Netw. Learn. Syst.* 29, 10–24. doi: 10.1109/TNNLS.2017.2716952

Chen, C. P., Liu, Z., and Feng, S. (2018). Universal approximation capability of broad learning system and its structural variations. *IEEE Trans. Neural Netw. Learn. Syst.* 30, 1191–1204. doi: 10.1109/TNNLS.2018.2866622

Chételat, G., Arbizu, J., Barthel, H., Garibotto, V., Law, I., Morbelli, S., et al. (2020). Amyloid-PET and 18F-FDG-PET in the diagnostic investigation of Alzheimer's disease and other dementias. *Lancet Neurol.* 19, 951–962. doi: 10.1016/S1474-4422(20)30314-8

Chu, F., Liang, T., Chen, C. P., Wang, X., and Ma, X. (2019). Weighted broad learning system and its application in non-linear industrial process modeling. *IEEE Trans. Neural Netw. Learn. Syst.* 31, 3017–3031. doi: 10.1109/TNNLS.2019.2935033

Ding, Y., Sohn, J. H., Kawczynski, M. G., Trivedi, H., Harnish, R., Jenkins, N. W., et al. (2019). A deep learning model to predict a diagnosis of Alzheimer disease by using 18F-FDG PET of the brain. *Radiology* 290, 456–464. doi: 10.1148/radiol.2018180958

Du, J., Vong, C. M., and Chen, C. P. (2020). Novel efficient RNN and LSTM-like architectures: recurrent and gated broad learning systems and their applications for text classification. *IEEE Trans. Cybern.* 51, 1586–1597. doi: 10.1109/TCYB.2020.2969705

Feng, S., and Chen, C. P. (2018). Fuzzy broad learning system: a novel neuro-fuzzy model for regression and classification. *IEEE Trans. Cybern.* 50, 414–424. doi: 10.1109/TCYB.2018.2857815

Forouzannezhad, P., Abbaspour, A., Li, C., Fang, C., Williams, U., Cabrerizo, M., et al. (2020). A Gaussian-based model for early detection of mild cognitive impairment using multimodal neuroimaging. *J. Neurosci. Methods* 333, 108544. doi: 10.1016/j.jneumeth.2019.108544

Gong, X., Zhang, T., Chen, C. P., and Liu, Z. (2021). Research review for broad learning system: algorithms, theory, and applications. *IEEE Trans. Cybern.* 52, 8922–8950. doi: 10.1109/TCYB.2021.3061094

Hamdi, M., Bourouis, S., Rastislav, K., and Mohmed, F. (2022). Evaluation of neuro images for the diagnosis of Alzheimer's disease using deep learning neural network. *Front. Public Health* 10, 35. doi: 10.3389/fpubh.2022.834032

He, K., Zhang, X., Ren, S., and Sun, J. (2016). "Deep residual learning for image recognition," in *Proceedings of the IEEE Conference on Computer Vision and Pattern Recognition* (Las Vegas, NV: IEEE). doi: 10.1109/CVPR.2016.90

Hoffman, J. M., Welsh-Bohmer, K. A., Hanson, M., Crain, B., Hulette, C., Earl, N., et al. (2000). FDG PET imaging in patients with pathologically verified dementia. *J. Nucl. Med.* 41, 1920–1928.

Huang, Y., Xu, J., Zhou, Y., Tong, T., Zhuang, X., and Alzheimer's Disease Neuroimaging Initiative (ADNI). (2019). Diagnosis of Alzheimer's disease *via* multi-modality 3D convolutional neural network. *Front. Neurosci.* 13, 509. doi: 10.3389/fnins.2019.00509

Jack Jr, C. R., Bernstein, M. A., Fox, N. C., Thompson, P., Alexander, G., Harvey, D., et al. (2008). The Alzheimer's disease neuroimaging initiative (ADNI): MRI methods. *J. Magnet. Reson. Imag. Off. J. Int. Soc. Magnet. Reson. Med.* 27, 685–691. doi: 10.1002/jmri.21049

Jagust, W., Gitcho, A., Sun, F., Kuczynski, B., Mungas, D., and Haan, M. (2006). Brain imaging evidence of preclinical Alzheimer's disease in normal aging. *Ann. Neurol. Off. J. Am. Neurol. Assoc. Child Neurol. Soc.* 59, 673–681. doi: 10.1002/ana.20799

Jara-Maldonado, M., Alarcon-Aquino, V., and Rosas-Romero, R. (2022). A new machine learning model based on the broad learning system and wavelets. *Eng. Appl. Artif. Intell.* 112, 104886. doi: 10.1016/j.engappai.2022.104886

Jessen, F., Wolfsgruber, S., Wiese, B., Bickel, H., Mösch, E., Kaduszkiewicz, H., et al. (2014). AD dementia risk in late MCI, in early MCI, and in subjective memory impairment. *Alzheimer's Dementia* 10, 76–83. doi: 10.1016/j.jalz.2012.09.017

Kobylecki, C., Langheinrich, T., Hinz, R., Vardy, E. R., Brown, G., Martino, M. E., et al. (2015). 18F-florbetapir PET in patients with frontotemporal dementia and Alzheimer disease. *J. Nucl. Med.* 56, 386–391. doi: 10.2967/jnumed.114.147454

Levin, F., Ferreira, D., Lange, C., Dyrba, M., Westman, E., Buchert, R., et al. (2021). Data-driven FDG-PET subtypes of Alzheimer's disease-related neurodegeneration. *Alzheimer's Res. Therapy* 13, 1–14. doi: 10.1186/s13195-021-00785-9

Liu, M., Cheng, D., Yan, W., and Alzheimer's Disease Neuroimaging Initiative. (2018). Classification of Alzheimer's disease by combination of convolutional and recurrent neural networks using FDG-PET images. *Front. Neuroinform.* 12, 35. doi: 10.3389/fninf.2018.00035

Lu, D., Popuri, K., Ding, G. W., Balachandar, R., Beg, M. F., and Alzheimer's Disease Neuroimaging Initiative. (2018). Multiscale deep neural network based analysis of FDG-PET images for the early diagnosis of Alzheimer's disease. *Med. Image Anal.* 46, 26–34. doi: 10.1016/j.media.2018.02.002

Marcus, C., Mena, E., and Subramaniam, R. M. (2014). Brain PET in the diagnosis of Alzheimer's disease. *Clin. Nucl. Med.* 39, e413. doi: 10.1097/RLU.0000000000000547

Mosconi, L., Tsui, W. H., Herholz, K., Pupi, A., Drzezga, A., Lucignani, G., et al. (2008). Multicenter standardized 18F-FDG PET diagnosis of mild cognitive impairment, Alzheimer's disease, and other dementias. *J. Nucl. Med.* 49, 390–398. doi: 10.2967/jnumed.107.045385

Nozadi, S. H., Kadoury, S., and Alzheimer's Disease Neuroimaging Initiative. (2018). Classification of Alzheimer's and MCI patients from semantically parcelled PET images: a comparison between AV45 and FDG-PET. *Int. J. Biomed. Imag.* 2018, 7430. doi: 10.1155/2018/1247430

Ossenkoppele, R., Tolboom, N., Foster-Dingley, J. C., Adriaanse, S. F., Boellaard, R., Yaqub, M., et al. (2012). Longitudinal imaging of Alzheimer pathology using [11C] PIB,[18F] FDDNP and [18F] FDG PET. *Eur. J. Nucl. Med. Mol. Imag.* 39, 990–1000. doi: 10.1007/s00259-012-2102-3

Pan, X., Adel, M., Fossati, C., Gaidon, T., and Guedj, E. (2018). Multilevel feature representation of FDG-PET brain images for diagnosing Alzheimer's disease. *IEEE J. Biomed. Health Inform.* 23, 1499–1506. doi: 10.1109/JBHI.2018.2857217

Pao, Y. H., and Takefuji, Y. (1992). Functional-link net computing: theory, system architecture, and functionalities. *Computer* 25, 76–79.

Singh, S., Srivastava, A., Mi, L., Caselli, R. J., Chen, K., Goradia, D., et al. (2017). "Deep-learning-based classification of FDG-PET data for Alzheimer's disease categories," in *Proceedings of the 13th International Conference on Medical Information Processing and Analysis* (Washington, DC: SPIE). doi: 10.1117/12.2294537

Suk, H. I., and Shen, D. (2013). "Deep learning-based feature representation for AD/MCI classification," in *International Conference on Medical Image Computing and Computer-Assisted Intervention* (Berlin, Heidelberg: Springer). doi: 10.1007/978-3-642-40763-5_72

Wu, G., and Duan, J. (2022). BLCov: a novel collaborative–competitive broad learning system for COVID-19 detection from radiology images. *Eng. Appl. Artif. Intell.* 115, 105323. doi: 10.1016/j.engappai.2022.105323

Zhang, L., Wang, M., Liu, M., and Zhang, D. (2020). A survey on deep learning for neuroimaging-based brain disorder analysis. *Front. Neurosci.* 14, 779. doi: 10.3389/fnins.2020.00779

frontiers | Frontiers in Neuroinformatics

TYPE Original Research
PUBLISHED 23 March 2023
DOI 10.3389/fninf.2023.1060511

Check for updates

OPEN ACCESS

EDITED BY
Fahmi Khalifa,
Morgan State University, United States

REVIEWED BY
Sneha Pandya,
Cornell University, United States
João Valente Duarte,
University of Coimbra, Portugal

*CORRESPONDENCE
Antonio Ricciardi
✉ antonio.ricciardi@ucl.ac.uk

RECEIVED 03 October 2022
ACCEPTED 28 February 2023
PUBLISHED 23 March 2023

CITATION
Ricciardi A, Grussu F, Kanber B, Prados F, Yiannakas MC, Solanky BS, Riemer F, Golay X, Brownlee W, Ciccarelli O, Alexander DC and Gandini Wheeler-Kingshott CAM (2023) Patterns of inflammation, microstructural alterations, and sodium accumulation define multiple sclerosis subtypes after 15 years from onset. *Front. Neuroinform.* 17:1060511. doi: 10.3389/fninf.2023.1060511

COPYRIGHT
© 2023 Ricciardi, Grussu, Kanber, Prados, Yiannakas, Solanky, Riemer, Golay, Brownlee, Ciccarelli, Alexander and Gandini Wheeler-Kingshott. This is an open-access article distributed under the terms of the Creative Commons Attribution License (CC BY). The use, distribution or reproduction in other forums is permitted, provided the original author(s) and the copyright owner(s) are credited and that the original publication in this journal is cited, in accordance with accepted academic practice. No use, distribution or reproduction is permitted which does not comply with these terms.

Patterns of inflammation, microstructural alterations, and sodium accumulation define multiple sclerosis subtypes after 15 years from onset

Antonio Ricciardi[1]*, Francesco Grussu[1,2], Baris Kanber[1,3], Ferran Prados[1,3,4], Marios C. Yiannakas[1], Bhavana S. Solanky[1], Frank Riemer[5], Xavier Golay[6], Wallace Brownlee[1], Olga Ciccarelli[1,7], Daniel C. Alexander[3] and Claudia A. M. Gandini Wheeler-Kingshott[1,8,9]

[1]NMR Research Unit, Queen Square MS Centre, Department of Neuroinflammation, UCL Queen Square Institute of Neurology, Faculty of Brain Sciences, University College London, London, United Kingdom, [2]Radiomics Group, Vall d'Hebron Institute of Oncology, Vall d'Hebron Barcelona Hospital Campus, Barcelona, Spain, [3]Centre for Medical Image Computing, Department of Medical Physics and Biomedical Engineering, University College London, London, United Kingdom, [4]eHealth Center, Universitat Oberta de Catalunya, Barcelona, Spain, [5]Mohn Medical Imaging and Visualization Centre, Department of Radiology, Haukeland University Hospital, Bergen, Norway, [6]Department of Brain Repair and Rehabilitation, UCL Queen Square Institute of Neurology, Faculty of Brain Sciences, University College London, London, United Kingdom, [7]NIHR UCLH Biomedical Research Centre, London, United Kingdom, [8]Department of Brain and Behavioural Sciences, University of Pavia, Pavia, Italy, [9]Brain Connectivity Research Center, IRCCS Mondino Foundation, Pavia, Italy

Introduction: Conventional MRI is routinely used for the characterization of pathological changes in multiple sclerosis (MS), but due to its lack of specificity is unable to provide accurate prognoses, explain disease heterogeneity and reconcile the gap between observed clinical symptoms and radiological evidence. Quantitative MRI provides measures of physiological abnormalities, otherwise invisible to conventional MRI, that correlate with MS severity. Analyzing quantitative MRI measures through machine learning techniques has been shown to improve the understanding of the underlying disease by better delineating its alteration patterns.

Methods: In this retrospective study, a cohort of healthy controls (HC) and MS patients with different subtypes, followed up 15 years from clinically isolated syndrome (CIS), was analyzed to produce a multi-modal set of quantitative MRI features encompassing relaxometry, microstructure, sodium ion concentration, and tissue volumetry. Random forest classifiers were used to train a model able to discriminate between HC, CIS, relapsing remitting (RR) and secondary progressive (SP) MS patients based on these features and, for each classification task, to identify the relative contribution of each MRI-derived tissue property to the classification task itself.

Results and discussion: Average classification accuracy scores of 99 and 95% were obtained when discriminating HC and CIS vs. SP, respectively; 82 and 83% for HC and CIS vs. RR; 76% for RR vs. SP, and 79% for HC vs. CIS. Different patterns of alterations were observed for each classification task, offering key insights in the understanding of MS phenotypes

pathophysiology: atrophy and relaxometry emerged particularly in the classification of HC and CIS vs. MS, relaxometry within lesions in RR vs. SP, sodium ion concentration in HC vs. CIS, and microstructural alterations were involved across all tasks.

KEYWORDS

MRI, multiple sclerosis, quantitative, multi-modal, diffusion, sodium, machine learning, random forest

1. Introduction

Multiple sclerosis (MS) is an immune-mediated, inflammatory, neurodegenerative disease of the central nervous system characterized by inflammatory demyelination and heterogeneous accrual of physical disability (Lucchinetti et al., 2000). The onset is determined by the first inflammatory episode suggestive of MS, referred to as clinically isolated syndrome (CIS), with CIS being recognized as the first clinical instance in the MS spectrum (Lublin et al., 2014). Further neurological symptoms may lead to a clinically defined diagnosis, as determined by the updated McDonald criteria (Thompson et al., 2018). Based on the clinical course, patients can be categorized into three types of relapse-onset MS: CIS, relapsing remitting (RR) and secondary progressive (SP). RR is characterized by clinically defined focal activity followed by periods of total or partial remission of neurological deficit, and the lack of disease progression between attacks; SP may follow from an initial RR course, with progressive worsening of neurological symptoms, with or without acute relapses. Primary progressive MS is associated with a progressive deterioration of clinical symptoms from onset (Lublin et al., 2014). Understanding why patients may develop different MS phenotypes over the years, or why only a small fraction of the diversity of clinical disability in MS can be explained by radiological evidence (*clinico-radiological paradox*) (Barkhof, 1999, 2002), are cause for further research.

Magnetic resonance imaging (MRI) is instrumental in the diagnosis and prognosis of MS, routinely used in clinical practice for the acquisition of qualitative images, e.g., proton density- (PD), T2- and T1-weighted, for lesion assessment. In the research environment, a much wider spectrum of dedicated, quantitative MRI techniques are employed for the study and characterization of MS pathophysiology, investigating the complex relationship between radiological evidence and clinical disability (Chard and Trip, 2017; Filippi et al., 2019). *In vivo* imaging biomarkers can be sensitive to inflammation, microstructural alterations, and even sodium ions accumulation, providing a window into the disease pathophysiology over time. Brain atrophy is a known indicator of disease progression since the early stages of MS, with recent studies providing further insight into the hierarchical recruitment of different brain regions over time (Eshaghi et al., 2018), although the integration of specifically cortical and sub-cortical regional volumetric measurements in clinical practice has yet to reach a consensus (Sastre-Garriga et al., 2020). Relaxometry and quantitative PD imaging have been shown to provide good biomarkers for inflammation and demyelination in normal appearing tissue (Neema et al., 2007; Mezer et al., 2013), invisible to the standard qualitative imaging. Through sensitivity to the diffusion of water molecules within the structured axonal environment of the brain, diffusion weighted imaging (DWI) has shown microstructural alterations in both lesions and normal appearing tissues, correlating with physical disability in progressive MS (Filippi et al., 2001; Collorone et al., 2020); recent studies have reported abnormalities at the early stages (Tur et al., 2020) and potential links to cognitive disability as well (Savini et al., 2019). Sodium (^{23}Na) imaging has been used to access the signal induced by sodium ions, showing promise in probing axonal function directly (Gandini Wheeler-Kingshott et al., 2018), with evidence of increased total sodium concentration (TSC) being reported in MS, correlating with disability and disease progression (Inglese et al., 2010; Paling et al., 2013; Maarouf et al., 2014). Whilst the potential of advanced MRI modalities is evident, they lack a unified consensus about their implementation, optimization and interpretation, and require, when compared to standard routine scans, additional acquisition times, costs and expertise, which make their application in clinics limited.

In this work, we explored a multi-modal dataset acquired in a cohort of patients with the same disease duration, where clinical and MRI assessments were performed 15 years from CIS, comprehending both routine and advanced MRI metrics sensitive to inflammation, microstructural alteration and sodium ions accumulation. Using a machine learning approach, we aimed to gain further understanding of which modalities are more likely to carry biophysically meaningful information for different classification tasks. Machine learning indeed has shown to be a key tool in the data-driven exploration of MRI datasets for the identification of patterns and biomarkers of disease, including the ability to identify discriminating factors of disease phenotypes against each other and healthy controls (HC) (Wottschel et al., 2015; Eshaghi et al., 2016). We therefore trained and tested a *random forest* algorithm to classify different subtypes of MS vs. HC and between each other, using a rich array of quantitative imaging features extracted from both clinical and advanced MRI data. Feature importance was calculated for each task and used to assess which metrics mostly contributed to the decision-making process. This provided us with novel insights into the pathophysiology of different MS subtypes, while also informing future studies toward more task-efficient MRI acquisitions.

2. Methods

A retrospective (Brownlee et al., 2019) multi-modal MRI dataset of HC, CIS, RR, and SP patients with same disease duration

was analyzed to provide evidence on what MRI features are best representative for different classification tasks.

2.1. Cohort

The cohort consisted of a total of 123 subjects: 29 HC (10 men, age: 35 ± 10 years old), 18 CIS (6 men, age: 47 ± 10 years old, EDSS: 0.4±0.5), 63 RR (15 men, age: 47±8 years old, EDSS: 2.2±1.1), and 13 SP (4 men, age: 48±8 years old, EDSS: 5.5±1.2). All MS patients (CIS, RR, SP) attended the MS center for clinical and radiological follow-up after a mean of 15 years from onset (Brownlee et al., 2019).

2.2. MRI protocol

Data were acquired on a 3T Philips Achieva MR system. The acquisition protocol included:

1. **PD/T2-w**. Dual-echo 2D PD/T2-weighted turbo spin-echo (resolution: 1 × 1 × 3mm^3, echo time TE: 19/85m, repetition time TR: 3,500ms, turbo factor: 10, echo spacing: 9.4ms, scan time: 4′2″).
2. **T1-w**. 2D T1-weighted spin-echo (resolution: 1 × 1 × 3mm^3, TE: 10ms, TR: 625ms, scan time: 5′43″).
3. **DWI**. Cardiac-gated, multi-shell, diffusion-weighted echo-planar imaging, with {8, 15, 30} isotropically distributed directions at *b*-values: {300, 711, 2000} s/mm^2 (resolution: 2.3 × 2.3 × 2.3mm^3, TE: 82ms, nominal TR (12 heart-beats): 13846ms, scan time: ∼ 16′).
4. **Sodium**. ^{23}Na imaging with 3D-cone sampling trajectory (resolution: 3 × 3 × 3mm^3, TE: 0.22ms, TR: 120ms, scan time: ∼ 18′). Two 4% agar phantoms with sodium concentration of 40 and 80mM were placed near the subject's head during the image acquisition for calibration purposes (Riemer et al., 2014).
5. **3DT1**. 3D sagittal T1-weighted magnetization-prepared rapid gradient echo (resolution: 1 × 1 × 1mm^3, TE: 3.1ms, TR: 6.9ms, inversion delay time: 823ms, flip angle: 8′, scan time: 6′32″).

All proton scans were acquired using a 32 channel head coil, whilst sodium imaging was performed using a single channel transmit-receive volume head coil (Rapid Biomedical, Rimpar, Germany). Patients were repositioned prior to the sodium imaging scans to allow for the coil change.

2.3. Image analysis

Lesion masks from Brownlee et al. (2019) studies were used. Brain tissue segmentation was performed on lesion-filled (Prados et al., 2016a) 3DT1 using the *Geodesic Information Flows* (GIF) tool (Cardoso et al., 2015), obtaining masks of white matter (WM), deep gray matter (dGM), and cortical gray matter (cGM).

PD/T2-weighted scans were initially acquired for lesion segmentation only; however, given the availability of T1-weighted scans with similar readout, they were also used to extract quantitative estimates of PD, T2, and T1 maps by fitting the relevant Bloch equations, using the *MyRelax* toolbox (Grussu et al., 2020). Further details are reported in the Supplementary material.

DWI data were corrected for motion and eddy current distortion using *FSL* (Andersson and Sotiropoulos, 2016). The *spherical mean technique* (SMT) multi-compartment model (Kaden et al., 2016) was used to analyse the DWI data, producing maps of intra-neurite volume fraction, intrinsic diffusivity and orientation dispersion entropy.

TSC maps were calculated by calibrating the ^{23}Na images by the signal intensity within the phantoms (Inglese et al., 2010; Riemer et al., 2014), which were segmented automatically (Prados et al., 2016b).

Mean values for quantitative PD, T2, and T1, intra-neurite volume fraction, intrinsic diffusivity, entropy, and TSC were calculated in normal appearing white matter (NAWM), dGM, cGM, and lesions, when present. Details about the calculation of the summary statistics are reported in the Supplementary material. The volume for the three tissue classes (WM, dGM, cGM) was also calculated from the brain segmentation, and divided by the total intra-cranial volume to take into account variability in head-sizes. In total, for each of the 123 subjects, 31 regional variables, or *biophysically meaningful features*, were therefore calculated.

Due to the HC group being significantly younger than the rest (average age 12 years lower, $p = 1\times10^{-6}$ from Kruskal–Wallis test), all features other than lesions-based ones were corrected for age using the HC as reference. A linear model, with age as independent variable and $\{\beta_0, \beta_1\}$ as intercept and slope, respectively, was fitted feature-wise on the HC data: the features that resulted significantly ($p < 0.05$) correlated with age were corrected by subtracting $\beta_1 \times$ age from the original data.

2.4. Classification analysis

After correcting for age, the data was *standardized* feature-wise such that the value distribution for each feature had mean of zero and standard deviation of one. The dataset was used to train and test a random forest algorithm over different binary classification tasks: HC vs. MS (that is RR and SP), CIS vs. MS, and all binary permutations of HC, CIS, RR, and SP. All HC and most CIS had no lesions, therefore lesion features were included only for the RR vs. SP classification task.

Classification was implemented using Python 3.7.4 (VanRossum and Drake, 2010) and the *scikit-learn* package (Pedregosa et al., 2011). Default parameters for the `ensemble.RandomForestClassifier` function were selected, with the number of trees set to 1,000 based on the available literature and previous experience on datasets with similar dimensionality. For each classification task, a 10-fold stratified cross-validation with 10 repetitions was implemented, for a total of 100 iterations. The classification performance was assessed by the average *receiver operating characteristic* (ROC) *area under the curve* (AUC) score on the test set across the 100 train/test iterations. Variable importance is defined by the improvement in the split-criterion attributed to each variable (feature) during training of the random forest. Variable importances were averaged across iterations, returning the mean feature ranking for the task;

10.3389/fninf.2023.1060511

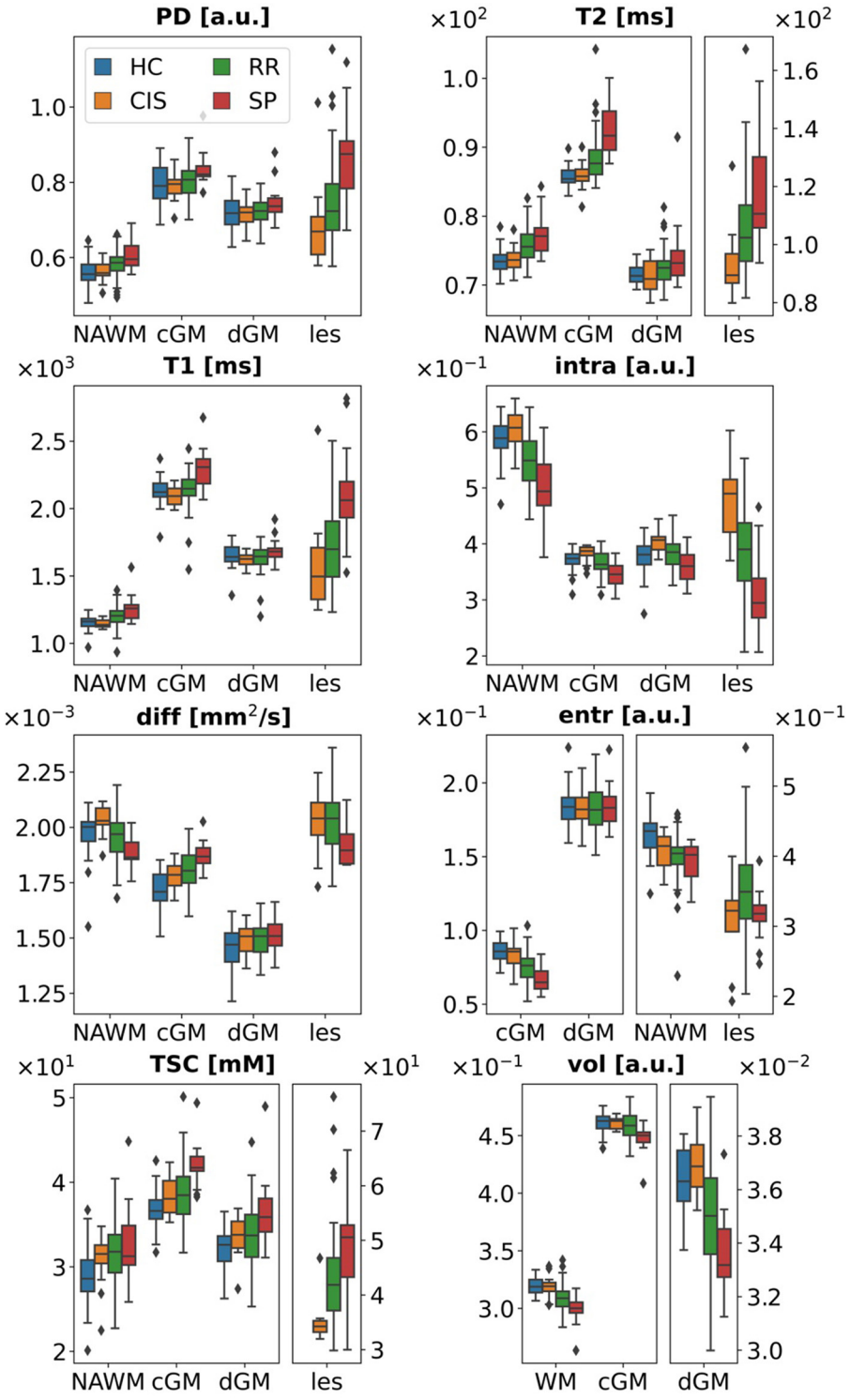

FIGURE 1
Age-corrected data. Data points for some tissue types have been plotted against different *y*-axes to better visualize boxplots across different ranges. PD, proton density; intra, intra-neurite volume fraction; diff, intrinsic diffusivity; entr, orientation dispersion entropy; TSC, total sodium concentration; vol, tissue volume; WM, white matter; NAWM, normal appearing white matter; cGM, cortical gray matter; dGM, deep gray matter; les, lesions; a.u., arbitrary units.

this allowed to identify the features that most contributed to each classification task, and thus are more likely to be biophysically meaningful with respect to the groups characterization.

In order to assess the significance of the classification results, the training and testing process was repeated identically 1,000 times with randomly permuted labels of the subjects at each repetition.

10.3389/fninf.2023.1060511

TABLE 1 ROC AUC classification results.

Tasks	Mean	Median $[Q_1, Q_3]$	p-value
HC - RR	0.82	0.83[0.72, 0.94]	< 0.001
HC - SP	0.99	1.00[1.00, 1.00]	< 0.001
HC - MS	0.84	0.88[0.76, 0.92]	< 0.001
CIS - RR	0.83	0.89[0.75, 1.00]	< 0.001
CIS - SP	0.95	1.00[1.00, 1.00]	< 0.001
CIS - MS	0.84	0.87[0.71, 1.00]	< 0.001
RR - SP	0.76	0.83[0.67, 1.00]	< 0.01
HC - CIS	0.79	0.83[0.67, 1.00]	< 0.01

p-values calculated through permutation test. HC, healthy controls; CIS, clinically isolated syndrome; RR, relapsing-remitting MS; SP, secondary progressive MS; MS, RR and SP; $Q_{1,3}$, 1st, 3rd quartile, respectively.

The distribution of the 1,000 mean ROC AUC scores defined the random classifier performance profile, which was used as reference to calculate the p-value associated to the classification performances on the original data.

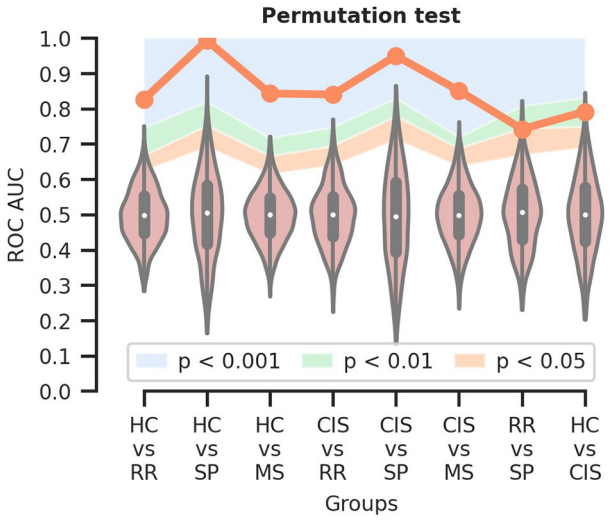

FIGURE 2
Permutation test to assess the statistical significance of the classification results. The orange line indicates the mean ROC AUC for each classification task; the colored areas delineate the different ranges of significance. HC, healthy controls; CIS, clinically isolated syndrome; RR, relapsing-remitting MS; SP, secondary progressive MS; MS, RR and SP.

3. Results

3.1. Age correction

Of the 24 non-lesion features, 5 resulted significantly correlated with age: quantitative T2 in dGM ($\beta_1 = -0.09$, $p = 0.002$), and cGM ($\beta_1 = -0.07$, $p = 0.02$), intrinsic diffusivity in dGM ($\beta_1 = 5 \times 10^{-6}$, $p = 0.02$), volume of dGM ($\beta_1 = 6.6 \times 10^{-5}$, $p = 0.006$) and cGM ($\beta_1 = 4.8 \times 10^{-4}$, $p = 0.009$). Fitting results for all features are reported in the Supplementary material. Age-corrected feature distributions are shown in Figure 1.

3.2. Classification results

ROC AUC scores for each task are reported in Table 1. In addition to the mean, the median and interquartile range $[Q_1, Q_3]$, with $Q_{1,3}$ indicating the 25-th and 75-th percentiles respectively, are also reported to assess dispersion instead of standard deviation, as the ROC AUC distribution over the 100 iterations was not symmetric, but skewed toward better-than-chance performance values. The best classification performances were obtained for the HC vs. SP and CIS vs. SP tasks, with mean ROC AUC scores of 0.99 and 0.95, respectively. Mean ROC AUC scores for HC vs. RR and CIS vs. RR were 0.82 and 0.83, and when discriminating HC and CIS against both the clinically defined MS groups, the performance scores fell in between. The lowest scores were observed for the RR vs. SP and HC vs. CIS tasks, with mean ROC AUC scores of 0.76 and 0.79, respectively. Mean ROC AUC, sensitivity and specificity scores have been also calculated with an random under-sampling method to correct for group imbalance, and reported in the Supplementary material.

3.3. Permutation test

The random classifier performance profiles for the different tasks are shown in Figure 2. Statistical significance of $0.001 < p < 0.01$ was observed for the RR vs. SP and HC vs. CIS classification tasks, whilst $p < 0.001$ was recorded for all others.

3.4. Feature importance

Average feature ranking for all classification tasks is shown in Figures 3, 4. Features have been color-coded to group MRI modalities from the same biophysical source (e.g., relaxometry parameters are in orange, diffusion microstructure in blue, sodium concentrations in green and tissue volume in gray); the top-ranking features contributing to 50% of the decision process for each task have been highlighted by a striped block and considered for interpretation. Overall, tissue volumes were the most meaningful when discriminating HC and CIS against clinically-defined MS; relaxometry parameters mainly in lesions had a role when discriminating the clinically-defined MS subtypes against each others; diffusion metrics were meaningful across all tasks, although particularly prominent in differentiating CIS vs. HC; TSC was mostly relevant when discriminating CIS against HC.

- **HC vs. RR**. RR patients showed a reduced WM and dGM volume, as well as reduced orientation dispersion entropy and increased T2 in NAWM and cGM with respect to HC. Increased intrinsic diffusivity in cGM also contributed to the classification task, with reduced intra-neurite volume fraction in NAWM at the 50% cumulative importance threshold.

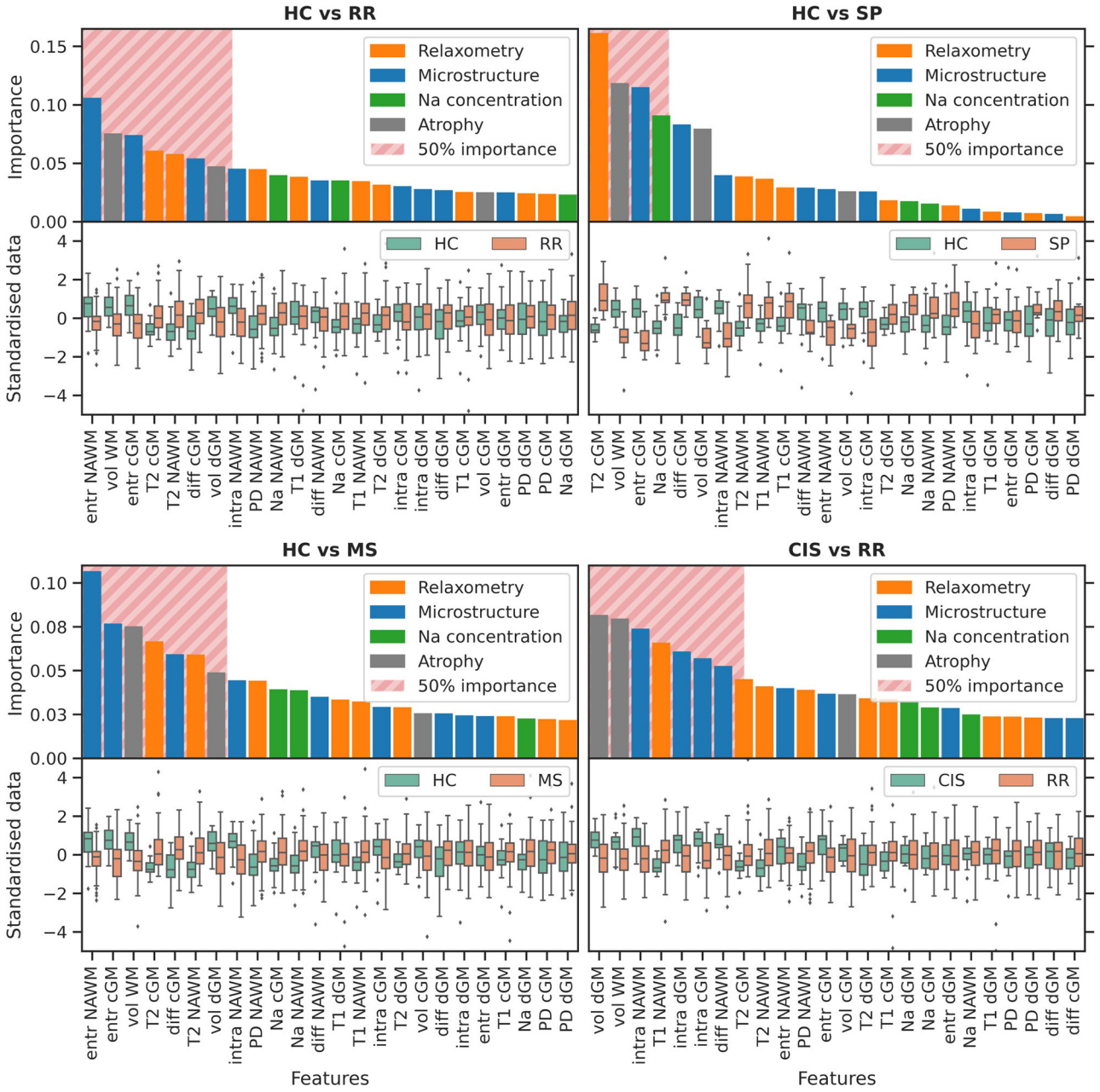

FIGURE 3
Variable importance. The bar-plot is color-coded to group MRI modalities from the same biophysical source. The striped block highlights the features contributing to 50% of the classification process. The *y*-axis is shared between columns. PD, proton density; intra, intra-neurite volume fraction; diff, intrinsic diffusivity; entr, orientation dispersion entropy; TSC, total sodium concentration; vol, tissue volume; WM, white matter; NAWM, normal appearing white matter; cGM, cortical gray matter; dGM, deep gray matter; les, lesions; HC, healthy controls; CIS, clinically isolated syndrome; RR, relapsing-remitting MS; SP, secondary progressive MS; MS, RR and SP. Continuing to Figure 4.

- **HC vs. SP**. The decision task was mostly driven by increased T2 in cGM, and reduced WM volume and entropy in cGM of SP compared to HC. Increased TSC and diffusivity in cGM were also observed in SP at the 50% threshold.
- **HC vs. MS**. Top-ranking features were distributed similarly to the HC vs. RR task.
- **CIS vs. RR**. Reduced dGM and WM volume mostly characterized RR compared to CIS, together with reduced intra-neurite volume fraction across all tissues, and increased T1 in NAWM. Reduced intrinsic diffusivity also emerged in NAWM in RR.
- **CIS vs. SP**. The task was driven mostly by reduced volume of all tissues in SP, and increased T2 in cGM. Reduced diffusivity and intra-neurite volume fraction in NAWM was also observed at the 50% threshold in SP compared to CIS.
- **CIS vs. MS**. Similar top-ranking features to the CIS vs. RR task were observed.

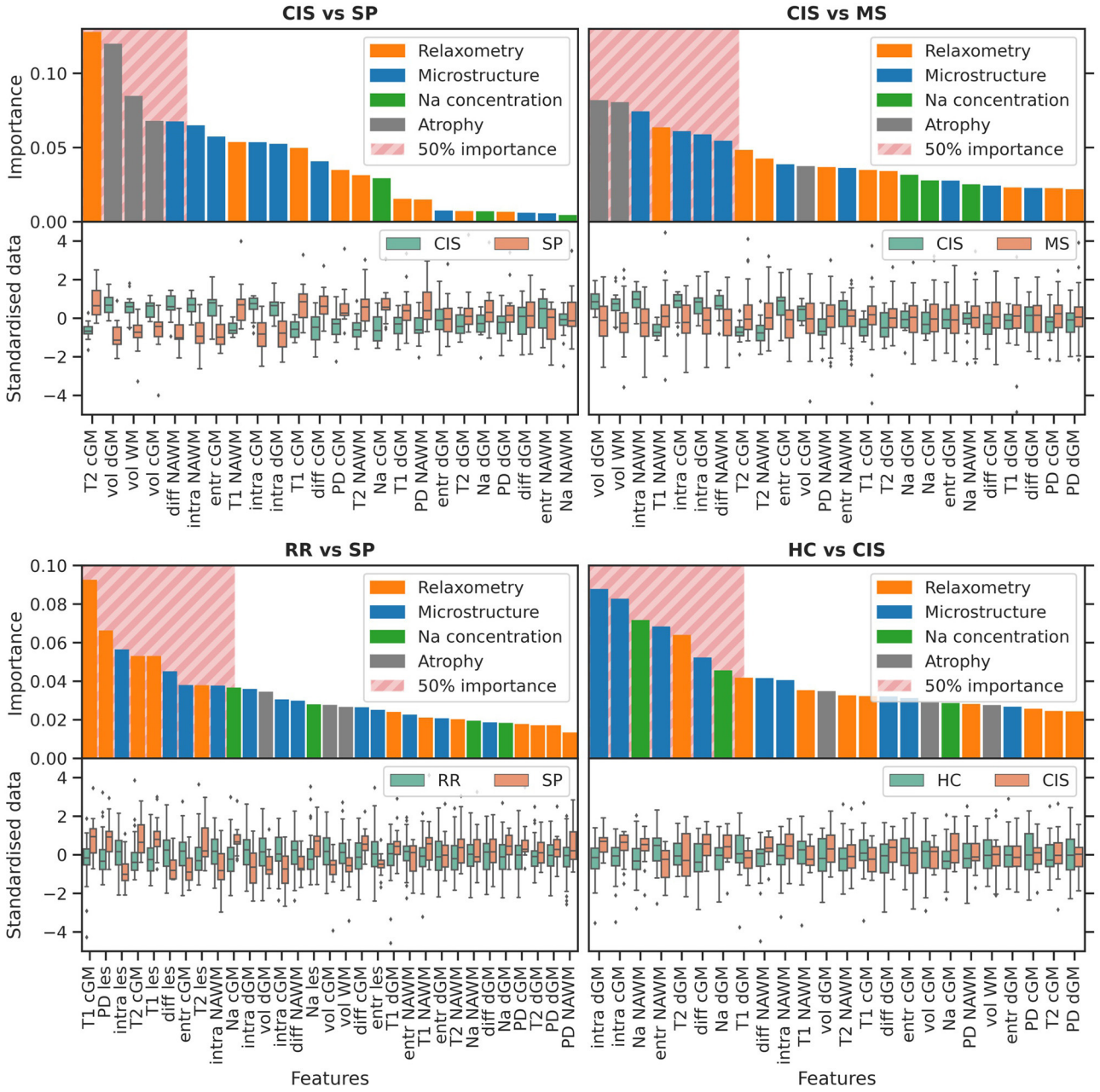

FIGURE 4
Variable importance. Continued from Figure 3.

- **RR vs. SP**. The task was driven mostly by relaxometry—increased PD, T2 and T1—and diffusion metrics—reduced intra-neurite volume fraction, diffusivity—alterations in lesions in SP compared to RR. Increased T1, T2 and entropy in cGM were also observed, with increased TSC in NAWM at the 50% threshold.
- **HC vs. CIS**. Increased TSC in NAWM and dGM in CIS compared to HC appeared as top-ranking features, together with increased intra-neurite volume fraction in dGM and cGM, reduced entropy in NAWM, and increased diffusivity in cGM. Reduced T2 and T1 in dGM were also observed in CIS.

4. Discussion

In this work, we used random forest classifiers to study the interaction between features extracted from both routine scans and advanced diffusion and sodium weighted imaging for the purpose of characterizing CIS and clinically-defined MS subtypes. The results show that a combination of advanced quantitative MRI and clinical features achieve classification scores between 76% and 99% depending on the task. Moreover, it is apparent that after 15 years from the initial CIS episode, features reflecting inflammation, microstructure changes and sodium accumulation play a very

different role in each MS subtype. Whether these alterations are present from the start or are the result of a 15 years evolution, it is not possible to say from this dataset, and requires targeted longitudinal studies.

- **Atrophy.** Brain atrophy was observed in the MS groups and emerged as a meaningful feature in all the classification tasks discriminating MS patients against HC and CIS. No strong involvement of brain volume features was observed instead when classifying MS phenotypes against each other, and in the HC vs. CIS task. Tissue volume loss in MS showed heterogeneous behavior across the different tissues, particularly with dGM consistently scoring higher than cGM, which is in line with previous findings of progressive recruitment of gray matter structures as part of MS neurodegeneration (Eshaghi et al., 2018; Soares et al., 2020). dGM significant involvement is well-known in the scientific community, however a consensus for the incorporation of *global* gray matter volumetrics into clinical practice has only recently been reached, and the specific inclusion of dGM structures (e.g., thalami, basal ganglia) in particular is still debated (Sastre-Garriga et al., 2020). Further research is recommended, with this work providing evidence in this direction.
- **Relaxometry.** Relaxometry features contributed partially to most tasks involving the clinically defined MS population, with prolonged T2 in cGM emerging particularly when discriminating SP against HC and CIS, a possible biomarker for the advanced cortical demyelination observed in the progressive stages of MS (Magliozzi et al., 2018). The strongest contribution was however observed in the RR vs. SP classification task across all relaxometry features, both in cGM and lesions: the involvement of quantitative parameters measured in lesions in the discrimination of MS phenotypes is indicative of the heterogeneous nature of MS pathogenesis and neurodegeneration (Lucchinetti et al., 2000). This result supports the need for adopting a more quantitative approach to lesion characterization in clinics than mere lesion load assessment. Reduced T2 in dGM was also observed in CIS with respect to HC: this reduction goes against a possible demyelination effect and could be due to residual (after age correction) iron deposition (Aquino et al., 2009). Further studies of iron deposition in MS, using for example quantitative susceptibility mapping and magnetic susceptibility source separation approaches, are recommended (Shin et al., 2021).
- **Diffusion imaging.** Diffusion imaging metrics were involved in all classification tasks, which is expected given that microstructural alterations are at the core of MS demyelination and neurodegeneration. Despite being the most ubiquitous set of feature across all tasks, diffusion metrics from multi-compartment models are also strongly model-dependent, hence prone to modeling artifacts and limitations, e.g., the lack of a myelin compartment, and results should be interpreted with care. Against HC, MS patients exhibited overall reduced orientation dispersion entropy, and reduced intra-neurite volume fraction against CIS. These results are in line with findings of reduced *fractional anisotropy* associated to higher fiber dispersion and neurite loss (Roosendaal et al., 2009). Reduced intrinsic diffusivity in SP was also observed with respect to CIS and RR, both in NAWM and lesions, but not in gray matter, which may be spurious, or an indicator of new lesion formation compatible with axonal undulation (Grussu et al., 2016). Increased intra-neurite volume fraction in CIS emerged in the classification against HC: whilst counter-intuitive in the context of neurite loss, this may be suggestive of axonal swelling, as further discussed below.
- **Sodium imaging.** TSC was particularly meaningful when discriminating CIS vs. HC, with increased TSC being observed in CIS in NAWM and dGM. Increased TSC was also observed in MS patients, albeit with a lower contribution with respect to other features, and has been reported in literature from the early stages of the disease (Maarouf et al., 2017). It has been associated with the over-expression and redistribution of sodium-potassium channels from the Ranvier nodes to newly demyelinated membrane: this is an adaptive response to the disruption of saltuatory conduction caused by demyelination, apt to preserve action potential transmission, limit the onset of neurological deficits, and facilitate recovery. This however also increases the axonal metabolism, as the proliferation of the sodium-potassium *active* pumps comes with higher energy expenditure which, if not satisfied, causes the accumulation of intra-cellular sodium. In MS, the impaired trophic support from oligodendrocites and mitochondrial dysfunction contribute to energy under-production which, coupled with the increased metabolic need, can lead to axonal degeneration due to metabolic failure secondary to chronic energy deprivation (Petracca et al., 2016). In the case of CIS, the increased TSC might be explained as a long lasting effect established in the brain following the initial inflammatory event. It may be speculated that this might be due to an over-expression of sodium channels at the onset of CIS to support neuronal function, which may also explain the increased intra-neurite volume fraction detected with diffusion imaging: indeed, the intra-cellular accumulation of sodium might induce axonal swelling through osmosis (Armstrong, 2003). To what extent this can happen before functional derangement accrues, leading to a more severe MS phenotype, is to be investigated.

Overall, the results of this unique dataset with MS patients of same disease duration, and a rich multi-modal quantitative MRI protocol, have shown that atrophy and relaxometry features contribute significantly to the discrimination of MS patients from HC and CIS; relaxometry in lesions emerges as particularly involved in the classification of MS phenotypes, which highlights the heterogeneity of MS pathophysiology. With both brain volumetry and relaxometry features being extracted from routine scans readily available in clinical practice, we have offered evidence of the hidden potential qualitative MRI data holds beyond lesion and tissue segmentation. Whilst advanced MRI acquisitions ought to be preferred when available, they are far from being routinely introduced in clinics; on the other hand, the use of routine scans

can pave the way to quantitative studies on large historical datasets otherwise lacking dedicated quantitative modalities. Advanced diffusion and sodium imaging have proven particularly sensitive to the characterization of MS phenotypes against each other, and CIS against HC, where differences in atrophy or relaxometry scores in normal appearing tissues were not as important, or not present at all. In these cases, dedicated quantitative MRI modalities showed their role in the quantification of subtle tissue microstructural and physiological alterations, otherwise invisible to conventional MRI, offering further insights on MS heterogeneous neurodegeneration. Specifically, CIS presenting subtle alterations compatible with MS histopathology (sodium ions accumulation and possible axonal swelling) may mark long lasting subtle damage accrued as a result of the first episode of neurologic symptoms. Alternatively, the observed alterations suggest that neuroprotective mechanisms may be at play in the stable CIS population, but, unlike with the clinically-defined MS patients, they do not lead to meaningful atrophy, inflammation, demyelination, and axonal loss. In other words, the ability to adapt to the increased metabolic demand without succumbing to energy failure, or avoiding axonal degeneration by excessive osmotic swelling, might be compensatory or even protective mechanisms, and as such key factors in what determines conversion, or lack thereof, to clinically defined MS.

Interestingly, what differentiates RR from a progressive form of the disease characterizing SP are changes in relaxometry parameters in the lesions. The classification task ranked as highest not microstructure changes or sodium accumulation in normal appearing tissue, but alterations of relaxometry parameters in the lesions of SP patients compared to RR. This could give an insight into the possible source of disease progression, driven not by the number or volume of the lesions, nor by diffuse damage of tissue, but by the severity and biophysical nature of lesion alterations. This therefore calls on monitoring relaxometry, as well as potentially others quantitative biophysically meaningful features, in the lesions as potential predictor of risks of progression.

The interpretation of these findings is of course conditional on this study's limitations. The statistical significance is hindered by the small sample size, especially tasks involving the SP group—only 13 subjects: although spurious results due to the many features may be expected, we strove to minimize their impact on the final outcome through careful examination of the data and corroboration with the published literature. In terms of classification tasks, the class imbalance between RR and SP likely caused the RR group to drive the classification results when discriminating HC or CIS against the whole MS cohort (RR and SP). Feature selection was performed implicitly by the random forest based on the relative contribution of each feature to the classification. No prior feature selection was performed as it would have reduced the exploratory power of this study. Each MRI modality came with its own limitations, which also must be taken into consideration, e.g., the multi-compartment diffusion model lacking a myelin volume fraction, or the use of surrogate quantitative PD, T2, and T1 extracted from routine scans not optimized to the scope. Particularly, the *MyRelax* algorithm for the calculation of quantitative T1 diverges in regions of cerebrospinal fluid, which were not of interest to this work; however, lesions also exhibit a similar behavior at their core, therefore the summary statistics for quantitative T1 in lesions is to be intended as representative more of the peripheral part of lesions, where the partial volume effect with cerebrospinal fluid is less pronounced, than the central part. Additional studies with larger sample size and histological evidence are required to substantiate these findings.

We showed that different MRI features appear to be biophysically meaningful when discriminating CIS and clinically defined MS phenotypes, with qualitative and quantitative MRI modalities offering specific insights for different classification tasks. Key to our results is highlighting the need for further studies focused on the role of quantitative MRI in the lesions of early CIS and MS subjects to score risks of progression. These findings can help in further understanding MS pathophysiology, as well as inform future studies toward more efficient acquisition protocols, better tailored to the scope.

Data availability statement

The raw data supporting the conclusions of this article will be made available by the authors, without undue reservation.

Ethics statement

The studies involving human participants were reviewed and approved by Research Ethics Committee 13/LO/1413. The patients/participants provided their written informed consent to participate in this study.

Author contributions

AR, OC, DA, and CGWK designed the study. WB enrolled the subjects and collected all the clinical data. MY acquired the MRI data, with support from BS, FR, XG, and CGWK. AR designed and performed the analyses with support from FG, BK, FP, DA, and CGWK. OC and CGWK provided support and guidance with the interpretation of the results. AR wrote the manuscript, with support from OC and CGWK, and comments from all authors. All authors contributed to the article and approved the submitted version.

Funding

This project has received funding under the European Union's Horizon 2020 Research and Innovation Programme under grant agreement No. 634541. FG received the support of a fellowship from "la Caixa" Foundation (ID 100010434). The fellowship code is "LCF/BQ/PR22/11920010". FG has also received support from the Beatriu de Pinós (2020 BP 00117) programme, funded by the Secretary of Universities and Research (Government of Catalonia). BK, FP, and OC are supported by the National Institute of Health Research Biomedical Research Centre at UCL and UCLH. EPSRC grants EP/M020533/1 and EP/J020990/01, MRC MR/T046422/1 and MR/T046473/1, Wellcome Trust award 221915/Z/20/Z, and the NIHR UCLH BRC support DCA's work in this area. CGWK

also receives funding from Horizon 2020 [Research and Innovation Action Grants Human Brain Project 945539 (SGA3)], BRC (#BRC704/CAP/CGW), MRC (#MR/S026088/1), and Ataxia UK.

Acknowledgments

We thank Patricia Mota for contributing in the development of the sodium imaging protocol, and Enrico Kaden for supporting the SMT image analysis.

Conflict of interest

The authors declare that the research was conducted in the absence of any commercial or financial relationships that could be construed as a potential conflict of interest.

Publisher's note

All claims expressed in this article are solely those of the authors and do not necessarily represent those of their affiliated organizations, or those of the publisher, the editors and the reviewers. Any product that may be evaluated in this article, or claim that may be made by its manufacturer, is not guaranteed or endorsed by the publisher.

Supplementary material

The Supplementary Material for this article can be found online at: https://www.frontiersin.org/articles/10.3389/fninf.2023.1060511/full#supplementary-material

References

Andersson, J. L., and Sotiropoulos, S. N. (2016). An integrated approach to correction for off-resonance effects and subject movement in diffusion MR imaging. *Neuroimage* 125, 1063–1078. doi: 10.1016/j.neuroimage.2015.10.019

Aquino, D., Bizzi, A., Grisoli, M., Garavaglia, B., Bruzzone, M. G., Nardocci, N., et al. (2009). Age-related iron deposition in the basal ganglia: quantitative analysis in healthy subjects. *Radiology* 252, 165–172. doi: 10.1148/radiol.2522081399

Armstrong, C. M. (2003). The Na/K pump, Cl ion, and osmotic stabilization of cells. *Proc. Natl. Acad. Sci. U.S.A.* 100, 6257–6262. doi: 10.1073/pnas.0931278100

Barkhof, F. (1999). MRI in multiple sclerosis: correlation with expanded disability status scale (EDSS). *Multiple Scler. J.* 5, 283–286. doi: 10.1177/135245859900500415

Barkhof, F. (2002). The clinico-radiological paradox in multiple sclerosis revisited. *Curr. Opin. Neurol.* 15, 239–245. doi: 10.1097/00019052-200206000-00003

Brownlee, W. J., Solanky, B., Prados, F., Yiannakas, M., Da Mota, P., Riemer, F., et al. (2019). Cortical grey matter sodium accumulation is associated with disability and secondary progressive disease course in relapse-onset multiple sclerosis. *J. Neurol. Neurosurg. Psychiatry* 90, 755–760. doi: 10.1136/jnnp-2018-319634

Cardoso, M. J., Modat, M., Wolz, R., Melbourne, A., Cash, D., Rueckert, D., et al. (2015). Geodesic information flows: spatially-variant graphs and their application to segmentation and fusion. *IEEE Trans. Med. Imaging* 34, 1976–1988. doi: 10.1109/TMI.2015.2418298

Chard, D., and Trip, S. A. (2017). Resolving the clinico-radiological paradox in multiple sclerosis. *F1000Res.* 6:1828. doi: 10.12688/f1000research.11932.1

Collorone, S., Cawley, N., Grussu, F., Prados, F., Tona, F., Calvi, A., et al. (2020). Reduced neurite density in the brain and cervical spinal cord in relapsing–remitting multiple sclerosis: a Noddi study. *Multiple Scler. J.* 26, 1647–1657. doi: 10.1177/1352458519885107

Eshaghi, A., Marinescu, R. V., Young, A. L., Firth, N. C., Prados, F., Jorge Cardoso, M., et al. (2018). Progression of regional grey matter atrophy in multiple sclerosis. *Brain* 141, 1665–1677. doi: 10.1093/brain/awy088

Eshaghi, A., Wottschel, V., Cortese, R., Calabrese, M., Sahraian, M. A., Thompson, A. J., et al. (2016). Gray matter MRI differentiates neuromyelitis optica from multiple sclerosis using random forest. *Neurology* 87, 2463–2470. doi: 10.1212/WNL.0000000000003395

Filippi, M., Brück, W., Chard, D., Fazekas, F., Geurts, J. J., Enzinger, C., et al. (2019). Association between pathological and MRI findings in multiple sclerosis. *Lancet Neurol.* 18, 198–210. doi: 10.1016/S1474-4422(18)30451-4

Filippi, M., Cercignani, M., Inglese, M., Horsfield, M., and Comi, G. (2001). Diffusion tensor magnetic resonance imaging in multiple sclerosis. *Neurology* 56, 304–311. doi: 10.1212/WNL.56.3.304

Gandini Wheeler-Kingshott, C. A., Riemer, F., Palesi, F., Ricciardi, A., Castellazzi, G., Golay, X., et al. (2018). Challenges and perspectives of quantitative functional sodium imaging (fNaI). *Front. Neurosci.* 12, 810. doi: 10.3389/fnins.2018.00810

Grussu, F., Battiston, M., Veraart, J., Schneider, T., Cohen-Adad, J., Shepherd, T. M., et al. (2020). Multi-parametric quantitative *in vivo* spinal cord MRI with unified signal readout and image denoising. *Neuroimage* 217, 116884. doi: 10.1016/j.neuroimage.2020.116884

Grussu, F., Schneider, T., Yates, R. L., Zhang, H., Wheeler-Kingshott, C. A. G., DeLuca, G. C., et al. (2016). A framework for optimal whole-sample histological quantification of neurite orientation dispersion in the human spinal cord. *J. Neurosci. Methods* 273, 20–32. doi: 10.1016/j.jneumeth.2016.08.002

Inglese, M., Madelin, G., Oesingmann, N., Babb, J., Wu, W., Stoeckel, B., et al. (2010). Brain tissue sodium concentration in multiple sclerosis: a sodium imaging study at 3 Tesla. *Brain* 133, 847–857. doi: 10.1093/brain/awp334

Kaden, E., Kelm, N. D., Carson, R. P., Does, M. D., and Alexander, D. C. (2016). Multi-compartment microscopic diffusion imaging. *Neuroimage* 139, 346–359. doi: 10.1016/j.neuroimage.2016.06.002

Lublin, F. D., Reingold, S. C., Cohen, J. A., Cutter, G. R., Sørensen, P. S., Thompson, A. J., et al. (2014). Defining the clinical course of multiple sclerosis: the 2013 revisions. *Neurology* 83, 278–286. doi: 10.1212/WNL.0000000000000560

Lucchinetti, C., Brück, W., Parisi, J., Scheithauer, B., Rodriguez, M., and Lassmann, H. (2000). Heterogeneity of multiple sclerosis lesions: implications for the pathogenesis of demyelination. *Ann. Neurol.* 47, 707–717. doi: 10.1002/1531-8249(200006)47:6<707::AID-ANA3>3.0.CO;2-Q

Maarouf, A., Audoin, B., Konstandin, S., Rico, A., Soulier, E., Reuter, F., et al. (2014). Topography of brain sodium accumulation in progressive multiple sclerosis. *Magn. Reson. Mater. Phys. Biol. Med.* 27, 53–62. doi: 10.1007/s10334-013-0396-1

Maarouf, A., Audoin, B., Pariollaud, F., Gherib, S., Rico, A., Soulier, E., et al. (2017). Increased total sodium concentration in gray matter better explains cognition than atrophy in MS. *Neurology* 88, 289–295. doi: 10.1212/WNL.0000000000003511

Magliozzi, R., Reynolds, R., and Calabrese, M. (2018). MRI of cortical lesions and its use in studying their role in MS pathogenesis and disease course. *Brain Pathol.* 28, 735–742. doi: 10.1111/bpa.12642

Mezer, A., Yeatman, J. D., Stikov, N., Kay, K. N., Cho, N.-J., Dougherty, R. F., et al. (2013). Quantifying the local tissue volume and composition in individual brains with magnetic resonance imaging. *Nat. Med.* 19, 1667–1672. doi: 10.1038/nm.3390

Neema, M., Stankiewicz, J., Arora, A., Dandamudi, V. S., Batt, C. E., Guss, Z. D., et al. (2007). T1-and T2-based MRI measures of diffuse gray matter and white matter damage in patients with multiple sclerosis. *J. Neuroimaging* 17, 16S–21S. doi: 10.1111/j.1552-6569.2007.00131.x

Paling, D., Solanky, B. S., Riemer, F., Tozer, D. J., Wheeler-Kingshott, C. A., Kapoor, R., et al. (2013). Sodium accumulation is associated with disability and a progressive course in multiple sclerosis. *Brain* 136, 2305–2317. doi: 10.1093/brain/awt149

Pedregosa, F., Varoquaux, G., Gramfort, A., Michel, V., Thirion, B., Grisel, O., et al. (2011). Scikit-learn: machine learning in Python. *J. Mach. Learn. Res.* 12, 2825–2830.

Petracca, M., Vancea, R. O., Fleysher, L., Jonkman, L. E., Oesingmann, N., and Inglese, M. (2016). Brain intra-and extracellular sodium concentration in multiple sclerosis: a 7 t MRI study. *Brain* 139, 795–806. doi: 10.1093/brain/awv386

Prados, F., Cardoso, M. J., Kanber, B., Ciccarelli, O., Kapoor, R., Wheeler-Kingshott, C. A. G., et al. (2016a). A multi-time-point modality-agnostic patch-based method for lesion filling in multiple sclerosis. *Neuroimage* 139, 376–384. doi: 10.1016/j.neuroimage.2016.06.053

Prados, F., Solanky, B. S., Alves Da Mota, P., Cardoso, M. J., Brownlee, W. J., Riemer, F., et al. (2016b). "Automatic sodium maps reconstruction using patchmatch algorithm for phantom detection," in *ISMRM* (Singapore).

Riemer, F., Solanky, B. S., Stehning, C., Clemence, M., Wheeler-Kingshott, C. A., and Golay, X. (2014). Sodium (23Na) ultra-short echo time imaging in the human

brain using a 3D-cones trajectory. *Magn. Reson. Mater. Phys. Biol. Med.* 27, 35–46. doi: 10.1007/s10334-013-0395-2

Roosendaal, S., Geurts, J. J., Vrenken, H., Hulst, H., Cover, K. S., Castelijns, J., et al. (2009). Regional DTI differences in multiple sclerosis patients. *Neuroimage* 44, 1397–1403. doi: 10.1016/j.neuroimage.2008.10.026

Sastre-Garriga, J., Pareto, D., Battaglini, M., Rocca, M. A., Ciccarelli, O., Enzinger, C., et al. (2020). Magnims consensus recommendations on the use of brain and spinal cord atrophy measures in clinical practice. *Nat. Rev. Neurol.* 16, 171–182. doi: 10.1038/s41582-020-0314-x

Savini, G., Pardini, M., Castellazzi, G., Lascialfari, A., Chard, D., D'Angelo, E., et al. (2019). Default mode network structural integrity and cerebellar connectivity predict information processing speed deficit in multiple sclerosis. *Front. Cell. Neurosci.* 13, 21. doi: 10.3389/fncel.2019.00021

Shin, H.-G., Lee, J., Yun, Y. H., Yoo, S. H., Jang, J., Oh, S.-H., et al. (2021). χ-separation: magnetic susceptibility source separation toward iron and myelin mapping in the brain. *Neuroimage* 240, 118371. doi: 10.1016/j.neuroimage.2021.118371

Soares, J., Sousa, T., d'Almeida, O. C., Batista, S., Sousa, L., Castelo-Branco, M., et al. (2020). "Investigating whole-brain MRI markers in multiple sclerosis–emerging dimensions in morphometric space," in *XV Mediterranean Conference on Medical and Biological Engineering and Computing–MEDICON 2019: Proceedings of MEDICON 2019* (Coimbra), 1644–1652.

Thompson, A. J., Banwell, B. L., Barkhof, F., Carroll, W. M., Coetzee, T., Comi, G., et al. (2018). Diagnosis of multiple sclerosis: 2017 revisions of the McDonald criteria. *Lancet Neurol.* 17, 162–173. doi: 10.1016/S1474-4422(17)30470-2

Tur, C., Grussu, F., Prados, F., Charalambous, T., Collorone, S., Kanber, B., et al. (2020). A multi-shell multi-tissue diffusion study of brain connectivity in early multiple sclerosis. *Multiple Scler. J.* 26, 774–785. doi: 10.1177/1352458519845105

VanRossum, G., and Drake, F. L. (2010). *The Python Language Reference*. Python Software Foundation, Amsterdam.

Wottschel, V., Alexander, D., Kwok, P., Chard, D., Stromillo, M., De Stefano, N., et al. (2015). Predicting outcome in clinically isolated syndrome using machine learning. *Neuroimage Clin.* 7, 281–287. doi: 10.1016/j.nicl.2014.11.021

frontiers | Frontiers in Neuroscience

TYPE Original Research
PUBLISHED 24 March 2023
DOI 10.3389/fnins.2023.1133834

Check for updates

OPEN ACCESS

EDITED BY
Ahmed Shalaby,
University of Texas Southwestern Medical Center, United States

REVIEWED BY
Yiyuan Han,
University of Essex, United Kingdom
Yunxia Li,
Huazhong University of Science and Technology, China

*CORRESPONDENCE
Banghua Yang
✉ yangbanghua@shu.edu.cn
Xiaoying Bi
✉ bixiaoying2013@163.com
Shu Zhou
✉ zhoushu.49@hotmail.com

SPECIALTY SECTION
This article was submitted to Brain Imaging Methods, a section of the journal Frontiers in Neuroscience

RECEIVED 29 December 2022
ACCEPTED 09 March 2023
PUBLISHED 24 March 2023

CITATION
Li Y, Yang B, Wang Z, Huang R, Lu X, Bi X and Zhou S (2023) EEG assessment of brain dysfunction for patients with chronic primary pain and depression under auditory oddball task.
Front. Neurosci. 17:1133834.
doi: 10.3389/fnins.2023.1133834

COPYRIGHT
© 2023 Li, Yang, Wang, Huang, Lu, Bi and Zhou. This is an open-access article distributed under the terms of the Creative Commons Attribution License (CC BY). The use, distribution or reproduction in other forums is permitted, provided the original author(s) and the copyright owner(s) are credited and that the original publication in this journal is cited, in accordance with accepted academic practice. No use, distribution or reproduction is permitted which does not comply with these terms.

EEG assessment of brain dysfunction for patients with chronic primary pain and depression under auditory oddball task

Yunzhe Li[1], Banghua Yang[1,2]*, Zuowei Wang[3], Ruyan Huang[3], Xi Lu[4], Xiaoying Bi[4]* and Shu Zhou[4]*

[1]School of Medicine, School of Mechatronic Engineering and Automation, Research Center of Brain Computer Engineering, Shanghai University, Shanghai, China, [2]Shanghai Shaonao Sensing Technology Ltd., Shanghai, China, [3]Division of Mood Disorders, Shanghai Hongkou Mental Health Center, Shanghai, China, [4]Department of Neurology, Shanghai Changhai Hospital, Second Military Medical University, Shanghai, China

In 2019, the International Classification of Diseases 11th Revision International Classification of Diseases (ICD-11) put forward a new concept of "chronic primary pain" (CPP), a kind of chronic pain characterized by severe functional disability and emotional distress, which is a medical problem that deserves great attention. Although CPP is closely related to depressive disorder, its potential neural characteristics are still unclear. This paper collected EEG data from 67 subjects (23 healthy subjects, 22 patients with depression, and 22 patients with CPP) under the auditory oddball paradigm, systematically analyzed the brain network connection matrix and graph theory characteristic indicators, and classified the EEG and PLI matrices of three groups of people by frequency band based on deep learning. The results showed significant differences in brain network connectivity between CPP patients and depressive patients. Specifically, the connectivity within the frontoparietal network of the Theta band in CPP patients is significantly enhanced. The CNN classification model of EEG is better than that of PLI, with the highest accuracy of 85.01% in Gamma band in former and 79.64% in Theta band in later. We propose hyperexcitability in attentional control in CPP patients and provide a novel method for objective assessment of chronic primary pain.

KEYWORDS

chronic primary pain (CPP), depressive disorder, EEG, phase lag index (PLI), brain networks, convolutional neural network (CNN)

1. Introduction

Chronic pain is defined as pain that lasts or recurs for more than 3 months, characterized by the interaction of biological, psychological, and social factors (Treede et al., 2015). At present, the etiology and pathogenesis of some chronic pain are not clear. The terms "somatoform pain disorders" or "functional pain syndromes" are usually used to describe this kind of pain. Such patients often go to various specialties of the hospital for repeatedly checking to legitimize their suffering, consuming a lot of medical resources. However, due to diagnostic uncertainty patients often feel guilty or angry and poorly understood. They

are dissatisfied with the curative effect, and even have a crisis of trust in doctors (Serbic et al., 2022). In 2019, the IASP expert group participated in the revision and release of the International Classification of Diseases 11th Revision (ICD-11), which proposed the concept of "chronic primary pain (CPP)" (Nicholas et al., 2019), advocating that it be incorporated as a disease in its own right rather than a symptom (Treede et al., 2019). This diagnosis needs to be considered and targeted when the cause of chronic pain is not clear but is accompanied by significant emotional abnormalities and functional impairment.

Although there are still some disputes on the concept of CPP, more and more studies suggest that CPP may lead to specific changes in brain plasticity, which could be expected to be an objective diagnostic indicator of CPP. The recent review found that the gray matter volume of the cingulate cortex and insula of CPP patients decrease significantly while the right striatum gray matter increases (Wang et al., 2022). The duration of pain symptoms is positively correlated with the right brain volume and negatively correlated with the volume of the right anterior cingulate cortex and the right middle frontal gyrus gray atter. At the same time, CPP induces dysfunction of descending pain modulation, which is closely related to the serotonin system (Tao et al., 2019).

Clinically, patients with chronic pain have a higher risk of having depressive symptoms (Yalcin and Barrot, 2014). This comorbidity may indicate overlapped underlying neural mechanisms in chronic pain and depressive disorders (DD). As un particular type of chronic pain characterized by severe functional disability and emotional distress, CPP may present closer relationship with DD. However, there is still a lack of mechanistic studies exploring the similarities and differences between the two, which could provide the clinician with important diagnosis and treatment tools (Burke et al., 2015; Harth and Nielson, 2019).

Compared with other brain imaging technologies, EEG has a time resolution of milliseconds, which can measure the changes in brain neurophysiology (Boloukian and Safi-Esfahani, 2020; Yasin et al., 2021). On one hand, there have been many studies on depression-related EEG markers. Some researchers mainly use the degree of prefrontal lateralization of normal people and patients with depression to achieve classification (Jesulola et al., 2015; Palmiero and Piccardi, 2017), and propose that EEG characteristics can predict the heterogeneity of individual antidepressant drug responses to a certain extent. It is mainly found that the activities of Theta and Alpha frequency bands in the prefrontal and parietal lobes are related to depression (Pigoni et al., 2019). The latest research is based on the resting state EEG model optimized by computer. It is found that the neural activity of the prefrontal lobe can predict the treatment response of patients with depression to antidepressants (Wu et al., 2020). On the other hand, important efforts have been made in EEG biomarkers for chronic pain, although there is still disagreement on specificity and replicability (Mouraux and Iannetti, 2018; Ploner and May, 2018). For example, resting-state Theta and Gamma synchrony in frontal areas (Ta Dinh et al., 2019) and greater frontoparietal connectivity of the alpha oscillations (Ye et al., 2019) have been involved in the pathophysiology of chronic pain. Using the tonic pain model, we and other researchers have demonstrated that prefrontal cortex-related functions (i.e., cognitive task performances) and brain activities measured by EEG are related to pain tolerance (Zhou et al., 2015a,b, 2020) and recovery (Rustamov et al., 2021). Therefore, the extraction of EEG features through machine learning and other methods can help in individualized diagnosis and therapeutic monitoring of CPP.

The auditory oddball task can study the characteristics of attention resource allocation, working memory and information updating (Isreal et al., 1980; Johnson, 1986; Polich, 1986; Murphy et al., 2014). The auditory P300 evoked by this paradigm has been well applied in psychiatric diseases, and is the main candidate electrophysiological biomarker of psychiatric diseases (Jeon and Polich, 2003). The functional connectivity of EEG signals, especially the analysis of complex brain networks, may be more important for exploring the mechanism of brain activity in a task state. It has been used to study psychological diseases such as Alzheimer's disease and autism (Steinmann et al., 2018; Bosch-Bayard et al., 2020). For functional brain networks, researchers have proposed many coupling methods, such as correlation-based method, partial order correlation-based method, and sparse method (Bullmore and Sporns, 2012; Sporns, 2013; Li et al., 2015; van den Heuvel et al., 2018). According to the existing research, the Phase Lag Index (PLI) is insensitive to the brain volume effect and can eliminate all indirect causality. Therefore, it is an excellent method to obtain functional brain network connectivity since the direct causality among the brain network nodes can be more accurately evaluated (Stam et al., 2007). Graph theory analysis involves filtering and transforming the functional connection matrix into a graph, and can be applied to investigate its topological structure or connectome of complex brain network (Farahani et al., 2019). Using this method, a recent systematic review has found significant group differences between chronic pain patients and healthy controls on certain overall graphical measures rather than nodal levels (Lenoir et al., 2021). Convolutional neural network (CNN) was used in the field of image recognition at the early stage and achieved very good classification results in the field of biological signal analysis, as well as good results in the field of auxiliary diagnosis of mental diseases (Acharya et al., 2018; Yao et al., 2020), but it has not been applied in the analysis and auxiliary diagnosis of chronic pain yet.

Therefore, this study will use task-state (i.e., auditory oddball paradigm) EEG feature extraction, mainly applying CNN as a deep learning algorithm for classification and complex brain network analysis to identify the neurophysiological characteristics of CPP different from DD, and meanwhile to explore its characteristic neural representation.

2. Materials and methods

2.1. Procedure

In this study, the auditory oddball task EEG data were collected from healthy subjects (HC) and patients with DD and CPP. First, using the PLI coupling to construct the brain functional connectivity network, the connectivity differences between groups of different brain regions in different frequency bands are compared and analyzed using graph theory and CNN. Then, the CNN algorithm is used to classify diseases based on EEG feature extraction in different frequency bands, providing a new method

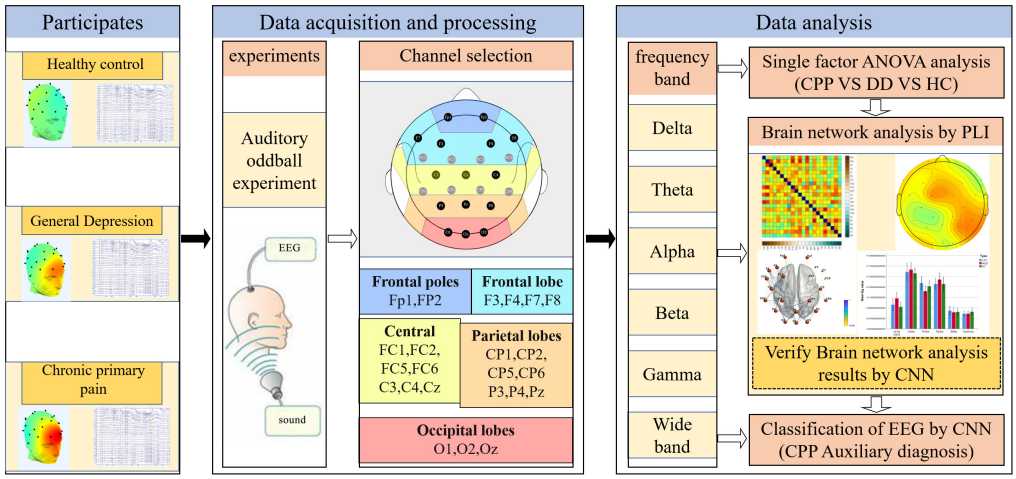

FIGURE 1
Flow chart of research methods. Collect EEG generated by auditory oddball stimulation in three groups of subjects, and then select 23 channels of interest for brain network analysis and CNN classification.

for objective evaluation of CPP. The processing flow of relevant data is shown in Figure 1.

2.2. Participates

In this study, twenty-two patients with CPP (13 females, 46 ± 9.62 years), twenty-two patients with DD (11 females, 46 ± 12.33 years), and twenty-three HCs (13 females, 49 ± 10.26 years) were recruited from the Shanghai Changhai Hospital, Shanghai Hongkou Mental Health Center and University of Shanghai, respectively, (Shanghai, China). All participants gave their written informed consent after the experimental procedure had been carefully explained. The research has been approved by the local research ethics committee.

Inclusion and exclusion criteria of subjects: chronic primary pain concerning the diagnostic criteria proposed by ICD-11: pain in one or more anatomical regions that (1) persists or recurs for longer than 3 months; (2) associated with significant emotional distress or functional disability (interference with activities of daily life and participation in social roles); (3) cannot be better accounted for by another chronic pain condition (American Psychiatric Association, 2013). Depressive disorder diagnosis was established according to the Diagnostic and Statistical Manual of Mental Disorders, 5th edition (DSM-V) criteria, as assessed by the structured clinical interview for DSM-V and Hamilton Depression Scale (HAMD). The two categories of patients also need to meet the following inclusion criteria: (1) Age 18–65 years old; (2) Junior high school degree or above; (3) Not taking medicine at the initial diagnosis or more than 6 months after drug withdrawal; (4) Volunteer to participate in this study and sign the informed consent form. Exclusion criteria: (1) Serious cognitive impairment or hearing disability, unable to cooperate in the completion of project-related assessment tests; (2) Serious physical diseases; (3) Severe psychiatric symptoms; (4) Abuse of psychoactive substances; (5) Suffering from diseases that can cause secondary chronic pain.

All subjects were instructed to fill in SDS for self-evaluation of depression level (Table 1). Two groups of patients were assessed by the physician with HAMD. The subjective and multidimensional experience of pain in CPP patients was quantitatively measured using the Short-Form McGill Pain Questionnaire (Dworkin et al., 2009). It comprises three subscales: a pain rating index (PRI) describing the qualities of pain, a 10 cm visual analog scale (VAS) describing the intensity of averaged daily pain during the past 2 weeks, and a present pain intensity (PPI) index describing the intensity of current pain.

2.3. Experimental paradigm

Auditory oddball task was applied. The stimulus materials for the auditory oddball task were composed of 30 target stimuli (1,200 Hz, 75 dB, 50 ms) and 200 standard stimuli (1,000 Hz, 75 dB, 50 ms). The stimuli were arranged in a pseudo-random order with an interval of 1,000–1,500 ms between each stimulus. Before the experiment, there was a training part consisting of 10 tones, including two target stimuli. Subjects were asked to identify the tones with a low probability of occurrence, count them in silence, and then report to the researchers. The experimental program was written by E-Prime 1.0 software of Psychology Software Tools in the United States. The presentation mode of the stimulus sequence is shown in Figure 2.

2.4. Data acquisition and preprocessing

The experimental data acquisition equipment is 32 channels high-density EEG acquisition equipment made by Brain Productions Company in Germany. The recording software is based on the Vision Recorder system developed by the above company. During the whole experiment, the electrode was within the range below 30 k Ω, and the sampling rate was 1,000 Hz. The EEG cap was set with a 0.1–100 Hz band-pass filter in the default

TABLE 1 Number of subjects in three categories (N), average age, years of education, sex ratio, the average score of HAMD, the average score of SDS, and the average score of McGill Questionnaire.

		HC	DD	CPP
N		23	22	22
Average Age/Year		49 ± 10.26	46 ± 12.33	46 ± 9.62
Education/Year		10 ± 2.72	10 ± 4.73	10 ± 4.37
Male/Female		10/13	11/11	9/13
HAMD scale		5.46 ± 2.37	19.61 ± 4.01	20.83 ± 3.74
SDS scale		47.25 ± 3.55	69.28 ± 6.72	70.36 ± 5.68
McGill Questionnaire	PRI	0.98 ± 0.87	1.26 ± 0.65	12.47 ± 1.59
	VAS	1.21 ± 0.73	1.74 ± 0.67	6.42 ± 2.33
	PPI	0.20 ± 0.20	0.25 ± 0.24	3.73 ± 0.47

setting of the headset. To reduce the calculation cost during data processing, the data was down-sampled to 250 Hz. The impedance of recording electrodes was kept at less than 5 k Ω. The collected data were preprocessed using the EEGLAB toolbox (v2019.1) of MATLAB (R2020a) software: select 23 electrodes were placed on the scalp based on the international 10–20 electrode placement system and take Cz as the reference electrode. See **Figure 1** for the selected electrodes and functional area division (Delorme and Makeig, 2004). Take the target stimulus as 0 times, select −0.2 s∼0.8 s data as a trial, and remove the components of eye and muscle electricity through independent component analysis.

2.5. Brain network construction and coupling

As **Figure 3** shows: (1) First, EEG data is collected and preprocessed; (2) To establish the functional connection, it is necessary to obtain the time series of brain activities in different regions; (3) According to these sequences, aggregation measurement is used to calculate the correlation of these sequences, so that the brain network is represented as a correlation matrix; (4) The consistency threshold method is applied to the matrix (30% of the connections are reserved) to retain the most significant part of the features so that the connection strength in different brain regions can be visually expressed; (5) Finally, the graph theory features are calculated and analyzed.

Before calculating PLI, the analytic signal based on the Hilbert transform is used to determine the instantaneous phase, to calculate the phase synchronization. The calculation formula of PLI is (Stam et al., 2007):

$$PLI_{xy}(f) = |< sign(\phi_x(f) - \phi_y(f)) >| \quad (1)$$

Where <> represents the expected value, $\emptyset_x(f) - \emptyset_y(f)$ represents the phase synchronization of x and y channels/brain region signals at f frequency. The value range of PLI is [0,1], where 1 represents complete phase synchronization and 0 represents no phase synchronization.

2.6. Graph theory analysis of complex brain network

Graph theory is a method that can be applied to brain networks. It can describe the topological structure of complex networks and the changes in different network metrics in networks. The diagram is composed of a group of nodes (electrode array) and their connections (edges). For the quantification of graph topology, there are many measures. In this study, the following indicators were selected to conduct in-depth research on the constructed functional brain network.

2.6.1. Node degree centrality (*DC*)

DC is the most direct metric to characterize node centrality in network analysis. The calculation formula for the degree centrality of a node is as follows (Boccaletti et al., 2006):

$$DC_i = \frac{k_i}{N-1} \quad (2)$$

Where, k_i represents the number of existing edges connected to node i, and $N-1$ represents the number of edges connected to node i and other nodes.

2.6.2. Node betweenness centrality (*BC*)

The intermediate number can reflect the importance of a node or edge in the network. It is the number of shortest paths through

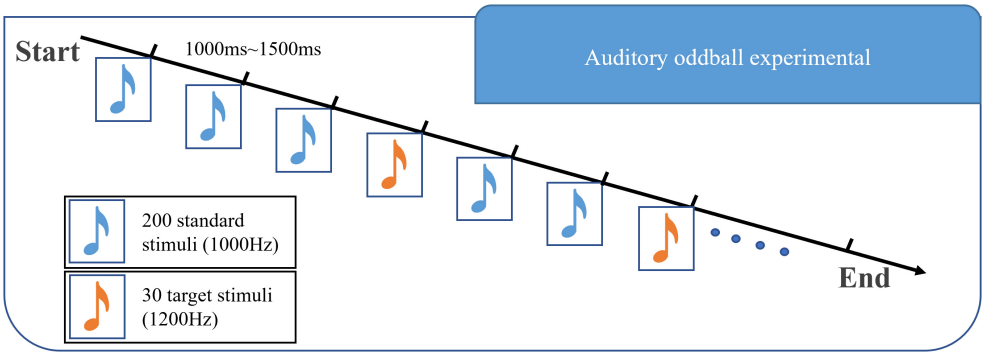

FIGURE 2
Diagram of the experimental paradigm in this paper. This experimental paradigm includes two kinds of stimuli: 1,000 Hz majority stimulus and 1,200 Hz target stimulus. The stimuli are arranged in a pseudo-random manner, with an interval of 1,000–1,500 ms between each stimulus.

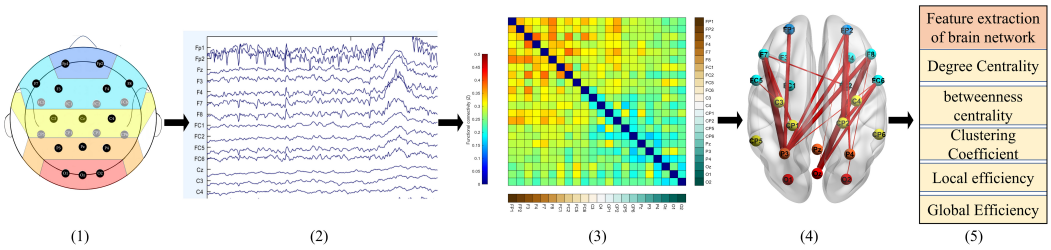

FIGURE 3
Typical construction process of functional brain network. From left to right : **(1)** the electrode of interest; **(2)** the preprocessed EEG; **(3)** the connection matrix calculated by PLI; **(4)** sparsely processed and mapped to the 3D human brain model; **(5)** carry out feature analysis on the sparse brain network.

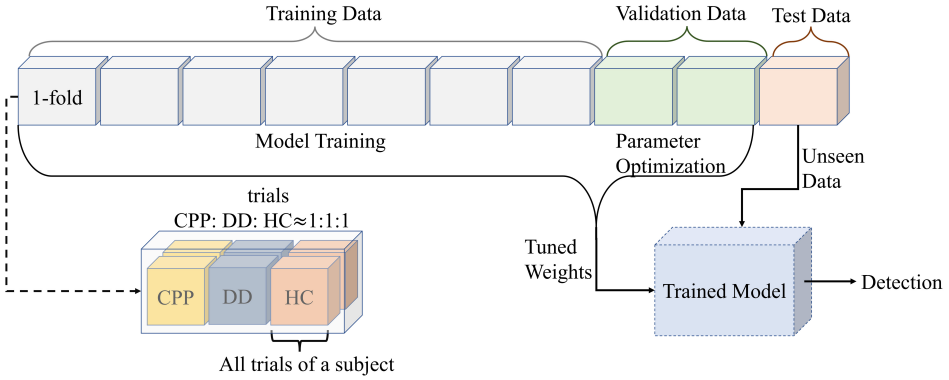

FIGURE 4
The data partition diagram used to create the model. Divide all data into 10-folds. The number of trials in each fold is the same, and the number of CPP, DD, and HC are uniform. At the same time, ensure that all data of each subject only exists in onefold. Divide the 10-folds into test set, validation set and training set according to 1:2:7. The training data is used for the training model, and the validation data is used for the parameter optimization. After adjusting the model weights for both sets of data together, the test set is used for prediction.

a node or edge in the network (Newman, 2005). It is defined as follows:

$$BC(i) = \frac{2\sum_{h<j\in V, h\neq 1, j\neq 1} ghj(i)}{(N-1)(N-2)ghj} \quad (3)$$

Where, g_{hj} is the number of all shortest paths from node $h \in V$ to node$j \in V$, V is the set of all nodes in the network, $g_{hj}(i)$ represents the number of all shortest paths from node $h \in V$ to node $j \in V$ passing through node i.

2.6.3. Clustering coefficient (*CC*)

CC Of brain region node refers to the ratio of the number of edges connected by all nodes adjacent to the node to the maximum possible number of edges connected between these adjacent nodes. *CC* is often used to describe the degree of network integration or node density. The *CC* of node i represents the ratio of the current number of edges between all its neighboring nodes to the maximum number of edges that can exist between all its neighboring nodes. The larger the *CC* is, the closer the local connection of the node in the network is (Freeman, 1978):

$$CC_i = \frac{2t_i}{k_i(k_i-1)} \quad (4)$$

CC_i is the clustering coefficient of node i, t_i is the number of triangles formed by node i, k_i is the degree of node i.

2.6.4. Local efficiency (E_{loc})

E_{loc} measures how to efficiently spread information through the direct adjacent nodes of the node, measuring the local information transmission capacity of the network. The local efficiency of any node i is (Stam et al., 2007):

$$E_{loc}(i) = \frac{1}{N_{G_i}(N_{G_i}-1)} \sum_{j\neq k\in G_i} \frac{1}{l_{j,k}} \quad (5)$$

G_i refers to the subgraph formed by the neighbors of node i, $l_{j,k}$ represents the shortest path length between nodes j, k.

2.6.5. Global efficiency (E_{glob})

Global Efficiency is used to represent the degree of aggregation of nodes in the graph, and is defined as follows (Stam et al., 2007):

$$E_{glob} = \frac{1}{N}\sum_{i=1}^{N} E_i = \frac{1}{N}\sum_{i=1}^{N} \frac{\sum_{j\in N, j\neq i} d_{ij}^{-1}}{N-1} \quad (6)$$

Where E_i represents the efficiency of node i.

2.7. Deep learning algorithm for classification

This paper uses a compact CNN that can be used for various EEG signal classification tasks, including event-related potentials

(ERP) (Prabhu et al., 2020). In addition, this article improves on the CNN and reduces the first AvgPool2d layer kernel size and stride by half, enabling CNN to classify the PLI matrix (22 × 22). Its architecture is shown in **Table 2**. The input of this model is raw EEG data, including channel number, and time sample. To limit the number of trainable parameters, the architecture adopts depth and separable convolution. The initial combination of 2D convolution and depth convolution allows each temporal filter to learn spatial filters (Schirrmeister et al., 2017). At the same time, the number of spatial filters learned from each feature map is controlled by the depth parameter. After each convolution, batch normalization is performed to achieve model stability. In addition, the dropout layer is used to significantly reduce overfitting (Mukhtar et al., 2021). The final multi-category classification layer uses the SoftMax function.

2.8. Model training

When using CNN for training, this study uses 10-fold cross-validation processing method, in which one random fold is used as the test set, the other twofolds are used as the validation set, and the rest as the training set. It also ensures that three types of subjects are evenly distributed in each fold and that the data of each subject only exists in the same fold. At the same time, each dataset (training set, validation set, and test set) is disordered before the training stage (**Figure 4**).

The network is trained using the backpropagation algorithm (Hung and Adeli, 1993) with a batch size (the number of training samples in iteration) of 32. An optimization algorithm, namely adaptive moment estimation (Adam) (Mukhtar et al., 2021) is adopted in this work to update the parameter of the proposed network structure. It was observed it enables the network to converge at a faster rate thereby improving the efficiency of the training process.

TABLE 2 The improved CNN network structure that classifies the PLI matrix, including the layer, the output shape of data, and the number of parameters.

Layer	Output shape	Param
Conv2d	[32, 8, 22, 22]	1,000
BatchNorm2d	[32, 8, 22, 22]	16
Conv2d With Constraint	[32, 16, 1,22]	352
BatchNorm2d	[32, 16, 1, 22]	32
ELU	[32, 16, 1, 22]	0
AvgPool2d	[32, 16, 1, 11]	0
Dropout	[32, 16, 1, 11]	0
Conv2d	[32, 16, 1, 12]	352
Conv2d	[32, 16, 1, 12]	256
BatchNorm2d	[32, 16, 1, 12]	32
ELU	[32, 16, 1, 12]	0
AvgPool2d	[32, 16, 1, 1]	0
Dropout	[32, 16, 1, 1]	0
Conv2d	[32, 3, 1, 1]	51
Log SoftMax	[32, 3, 1, 1]	0

The following equation is used to update the 1st-moment estimate (Kingma and Ba, 2014). All operations on vectors are element by element.

$$m_t = \beta_1 m_{t-1} + (1-\beta_1)\left[\frac{\partial c}{\partial \theta}\right]_t \tag{7}$$

TABLE 3 One-Way ANOVA analysis of the mean values of brain networks in three groups of people (95% confidence interval).

Frequency band	Sum of squares	Mean square	F	P
Wide band	0.044	0.22	57.617	< 0.0001
Delta	0.008	0.004	7.670	0.001
Theta	0.027	0.014	74.315	< 0.0001
Alpha	3.984	1.992	195.245	< 0.0001
Beta	< 0.0001	< 0.0001	1.560	0.218
Gamma	0.001	< 0.0001	7.662	0.001

TABLE 4 Significant *P*-Values for *post-hoc* comparisons based on Tukey's method of ANOVA.

Frequency band	CPP vs. DD	CPP vs. HC	DD vs. HC
Wide band	0.995	< 0.0001	< 0.0001
Delta	0.025	0.500	0.001
Theta	< 0.0001	< 0.0001	< 0.0001
Alpha	< 0.0001	0.601	< 0.0001
Gamma	0.079	0.001	0.211

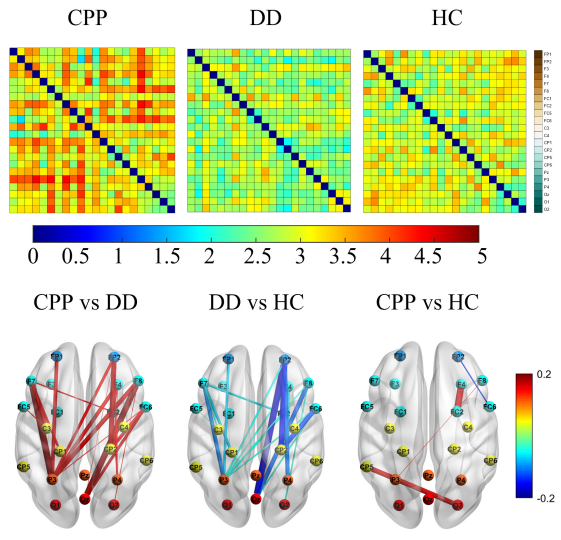

FIGURE 5
The above figure shows θ the functional connection matrix of band CPP, DD, and HC have a value range of [0, 5], and its electrode channels from top to bottom are FP1, FP2, F3, F4, F7, F8, FC1, FC2, FC5, FC6, C3, C4, CP1, CP2, CP5, CP6, Pz, P3, P4, Oz, O1, and O2. The following figure shows that the matrix values are subtracted (from left to right are CPP-DD, DD-HC, CPP-HC) and the most significant difference characteristics are retained by 30%, and its value range is [−0.2, 0.2].

Where m, t, c, θ_t and $\frac{\partial c}{\partial \theta}$ are defined as the 1st-moment vector, timestep, cost function, resulting parameters (weights), and gradient, respectively. The parameters β_1 and β_2 represent the exponential decay rates which are chosen to be 0.9 and 0.999, respectively, (Kingma and Ba, 2014).

The following equation is used to update the 2nd-moment estimate (Kingma and Ba, 2014).

$$v_t = \beta_2 v_{t-1} + (1-\beta_2)\left[\frac{\partial c}{\partial \theta}\right]_t^2 \quad (8)$$

The following equations are used to compute the 1st and 2nd-moment estimates, respectively, (Kingma and Ba, 2014).

$$\hat{m}_t = \frac{\hat{m}_t}{1-\beta_1^t} \quad (9)$$

$$\hat{v}_t = \frac{\hat{m}_t}{1-\beta_2^t} \quad (10)$$

In addition, the following equation is used to update the weights of links connecting the layers (Kingma and Ba, 2014).

$$\theta_t = \left[1 - \frac{\alpha\lambda(1-\beta_1)}{\sqrt{\hat{\upsilon}_t}+\epsilon}\right]\theta_{t-1} - \frac{\alpha\hat{m}_t}{\sqrt{\hat{\upsilon}_t}+\epsilon} \quad (11)$$

Where α and ϵ denote the learning rate and numerical value and are set at 1×10^{-4} and10^{-8}, respectively, in this work. The variable λ, known as the regularization parameter, is also one of the essential parameters during training to prevent data overfitting. It is tuned to 0.2 in this work.

To avoid overfitting and improve the generalization, the dropout (Srivastava et al., 2014) technique is applied to the fully-connected layers 6 and 12. During training for each mini-batch, some of the neurons from these layers are selected randomly and dropped. This forces the model to learn from a subset of input features and not the entire input features. The value is set to 0.5, i.e., the probability of a neuron being retained during training is 50% and the probability of a neuron being rejected is 50%.

In this paper, the negative log-likelihood loss function is used to deal with multi-classification problems (de Boer et al., 2005). The input is the logarithmic probability value. For the batch data $D(x, y)$ containing N samples, x is the output of the neural network and is normalized and logarithm zed. y is the category label corresponding to the sample, and each sample may be one of C categories.

l_n is the loss corresponding to the nth sample, the value range is [0, C-1]:

$$l_n = -w_{y_n} x_{n,yn} \quad (12)$$

w is used for sample imbalance between multiple categories:

$$w_c = weight[c] \cdot 1\{c \neq ignore\_index\} \quad (13)$$

The default value of reduction is mean, and the corresponding $l(x, y)$ is:

$$1\,(x, y) = \sum_{n=1}^{N} \frac{1}{\sum_{n=1}^{N} w_{y_n}} l_n \quad (14)$$

2.9. Technology validation

F1 Score is an indicator used to measure the accuracy of the two-class model in statistics. It can be seen as a weighted average of the model's accuracy and recall. Its value range is [0, 1]. The larger the value is, the better the model is.

$$F1 - score = \frac{2(recall * precision)}{recall + precision} \quad (15)$$

In multi-classification problems, Macro-F1 is usually used (Supratak et al., 2017).

$$macro - F1 = \frac{1}{n}\sum_{i=1}^{n} F1 - score_i \quad (16)$$

Where n is the number of categories and i is the number of categories.

2.10. Statistical analysis

SPSS software was used for statistical analysis. One-way analysis of variance analysis (ANOVA) was used for the comparative analysis of brain networks of three groups, where group category was used as a factor, and the average value of each channel after the superposition of the brain network connection matrix was used as a dependent variable. The Tukey method was used as a *post hoc* analysis for testing differences between groups.

3. Results

3.1. Functional connectivity

One-way ANOVA found that the brain networks of the three groups are statistically different except for the Beta band (**Table 3**). Further *post hoc* analysis based on the Tukey method (**Table 4**) shows that in the Gamma band there was difference in network characteristics between CPP and HC subjects but not between CPP and DD or DD and HC. In Delta and Alpha bands, a significant difference was present between CPP and DD, DD and HC, but not between CPP and HC. In the Theta frequency band only, the *P*-values between groups were all less than 0.05, indicating that different groups possess independent brain network characteristics in this frequency band.

To further explore the specific differences in brain networks among the three groups, we carried out a functional connectivity matrix analysis of CPP, DD, and HC and compared the differences after subtraction and the consistency threshold method. See **Figure 5** for Theta band results (see **Supplementary material** for results in other bands). The results show that in the CPP group, the Theta frequency band connection between parieto-occipital electrodes (P3, O2) and prefrontal electrodes (FP1, FP2) is significantly enhanced (the connection strength of 4–5); in the HC group, the connections between electrode Cp5 and O2, electrode FC2 and F4 are slightly enhanced (the connection strength of 3–4); in DD group, the connection strength is the weakest (the connection strength of 1–3). Further difference comparison shows that the CPP group has significantly increased connectivity between the prefrontal area and the posterior parietal area compared with the DD group, while the difference between CPP and HC groups is mainly reflected in the stronger connectivity of CP5-O2 and

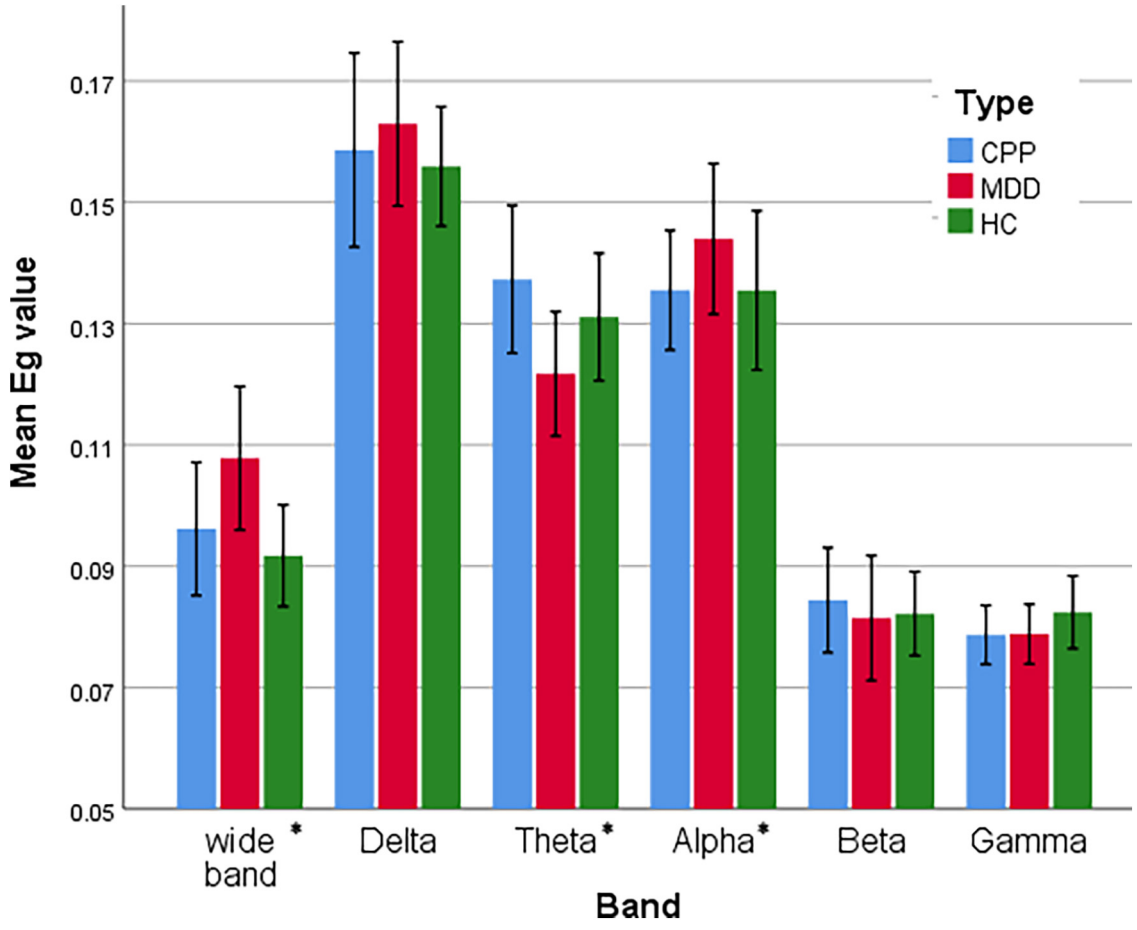

FIGURE 6
Statistical comparison chart of overall efficiency of three groups of people in six frequency bands. The error interval takes the value of 95%. *$P < 0.05$.

F4-FC2; Compared to HC group, the connectivity strength of brain network in DD subjects is inhibited, mainly in the form of weakened connectivity between the parieto-occipital area and the prefrontal area.

3.2. Complex brain network

We further analyzed and compared the global feature revealed by E_{glob}, as shown in Figure 6. The E_{glob} of DD subjects in Delta and Alpha bands is higher than the other two groups of subjects, while it is inhibited in the Theta band. This is also verified by the classification results of the PLI matrix using CNN (see Section "3.3. Classification accuracy of different frequency bands"). The difference between CPP and HC subjects is mainly reflected in the significant enhancement of the Theta band.

At the node level, *DC*, *BC*, E_{loc}, and *CC* of the three groups in the Theta band is also different, as shown in Figure 7. The *DC* intensity of CPP subjects is higher in the right frontal and left parieto-occipital region than in the other two groups. This result is consistent with the aforementioned trend of brain network connection intensity in the Theta band. In the distribution of *BC*, the intensity in the central area of CPP subjects is lower than that of the other two groups, and the intensity of *BC* in the prefrontal and temporal areas of CPP and DD is lower than that of HC subjects. Similarly, the E_{loc} intensity in the central area of CPP subjects is also lower than that of the other two groups, and the overall E_{loc} intensity of DD subjects is lower than that of the other two groups. In the distribution of *CC*, the overall distribution of the three groups is similar, but the left frontal lobe intensity is higher in the CPP and DD groups.

3.3. Classification accuracy of different frequency bands

CNN was first used to classify the EEG of three groups of subjects. Further, this paper used the improved CNN model to classify the PLI matrix of three groups of subjects to verify the above brain network analysis results. After 1,000 training epochs, the loss rate, and verification loss rate of the two classifications began to converge to 0 and 0.8, respectively, while the training accuracy and verification accuracy converged to 1 and 0.3, respectively, which proved that the network structure was stable (Figure 8). Figure 9 shows that both sets of classifications have achieved ideal accuracy in six frequency bands: in the classification of EEG, the Gamma

band has the highest accuracy of 85.01%, followed by the Theta band with 81.37%; in the classification of PLI, the highest frequency band of Theta is 79.64%, followed by Delta and Gamma with 77.81 and 77.47%. The results of Macro-F1 in **Figure 10** show that the classification model of EEG is better than that of PLI. Except for the Beta frequency band, the Macro-F1 evaluation of other frequency bands are above 0.65, and the PLI classification model is also above 0.6 except for the Beta frequency band.

4. Discussion

In this study, the CNN algorithm was used to classify CPP, DD, and HC through EEG activities evoked by the auditory oddball paradigm, and the brain network and complex connectivity of the three groups were investigated. Our main results show that the deep learning approach of CNN exhibits successful classification for all the three groups, with the highest classification accuracy in the Gamma band and the second highest classification accuracy in the Theta band. Brain network analysis reveals a stronger phase-based connection within the frontoparietal network in the Theta band in CPP subjects. The same trend is also reflected in the degree centrality and global efficiency.

The analysis of the characteristics of CPP brain network connectivity in this study reveals that the connectivity of the brain networks in the prefrontal and posterior area of CPP patients is significantly increased in the Theta band. Graph theory analysis shows that CPP patients has increased the overall efficiency and stronger centrality at the node level in the right frontal regions and left parietal occipital regions. Despite the limited spatial resolution of the EEG, it has been found that the area with increased network connectivity in the Theta band characteristic of CPP is highly overlapped with frontoparietal network (FPN). This network is also often referred as the central executive network, whose activity is important for goal-directed cognitive tasks, including working memory, planning, judgment, and decision-making (Kelly et al., 2008; Menon, 2011). Important FPN regions are the dorsolateral prefrontal cortex and the posterior parietal cortex. Previous studies have shown that the increased functional connectivity in the prefrontal cortex is crucial for the chronicity of pain (Baliki et al., 2012; Hashmi et al., 2013; Vachon-Presseau et al., 2016). At the same time, the function of prefrontal cortex is closely related to the perception of chronic pain and its related negative emotions, cognitive changes, and avoidance behaviors (Baliki and Apkarian, 2015; Kragel et al., 2018; May et al., 2019). Theta event-related synchronization (ERS) observed in prefrontal regions during the oddball task is thought to primarily reflect activation of neural networks involved in allocation of attention related to target stimuli (Missonnier et al., 2006). Migraine patients presented an enhanced phase-synchronization in the theta frequency range during auditory attention tasks (Vilà-Balló et al., 2021). Similar to our results, these findings could indicate the presence of a hypersensitivity to auditory stimuli and hyperexcitability in attentional control in CPP patients. Therefore, the neurological profile of CPP patients may be characterized by impaired FPN function, resulting in dysfunctional adaptive strategies for individuals to perceive stimulus (including pain) both cognitively (how the individual feels) and behaviorally (what the individual does).

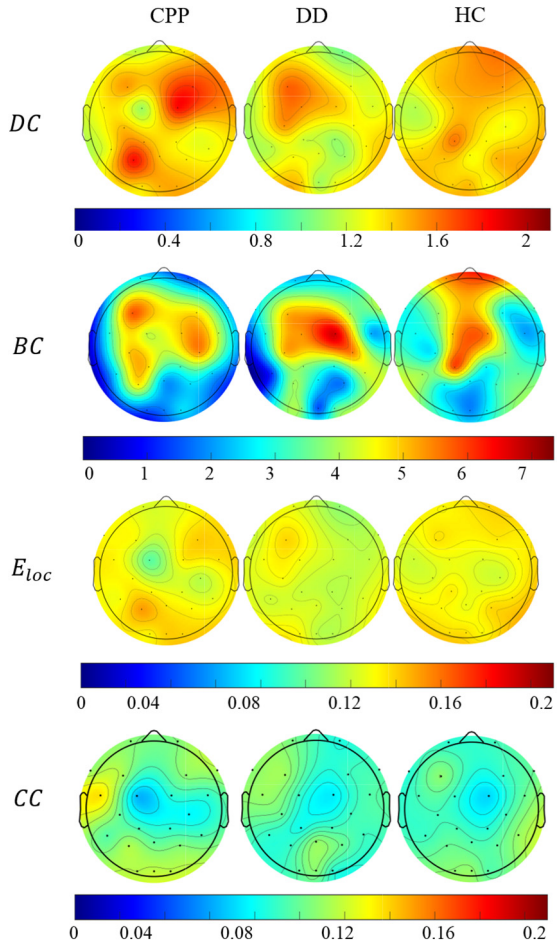

FIGURE 7
The average distribution of degree centrality, median centrality, local efficiency, and clustering coefficient of the three groups of people in Theta band.

EEG has been used to classify depression correctly with great accuracy in many studies (de Aguiar Neto and Rosa, 2019). Many previous studies analyzed the oscillatory power spectrum at rest. We first investigate neural response induced by oddball task in CPP and DD patients. Our deep learning results show that the classification accuracy of EEG activities in the theta, alpha, beta and gamma bands can reach more than 80% during the oddball task for the three groups, with the best classification accuracy in the gamma band. Furthermore, the classification model of EEG is better than that of connectivity (i.e., PLI). Neural activity evoked by deviant stimuli in oddball paradigm has been related to attention and memory updating for discrete events. A significant increase in the relative power of theta can be observed in healthy subjects, while a decrease in the higher frequency bands (Gomez-Pilar et al., 2016). Theta oscillatory response induced by oddball paradigm is restricted to the bilateral frontal cortex, particularly in the dorsolateral, and medial prefrontal areas, while 30–60 Hz bands can be visualized over the bilateral central region (Ishii et al., 2009). Theta oscillation is considered to be closely related to cognitive functions, such as attention and memory processing (Buzsáki, 2002;

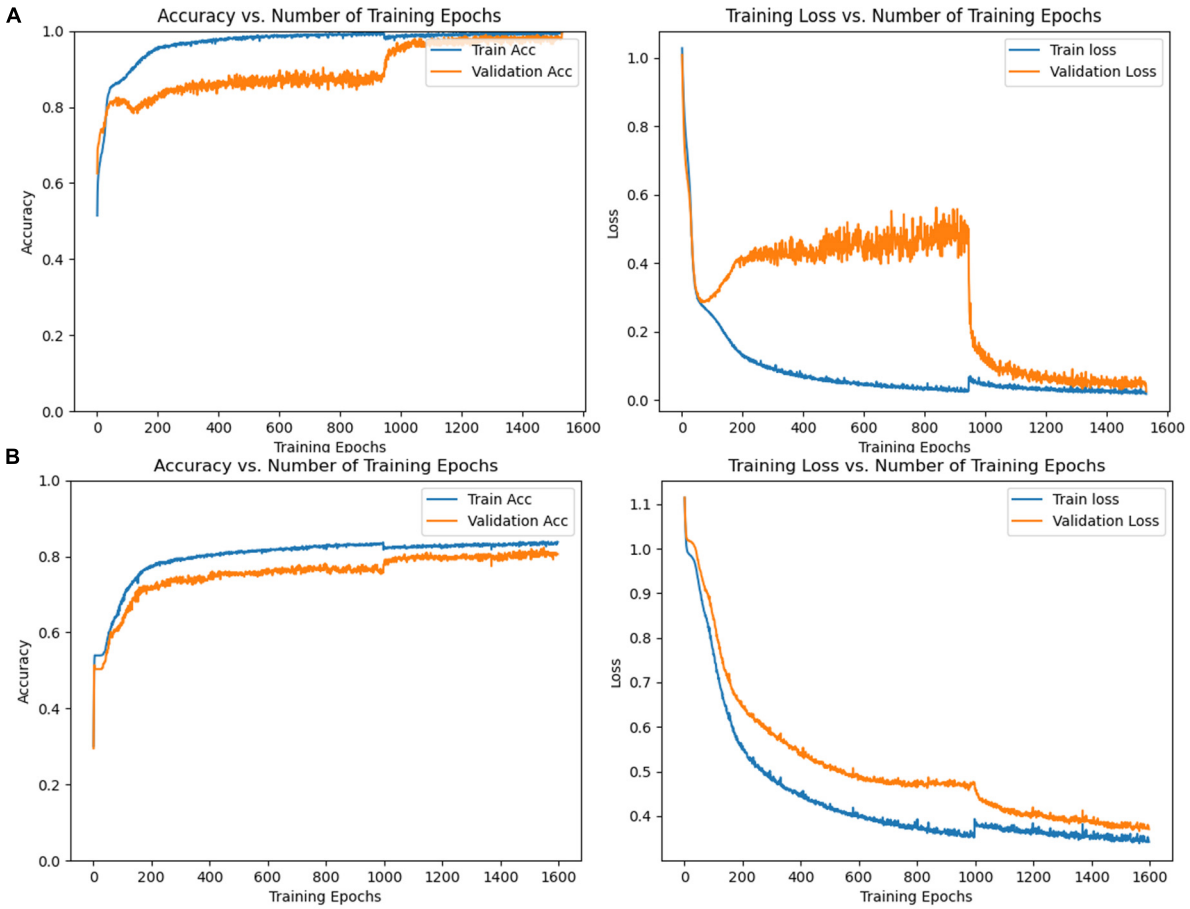

FIGURE 8
(A) Accuracy and loss rate change curve of training set and validation set trained with EEG, **(B)** accuracy and loss rate change curve of the training set and validation set trained with PLI matrix.

Wang and Ding, 2011). Gamma oscillation may represent the basic characteristics of neuron signal and communication, which seems to be particularly relevant to the local processing and feedforward communication of current important stimuli (Donner and Siegel, 2011; Fries, 2015; Ploner et al., 2017). Interestingly, resting-state Gamma in prefrontal cortex, on one hand, has been considered as a reliable marker for major depression, as this brain region is heavily implicated in mood and emotional regulation (Fitzgerald and Watson, 2018). On the other hand, a latest systematic review reports Gamma oscillations in the prefrontal cortex as a promising biomarker for tonic and chronic pains (Li et al., 2023). Considering resting-state activities could impact task-induced activities, the results we found for optimal classification accuracy in the gamma band may be interpretable.

Our findings reveal that significant difference in brain network connectivity (i.e., PLI) is in Theta band, while the second highest accuracy in EEG classification is achieved in the Theta band, and the highest classification accuracy is in the Gamma band. This could be explained by following reasons. First, the classification accuracy of PLI matrix is generally lower than that of EEG. This difference is due to the loss of characteristic information such as the time domain and frequency domains when using PLI to calculate brain network connection matrix. Second, it has been observed that there is significant phase synchronization between frontal and posterior electrodes during auditory oddball task in the Gamma and Theta bands, which has been interpreted as a functional connectivity among cortical regions devoted to the task execution (Choi et al., 2010). Given the vital role of Gamma activity in the neural communications between different brain structures and networks (Fries, 2015), our result could be related to this Theta-Gamma synchronization. Future analysis on Theta-Gamma synchronization may further explore the underlying neural mechanisms.

The current deep learning method shows that it is of great significance to apply CNN to EEG data of auditory stimulation state to distinguish among CPP, DD, and HC subjects with an accuracy rate of more than 80%. First, it suggests that the EEG of each frequency band may play a role in the pathophysiology of CPP. Second, the current approach may be a step toward an EEG-based auxiliary diagnosis of CPP. Third, the abnormal pattern of EEG activity in CPP patients may represent a potential new therapeutic target, such as intervention through non-invasive brain stimulation technology or neural feedback methods. In particular, the emerging transcranial magnetic stimulation can modulate the oscillation and synchronization of neurons at specific frequencies, so it may be a promising method for pain modulation (Polanía et al., 2018).

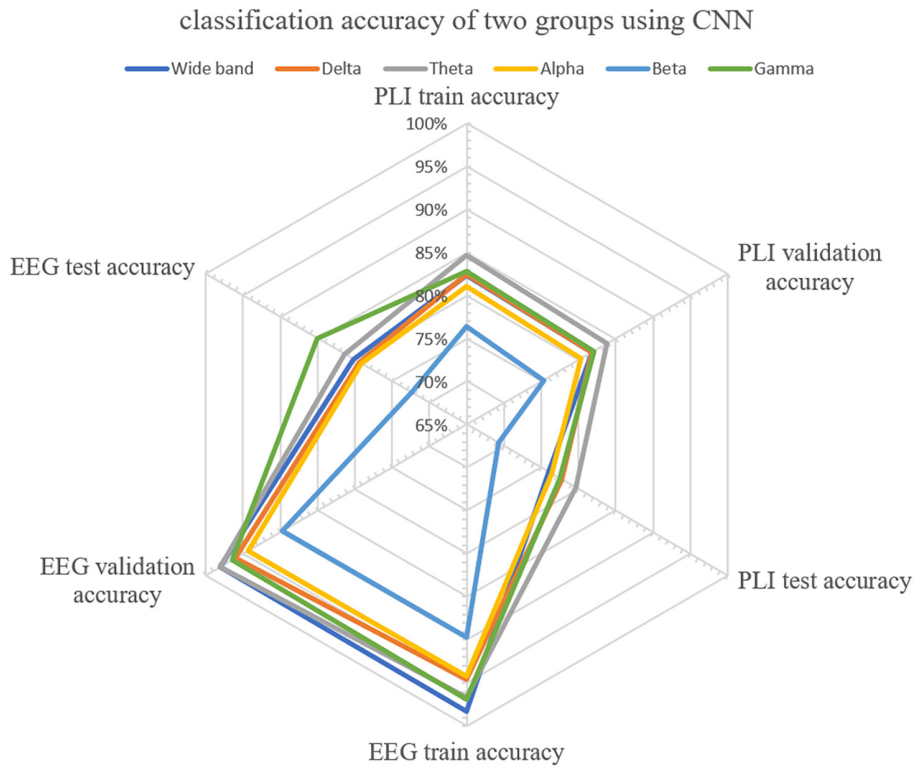

FIGURE 9
Accuracy distribution of classification of EEG and PLI matrices of three groups of people using CNN in six frequency bands.

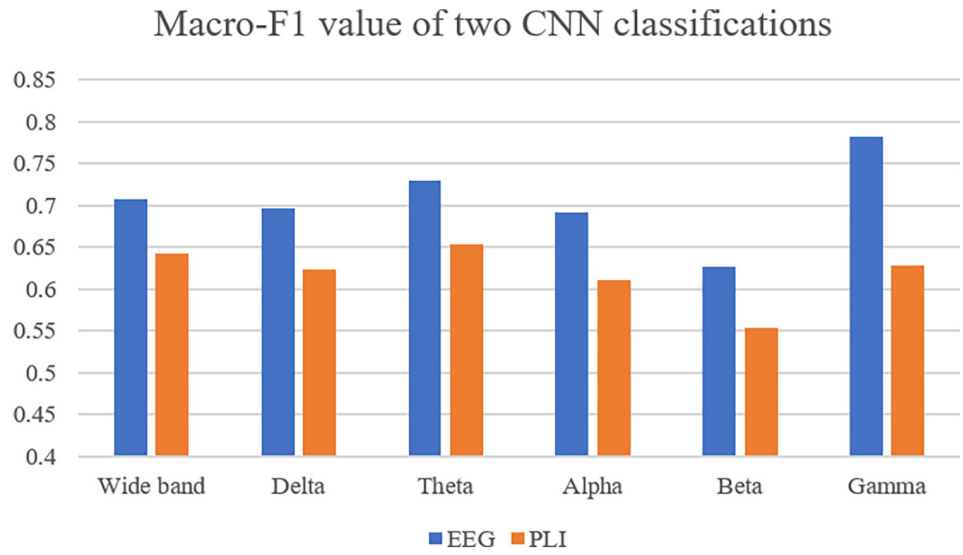

FIGURE 10
Use Macro-F1 to evaluate the model obtained from two kinds of data in six frequency bands.

5. Conclusion

In conclusion, our results indicate that there are significant differences among CPP, DD, and HC subjects in the characteristics of auditory oddball-induced EEG activities, suggesting that CPP has its unique neuroelectrophysiological manifestations. The connectivity of theta band in FPN-related brain regions is significantly enhanced in CPP patients, thus contributing to better understanding of the brain mechanism of CPP. Our research provides a novel approach for the objective assessment of CPP. The non-invasive brain stimulation and neural feedback approaches targeting Theta and Gamma oscillation and FPN networks may be a potential treatment scheme.

Data availability statement

The raw data supporting the conclusions of this article will be made available by the authors, without undue reservation.

Ethics statement

The studies involving human participants were reviewed and approved by the experimental procedures involving human subjects described in this paper were approved by the Shanghai Changhai Hospital Review Board. The patients/participants provided their written informed consent to participate in this study.

Author contributions

YL: software, validation, writing – original draft, and visualization. BY: conceptualization, methodology, resources, project administration, and funding acquisition. ZW: resources, data curation, and project administration. RH and XL: data curation. XB: conceptualization, investigation, and project administration. SZ: methodology, validation, writing – review and editing, and funding acquisition. All authors contributed to the article and approved the submitted version.

Funding

The project is supported by the National Key Research and Development Program of China (Nos. 2022YFC3602700 and 2022YFC3602703), National Natural Science Foundation of China (No. 81801093), Clinical Research Foundation of Shanghai Municipal Health Commission (No. 20204Y0417), Shanghai Major Science and Technology Project (No. 2021SHZDZX), National Defense Basic Scientific Research Program of China (Defense Industrial Technology Development Program) (grant No. JCKY2021413B005), and Shanghai Industrial Collaborative Technology Innovation Project (No. XTCX-KJ-2022-2-14).

Conflict of interest

BY was employed by Shanghai Shaonao Sensing Technology Ltd.

The remaining authors declare that the research was conducted in the absence of any commercial or financial relationships that could be construed as a potential conflict of interest.

Publisher's note

All claims expressed in this article are solely those of the authors and do not necessarily represent those of their affiliated organizations, or those of the publisher, the editors and the reviewers. Any product that may be evaluated in this article, or claim that may be made by its manufacturer, is not guaranteed or endorsed by the publisher.

Supplementary material

The Supplementary Material for this article can be found online at: https://www.frontiersin.org/articles/10.3389/fnins.2023.1133834/full#supplementary-material

References

Acharya, U. R., Oh, S. L., Hagiwara, Y., Tan, J. H., and Adeli, H. (2018). Deep convolutional neural network for the automated detection and diagnosis of seizure using EEG signals. *Comput. Biol. Med.* 100, 270–278. doi: 10.1016/j.compbiomed.2017.09.017

American Psychiatric Association (2013). *Diagnostic and statistical manual of mental disorders. DSM-5-TR*. Virginia, VA: American Psychiatric Association.

Baliki, M. N., and Apkarian, A. V. (2015). Nociception, pain, negative moods, and behavior selection. *Neuron* 87, 474–491. doi: 10.1016/j.neuron.2015.06.005

Baliki, M. N., Petre, B., Torbey, S., Herrmann, K. M., Huang, L., Schnitzer, T. J., et al. (2012). Corticostriatal functional connectivity predicts transition to chronic back pain. *Nat. Neurosci.* 15, 1117–1119. doi: 10.1038/nn.3153

Boccaletti, S., Latora, V., Moreno, Y., Chavez, M., and Hwang, D. (2006). Complex networks: Structure and dynamics. *Phys. Rep.* 424, 175–308. doi: 10.1016/j.physrep.2005.10.009

Boloukian, B., and Safi-Esfahani, F. (2020). Recognition of words from brain-generated signals of speech-impaired people: Application of autoencoders as a neural Turing machine controller in deep neural networks. *Neural Netw.* 121, 186–207. doi: 10.1016/j.neunet.2019.07.012

Bosch-Bayard, J., Girini, K., Biscay, R. J., Valdes-Sosa, P., Evans, A. C., and Chiarenza, G. A. (2020). Resting EEG effective connectivity at the sources in developmental dysphonetic dyslexia. Differences with non-specific reading delay. *Int. J. Psychophysiol.* 153, 135–147. doi: 10.1016/j.ijpsycho.2020.04.021

Bullmore, E., and Sporns, O. (2012). The economy of brain network organization. *Nat. Rev. Neurosci.* 13, 336–349. doi: 10.1038/nrn3214

Burke, N. N., Finn, D. P., and Roche, M. (2015). Neuroinflammatory mechanisms linking pain and depression. *Mod. Trends Pharmacopsychiatry* 30, 36–50. doi: 10.1159/000435931

Buzsáki, G. (2002). Theta oscillations in the hippocampus. *Neuron* 33, 325–340. doi: 10.1016/S0896-6273(02)00586-X

Choi, J. W., Jung, K.-Y., Kim, C. H., and Kim, K. H. (2010). Changes in gamma- and theta-band phase synchronization patterns due to the difficulty of auditory oddball task. *Neurosci. Lett.* 468, 156–160. doi: 10.1016/j.neulet.2009.10.088

de Aguiar Neto, F. S., and Rosa, J. L. G. (2019). Depression biomarkers using non-invasive EEG: A review. *Neurosci. Biobehav. Rev.* 105, 83–93. doi: 10.1016/j.neubiorev.2019.07.021

de Boer, P.-T., Kroese, D. P., Mannor, S., and Rubinstein, R. Y. (2005). A tutorial on the cross-entropy method. *Ann. Oper. Res.* 134, 19–67. doi: 10.1007/s10479-005-5724-z

Delorme, A., and Makeig, S. (2004). EEGLAB: An open source toolbox for analysis of single-trial EEG dynamics including independent component analysis. *J. Neurosci. Methods* 134, 9–21. doi: 10.1016/j.jneumeth.2003.10.009

Donner, T. H., and Siegel, M. (2011). A framework for local cortical oscillation patterns. *Trends Cogn. Sci.* 15, 191–199. doi: 10.1016/j.tics.2011.03.007

Dworkin, R. H., Turk, D. C., Revicki, D. A., Harding, G., Coyne, K. S., Peirce-Sandner, S., et al. (2009). Development and initial validation of an expanded and revised version of the short-form McGill pain questionnaire (SF-MPQ-2). *Pain* 144, 35–42. doi: 10.1016/j.pain.2009.02.007

Farahani, F. V., Karwowski, W., and Lighthall, N. R. (2019). Application of graph theory for identifying connectivity patterns in human brain networks: A systematic review. *Front. Neurosci.* 13:585. doi: 10.3389/fnins.2019.00585

Fitzgerald, P. J., and Watson, B. O. (2018). Gamma oscillations as a biomarker for major depression: An emerging topic. *Transl. Psychiatry* 8:177. doi: 10.1038/s41398-018-0239-y

Freeman, L. C. (1978). Centrality in social networks conceptual clarification. *Soc. Netw.* 1, 215–239. doi: 10.1016/0378-8733(78)90021-7

Fries, P. (2015). Rhythms for cognition: Communication through coherence. *Neuron* 88, 220–235. doi: 10.1016/j.neuron.2015.09.034

Gomez-Pilar, J., Martín-Santiago, O., Suazo, V., de Azua, S. R., Haidar, M. K., Gallardo, R., et al. (2016). Association between electroencephalographic modulation, psychotic-like experiences and cognitive performance in the general population: EEG modulation, cognition and PLE. *Psychiatry Clin. Neurosci.* 70, 286–294. doi: 10.1111/pcn.12390

Harth, M., and Nielson, W. R. (2019). Pain and affective distress in arthritis: Relationship to immunity and inflammation. *Exp. Rev. Clin. Immunol.* 15, 541–552. doi: 10.1080/1744666X.2019.1573675

Hashmi, J. A., Baliki, M. N., Huang, L., Baria, A. T., Torbey, S., Hermann, K. M., et al. (2013). Shape shifting pain: Chronification of back pain shifts brain representation from nociceptive to emotional circuits. *Brain* 136, 2751–2768. doi: 10.1093/brain/awt211

Hung, S. L., and Adeli, H. (1993). Parallel backpropagation learning algorithms on CRAY Y-MP8/864 supercomputer. *Neurocomputing* 5, 287–302. doi: 10.1016/0925-2312(93)90042-2

Ishii, R., Canuet, L., Herdman, A., Gunji, A., Iwase, M., Takahashi, H., et al. (2009). Cortical oscillatory power changes during auditory oddball task revealed by spatially filtered magnetoencephalography. *Clin. Neurophysiol.* 120, 497–504. doi: 10.1016/j.clinph.2008.11.023

Isreal, J. B., Wickens, C. D., Chesney, G. L., and Donchin, E. (1980). The event-related brain potential as an index of display-monitoring workload. *Hum. Factors* 22, 211–224. doi: 10.1177/001872088002200210

Jeon, Y.-W., and Polich, J. (2003). Meta-analysis of P300 and schizophrenia: Patients, paradigms, and practical implications. *Psychophysiology* 40, 684–701. doi: 10.1111/1469-8986.00070

Jesulola, E., Sharpley, C. F., Bitsika, V., Agnew, L. L., and Wilson, P. (2015). Frontal alpha asymmetry as a pathway to behavioural withdrawal in depression: Research findings and issues. *Behav. Brain Res.* 292, 56–67. doi: 10.1016/j.bbr.2015.05.058

Johnson, R. (1986). For distinguished early career contribution to psychophysiology: Award address, 1985. A triarchic model of P300 amplitude. *Psychophysiology* 23, 367–384. doi: 10.1111/j.1469-8986.1986.tb00649.x

Kelly, A. M. C., Uddin, L. Q., Biswal, B. B., Castellanos, F. X., and Milham, M. P. (2008). Competition between functional brain networks mediates behavioral variability. *Neuroimage* 39, 527–537. doi: 10.1016/j.neuroimage.2007.08.008

Kingma, D. P., and Ba, J. (2014). Adam: A method for stochastic optimization. *arXiv* [Preprint]. doi: 10.48550/ARXIV.1412.6980

Kragel, P. A., Kano, M., Van Oudenhove, L., Ly, H. G., Dupont, P., Rubio, A., et al. (2018). Generalizable representations of pain, cognitive control, and negative emotion in medial frontal cortex. *Nat. Neurosci.* 21, 283–289. doi: 10.1038/s41593-017-0051-7

Lenoir, D., Cagnie, B., Verhelst, H., and De Pauw, R. (2021). Graph measure based connectivity in chronic pain patients: A systematic review. *Pain Physician* 24, E1037–E1058.

Li, Y., Cao, D., Wei, L., Tang, Y., and Wang, J. (2015). Abnormal functional connectivity of EEG gamma band in patients with depression during emotional face processing. *Clin. Neurophysiol.* 126, 2078–2089. doi: 10.1016/j.clinph.2014.12.026

Li, Z., Zhang, L., Zeng, Y., Zhao, Q., and Hu, L. (2023). Gamma-band oscillations of pain and nociception: A systematic review and meta-analysis of human and rodent studies. *Neurosci. Biobehav. Rev.* 146:105062. doi: 10.1016/j.neubiorev.2023.105062

May, E. S., Nickel, M. M., Ta Dinh, S., Tiemann, L., Heitmann, H., Voth, I., et al. (2019). Prefrontal gamma oscillations reflect ongoing pain intensity in chronic back pain patients. *Hum. Brain. Mapp.* 40, 293–305. doi: 10.1002/hbm.24373

Menon, V. (2011). Large-scale brain networks and psychopathology: A unifying triple network model. *Trends Cogn. Sci.* 15, 483–506. doi: 10.1016/j.tics.2011.08.003

Missonnier, P., Deiber, M.-P., Gold, G., Millet, P., Gex-Fabry Pun, M., Fazio-Costa, L., et al. (2006). Frontal theta event-related synchronization: Comparison of directed attention and working memory load effects. *J. Neural Transm.* 113, 1477–1486. doi: 10.1007/s00702-005-0443-9

Mouraux, A., and Iannetti, G. D. (2018). The search for pain biomarkers in the human brain. *Brain* 141, 3290–3307. doi: 10.1093/brain/awy281

Mukhtar, H., Qaisar, S. M., and Zaguia, A. (2021). Deep convolutional neural network regularization for alcoholism detection using EEG signals. *Sensors* 21:5456. doi: 10.3390/s21165456

Murphy, P. R., O'Connell, R. G., O'Sullivan, M., Robertson, I. H., and Balsters, J. H. (2014). Pupil diameter covaries with BOLD activity in human locus coeruleus. *Hum. Brain Mapp.* 35, 4140–4154. doi: 10.1002/hbm.22466

Newman, M. E. J. (2005). A measure of betweenness centrality based on random walks. *Soc. Netw.* 27, 39–54. doi: 10.1016/j.socnet.2004.11.009

Nicholas, M., Vlaeyen, J., Rief, W., Barke, A., Aziz, Q., Benoliel, R., et al. (2019). The IASP classification of chronic pain for ICD-11: Chronic primary pain. *Pain* 160, 28–37. doi: 10.1097/j.pain.0000000000001390

Palmiero, M., and Piccardi, L. (2017). Frontal EEG asymmetry of mood: A mini-review. *Front. Behav. Neurosci.* 11:224. doi: 10.3389/fnbeh.2017.00224

Pigoni, A., Delvecchio, G., Madonna, D., Bressi, C., Soares, J., and Brambilla, P. (2019). Can machine learning help us in dealing with treatment resistant depression? A review. *J. Affect. Disord.* 259, 21–26. doi: 10.1016/j.jad.2019.08.009

Ploner, M., and May, E. S. (2018). Electroencephalography and magnetoencephalography in pain research—current state and future perspectives. *Pain* 159, 206–211. doi: 10.1097/j.pain.0000000000001087

Ploner, M., Sorg, C., and Gross, J. (2017). Brain rhythms of pain. *Trends Cogn. Sci.* 21, 100–110. doi: 10.1016/j.tics.2016.12.001

Polanía, R., Nitsche, M. A., and Ruff, C. C. (2018). Studying and modifying brain function with non-invasive brain stimulation. *Nat. Neurosci.* 21, 174–187. doi: 10.1038/s41593-017-0054-4

Polich, J. (1986). P300 development from auditory stimuli. *Psychophysiology* 23, 590–597. doi: 10.1111/j.1469-8986.1986.tb00677.x

Prabhu, S., Murugan, G., Cary, M., Arulperumjothi, M., and Liu, J.-B. (2020). On certain distance and degree based topological indices of Zeolite LTA frameworks. *Mater. Res. Express* 7:55006. doi: 10.1088/2053-1591/ab8b18

Rustamov, N., Sharma, L., Chiang, S. N., Burk, C., Haroutounian, S., and Leuthardt, E. C. (2021). Spatial and frequency-specific electrophysiological signatures of tonic pain recovery in humans. *Neuroscience* 465, 23–37. doi: 10.1016/j.neuroscience.2021.04.008

Schirrmeister, R. T., Springenberg, J. T., Fiederer, L. D. J., Glasstetter, M., Eggensperger, K., Tangermann, M., et al. (2017). Deep learning with convolutional neural networks for EEG decoding and visualization: Convolutional neural networks in EEG analysis. *Hum. Brain Mapp.* 38, 5391–5420. doi: 10.1002/hbm.23730

Serbic, D., Evangeli, M., Probyn, K., and Pincus, T. (2022). Health-related guilt in chronic primary pain: A systematic review of evidence. *Br. J. Health Psychol.* 27, 67–95. doi: 10.1111/bjhp.12529

Sporns, O. (2013). Network attributes for segregation and integration in the human brain. *Curr. Opin. Neurobiol.* 23, 162–171. doi: 10.1016/j.conb.2012.11.015

Srivastava, N., Hinton, G., Krizhevsky, A., Sutskever, I., and Salakhutdinov, R. (2014). Dropout: A simple way to prevent neural networks from overfitting. *J. Mach. Learn. Res.* 15, 1929–1958.

Stam, C. J., Nolte, G., and Daffertshofer, A. (2007). Phase lag index: Assessment of functional connectivity from multi channel EEG and MEG with diminished bias from common sources. *Hum. Brain Mapp.* 28, 1178–1193. doi: 10.1002/hbm.20346

Steinmann, S., Meier, J., Nolte, G., Engel, A. K., Leicht, G., and Mulert, C. (2018). The callosal relay model of interhemispheric communication: New evidence from effective connectivity analysis. *Brain Topogr.* 31, 218–226. doi: 10.1007/s10548-017-0583-x

Supratak, A., Dong, H., Wu, C., and Guo, Y. (2017). DeepSleepNet: A model for automatic sleep stage scoring based on raw single-channel EEG. *IEEE Trans. Neural Syst. Rehabil. Eng.* 25, 1998–2008. doi: 10.1109/TNSRE.2017.2721116

Ta Dinh, S., Nickel, M. M., Tiemann, L., May, E. S., Heitmann, H., Hohn, V. D., et al. (2019). Brain dysfunction in chronic pain patients assessed by resting-state electroencephalography. *Pain* 160, 2751–2765. doi: 10.1097/j.pain.0000000000001666

Tao, Z.-Y., Wang, P.-X., Wei, S.-Q., Traub, R. J., Li, J.-F., and Cao, D.-Y. (2019). The role of descending pain modulation in chronic primary pain: Potential application of drugs targeting serotonergic system. *Neural Plasticity* 2019, 1–16. doi: 10.1155/2019/1389296

Treede, R. D., Rief, W., Barke, A., Aziz, Q., Bennett, M. I., Benoliel, R., et al. (2015). A classification of chronic pain for ICD-11. *Pain* 156, 1003–1007. doi: 10.1097/j.pain.0000000000000160

Treede, R.-D., Rief, W., Barke, A., Aziz, Q., Bennett, M. I., Benoliel, R., et al. (2019). Chronic pain as a symptom or a disease: The IASP classification of chronic pain for the international classification of diseases (ICD-11). *Pain* 160, 19–27. doi: 10.1097/j.pain.0000000000001384

Vachon-Presseau, E., Tétreault, P., Petre, B., Huang, L., Berger, S. E., Torbey, S., et al. (2016). Corticolimbic anatomical characteristics predetermine risk for chronic pain. *Brain* 139, 1958–1970. doi: 10.1093/brain/aww100

van den Heuvel, M. I., Turk, E., Manning, J. H., Hect, J., Hernandez-Andrade, E., Hassan, S. S., et al. (2018). Hubs in the human fetal brain network. *Dev. Cogn. Neurosci.* 30, 108–115. doi: 10.1016/j.dcn.2018.02.001

Vilà-Balló, A., Marti-Marca, A., Torres-Ferrús, M., Alpuente, A., Gallardo, V. J., and Pozo-Rosich, P. (2021). Neurophysiological correlates of abnormal auditory processing in episodic migraine during the interictal period. *Cephalalgia* 41, 45–57. doi: 10.1177/0333102420951509

Wang, X., and Ding, M. (2011). Relation between P300 and event-related theta-band synchronization: A single-trial analysis. *Clin. Neurophysiol.* 122, 916–924. doi: 10.1016/j.clinph.2010.09.011

Wang, Z., Yuan, M., Xiao, J., Chen, L., Guo, X., Dou, Y., et al. (2022). Gray matter abnormalities in patients with chronic primary pain: A coordinate-based meta-analysis. *Pain Physician* 25, 1–13.

Wu, W., Zhang, Y., Jiang, J., Lucas, M. V., Fonzo, G. A., Rolle, C. E., et al. (2020). An electroencephalographic signature predicts antidepressant response in major depression. *Nat. Biotechnol.* 38, 439–447. doi: 10.1038/s41587-019-0397-3

Yalcin, I., and Barrot, M. (2014). The anxiodepressive comorbidity in chronic pain. *Curr. Opin. Anaesthesiol.* 27, 520–527. doi: 10.1097/ACO.0000000000000116

Yao, Q., Wang, R., Fan, X., Liu, J., and Li, Y. (2020). Multi-class arrhythmia detection from 12-lead varied-length ECG using attention-based time-incremental convolutional neural network. *Inf. Fusion* 53, 174–182. doi: 10.1016/j.inffus.2019.06.024

Yasin, S., Hussain, S. A., Aslan, S., Raza, I., Muzammel, M., and Othmani, A. (2021). EEG based major depressive disorder and Bipolar disorder detection using neural networks: A review. *Comput. Methods Programs Biomed.* 202:106007. doi: 10.1016/j.cmpb.2021.106007

Ye, Q., Yan, D., Yao, M., Lou, W., and Peng, W. (2019). Hyperexcitability of cortical oscillations in patients with somatoform pain disorder: A resting-state EEG study. *Neural Plasticity* 2019, 1–10. doi: 10.1155/2019/2687150

Zhou, S., Després, O., Pebayle, T., and Dufour, A. (2015a). Age-related decline in cognitive pain modulation induced by distraction: Evidence from event-related potentials. *J. Pain* 16, 862–872. doi: 10.1016/j.jpain.2015.05.012

Zhou, S., Kemp, J., Després, O., Pebayle, T., and Dufour, A. (2015b). The association between inhibition and pain tolerance in the elderly: Evidence from event-related potentials: Inhibition and pain in aging. *Eur. J. Pain* 19, 669–676. doi: 10.1002/ejp.588

Zhou, S., Lithfous, S., Després, O., Pebayle, T., Bi, X., and Dufour, A. (2020). Involvement of frontal functions in pain tolerance in aging: Evidence from neuropsychological assessments and gamma-band oscillations. *Front. Aging Neurosci.* 12:131. doi: 10.3389/fnagi.2020.00131

frontiers | Frontiers in Neuroscience

TYPE Original Research
PUBLISHED 27 March 2023
DOI 10.3389/fnins.2023.1132607

Check for updates

OPEN ACCESS

EDITED BY
Fahmi Khalifa,
Morgan State University, United States

REVIEWED BY
Yaser A. ElNakieb,
University of Louisville, United States
Fengchun Wu,
The Affiliated Brain Hospital of Guangzhou Medical University, China

*CORRESPONDENCE
Xiangrong Zhang
✉ drxrz@hotmail.com
Zhijun Zhang
✉ janemengzhang@vip.163.com

SPECIALTY SECTION
This article was submitted to Brain Imaging Methods, a section of the journal Frontiers in Neuroscience

RECEIVED 27 December 2022
ACCEPTED 06 March 2023
PUBLISHED 27 March 2023

CITATION
Zhu W, Wang Z, Yu M, Zhang X and Zhang Z (2023) Using support vector machine to explore the difference of function connection between deficit and non-deficit schizophrenia based on gray matter volume. *Front. Neurosci.* 17:1132607. doi: 10.3389/fnins.2023.1132607

COPYRIGHT
© 2023 Zhu, Wang, Yu, Zhang and Zhang. This is an open-access article distributed under the terms of the Creative Commons Attribution License (CC BY). The use, distribution or reproduction in other forums is permitted, provided the original author(s) and the copyright owner(s) are credited and that the original publication in this journal is cited, in accordance with accepted academic practice. No use, distribution or reproduction is permitted which does not comply with these terms.

Using support vector machine to explore the difference of function connection between deficit and non-deficit schizophrenia based on gray matter volume

Wenjing Zhu[1,2], Zan Wang[1], Miao Yu[3], Xiangrong Zhang[3]* and Zhijun Zhang[1,2]*

[1]Department of Neurology, School of Medicine, Affiliated Zhongda Hospital, Research Institution of Neuropsychiatry, Southeast University, Nanjing, China, [2]Affiliated Mental Health Center, Hangzhou Seventh People's Hospital, Zhejiang University School of Medicine, Hangzhou, Zhejiang, China, [3]Department of Geriatric Psychiatry, Affiliated Nanjing Brain Hospital, Nanjing Medical University, Nanjing, China

Objective: Schizophrenia can be divided into deficient schizophrenia (DS) and non-deficient schizophrenia (NDS) according to the presence of primary and persistent negative symptoms. So far, there are few studies that have explored the differences in functional connectivity (FC) between the different subtypes based on the region of interest (ROI) from GMV (Gray matter volume), especially since the characteristics of brain networks are still unknown. This study aimed to investigate the alterations of functional connectivity between DS and NDS based on the ROI obtained by machine learning algorithms and differential GMV. Then, the relationships between the alterations and the clinical symptoms were analyzed. In addition, the thalamic functional connection imbalance in the two groups was further explored.

Methods: A total of 16 DS, 31 NDS, and 38 health controls (HC) underwent resting-state fMRI scans, patient group will further be evaluated by clinical scales including the Brief Psychiatric Rating Scale (BPRS), the Scale for the Assessment of Negative Symptoms (SANS), and the Scale for the Assessment of Positive Symptoms (SAPS). Based on GMV image data, a support vector machine (SVM) is used to classify DS and NDS. Brain regions with high weight in the classification were used as seed points in whole-brain FC analysis and thalamic FC imbalance analysis. Finally, partial correlation analysis explored the relationships between altered FC and clinical scale in the two subtypes.

Results: The relatively high classification accuracy is obtained based on the SVM. Compared to HC, the FC increased between the right inferior parietal lobule (IPL.R) bilateral thalamus, and lingual gyrus, and between the right inferior temporal gyrus (ITG.R) and the Salience Network (SN) in NDS. The FC between the right thalamus (THA.R) and Visual network (VN), between ITG.R and right superior occipital gyrus in the DS group was higher than that in HC. Furthermore, compared with NDS, the FC between the ITG.R and the left superior and middle frontal gyrus decreased in the DS group. The thalamic FC imbalance,

which is characterized by frontotemporal-THA.R hypoconnectivity and sensory motor network (SMN)-THA.R hyperconnectivity was found in both subtypes. The FC value of THA.R and SMN was negatively correlated with the SANS score in the DS group but positively correlated with the SAPS score in the NDS group.

Conclusion: Using an SVM classification method and based on an ROI from GMV, we highlighted the difference in functional connectivity between DS and NDS from the local to the brain network, which provides new information for exploring the neural physiopathology of the two subtypes of schizophrenic.

KEYWORDS

deficit schizophrenia, functional connectivity, resting-state fMRI, gray matter volume, support vector machine

1. Introduction

Due to the absence of objective biological markers, schizophrenic diagnosis and treatment constitute one of the most complex clinical challenges of modern psychiatry, and extreme heterogeneity among patients further hinders the present research (Kirkpatrick et al., 2019; Goldsmith et al., 2021). Therefore, researchers try to parse the symptomatology of schizophrenia into more homogeneous diagnostic categories. Deficit schizophrenia (DS), proposed by Carpenter et al. (1988), is a homogeneous subtype characterized by a trait-like feature of primary and prominent negative symptoms. However, DS patients have more severe negative symptoms, worse long-term prognosis, greater cognitive impairment, lower recovery rates, and a high frequency of family history with schizophrenia (Kirkpatrick et al., 2001; Strauss et al., 2010; Potvin et al., 2021). Therefore, differentiating the two subtypes may have important implications for understanding the psychopathology and improving clinical interventions in these two subgroups of schizophrenia.

Magnetic resonance imaging (MRI) is widely used in a variety of mental illness and nervous system disease research, and provided early promise for the discovery of the neuroanatomical differences between the two subtypes of schizophrenia (Wang et al., 2015; Lei et al., 2019). Some studies found excessive DS-specific brain structural changes in gray matter volume (GMV), white matter volume, CSF volume, and cortical structure; including frontal, parietal, and temporal regions (Fischer et al., 2012; Podwalski et al., 2022). However, previous functional neuroimaging studies about the functional connectivity differences between these two subgroups of schizophrenia based on ROI from GMV are scarce.

Several studies have reported different patterns of FC abnormalities in DS and NDS patients, although the results remain inconclusive. For example, Ke et al. (2010) suggested that schizophrenia exhibiting positive symptoms had significantly increased leftward asymmetry of functional connectivity, but the negative symptom group exhibited increased rightward asymmetry of functional connectivity, and the strength of the asymmetry in these regions was correlated with symptom ratings. Zhou et al. (2019a) probed numerous abnormal FCs of nerve pathways between the two patient groups, mainly concentrated in the frontooccipital, frontotemporal, and insula-visual cortex, as well as the temporooccipital pathway. In addition, a recent study demonstrated abnormal patterns of FC in the nucleus accumbens network between DS and NDS (Zhou et al., 2021). Meanwhile, using the independent component analysis (ICA) method, further studies found the modular-level alterations in DS compared with the NDS and healthy controls, and the distinct and common disruptions mainly focus on SN, sensory motor network (SMN), DMN, and VN (Yu et al., 2017; Zhou et al., 2019b; Fan et al., 2022). Nevertheless, the limitations of these earlier studies about FC of DS/NDS were that such functional brain connectivity results can be biased by the selection of seed region or spatial network template. Alternatively, there has been a paucity of studies mentioning the thalamocortical imbalance in the two subtypes of schizophrenia which is characterized by prefrontal-thalamic hypoconnectivity and sensorimotor-thalamic hyperconnectivity observed in resting-state fMRI studies, and has been implicated in the pathophysiology of schizophrenia (Anticevic et al., 2015; Avram et al., 2018; Wu et al., 2022).

Support vector machine (SVM), which is one of the most commonly used machine learning (ML) methods in pattern recognition (Lei et al., 2020), has been widely utilized as a powerful computational approach to classify schizophrenic patients from healthy controls and predict outcomes based on neuroimaging data (Wang et al., 2018; Chang et al., 2021). There are also very few studies that use SVM to classify and predict DS and NDS. Based on tryptophan catabolites and Consortium To Establish a Registry for Alzheimer's disease features, Kanchanatawan et al. (2018) used SVM to strongly segregate deficit from non-deficit schizophrenia and healthy controls. On the other hand, 144 patients were successfully classified as deficit patients using an SVM classifier based on severity, persistence over time, and possible secondary sources (e.g., depression) of negative symptoms in the research of Fervaha et al. (2016). However, few studies use magnetic resonance data to classify DS and NDS. Based on effective feature selection of these image data, SVM can find more objective seed regions for functional connectivity analysis of schizophrenia. In the present study, we applied SVM to discriminate DS from NDS using their GMV data. Then, the high-weight classified brain regions were used as seed points in whole-brain FC analysis and thalamic FC imbalance analysis of DS and NDS. Finally, we investigated the relationship between altered FC and clinical scale. We hypothesized that (1) Using the SVM classification method, this study can achieve the classification of two subtypes of schizophrenia and obtain key

brain regions from analysis of GMV. (2) This study can find the difference in functional connectivity between DS and NDS from the local to the brain network, which provides new information for exploring the neural physiopathology of the two subtypes of schizophrenic. (3) Observed altered FC between DS, NDS, and HC will also be correlated with clinical scale.

2. Materials and methods

2.1. Participants

A total of 86 naturally right-handed Han Chinese participants ranging in age from 20 to 65 years were recruited in this study, 48 schizophrenia patients and 38 matched healthy controls. All the patients were recruited from the psychiatric rehabilitation unit of Yangzhou Wutaishan Hospital, Jiangsu Province, China. The inclusion criteria for the patients are: (1) An explicit diagnosis of schizophrenia according to the Diagnostic and Statistical Manual of Mental Disorders, Fifth Edition (DSM-V); (2) Presenting stable psychiatric symptoms after antipsychotic medication for at least 12 months before participation. The exclusion criteria for the patients are: (1) Severe neuropsychiatric comorbidities, such as head trauma or intellectual disability; (2) Alcoholism or substance abuse; (3) Physical therapy including electroconvulsive therapy; (4) Contraindications for MRI; (5) Noticeable head motion (>3 mm in translation or 3° in rotation). One patient was excluded because of large head motion, the remaining 47 patients were enrolled in the final research. According to the Chinese version of the Schedule for Deficit Syndrome (SDS) (Wang et al., 2008), patients were divided into two groups: DS and NDS groups, including 16 DS patients and 32 NDS patients, respectively. Patients with two of the following symptoms present at a moderately severe level and persistent over 12 months were defined as having DS: restricted affect, diminished emotional range, poverty of speech, curbing of interests, diminished sense of purpose, and diminished social drive; all the symptoms required the absence of secondary sources (e.g., medication side effects, depression, etc.). In total, 38 gender-, age-, and handedness-matched HC volunteers were recruited from the communlocal advertisements. Unstructured clinical interviews were conducted to exclude HCs who had a history of organic brain disorders, intellectual disability, or severe head trauma as well as a history of personal or family psychiatric disorder. All participants gave informed consent to participate in this study, which was approved by the Institutional Ethical Committee for clinical research of Zhongda Hospital Affiliated with Southeast University.

2.2. Assessments of clinical symptoms and antipsychotic treatment

The severity of the schizophrenic symptoms was evaluated by the Brief Psychiatric Rating Scale (BPRS), the Scale for the Assessment of Negative Symptoms (SANS), and the Scale for the Assessment of Positive Symptoms (SAPS). All patients received antipsychotic medications according to the case clinician's preference for at least 12 months before participation. The details of treatment were assessed from patients' or their guardians' reports and hospital records. The dosage of antipsychotic medication of each patient was recorded and converted to chlorpromazine-equivalent mean daily dosages (MDD) (Woods, 2003). **Table 1** illustrates the clinical and demographic data of all participants.

2.3. Multimodal MRI data acquisition

All participants were scanned by a 3T MR system (GE HDx, Chicago, IL, USA) with an eight-channel phased array head coil in the Subei Hospital of Jiangsu Province, Yangzhou, China. T1-weighted images were acquired by three-dimensional spoiled gradient echo sequence as follows: repetition time (TR) = 11.94 ms, echo time (TE) = 5.044 ms, flip angle = 15°, slice thickness = 1 mm without gap, number of slices = 172, field of view (FOV) = 240 × 240 mm, matrix size = 256 × 256. In addition, R-fMRI data were acquired with a gradient recalled echo echo-planar imaging (GRE-EPI) sequence: repetition time (TR) = 2,000 ms, echo time (TE) = 25 ms, flip angle = 90°, number of slices = 35, field of view (FOV) = 240 × 240 mm, slice thickness = 4 mm without gap, matrix size = 64 × 64, voxel size = 4 × 4 × 4 mm^3, 240 volumes. All participants were asked to lie quietly awake in the scanner with their eyes closed, and their heads were cozily positioned with cushions inside the coil during the MRI scan to minimize head motion.

2.4. Image preprocessing and VBM analysis

The Statistical Parametric Mapping 8 (SPM8)[1] and Data Processing & Analysis for Brain Imaging (DPABI)[2] were applied to preprocess the fMRI data in MATLAB.[3] The data preprocessing includes the following steps: (1) discarding of the first 10 volumes to achieve equilibrium and a steady-state; (2) slice timing correction; (3) realignment: head motion parameters were computed by estimating the translation in each direction and the angular rotation on each axis for each volume, we required the translational or rotational motion parameters less than 3 mm or 3°, The frame-wise displacement (FD), which indexes the volume-to-volume changes in head position was also calculated; (4) spatially normalized: individual structural images were firstly co-registered with the mean functional image; then the transformed structural images were segmented and normalized to the Montreal Neurological Institute (MNI) space using a high-level non-linear warping algorithm which use the exponentiated Lie algebra (DARTEL) technique (Ashburner, 2007) to acquire the diffeomorphic anatomical registration, Finally, each functional volume was spatially normalized to MNI space using the deformation parameters estimated during the above step and resampled into a 3 mm cubic voxel; (5) Nuisance covariates regression: six head motion parameters, cerebrospinal fluid signals,

1 http://www.fil.ion.ucl.ac.uk/spm/software/spm8/
2 http://rfmri.org/dpabi
3 http://www.mathworks.com/products/matlab/

TABLE 1 Demographic and clinical characteristics.

	DS (n = 16)	NDS (n = 31)	HC (n = 38)	[b]T/F/χ^2	P-value
Gender (Male/female)[a]	9/7	16/15	20/18	0.09	0.954
Age	50.63 ± 9.73	45.13 ± 5.33	45.71 ± 9.63	2.54	0.085
Educational years	8.75 ± 2.05	9.29 ± 1.95	10.74 ± 2.73	5.34	0.007
BPRS-T	32 ± 2.81	27.32 ± 2.15	–	6.36	0.000
SAPS-T	9.06 ± 3.68	10.13 ± 4.51	–	–0.82	0.419
SANS-T	55.25 ± 8.06	32.16 ± 5.71	–	11.39	0.000
Antipsychotic (n)[c]	16	31	–	–	–
Antipsychotic medication[d], day/mg	446.23 ± 259.21	483.82 ± 238.03	–	0.86	0.591
FD value	0.13 ± 0.11	0.12 ± 0.17	0.11 ± 0.24	2.57	0.286

DS, deficit schizophrenia; NDS, non-deficit schizophrenia; HC, healthy control; BPRS, Brief Psychiatric Rating Scale; SAPS, Scale for the Assessment of Positive Symptoms; SANS, Scale for the Assessment of Negative Symptoms; FD, frame-wise displacement, used to evaluate head motion during scanning.
[a]Data are presented as mean ± standard deviation except gender.
[b]Comparisons were performed with a chi-square test for the variable of gender and independent samples t-tests for other variables. Adjusted age and education were employed as covariates. Bonferroni correction was used for post-hoc comparisons.
[c]All participants were taking atypical antipsychotics.
[d]Chlorpromazine equivalent doses were calculated.

white matter signals, and global mean signals were regressed from the data as corrected values; (6) spatial smoothing with a Gaussian kernel of 8 × 8 × 8 mm^3.

T1-weighted structural brain images were visually inspected for motion and artifacts before VBM analysis and for segmentation errors prior to inclusion in the group analyses. Firstly, the VBM8 toolbox[4] was adopted to preprocess and segment images that passed quality control into gray matter, white matter, and cerebrospinal fluid. Then, the images underwent non-linear normalization to MNI space with the DARTEL algorithm after bias correction and segmentation. The images were modulated by non-linear warping only. Finally, the normalized gray matter images were smoothed with a 6mm kernel and used as characteristic parameters for the SVM method to determine the ROIs for functional connectivity.

2.5. Determination of ROI with SVM method and functional connectivity analysis

In order to classify the three groups of HCs, DS, and NDS, and to find the brain regions with GMV differences between the two subtypes of schizophrenia through imaging data, we adopted the Pattern Recognition for Neuroimaging Toolbox (PRoNTo)[5] (Schrouff et al., 2013) which we ran on Matlab, aiming to facilitate the interaction between machine learning and neuroimaging communities. Based on PRoNTo software, we then applied linear kernel Support vector machines (SVM) which is one of the most commonly used machine learning techniques in neuroimaging to achieve the classification. In the SVM training phase, Spatiotemporal images of the GMV for each subject from two subtypes are calculated as features, and weights are assigned to these features for maximal separation between the groups using a hyperplane, which serves as the decision boundary. Classification labels are determined by the sign of the total feature weights multiplied by the test sample. We use the default soft-margin parameter of C = 1. Meanwhile, a 10-fold cross-validation scheme we employed to assess the performance of models generated by these algorithms. Subsequently, we calculated the brain regions that accounted for the top 1% of classification weights, and the numerical values obtained from these high classification weight GMV regions were extracted with the Resting-State fMRI Data Analysis Toolkit (REST),[6] using these brain regions with high classification weight as masks. Thereafter, GMV values were converted to Z-values *via* Fisher Z transformation and used for the correlation analysis. The study then selected the brain regions whose GMV values negatively correlated with the SANS score as seed points to construct the FC analysis.

In the present study, these high-weight classified brain regions between DS and NDS were used as regions of interest for whole-brain-based FC analysis. Pearson correlation analysis was carried out to obtain the correlation coefficient (r-value) of the mean time series between the seed point and the whole-brain voxel in each participant. Fisher Z transformation was then performed to convert the r value to the Z value, which conforms to the normal distribution. Part of the numerical values resulting from regions of altered FC was extracted with REST using altered regions as masks and were later used for correlation analysis.

2.6. Statistical analyses

The statistical descriptive analyses of demographic and clinical scales were conducted using the SPSS 17.0 software package.

4 http://dbm.neuro.uni-jena.de/vbm
5 www.mlnl.cs.ucl.ac.uk/pronto
6 http://resting-fmri.sourceforge.net/

These parameters were compared with the chi-squared test, the two-sample *t*-tests, and the analysis of variance (ANOVA) appropriately. ANOVA was performed using the DPABI to investigate differences in whole-brain FC among DS, NDS, and HC groups. Age and education were used as covariates. False discovery rate (FDR) correction was performed for multiple comparisons at the voxel level. The statistical threshold was set at a corrected $p < 0.05$. The associations between the valuable GMV and FC of brain regions and Clinical scale value in both the DS and NDS groups were performed with Partial correlation analysis (age, education, and chlorpromazine equivalent as covariates).

3. Results

3.1. Demographic and clinical characteristics

Table 1 describes the demographic, clinical scale, and head motion data of 16 DS patients, 31 NDS patients, and 38 HCs. There was no significant difference between the three groups in terms of age, gender, and head motion. Compared with the DS patients, patients with NDS presented higher scores in SAPS-T and lower scores in BPRS-T and SANS-T. Both groups of patients received antipsychotic medications including olanzapine, risperidone, quetiapine, clozapine, and other commonly used antipsychotics, and there was no statistical difference in the chlorpromazine equivalent doses of the two groups ($p > 0.05$).

3.2. Classification performance and regions contributing to discrimination between DS and NDS

The classification performance for the GMV feature is summarized in Table 2. Total classification accuracy between DS and NDS was 78.6%, and the illustration of classification is presented in Figure 1, ROC curve of GMV was also obtained with the SVM classifier [Figure 1B, Area Under Curve (AUC) = 0.84]. Regions that contributed to GMV discrimination and accounted for the top 1% of classification weights included right inferior parietal lobule, right upper parietal, left upper parietal, left precentral gyrus, right precentral gyrus, postcentral gyrus, paracentral lobule, precuneus, right inferior temporal gyrus, right thalamus, and cerebellum (Supplementary Figure 1). Then, the GMV values of these 11 high-weight classified brain regions were extracted with REST and were later used for correlation analysis. The results of correlation analysis suggest that six brain regions whose GMV values were negatively correlated with the SANS scale included the right inferior parietal lobule, right upper parietal lobule, left precentral gyrus, precuneus, right inferior temporal gyrus, and right thalamus (shown in Figure 2). But the GMV values were not significantly correlated with other scales.

3.3. Functional connectivity

Functional connectivity analysis based on three seed points between patients and HC. As shown in Figures 3, 4, some abnormal FCs were found among the three groups. Compared to HC, the FC of IPL.R with bilateral thalamus and lingual gyrus, of ITG.R with SN was enhanced in NDS. Both DS groups and NDS groups were found to have an imbalance in thalamic FC which was enhanced between THA.R and SMN but decreased between THA.R and the frontotemporal area. In addition, the FC enhanced between the THA.R and VN, between ITG.R and right superior occipital gyrus in DS group. The FC decreased between the ITG.R and the left superior and middle frontal gyrus in the DS group when compared with NDS.

3.4. Altered FC of THA-R between DS, NDS, and HCs, and its relationship with clinical symptoms

The brain regions with altered FC of THA-R were mentioned in Table 3 and the relationship was mentioned in Figure 5, results show that compared with HC, the FC enhanced between THA.R and SMN, but decreased between THA.R and frontotemporal area both in the DS and NDS groups. In addition, the FC between the THA.R and VN was also enhanced in the DS group. The FC value of THA.R and SMN in the DS group was negatively correlated with the SANS score ($P < 0.05$). But the FC value of THA.R and SMN in the NDS group was positively correlated with the SAPS score ($P < 0.05$).

4. Discussion

The main findings of the current work are as follows: (1) The classification accuracy of SVM was 78.60% between DS and NDS, and 84.63% between DS and HC, six important regions of interest related to clinical symptoms were obtained from the classification between DS and NDS; (2) Compared to HC, the FC increased between IPL.R and bilateral thalamus, and lingual gyrus, between ITG.R and SN in NDS. Alternatively, the FC enhanced between

TABLE 2 Classification results of deficit schizophrenia (DS)/non-deficit schizophrenia (NDS)/healthy control (HC) using support vector machine (SVM) classifier based on gray matter volume (GMV).

Groups	Total accuracy	Balanced accuracy (BA)	BA *p*-value	AUC
DS/NDS	78.60%	72.63%	0.003	0.84
DS/HC	84.63%	76.05%	0.001	0.85
HC/NDS	83.26%	75.59%	0.001	0.84

AUC, area under curve.

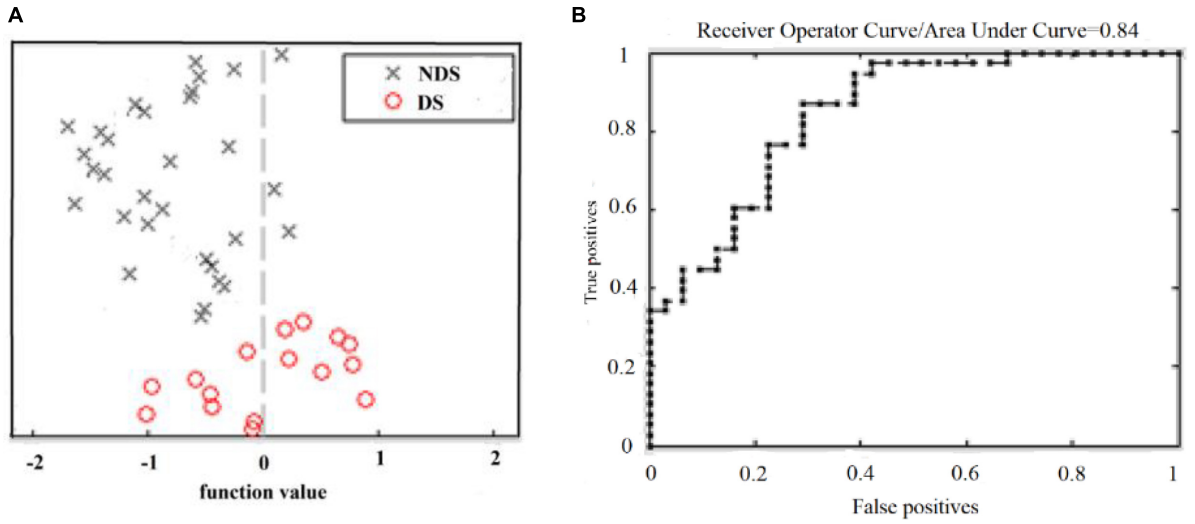

FIGURE 1
Classification between DS and NDS based on GMV. **(A)** Classification plot for training on DS/NDS data and testing on DS/NDS data using GMV. **(B)** ROC curve obtained by classifying DS and NDS using an SVM classifier. DS, deficit schizophrenia; NDS, non-deficit schizophrenia; GMV, gray matter volume; ROC, receiver operating characteristic curve; SVM, support vector machine.

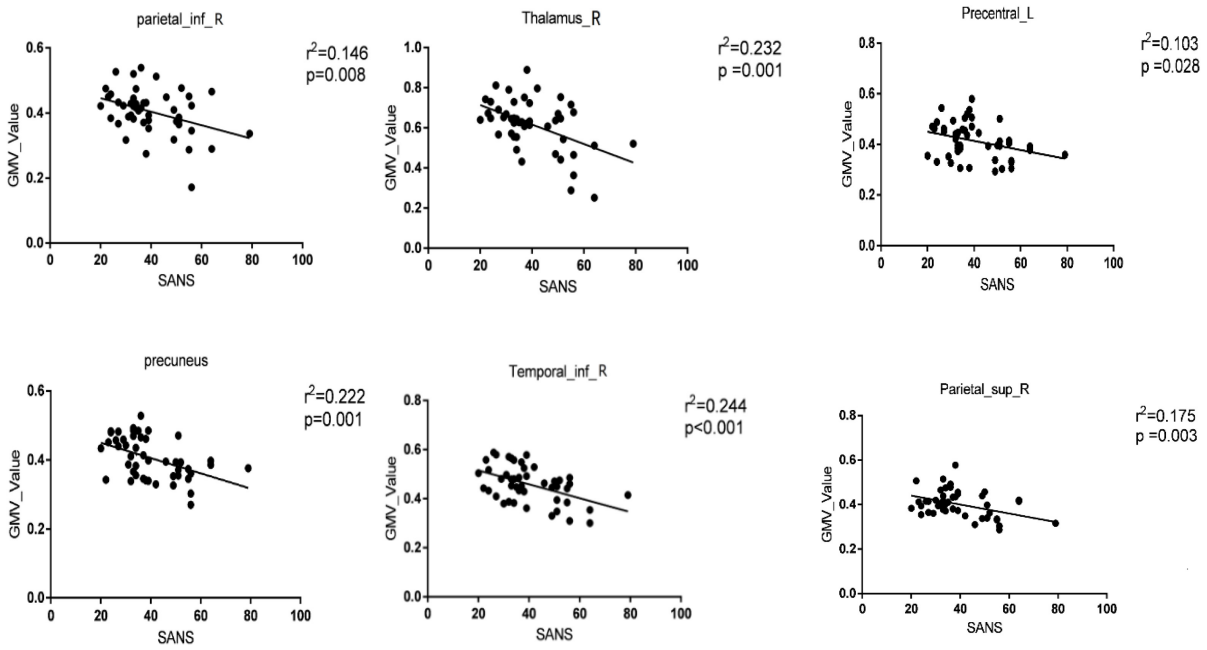

FIGURE 2
Significant correlations between the gray matter volume (GMV) values of brain regions with classification weights in the top 1% and clinical features in the whole patient group [deficit schizophrenia (DS) group and non-deficit schizophrenia (NDS) group]. The significance threshold was set at $p < 0.05$ (uncorrected). Parietal_inf_R, right inferior parietal lobule; Thalamus_R, right thalamus; Precentral_L, left precentral gyrus; Temporal_inf_R, right inferior temporal gyrus; Parietal_sup_R, right upper parietal lobule.

the THA.R and VN, ITG.R, and right superior occipital gyrus in the DS group. Compared with NDS, the FC between the ITG.R and the left superior and middle frontal gyrus decreased in the DS group; (3) Thalamic FC imbalance analysis suggested that the FC enhanced between THA.R and SMN, but decreased between THA.R and frontotemporal area both in DS and NDS groups. Interestingly, the FC value of THA.R and SMN in the DS group was negatively correlated with the SANS score, but the FC value of THA.R and SMN in the NDS group was positively correlated with the SAPS score. To the best of our knowledge, this is the first study using machine learning methods to classify the two subtypes of schizophrenia from normal controls based on GMV and perform whole-brain functional connectivity analysis based on ROI with less bias obtained from the classification. This study further explores the neural physiopathology of the two subtypes of schizophrenia.

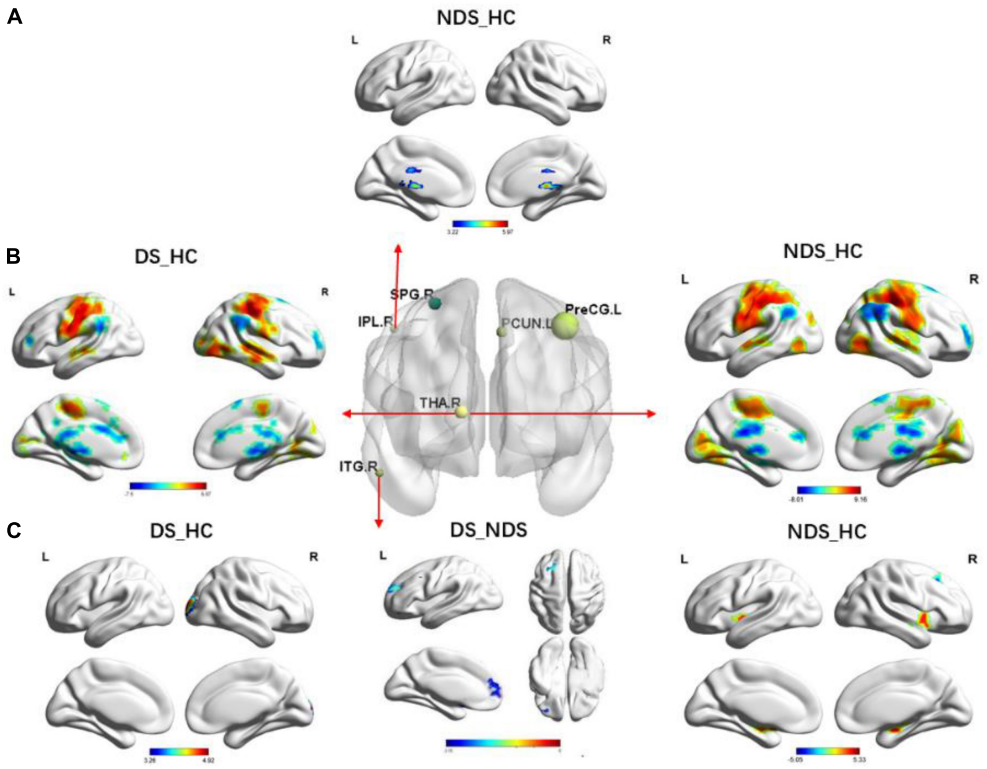

FIGURE 3
Group comparisons of functional connectivity (FC) in six region of interests (ROIs) among deficit schizophrenia (DS), non-deficient schizophrenia (NDS), and health controls (HC). **(A)** Group analyses of the FC in the right inferior parietal lobule between NDS and HC groups. The significance threshold was set at $p < 0.05$ after false discovery rate (FDR) was corrected (voxel $p < 0.05$, cluster size ≥ 146). **(B)** Group analyses of the FC in the right thalamus between patients and HC groups. The significance threshold was set at $p \leq 0.05$ after FDR was corrected (voxel $p < 0.05$, cluster size ≥ 200). **(C)** Group analyses of the FC in the right inferior temporal gyrus between patients and HC groups. The significance threshold was set at $p < 0.05$ after FDR was corrected (voxel $p < 0.05$, cluster size $\geq 162/100/100$). The blue regions indicate the regions where patients had lower FC compared to HC; the red areas show the regions where patients had greater FC compared to HC, when DS vs. NDS, and the blue regions indicate the regions where DS had lower FC compared to NDS. IPL.R, right inferior parietal lobule; THA.R, right thalamus; ITG.R, right inferior temporal gyrus; FC, functional connectivity.

There are few previous studies based on electrophysiological, neurocognitive testing, oxidative stress toxicity, neuroimmune and other parameters, using machine learning methods to classify DS, NDS, and normal controls; correspondingly, the classification accuracy is in the range of 70–85% (Kanchanatawan et al., 2018; Maes et al., 2020; Taylor et al., 2020). Unlike these past studies, the current study extracts features from GMV image maps, uses the SVM method to classify DS and NDS, the six important brain regions for distinguishing DS and NDS, and their GMV values were negatively correlated with the SANS scale, including right inferior parietal lobule, right upper parietal, left precentral gyrus, precuneus, right inferior temporal gyrus, and right thalamus.

The results of previous MRI studies of DS and NDS have shown that the frontal lobe, temporal lobe, and precuneus are the main areas of gray matter reduction, the degree of reduction was also negatively correlated with negative symptoms, results of this research are consistent with these findings. Positive symptoms such as hallucinations, delusions, and thinking disorders are important differences between DS and NDS. Meanwhile, the temporal lobe is related to auditory and language processing and thought, so it may be the material basis for the difference in positive symptoms between the two types of patients. The precuneus plays a major role in higher-order self-processes and the attribution of emotion to self and others. The precuneus gray matter volume is significantly different between DS and NDS subtypes, which may explain why patients with deficient schizophrenia have difficulty in emotional expression.

Several functional connectivity and local network abnormalities, involving the thalamus, inferior parietal gyrus, salience network, sensory motor network, and visual network, were found in both the DS and NDS groups compared with the HCs. It has been reported previously that most of these regions have abnormal functional connectivity in patients with schizophrenia (Skudlarski et al., 2010; Zalesky et al., 2011). The thalamus is an important nerve nucleus within the brain and is a secondary conduction pathway that plays the role of upward conduction for all sensations except smell. In addition, the thalamus is also involved in people's emotional activities, thalamus damage will lead to emotional disorders, but also cognitive function, speech function decline, and so on (Avram et al., 2018; Wu et al., 2022). In the present study, FC between the THA.R and VN was enhanced in DS group when compared with HC, which represents an abnormal visual process in order to improve neurocognitive function in DS patients, thus may indicate a unique neuropathological mechanism in this schizophrenia subgroup. The present findings also demonstrated hypo-connectivity between the right ITG and

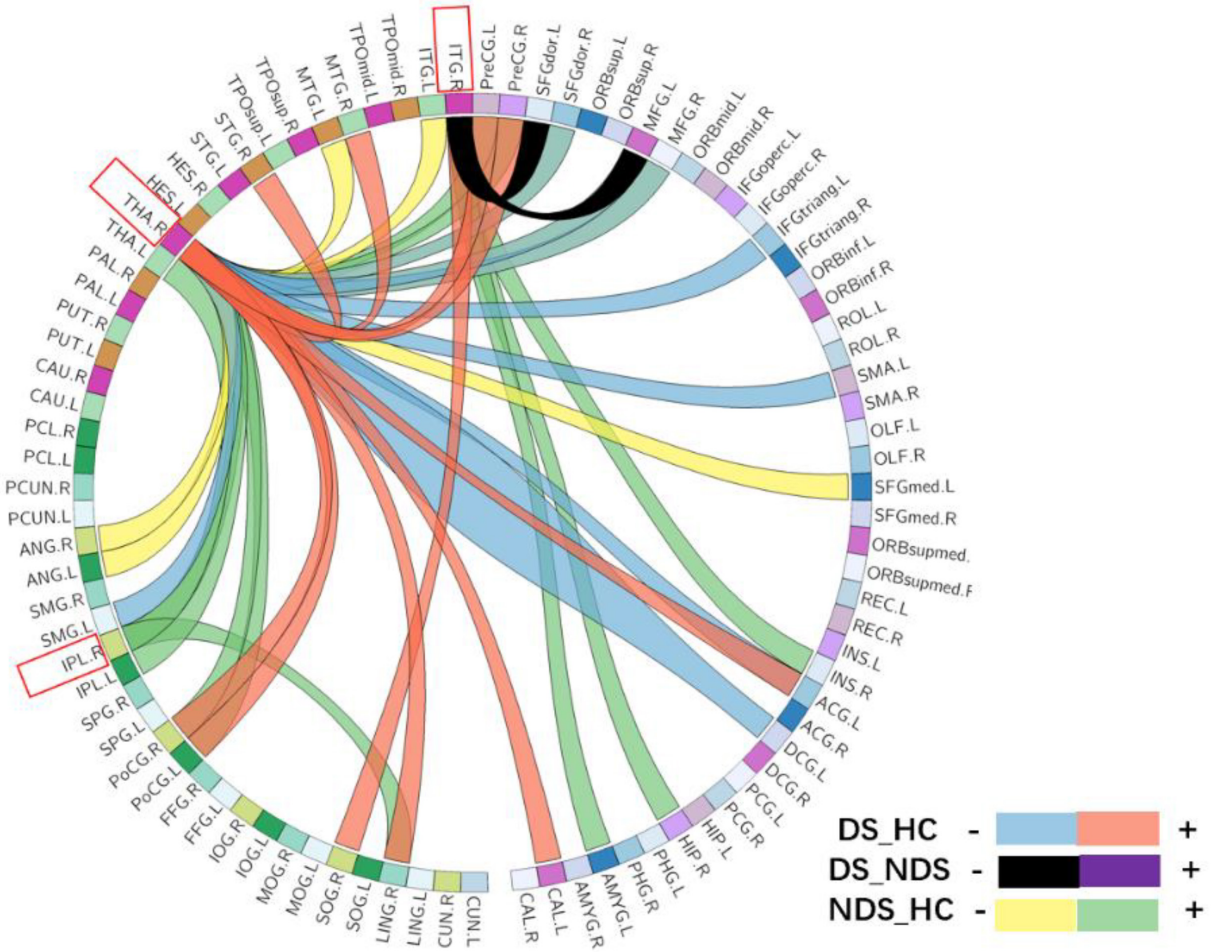

FIGURE 4
The circular graph obtained by comparing the functional connections between the three groups based on the three region of interests (ROIs) (IPL.R, THA.R, ITG.R). IPL.R, right inferior parietal lobule; THA.R, right thalamus; ITG.R, right inferior temporal gyrus.

left superior/middle frontal gyrus in the DS group relative to the NDS group. Previously published studies have shown that the right ITG, important for language formulation and face perception (Schultz et al., 2000; Dien et al., 2013), has been reported to have volume reduction in DS patients. Furthermore, abnormally increased activation of the right ITG was found to be related to deficits in facial recognition and interpersonal communication in autistic patients (Schultz et al., 2000), which are phenotypically similar to the negative symptoms of schizophrenia. Part of the frontoparietal circuitry comprises the mirror neuron system, which is activated during basic emotion understanding and emotion experience sharing. Therefore, all these combined factors can be analyzed to show that the hypo-connectivity between the right ITG and frontal-parietal circuit in DS patients is likely to be a potential neural mechanism for the prominence of negative symptoms.

Published data (Anticevic et al., 2015; Li et al., 2017; Avram et al., 2018) support the hypothesis that thalamocortical imbalance may be one inherent feature of schizophrenia. The results of this study are consistent with the hypothesis that the FC enhanced between THA.R and SMN, but decreased between THA.R and frontotemporal area both in DS and NDS groups when compared with HC. In addition, the FC value of THA.R and SMN in the DS group was negatively correlated with the SANS score, but the FC value of THA.R and SMN in the NDS group was positively correlated with the SAPS score. Previous studies have shown that the SMN mainly regulating sensory and motor functions, is the core network that is vulnerable to dysfunction in emotional functions, emotion recognition, and cognitive functions of psychiatric disorders (Wood et al., 2016; Davis et al., 2017). The conclusions have also been presented in previous studies, for instance, Cheng et al. (2015) reported an association between sensorimotor cortico-thalamic hyperconnectivity and negative symptoms. Anticevic et al. (2014) reported an association with general psychopathology. Combining these studies, it can be speculated that the presence of persistently progressive negative symptoms in patients with DS further exacerbates sensorimotor cortico-thalamic hyperconnectivity.

In conclusion, the present study investigates functional connectivity alterations between DS and NDS from the local to the whole and their relationships with clinical symptoms based on the regions of interest obtained by the SVM classifier, and the results obtained a relatively high classification accuracy. Based on the

TABLE 3 Altered regions of functional connectivity (FC) analysis based on the region of interest (ROI) of right thalamus (THA-R).

Brain regions	Peak MNI coordinate			F/t	Cluster size
	X	Y	Z		
ANCOVA					
L-postcentral/L-precentral/L-parietal_inf	−51	−21	36	53.13	1,158
R-postcentral/R-precentral	45	−30	60	43.39	943
R-temporal_mid/R-temporal_sup	57	−15	−6	27.23	171
R-occipital_inf/R-occipital_mid	42	−78	−3	27.54	101
R-lingual	18	−45	−12	31.69	250
L-cingulum_ant	0	15	27	27.54	84
DS vs. HC					
L-postcentral/L-precentral/L-parietal_inf/ L-paracentral lobule	-51	−21	36	6.68	1,319
R-postcentral/R-precentral	45	−27	60	6.87	1,039
R-lingual/R-calcarine	18	−75	−12	5.20	625
R-temporal_mid/R-temporal_sup	57	−33	3	5.41	246
L-cingulum_ant	0	15	27	−5.07	142
NDS vs. HC					
B-postcentral/B-precentral/L-parietal_inf	−48	−24	45	9.16	6,210
B-lingual	45	−75	0	6.34	1,976
L-occipital_inf	−48	−72	−6	5.28	102
R-frontal_sup/R-frontal_mid	30	57	18	−4.51	95
B-cingulum_ant	6	30	18	−4.62	173
B-augular	57	−48	36	−5.78	441
DS vs. NDS	None	–	–	–	–

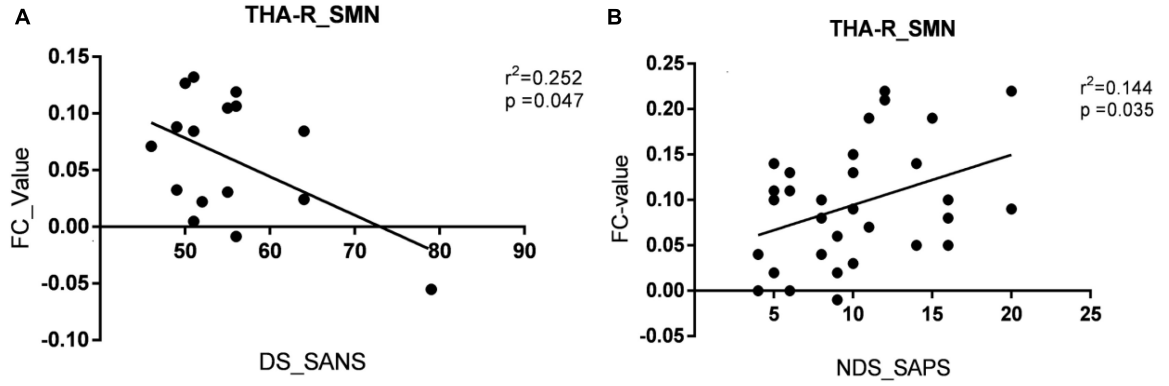

FIGURE 5
The relationships between altered functional connectivity (FC) value of right thalamus (THA-R) with clinical symptoms. **(A)** The relationships between the FC value of THA.R and SMN with the Scale for the Assessment of Negative Symptoms (SANS) score in the deficient schizophrenia (DS) group. **(B)** The relationships between the FC value of THA.R and SMN with the Scale for the Assessment of Positive Sympt (SAPS) score in the non-deficient schizophrenia (NDS) group. The significance threshold was set at $p < 0.05$. SMN, sensory motor network. THA-R_SMN, FC of right thalamus and the sensory-motor network; DS_SANS, scoring on the SANS in the DS group; NDS_SAPS, scoring on the SAPS in the NDS group.

ROIs, including IPL.R, ITG.R, and THA.R, this study demonstrated the FC between the THA.R and VN enhanced in the DS group when compared with HC, FC between the right ITG and left superior/middle frontal gyrus decreased in DS group relative to NDS group. The findings of this study corroborate the previous conclusion of the hypothesis that thalamocortical imbalance in both of the two subtypes of schizophrenia. In addition, the FC value of THA.R and SMN in the DS group was negatively correlated with the SANS score, but the FC value of THA.R and SMN in the NDS group was positively correlated with the SAPS score, which deepens the understanding of the pathological mechanism of the two subtypes of schizophrenia.

5. Limitations

Some limitations of this study should be addressed. First, our study enrolled a small sample size. Larger samples in the future are needed to confirm current findings. Second, only one machine learning method of support vector machine is used for classification in this study, and the classification accuracy is not very high. So later research can improve the performance of the classifier. Third, this study only included the right thalamus in the study of thalamocortical imbalance, which will make the attribution of thalamic FC imbalance analysis in the two subtypes of schizophrenia incomplete.

Data availability statement

The original contributions presented in this study are included in the article/**Supplementary material**, further inquiries can be directed to the corresponding authors.

Ethics statement

The studies involving human participants were reviewed and approved by the Institutional Ethical Committee for Clinical Research of Zhongda Hospital Affiliated to Southeast University. The patients/participants provided their written informed consent to participate in this study.

Author contributions

ZZ and XZ supervised the present study. WZ and ZW performed the analysis and wrote the manuscript. XZ and MY helped to collect data. All authors contributed to the article and approved the submitted version.

Funding

This work was supported by funding from the Youth Innovative Talent Support Program Fund of the Zhejiang Provincial Department of Health (2022RC061) and R&D Plan of Key Fields in Guangdong Province (2018B030334001).

Conflict of interest

The authors declare that the research was conducted in the absence of any commercial or financial relationships that could be construed as a potential conflict of interest.

Publisher's note

All claims expressed in this article are solely those of the authors and do not necessarily represent those of their affiliated organizations, or those of the publisher, the editors and the reviewers. Any product that may be evaluated in this article, or claim that may be made by its manufacturer, is not guaranteed or endorsed by the publisher.

Supplementary material

The Supplementary Material for this article can be found online at: https://www.frontiersin.org/articles/10.3389/fnins.2023.1132607/full#supplementary-material

References

Anticevic, A., Cole, M., Repovs, G., Murray, J., Brumbaugh, M., Winkler, A., et al. (2014). Characterizing thalamo-cortical disturbances in schizophrenia and bipolar illness. *Cereb. Cortex.* 24, 3116–3130. doi: 10.1093/cercor/bht165

Anticevic, A., Haut, K., Murray, J., Repovs, G., Yang, G., Diehl, C., et al. (2015). Association of thalamic dysconnectivity and conversion to psychosis in youth and young adults at elevated clinical risk. *JAMA Psychiatry* 72, 882–891. doi: 10.1001/jamapsychiatry.2015.0566

Ashburner, J. (2007). A fast diffeomorphic image registration algorithm. *NeuroImage* 38, 95–113. doi: 10.1016/j.neuroimage.2007.07.007

Avram, M., Brandl, F., Bäuml, J., and Sorg, C. (2018). Cortico-thalamic hypo- and hyperconnectivity extend consistently to basal ganglia in schizophrenia. *Neuropsychopharmacology* 43, 2239–2248. doi: 10.1038/s41386-018-0059-z

Carpenter Jr., W. T., Heinrichs, D. W., and Wagman, A. M. (1988). Deficit and nondeficit forms of schizophrenia: The concept. *Am. J. Psychiatry* 145, 578–583. doi: 10.1176/ajp.145.5.578

Chang, Q., Li, C., Tian, Q., Bo, Q., Zhang, J., Xiong, Y., et al. (2021). Classification of first-episode schizophrenia, chronic schizophrenia and healthy control based on brain network of mismatch negativity by graph neural network. *IEEE Trans. Neural Syst. Rehabil. Eng.* 29, 1784–1794. doi: 10.1109/TNSRE.2021.3105669

Cheng, W., Palaniyappan, L., Li, M., Kendrick, K., Zhang, J., Luo, Q., et al. (2015). Voxel-based, brain-wide association study of aberrant functional connectivity in schizophrenia implicates thalamocortical circuitry. *NPJ Schizophr.* 1:15016.

Davis, J. D., Winkielman, P., and Coulson, S. (2017). Sensorimotor simulation and emotion processing: impairing facial action increases semantic retrieval demands. *Cogn. Affect. Behav. Neurosci.* 17, 652–664. doi: 10.3758/s13415-017-0503-2

Dien, J., Brian, E., Molfese, D., and Gold, B. (2013). Combined ERP/fMRI evidence for early word recognition effects in the posterior inferior temporal gyrus. *Cortex* 49, 2307–2321. doi: 10.1016/j.cortex.2013.03.008

Fan, L., Yu, M., Pinkham, A., Zhu, Y., Tang, X., Wang, X., et al. (2022). Aberrant large-scale brain modules in deficit and non-deficit schizophrenia. *Prog. Neuropsychopharmacol. Biol. Psychiatry* 113:110461. doi: 10.1016/j.pnpbp.2021.110461

Fervaha, G., Agid, O., Foussias, G., Siddiqui, I., Takeuchi, H., and Remington, G. (2016). Neurocognitive impairment in the deficit subtype of schizophrenia. *Eur. Arch. Psychiatry Clin. Neurosci.* 266, 397–407.

Fischer, B., Keller, W., Arango, C., Pearlson, G., McMahon, R., Meyer, W., et al. (2012). Cortical structural abnormalities in deficit versus nondeficit schizophrenia. *Schizophr. Res.* 136, 51–54. doi: 10.1016/j.schres.2012.01.030

Goldsmith, D., Massa, N., Miller, B., Miller, A., and Duncan, E. (2021). The interaction of lipids and inflammatory markers predict negative symptom severity in patients with schizophrenia. *NPJ* 7:50. doi: 10.1038/s41537-021-00179-8

Kanchanatawan, B., Sriswasdi, S., Thika, S., Sirivichayakul, S., Carvalho, A., Geffard, M., et al. (2018). Deficit schizophrenia is a discrete diagnostic category

defined by neuro-immune and neurocognitive features: results of supervised machine learning. *Metab. Brain Dis.* 33, 1053–1067. doi: 10.1007/s11011-018-0208-4

Ke, M., Zou, R., Shen, H., Huang, X., Zhou, Z., Liu, Z., et al. (2010). Bilateral functional asymmetry disparity in positive and negative schizophrenia revealed by resting-state fMRI. *Psychiatry Res.* 182, 30–39. doi: 10.1016/j.pscychresns.2009.11.004

Kirkpatrick, B., Buchanan, R. W., Ross, D. E., and Carpenter, W. T. Jr. (2001). A separate disease within the syndrome of schizophrenia. *Arch. General Psychiatry* 58, 165–171.

Kirkpatrick, B., Gurbuz Oflezer, O., Delice Arslan, M., Hack, G., and Fernandez-Egea, E. (2019). An early developmental marker of deficit versus nondeficit schizophrenia. *Schizophr. Bull.* 45, 1331–1335. doi: 10.1093/schbul/sbz024

Lei, D., Pinaya, W., Young, J., van Amelsvoort, T., Marcelis, M., Donohoe, G., et al. (2020). Integrating machining learning and multimodal neuroimaging to detect schizophrenia at the level of the individual. *Hum. Brain Mapp.* 41, 1119–1135. doi: 10.1002/hbm.24863

Lei, W., Kirkpatrick, B., Wang, Q., Deng, W., Li, M., Guo, W., et al. (2019). Progressive brain structural changes after the first year of treatment in first-episode treatment-naive patients with deficit or nondeficit schizophrenia. *Psychiatry Res. Neuroimaging* 288, 12–20.

Li, T., Wang, Q., Zhang, J., Rolls, E., Yang, W., Palaniyappan, L., et al. (2017). Brain-wide analysis of functional connectivity in first-episode and chronic stages of schizophrenia. *Schizophr. Bull.* 43, 436–448.

Maes, M., Sirivichayakul, S., Matsumoto, A., Michelin, A., de Oliveira Semeao, L., de Lima Pedrao, J., et al. (2020). Lowered antioxidant defenses and increased oxidative toxicity are hallmarks of deficit schizophrenia: a nomothetic network psychiatry approach. *Mol. Neurobiol.* 57, 4578–4597. doi: 10.1007/s12035-020-02047-5

Podwalski, P., Tyburski, E., Szczygieł, K., Rudkowski, K., Waszczuk, K., Andrusewicz, W., et al. (2022). Psychopathology and integrity of the superior longitudinal fasciculus in deficit and nondeficit schizophrenia. *Brain Sci.* 12:267. doi: 10.3390/brainsci12020267

Potvin, S., Giguere, C., and Mendrek, A. (2021). Functional connectivity during visuospatial processing in schizophrenia: a classification study using lasso regression. *Neuropsychiatr. Dis. Treat.* 17, 1077–1087. doi: 10.2147/NDT.S304434

Schrouff, J., Rosa, M. J., Rondina, J. M., Marquand, A. F., Chu, C., Ashburner, J., et al. (2013). PRoNTo: pattern recognition for neuroimaging toolbox. *Neuroinformatics* 11, 319–337.

Schultz, R., Gauthier, I., Klin, A., Fulbright, R., Anderson, A., Volkmar, F., et al. (2000). Abnormal ventral temporal cortical activity during face discrimination among individuals with autism and Asperger syndrome. *Arch. Gen. Psychiatry* 57, 331–340. doi: 10.1001/archpsyc.57.4.331

Skudlarski, P., Jagannathan, K., Anderson, K., Stevens, M., Calhoun, V., Skudlarska, B., et al. (2010). Brain connectivity is not only lower but different in schizophrenia: a combined anatomical and functional approach. *Biol. Psychiatry* 68, 61–69.

Strauss, G., Harrow, M., Grossman, L., and Rosen, C. (2010). Periods of recovery in deficit syndrome schizophrenia: a 20-year multi-follow-up longitudinal study. *Schizophr. Bull.* 36, 788–799. doi: 10.1093/schbul/sbn167

Taylor, J., Larsen, K., and Garrido, M. (2020). Multi-dimensional predictions of psychotic symptoms via machine learning. *Hum. Brain Mapp.* 41, 5151–5163. doi: 10.1002/hbm.25181

Wang, H., Rau, C., Li, Y., Chen, Y., and Yu, R. (2015). Disrupted thalamic resting-state functional networks in schizophrenia. *Front. Behav. Neurosci.* 9:45. doi: 10.3389/fnbeh.2015.00045

Wang, S., Zhang, Y., Lv, L., Wu, R., Fan, X., Zhao, J., et al. (2018). Abnormal regional homogeneity as a potential imaging biomarker for adolescent-onset schizophrenia: a resting-state fMRI study and support vector machine analysis. *Schizophr. Res.* 192, 179–184. doi: 10.1016/j.schres.2017.05.038

Wang, X., Yao, S., Kirkpatrick, B., Shi, C., and Yi, J. (2008). Psychopathology and neuropsychological impairments in deficit and nondeficit schizophrenia of Chinese origin. *Psychiatry Res.* 158, 195–205. doi: 10.1016/j.psychres.2006.09.007

Wood, A., Rychlowska, M., Korb, S., and Niedenthal, P. (2016). Fashioning the face: sensorimotor simulation contributes to facial expression recognition. *Trends Cogn. Sci.* 20, 227–240. doi: 10.1016/j.tics.2015.12.010

Woods, S. W. (2003). Chlorpromazine equivalent doses for the newer atypical anti-psychotics. *J. Clin. Psychiatry* 64, 663–667. doi: 10.4088/jcp.v64n0607

Wu, G., Palaniyappan, L., Zhang, M., Yang, J., Xi, C., Liu, Z., et al. (2022). Imbalance between prefronto-thalamic and sensorimotor-thalamic circuitries associated with working memory deficit in schizophrenia. *Schizophr. Bull.* 48, 251–261. doi: 10.1093/schbul/sbab086

Yu, M., Dai, Z., Tang, X., Wang, X., Zhang, X., Sha, W., et al. (2017). Convergence and divergence of brain network dysfunction in deficit and non-deficit schizophrenia. *Schizophr. Bull.* 43, 1315–1328.

Zalesky, A., Fornito, A., Seal, M., Cocchi, L., Westin, C., Bullmore, E., et al. (2011). Disrupted axonal fiber connectivity in schizophrenia. *BiolPsychiatry* 69, 80–89.

Zhou, C., Tang, X., You, W., Wang, X., Zhang, X., Zhang, X., et al. (2019a). Altered patterns of the fractional amplitude of low-frequency fluctuation and functional connectivity between deficit and non-deficit schizophrenia. *Front. Psychiatry* 10:680. doi: 10.3389/fpsyt.2019.00680

Zhou, C., Yu, M., Tang, X., Wang, X., Zhang, X., Zhang, X., et al. (2019b). Convergent and divergent altered patterns of default mode network in deficit and non-deficit schizophrenia. *Prog. Neuropsychopharmacol. Biol. Psychiatry* 89, 427–434. doi: 10.1016/j.pnpbp.2018.10.012

Zhou, C., Xue, C., Chen, J., Amdanee, N., Tang, X., Zhang, H., et al. (2021). Altered functional connectivity of the nucleus accumbens network between deficit and non-deficit schizophrenia. *Front. Psychiatry* 12:704631. doi: 10.3389/fpsyt.2021.704631

frontiers | Frontiers in Neuroscience

TYPE Original Research
PUBLISHED 11 April 2023
DOI 10.3389/fnins.2023.1157858

Check for updates

OPEN ACCESS

EDITED BY
Fahmi Khalifa,
Morgan State University, United States

REVIEWED BY
Angel Mota,
MEDS4VETS: Medical Care for Veterans Abroad, Dominican Republic
Liwei Hu,
Shanghai Children's Medical Center, China

*CORRESPONDENCE
Yuting Zhang
✉ zhangyuting@cqmu.edu.cn
Lusheng Li
✉ lilusheng@cqmu.edu.cn

†These authors have contributed equally to this work and share last authorship

SPECIALTY SECTION
This article was submitted to Brain Imaging Methods, a section of the journal Frontiers in Neuroscience

RECEIVED 03 February 2023
ACCEPTED 27 March 2023
PUBLISHED 11 April 2023

CITATION
Wang Y, Wang L, Qin B, Hu X, Xiao W, Tong Z, Li S, Jing Y, Li L and Zhang Y (2023) Preoperative prediction of sonic hedgehog and group 4 molecular subtypes of pediatric medulloblastoma based on radiomics of multiparametric MRI combined with clinical parameters.
Front. Neurosci. 17:1157858.
doi: 10.3389/fnins.2023.1157858

COPYRIGHT
© 2023 Wang, Wang, Qin, Hu, Xiao, Tong, Li, Jing, Li and Zhang. This is an open-access article distributed under the terms of the Creative Commons Attribution License (CC BY). The use, distribution or reproduction in other forums is permitted, provided the original author(s) and the copyright owner(s) are credited and that the original publication in this journal is cited, in accordance with accepted academic practice. No use, distribution or reproduction is permitted which does not comply with these terms.

Preoperative prediction of sonic hedgehog and group 4 molecular subtypes of pediatric medulloblastoma based on radiomics of multiparametric MRI combined with clinical parameters

Yuanlin Wang[1], Longlun Wang[1], Bin Qin[1], Xihong Hu[2], Wenjiao Xiao[1], Zanyong Tong[1], Shuang Li[1], Yang Jing[3], Lusheng Li[4*†] and Yuting Zhang[1*†]

[1]Ministry of Education Key Laboratory of Child Development and Disorders, Chongqing Key Laboratory of Pediatrics, National Clinical Research Center for Child Health and Disorders, China International Science and Technology Cooperation Base of Child Development and Critical Disorders, Department of Radiology, Children's Hospital of Chongqing Medical University, Chongqing, China, [2]Department of Radiology, Children's Hospital of Fudan University, Shanghai, China, [3]Huiying Medical Technology Co., Ltd., Beijing, China, [4]Ministry of Education Key Laboratory of Child Development and Disorders, Chongqing Key Laboratory of Pediatrics, National Clinical Research Center for Child Health and Disorders, China International Science and Technology Cooperation Base of Child Development and Critical Disorders, Department of Neurosurgery, Children's Hospital of Chongqing Medical University, Chongqing, China

Purpose: To construct a machine learning model based on radiomics of multiparametric magnetic resonance imaging (MRI) combined with clinical parameters for predicting Sonic Hedgehog (SHH) and Group 4 (G4) molecular subtypes of pediatric medulloblastoma (MB).

Methods: The preoperative MRI images and clinical data of 95 patients with MB were retrospectively analyzed, including 47 cases of SHH subtype and 48 cases of G4 subtype. Radiomic features were extracted from T1-weighted imaging (T1), contrast-enhanced T1 weighted imaging (T1c), T2-weighted imaging (T2), T2 fluid-attenuated inversion recovery imaging (T2FLAIR), and apparent diffusion coefficient (ADC) maps, using variance thresholding, SelectKBest, and Least Absolute Shrinkage and Selection Operator (LASSO) regression algorithms. The optimal features were filtered using LASSO regression, and a logistic regression (LR) algorithm was used to build a machine learning model. The receiver operator characteristic (ROC) curve was plotted to evaluate the prediction accuracy, and verified by its calibration, decision and nomogram. The Delong test was used to compare the differences between different models.

Results: A total of 17 optimal features, with non-redundancy and high correlation, were selected from 7,045 radiomics features, and used to build an LR model. The model showed a classification accuracy with an under the curve (AUC) of 0.960 (95% CI: 0.871–1.000) in the training cohort and 0.751 (95% CI: 0.587–0.915) in the testing cohort, respectively. The location of the tumor, pathological type, and hydrocephalus status of the two subtypes of patients differed significantly ($p < 0.05$). When combining radiomics features and clinical parameters to

construct the combined prediction model, the AUC improved to 0.965 (95% CI: 0.898–1.000) in the training cohort and 0.849 (95% CI: 0.695–1.000) in the testing cohort, respectively. There was a significant difference in the prediction accuracy, as measured by AUC, between the testing cohorts of the two prediction models, which was confirmed by Delong's test (p = 0.0144). Decision curves and nomogram further validate that the combined model can achieve net benefits in clinical work.

Conclusion: The combined prediction model, constructed based on radiomics of multiparametric MRI and clinical parameters can potentially provide a non-invasive clinical approach to predict SHH and G4 molecular subtypes of MB preoperatively.

KEYWORDS

medulloblastoma, radiomics, molecular subtypes, machine learning, prediction models

1. Introduction

Medulloblastoma (MB) is one of the most common malignant brain tumors, and accounts for 15–20% of central nervous system tumors in children and 40% of tumors in the posterior cranial fossa (Kumar et al., 2015; Massimino et al., 2016; Northcott et al., 2019). Prior to the emergence of molecular diagnostics, MB was classified histologically into subtypes including classic, extensive nodularity, desmoplastic or nodular, and large cell or anaplastic. However, recent studies have found that histopathological classification does not provide better prediction for the prognosis of patients and guidance of clinical treatment (Louis et al., 2016; Massimino et al., 2016).

With the development of molecular diagnostic techniques, the 2016 World Health Organization (WHO) classification of central nervous system tumors classified MB into four molecular subtypes, including wingless (WNT), sonic hedgehog (SHH, TP53 mutant, or wild type), Group 3 (G3), and Group 4 (G4) (Louis et al., 2016). Different molecular subtypes have different molecular mechanisms, clinical characteristics, and prognosis (Eid and Heabah, 2021; Fang et al., 2022). The WNT-activated type, which accounts for approximately 10% of MB, with a 1:1 male and female incidence ratio, originates in the rhombomere lip and dorsal brainstem of older children, has the best clinical outcomes, and is usually accompanied by an exon 3 activating mutation in *CTNNB1* and Chromosome 6 monomers (Ramaswamy et al., 2016; Colafati et al., 2018). The SHH-activated type, which accounts for approximately 30% of MB, originating from cerebellar granule cells, has a moderate prognosis, and the common molecular variants are *TP53*, *PTCH1*, *SUFU*, *SMO*, and other genes mutations (Colafati et al., 2018; Waszak et al., 2018; Hovestadt et al., 2019). In the non-WNT/SHH-activated type (G3 and G4), which accounts for approximately 25 and 35% of MB, respectively, the main common molecular variants are frequent *MYC*, *MYCN*, and, *OTX2* amplification. Patients in the G4 group with i17q or chromosome 11 deletion have a better prognosis compared to G3, but the prognosis of G4 is significantly worse compared to SHH or WNT-activated types (Zhao et al., 2016; Archer et al., 2017).

The published methods of molecular classification are invasive, relying mostly on gene expression and methylation analyses. In recent years, rapid advances in radiomics and machine learning techniques have made it possible to preoperatively predict MB molecular subtypes non-invasively. Radiomics is a quantitative analysis method of standard medical imaging that extracts a large number of quantitative features from CT, MRI, and PET images through advanced image analysis tools combined with statistical analysis and is now widely used in various clinical fields, such as increasing precision in diagnosis, predicting prognosis and therapy response (Hassani et al., 2019; Chu et al., 2021; Liang et al., 2021; Zhai et al., 2021; Guiot et al., 2022).

Recently, some studies have used a single MRI sequence or ADC values to construct prediction models for the prediction of MB molecular subtypes (Iv et al., 2019; Gonçalves et al., 2022; Saju et al., 2022). However, the results are still unstable, and there are fewer reports on constructing prediction models based on multiparametric MRI combined with clinical parameters for the prediction of MB molecular subtype. It was found that SHH and G4 were the most common molecular subtypes of MB in children, and the prognosis differed significantly between these two subtypes (Taylor et al., 2012). Total resection of the tumor in patients with G4 type has great importance in improving progression-free survival, especially in the presence of metastatic tumor spread preoperatively (Packer and Vezina, 2008; Thompson et al., 2016, 2018). Therefore, early preoperative prediction of molecular subtypes can help tailor individualized treatment and improve long-term prognosis.

In this study, we retrospectively analyzed MRI images and clinical data of 95 patients with MB to construct a machine learning model based on radiomics of multiparametric MRI combined with clinical parameters for predicting SHH and G4 molecular subtypes of pediatric MB.

2. Materials and methods

2.1. Patient characteristics

The Institutional Review Committees of our hospital approved the study. MRI imaging data and clinical data of patients with MB who were treated and followed up in the Children's Hospital

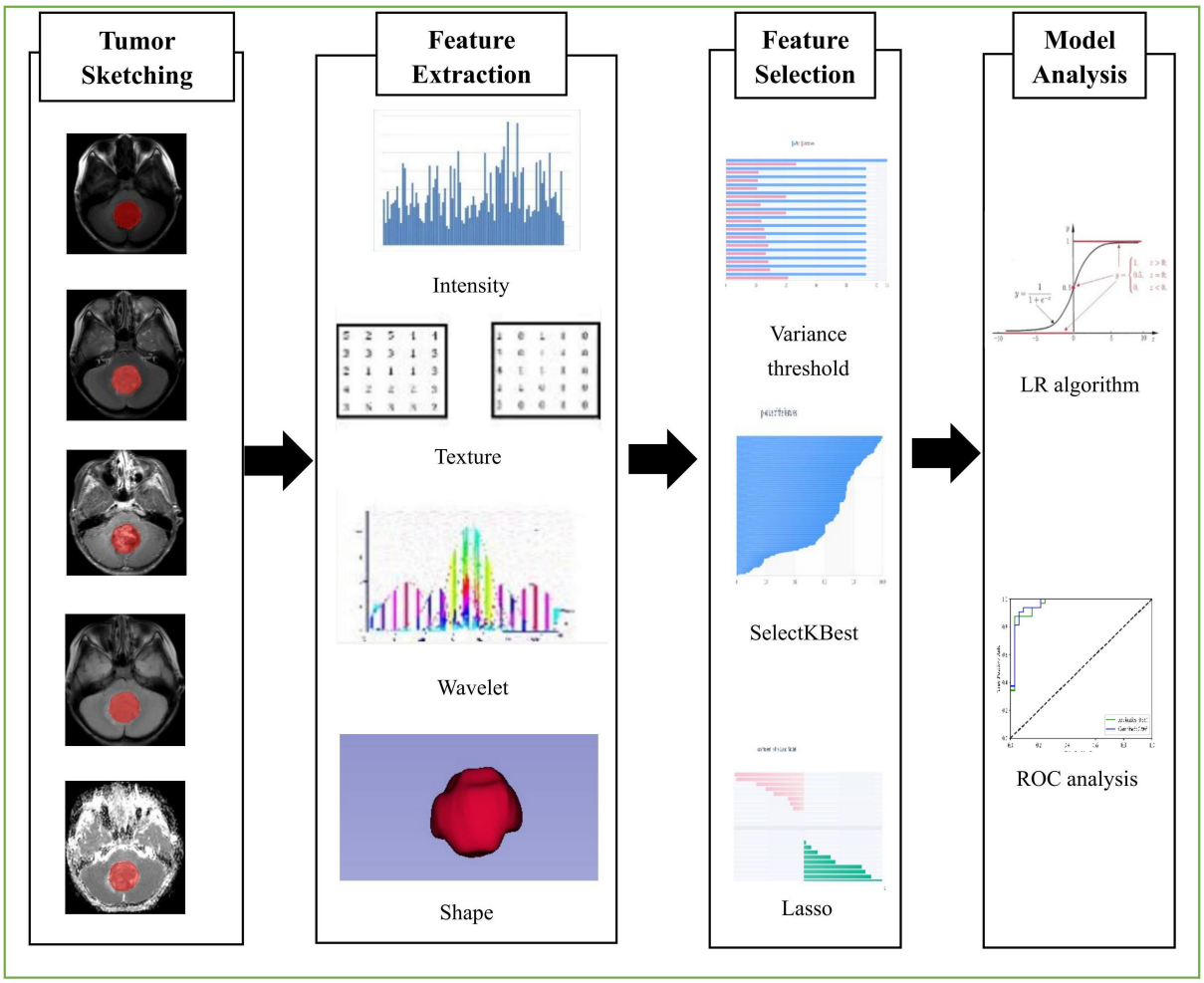

FIGURE 1
Flowchart shows the process of radiomics in this study, including tumor sketching, feature extraction, feature selection, and model analysis.

of Chongqing Medical University and the Children's Hospital of Fudan University from October 2015 to October 2022 were collected. Inclusion criteria were: (1) availability of sufficient image quality preoperative, including axial T1, T2, T1C, T2FLAIR, and ADC maps; (2) availability of postoperative pathological and molecular subtype; (3) availability of complete clinical follow-up data. Exclusion criteria: molecular subtypes that could not be modeled due to the small number of cases were excluded. Exclusion criteria were: molecular subtypes that have fewer cases failed to build a model. 12 cases of WNT, 17 cases of G3, and 1 case of not otherwise specified (NOS) were excluded. Finally, 47 cases of SHH group and 48 cases of G4 group (90 cases from the Children's Hospital of Chongqing Medical University and 5 cases from the Children's Hospital of Fudan University) were enrolled.

2.2. Detection methods of molecular subtypes

The acquisition of molecular subtypes includes transcriptome-related assays and genome-related assays. Transcriptome assay use RNAseq methods to detect the expression levels of genes in the subjects, which can assist in determining the molecular subtype and prognosis of MB through the assessment of the expression levels of genes related to molecular typing. Genomic assay cover common variant types, including point mutations, insertions, deletions, amplifications, and fusions, in 687 genes related to tumors. This includes genetic variants highly related to the molecular subtype of MB molecular typing and other genetic variants related to molecular typing and drug use.

2.3. MRI acquisition

All patients underwent brain MR imaging at 1.5T or 3.0T (Signa EXCITE HD, GE Healthcare, Chicago, IL, United States; Discovery MR750, GE Healthcare, Milwaukee, WI, United States; Achieva, Philips Healthcare, Best, Netherlands), with scanning sequences encompassing axial T1, T2, T2FLAIR, T1c, and DWI (*b*-value taken as 1,000, with subsequent post-processing for ADC map generation). Details of the parameters for all the sequence acquisition are available in Supplementary Table 1.

TABLE 1 Clinical information of SHH and G4 groups.

Clinical data	SHH (n = 47)	G4 (n = 48)	P-value
Hydrocephalus			
Absent	35	45	0.022
Present	12	3	
Location			
Cerebellum	23	2	0
Midline	24	46	
Pathological typing			
Classic	11	46	0
Desmoplastic or nodular	32	0	
Large cell or anaplastic	2	2	
Extensive nodularity	2	0	
Age ($x \pm s$, year)	6.75 ± 3.54	7.50 ± 2.97	0.217
Sex			
Female	15	18	0.568
Male	32	30	
Renal function			
Abnormal	1	0	0.495
Normal	46	48	
Liver function			
Abnormal	2	1	0.985
Normal	45	47	
Preoperative metastases			
Absent	7	6	0.734
Present	40	42	
Intracranial hypertension			
Absent	40	45	0.299
Present	7	3	
Ataxia			
Absent	13	18	0.306
Present	34	30	
Follow up recurrence or metastases			
Absent	12	9	0.426
Present	35	39	

2.4. Image uploading and tumor sketching

The steps of radiomics analysis are shown in Figure 1. Five sequence images of each patient were uploaded using the big data artificial intelligence research cloud platform developed by Huiying Medical Technology (Beijing) Co. A physician manually outlined regions of interest (ROI) for each sequence, layer by layer, for each case, using the platform's built-in tools. An automatic computer-generated 3D volume of interest (VOI) of the lesion was obtained. The tumor boundary was outlined without peritumoral edema and reviewed by an experienced pediatric radiologist with 10 years of expertise in neuroimaging. If the regional variation was more than 5%, the boundary was decided by a senior physician, and neither of the two physicians knew the patient's information during this procedure.

TABLE 2 Seventeen optimal radiomic features.

Radiomic feature	Radiomic class	Filter
High gray level zone emphasis is	glszm	MB-ADC_wavelet-HHL
High gray level zone emphasis	glszm	MB-FLAIR_wavelet-LHH
Large dependence low gray level emphasis	gldm	MB-T2_wavelet-LLL
Run variance	glrlm	MB-FLAIR_wavelet-LLH
Busyness	ngtdm	MB-ADC_wavelet-LLH
Zone entropy	glszm	MB-FLAIR_wavelet-LLH
Zone variance	glszm	MB-FLAIR_wavelet-HHL
Skewness	firstorder	MB-T1_wavelet-HLL
Kurtosis	firstorder	MB-ADC_exponential
Dependence variance	gldm	MB-FLAIR_wavelet-LHL
High gray level zone emphasis	glszm	MB-T1C_wavelet-HHL
Size zone non-uniformity	glszm	MB-FLAIR_wavelet-HLL
Variance	firstorder	MB-T1C_wavelet-LLL
Small area high gray level emphasis	glszm	MB-ADC_wavelet-HHH
Zone entropy	glszm	MB-FLAIR_original
Zone entropy	glszm	MB-FLAIR_logarithm
Range	firstorder	MB-FLAIR_logarithm

2.5. Radiomics feature extraction

A total of 7,045 quantitative imaging radiomics features were extracted from the outlined ROIs using the open source Python language environment toolkit Pyradiomics based on the Huiying Big Data research platform, and these features can be classified into four categories: ① Intensity statistics characterization: The distribution of voxel intensities within MR images is described quantitatively by commonly used and basic metrics. ② Shape and size features: These features reflect the shape and size of the ROI. ③ Texture features: Based on the gray level run-length and gray level co-occurrence texture matrix calculation, we get the texture features that can quantify the difference of regional heterogeneity. ④ High-order statistical features, intensity, and texture features of the transformed image are calculated again using various filters such as exponential, logarithmic, square, square root, and wavelet (including wavelet-LHL, wavelet-LHH, wavelet-HLL, wavelet-LLH, wavelet-HLH, wavelet-HHL, and wavelet-LLL).

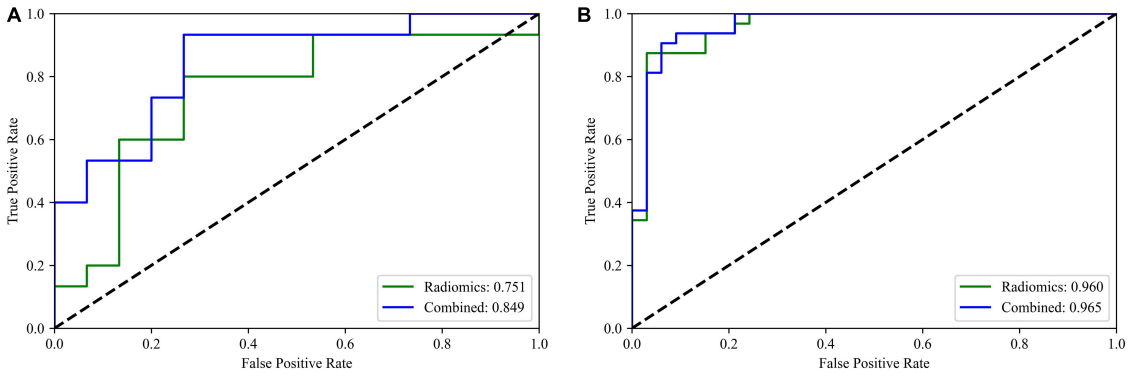

FIGURE 2
(A,B) ROC curves of the radiomics and combined model on the testing cohort and training cohort, respectively.

2.6. Feature selection

As described above, we extracted quantitative imaging radiomics features from the five-sequence image ROIs of 95 patients. However, it is unlikely that all of these extracted features will be useful for a given task. Therefore, using feature downscaling to filter the specific features that are most relevant to this study for best performance is a necessary step. To reduce redundant features, feature selection methods include variance threshold (threshold value = 0.8), SelectKBest, and the least absolute shrinkage and selection operator (LASSO). For the variance threshold, the threshold value is 0.8, so feature values with variances less than 0.8 are removed. The SelectKBest method is a univariate feature selection method that uses *p*-values to analyze the relationship between features and classification results, which will allow screening all features with *p*-values less than 0.05. For LASSO regression, the L1 regularizer is used as the cost function, with a maximum number of iterations of 1,000. Finally, we obtain 17 optimal feature subsets.

2.7. Machine learning classification

Based on the selected feature subsets, the LR algorithm was used to construct the radiomics feature model and the combined model of radiomics features and clinical parameters, respectively, and the patients were divided into training and testing cohorts by the random grouping method in the ratio of 7:3 to obtain the classification prediction results.

TABLE 3 AUC, 95% CI, sensitivity, and specificity of radiomics model in training cohort and testing cohort.

Cohort	AUC	95% CI	Sensitivity	Specificity
Training cohort	0.960	0.871–1.000	0.880	0.850
Testing cohort	0.751	0.587–0.915	0.730	0.730

TABLE 4 AUC, 95% CI, sensitivity and specificity of combined model in training cohort and testing cohort.

Cohort	AUC	95% CI	Sensitivity	Specificity
Training cohort	0.965	0.898–1.000	0.910	0.940
Testing cohort	0.849	0.695–0.915	0.800	0.730

2.8. Statistical analysis

Clinical data were statistically analyzed using SPSS 25.0 statistical software. Measurement data that conforms to a normal distribution were presented as $x \pm s$, and the independent samples *t*-test was used to compare the differences between groups. Categorical data were tested using the χ^2 test or Fisher's exact test, and differences were considered statistically significant at $P < 0.05$. For the machine learning results, ROC curves were used in the training cohort and testing cohort to compare model prediction accuracy and calculate AUC, sensitivity, and specificity. The Delong test was used to compare the AUC differences between the ROC curves of the two models, and $P < 0.05$ was considered statistically significant.

3. Results

3.1. Clinical features

A total of 95 patients with MB were enrolled in this study, including 47 cases of SHH and 48 cases of G4. The clinical data such as gender, age, tumor location, clinical symptoms and physical signs, hydrocephalus status, metastasis or recurrence status, blood biochemical indexes, and pathological typing were collected. There were no significant differences in age, gender, renal function, liver function, intracranial hypertension, ataxia and preoperative metastases, recurrence or metastases at follow-up between these two groups ($P > 0.05$). Pre-dominant pathological typing was desmoplastic or nodular in SHH and classic in G4. The tumor location was mainly in the cerebellum (cerebellar hemisphere or pontine arm) in SHH and in the midline (four ventricles or cerebellar vermis) in G4. Compared with patients in SHH, those in G4 had a higher likelihood of developing hydrocephalus. These differences between groups were statistically significant ($P < 0.05$), as shown in Table 1.

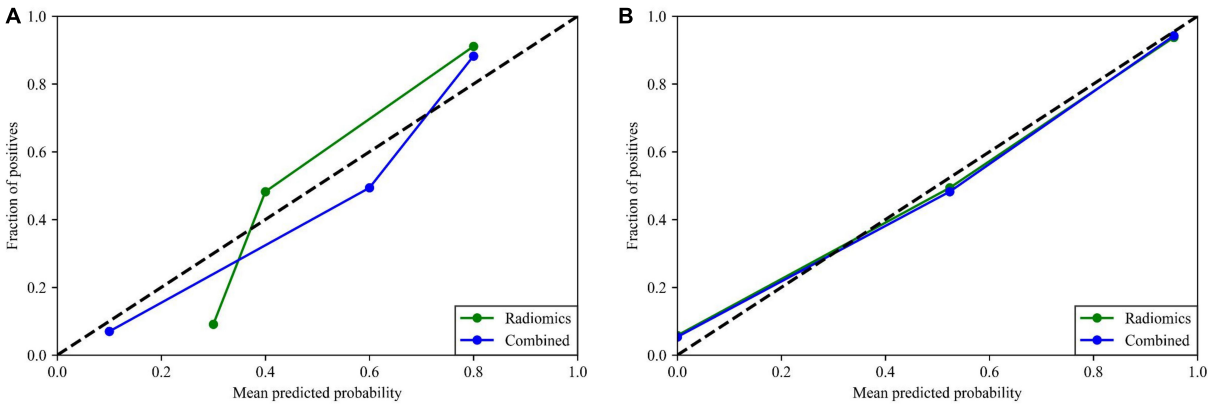

FIGURE 3
(A,B) Calibration curves of the radiomics and combined model on the testing cohort and training cohort, respectively.

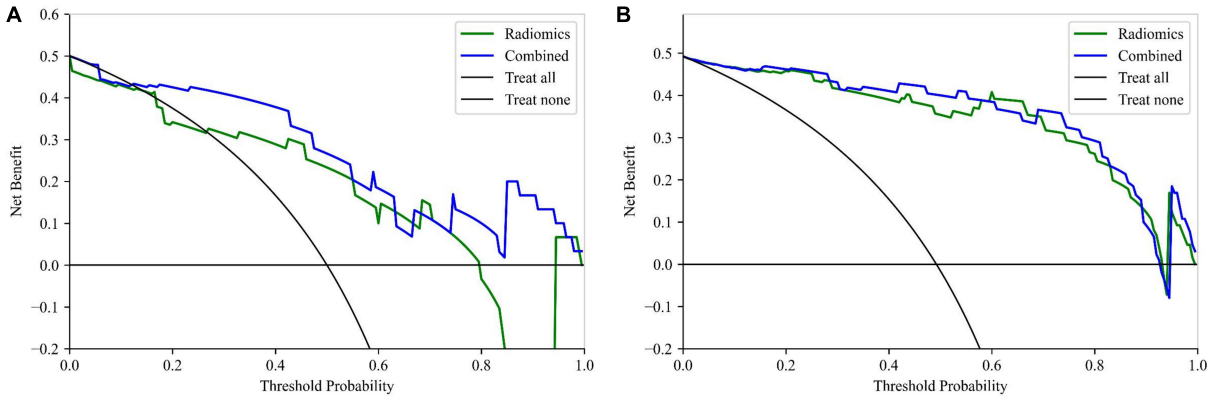

FIGURE 4
(A,B) Decision curves of the radiomics and combined model on the testing cohort and training cohort, respectively.

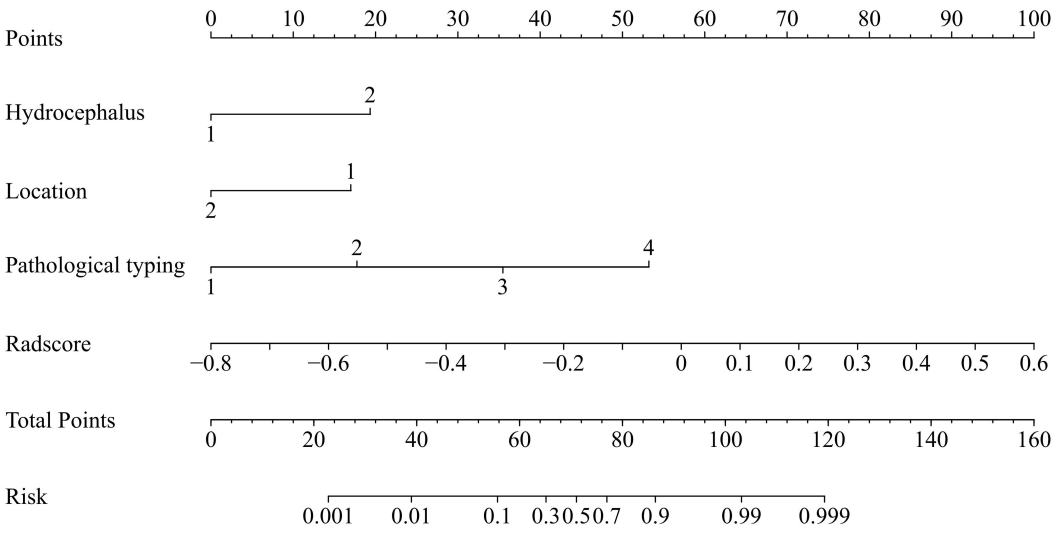

FIGURE 5
Nomogram based on clinical and radiomics score.

TABLE 5 Delong test result.

	Training cohort radiomics model/Combined model	Testing cohort radiomics model/Combined model
AUC	0.960/0.965	0.751/0.849
P-value	0.4604	0.0144

3.2. Radiomic features

A total of 7,045 quantitative imaging features were extracted from the five sequence images of 95 patients, and 17 optimal feature sets, including 13 texture features and 4 intensity features, were obtained after dimensionality reduction using variance threshold (threshold = 0.8), SelectKBest, and the LASSO regression algorithm. The details were shown in **Table 2**.

3.3. Model performance

In the radiomics feature model, the AUC was 0.960 (95% CI: 0.871−1.000), and the sensitivity and specificity were 0.880 and 0.850, respectively, in the training cohort. In the testing cohort, the AUC was 0.751 (95% CI: 0.587−0.915), and the sensitivity and specificity were 0.730 and 0.730, respectively. In the radiomics features and clinical parameters combined model, the AUC was 0.965 (95% CI: 0.898−1.000), and the sensitivity and specificity were 0.910 and 0.940, respectively, in the training cohort. In the testing cohort, the AUC was 0.849 (95% CI: 0.695−1.000), and the sensitivity and specificity were 0.800 and 0.730, respectively. The ROC curves for both the training and testing cohorts are shown in **Figures 2A, B** and **Tables 3**, **4**. The calibration curves show the goodness of fit between the predicted molecular subtypes and actual molecular subtypes in both the training and testing cohort for the radiomics model and the combined model (**Figures 3A, B**). The decision curves show that the combined model outperforms the radiomics model in terms of net benefit (**Figures 4A, B**). The clinical utility of both prediction models is demonstrated by the nomogram (**Figure 5**).

Delong test results showed the difference of prediction accuracy measured by AUC in the testing cohort of the two prediction models has statistical significance. The results were shown in **Table 5**.

4. Discussion

Medulloblastoma is a highly aggressive brain tumor, the therapeutic strategies and clinical prognosis vary significantly among molecular subtypes. The published methods of molecular classification are invasive, relying mostly on gene expression and methylation analyses. Due to the tumor tissue heterogeneity, the biopsy tissue specimens cannot fully capture the whole tumor tissue information. In this study, we extracted radiomics features of the entire tumor region and combined them with clinical parameters to build a prediction model for SHH and G4 molecular subtypes of pediatric MB. The results showed that the combined model had significant classification efficacy with an AUC > 0.8 in the testing cohort, potentially providing a non-invasive clinical approach to preoperatively predict SHH and G4 molecular subtypes of MB.

In this study, we used clinical characteristics, including hydrocephalus status, tumor location, and pathological type, to construct a combined model for predicting SHH and G4 molecular subtypes of MB. In our study, there were no significant differences in age and gender between the two molecular subtypes, which is not consistent with the previous studies reported by Taylor et al. (2012) and Eid and Heabah (2021). We suspect that this may be due to the small sample size of our cohort. Similar to a recent study by Yan et al. (2020) that enrolled 122 patients, our study also showed that the tumor location and hydrocephalus status differed in molecular subtypes and were combined in the model to improve predictive efficacy.

In our study, 17 optimal radiomics features were selected, containing 13 texture features and 4 intensity features. A multicenter study of 263 patients from 12 children's hospitals reported that texture features and first-order intensity features contributed the most to improving the predictive efficacy of the model (Zhang et al., 2022). In the study by Yan et al. (2020), three texture features and eight intensity features were extracted to construct the model. Also, in the study by Chang et al. (2021), 38 children from Taipei showed significant differences in eight textural features among different molecular subtypes. In a systematic review and meta-analysis on radiomics-based machine learning for predicting molecular subtypes of MB (Karabacak et al., 2022), five articles enrolled 420 patients with MB, and the results showed that the mean AUC of prediction models for all MB molecular subtypes was >0.8, indicating a greater possibility of predicting MB molecular subtypes by radiomics studies. Compared with the above-mentioned studies, our study used comprehensive image features of five sequences including T1, T2, T1C, T2FLAIR, and ADC maps, and combined them with clinical parameters to construct a combined model with improved prediction accuracy. The AUC was 0.965 in the training cohort and 0.849 in the testing cohort, respectively, which can be used to facilitate the prediction of SHH and G4 molecular subtypes of MB preoperatively.

This study had some limitations. First, the number of cases in the SHH and G4 groups enrolled in this study was relatively small, and the WNT and G3 groups were not included in the study because the number of cases did not meet the modeling requirements. Further expansion of the sample size is needed to conduct a multicenter, prospective study. Second, the results of this study lack external validation to better assess the generalizability of the model, which still needs further investigation.

5. Conclusion

In summary, our study demonstrated that a combined prediction model based on the radiomics features of multiparametric MRI and clinical parameters can effectively predict the SHH and G4 molecular subtypes of MB prior to surgery. These findings highlight the potential of radiomics and machine learning techniques for non-invasive preoperative prediction of MB molecular subtypes.

Data availability statement

The original contributions presented in this study are included in the article/Supplementary material, further inquiries can be directed to the corresponding authors.

Ethics statement

Written informed consent was obtained from the individual(s), and minor(s)' legal guardian/next of kin, for the publication of any potentially identifiable images or data included in this article.

Author contributions

YW wrote the manuscript and which was revised by the YZ and LL. LW, BQ, and YJ contributed to the data processing and statistical analysis. WX, XH, ZT, and SL contributed to the data collection. All authors contributed to the article and approved the submitted version.

Funding

This study was supported by the grants from Chongqing Medical Scientific Research Project (Joint Project of Chongqing Health Commission and Science and Technology Bureau) (No. 2023ZDXM023).

Conflict of interest

YJ was employed by Huiying Medical Technology Co., Ltd.

The remaining authors declare that the research was conducted in the absence of any commercial or financial relationships that could be construed as a potential conflict of interest.

Publisher's note

All claims expressed in this article are solely those of the authors and do not necessarily represent those of their affiliated organizations, or those of the publisher, the editors and the reviewers. Any product that may be evaluated in this article, or claim that may be made by its manufacturer, is not guaranteed or endorsed by the publisher.

Supplementary material

The Supplementary Material for this article can be found online at: https://www.frontiersin.org/articles/10.3389/fnins.2023.1157858/full#supplementary-material

References

Archer, T., Mahoney, E., and Pomeroy, S. (2017). Medulloblastoma: molecular classification-based personal therapeutics. *Neurotherapeutics* 14, 265–273. doi: 10.1007/s13311-017-0526-y

Chang, F., Wong, T., Wu, K., Lu, C., Weng, T., Liang, M., et al. (2021). Magnetic resonance radiomics features and prognosticators in different molecular subtypes of pediatric medulloblastoma. *PLoS One* 16:e0255500. doi: 10.1371/journal.pone.0255500

Chu, H., Liu, Z., Liang, W., Zhou, Q., Zhang, Y., Lei, K., et al. (2021). Radiomics using CT images for preoperative prediction of futile resection in intrahepatic cholangiocarcinoma. *Eur. Radiol.* 31, 2368–2376. doi: 10.1007/s00330-020-07250-5

Colafati, G., Voicu, I., Carducci, C., Miele, E., Carai, A., Di Loreto, S., et al. (2018). MRI features as a helpful tool to predict the molecular subgroups of medulloblastoma: state of the art. *Ther. Adv. Neurol. Disord.* 11:1756286418775375. doi: 10.1177/1756286418775375

Eid, A., and Heabah, N. (2021). Medulloblastoma: clinicopathological parameters, risk stratification, and survival analysis of immunohistochemically validated molecular subgroups. *J. Egypt. Natl. Canc. Inst.* 33:6. doi: 10.1186/s43046-021-00060-w

Fang, F., Rosenblum, J., Ho, W., and Heiss, J. (2022). New developments in the pathogenesis, therapeutic targeting, and treatment of pediatric medulloblastoma. *Cancers* 14:2285. doi: 10.3390/cancers14092285

Gonçalves, F., Tierradentro-Garcia, L., Kim, J., Zandifar, A., Ghosh, A., Viaene, A., et al. (2022). The role of apparent diffusion coefficient histogram metrics for differentiating pediatric medulloblastoma histological variants and molecular groups. *Pediatr. Radiol.* 52, 2595–2609. doi: 10.1007/s00247-022-05411-w

Guiot, J., Vaidyanathan, A., Deprez, L., Zerka, F., Danthine, D., Frix, A., et al. (2022). A review in radiomics: making personalized medicine a reality via routine imaging. *Med. Res. Rev.* 42, 426–440. doi: 10.1002/med.21846

Hassani, C., Varghese, B., Nieva, J., and Duddalwar, V. (2019). Radiomics in pulmonary lesion imaging. *Am. J. Roentgenol.* 212, 497–504. doi: 10.2214/AJR.18.20623

Hovestadt, V., Smith, K., Bihannic, L., Filbin, M., Shaw, M., Baumgartner, A., et al. (2019). Resolving medulloblastoma cellular architecture by single-cell genomics. *Nature* 572, 74–79. doi: 10.1038/s41586-019-1434-6

Iv, M., Zhou, M., Shpanskaya, K., Perreault, S., Wang, Z., Tranvinh, E., et al. (2019). MR imaging-based radiomic signatures of distinct molecular subgroups of medulloblastoma. *Am. J. Neuroradiol.* 40, 154–161. doi: 10.3174/ajnr.A5899

Karabacak, M., Ozkara, B., Ozturk, A., Kaya, B., Cirak, Z., Orak, E., et al. (2022). Radiomics-based machine learning models for prediction of medulloblastoma subgroups: a systematic review and meta-analysis of the diagnostic test performance. *Acta Radiol.* [Epub ahead of print]. doi: 10.1177/02841851221143496

Kumar, L., Deepa, S., Moinca, I., Suresh, P., and Naidu, K. (2015). Medulloblastoma: a common pediatric tumor: prognostic factors and predictors of outcome. *Asian J. Neurosurg.* 10:50. doi: 10.4103/1793-5482.151516

Liang, H., Chen, Z., Wei, F., Yang, R., and Zhou, H. (2021). Bibliometrics research on radiomics of lung cancer. *Transl. Cancer Res.* 10, 3757–3771. doi: 10.21037/tcr-21-1277

Louis, D., Perry, A., Reifenberger, G., von Deimling, A., Figarella-Branger, D., Cavenee, W., et al. (2016). The 2016 World Health Organization classification of tumors of the central nervous system: a summary. *Acta Neuropathol.* 131, 803–820. doi: 10.1007/s00401-016-1545-1

Massimino, M., Biassoni, V., Gandola, L., Garrè, M., Gatta, G., Giangaspero, F., et al. (2016). Childhood medulloblastoma. *Crit. Rev. Oncol. Hematol.* 105, 35–51. doi: 10.1016/j.critrevonc.2016.05.012

Northcott, P. A., Robinson, G., Kratz, C., Mabbott, D., Pomeroy, S., Clifford, S., et al. (2019). Medulloblastoma. *Nat. Rev. Dis. Primers* 5:11. doi: 10.1038/s41572-019-0063-6

Packer, R., and Vezina, G. (2008). Management of and prognosis with medulloblastoma: therapy at a crossroads. *Arch. Neurol.* 65, 1419–1424. doi: 10.1001/archneur.65.11.1419

Ramaswamy, V., Remke, M., Bouffet, E., Bailey, S., Clifford, S., Doz, F., et al. (2016). Risk stratification of childhood medulloblastoma in the molecular era: the current consensus. *Acta Neuropathol.* 131, 821–831. doi: 10.1007/s00401-016-1569-6

Saju, A., Chatterjee, A., Sahu, A., Gupta, T., Krishnatry, R., Mokal, S., et al. (2022). Machine-learning approach to predict molecular subgroups of medulloblastoma using multiparametric MRI-based tumor radiomics. *Br. J. Radiol.* 95:20211359. doi: 10.1259/bjr.20211359

Taylor, M., Northcott, P., Korshunov, A., Remke, M., Cho, Y., Clifford, S., et al. (2012). Molecular subgroups of medulloblastoma: the current consensus. *Acta Neuropathol.* 123, 465–472. doi: 10.1007/s00401-011-0922-z

Thompson, E., Bramall, A., Herndon, J., Taylor, M., and Ramaswamy, V. (2018). The clinical importance of medulloblastoma extent of resection: a systematic review. *J. Neurooncol.* 139, 523–539. doi: 10.1007/s11060-018-2906-5

Thompson, E., Hielscher, T., Bouffet, E., Remke, M., Luu, B., Gururangan, S., et al. (2016). Prognostic value of medulloblastoma extent of resection after accounting for molecular subgroup: a retrospective integrated clinical and molecular analysis. *Lancet Oncol.* 17, 484–495. doi: 10.1016/S1470-2045(15)00581-1

Waszak, S., Northcott, P., Buchhalter, I., Robinson, G., Sutter, C., Groebner, S., et al. (2018). Spectrum and prevalence of genetic predisposition in medulloblastoma: a retrospective genetic study and prospective validation in a clinical trial cohort. *Lancet Oncol.* 19, 785–798. doi: 10.1016/S1470-2045(18)30242-0

Yan, J., Liu, L., Wang, W., Zhao, Y., Li, K., Li, K., et al. (2020). Radiomic features from multi-parameter MRI combined with clinical parameters predict molecular subgroups in patients with medulloblastoma. *Front. Oncol.* 10:558162. doi: 10.3389/fonc.2020.558162

Zhai, Y., Song, D., Yang, F., Wang, Y., Jia, X., Wei, S., et al. (2021). Preoperative prediction of meningioma consistency via machine learning-based radiomics. *Front. Oncol.* 11:657288. doi: 10.3389/fonc.2021.657288

Zhang, M., Wong, S., Wright, J., Wagner, M., Toescu, S., Han, M., et al. (2022). MRI radiogenomics of pediatric medulloblastoma: a multicenter study. *Radiology* 304, 406–416. doi: 10.1148/radiol.212137

Zhao, F., Ohgaki, H., Xu, L., Giangaspero, F., Li, C., Li, P., et al. (2016). Molecular subgroups of adult medulloblastoma: a long-term single-institution study. *Neuro Oncol.* 18, 982–990. doi: 10.1093/neuonc/now050

frontiers | Frontiers in Neuroscience

TYPE Original Research
PUBLISHED 14 June 2023
DOI 10.3389/fnins.2023.1179963

Check for updates

OPEN ACCESS

EDITED BY
Fahmi Khalifa,
Morgan State University, United States

REVIEWED BY
Ru-dong Chen,
Shandong Provincial Hospital, China
Peng Wu,
Soochow University, China

*CORRESPONDENCE
Jian Guo
jian_guo@scu.edu.cn
Li He
heli2003new@126.com

†These authors have contributed equally to this work

RECEIVED 05 March 2023
ACCEPTED 26 May 2023
PUBLISHED 14 June 2023

CITATION
Bao J, Gan X, Feng W, Li Y, Qiu Y, Zhou M, Guo J and He L (2023) Abnormal flow pattern of low wall shear stress and high oscillatory shear index in spontaneous vertebral artery dissection with vertebral artery hypoplasia. *Front. Neurosci.* 17:1179963. doi: 10.3389/fnins.2023.1179963

COPYRIGHT
© 2023 Bao, Gan, Feng, Li, Qiu, Zhou, Guo and He. This is an open-access article distributed under the terms of the Creative Commons Attribution License (CC BY). The use, distribution or reproduction in other forums is permitted, provided the original author(s) and the copyright owner(s) are credited and that the original publication in this journal is cited, in accordance with accepted academic practice. No use, distribution or reproduction is permitted which does not comply with these terms.

Abnormal flow pattern of low wall shear stress and high oscillatory shear index in spontaneous vertebral artery dissection with vertebral artery hypoplasia

Jiajia Bao[1†], Xinling Gan[1†], Wentao Feng[2], Yanbo Li[1], Yue Qiu[3], Muke Zhou[1], Jian Guo[1*] and Li He[1*]

[1]Department of Neurology, West China Hospital, Sichuan University, Chengdu, China, [2]Key Laboratory of Biomechanics and Mechanobiology (Beihang University) Ministry of Education, Beijing Advanced Innovation Center for Biomedical Engineering, School of Biological Science and Medical Engineering, Beihang University, Beijing, China, [3]Department of Applied Mechanics, Sichuan University, Chengdu, China

Introduction: Spontaneous vertebral artery dissection (sVAD) might tend to develop in vertebral artery hypoplasia (VAH) with hemodynamic dysfunction and it is crucial to assess hemodynamics in sVAD with VAH to investigate this hypothesis. This retrospective study aimed to quantify hemodynamic parameters in patients with sVAD with VAH.

Methods: Patients who had suffered ischemic stroke due to an sVAD of VAH were enrolled in this retrospective study. The geometries of 14 patients (28 vessels) were reconstructed using Mimics and Geomagic Studio software from CT angiography (CTA). ANSYS ICEM and ANSYS FLUENT were utilized for mesh generation, set boundary conditions, solve governing equations, and perform numerical simulations. Slices were obtained at the upstream area, dissection or midstream area and downstream area of each VA. The blood flow patterns were visualized through instantaneous streamline and pressure at peak systole and late diastole. The hemodynamic parameters included pressure, velocity, time-averaged blood flow, time-averaged wall shear stress (TAWSS), oscillatory shear index (OSI), endothelial cell action potential (ECAP), relative residence time (RRT) and time-averaged nitric oxide production rate (TAR_{NO}).

Results: Significant focal increased velocity was present in the dissection area of steno-occlusive sVAD with VAH compared to other nondissected areas (0.910m/s vs. 0.449 vs. 0.566, $p<0.001$), while focal slow flow velocity was observed in the dissection area of aneurysmal dilatative sVAD with VAH according to velocity streamlines. Steno-occlusive sVAD with VAH arteries had a lower time-averaged blood flow (0.499cm^3/s vs. 2.268, $p<0.001$), lower TAWSS (1.115Pa vs. 2.437, $p= 0.001$), higher OSI (0.248 vs. 0.173, $p=0.006$), higher ECAP (0.328Pa^{-1} vs. 0.094, $p=0.002$), higher RRT (3.519Pa^{-1} vs. 1.044, $p=0.001$) and deceased TAR_{NO} (104.014nM/s vs. 158.195, $p<0.001$) than the contralateral VAs.

Conclusion: Steno-occlusive sVAD with VAH patients had abnormal blood flow patterns of focal increased velocity, low time-averaged blood flow, low TAWSS, high OSI, high ECAP, high RRT and decreased TAR_{NO}. These results provide a good basis for further investigation of sVAD hemodynamics and support the applicability of the CFD method in testing the hemodynamic hypothesis of

sVAD. More detailed hemodynamic conditions with different stages of sVAD are warranted in the future.

KEYWORDS

spontaneous vertebral artery dissection, vertebral artery hypoplasia, hemodynamic characteristics, blood flow patterns, computational fluid dynamics, nitric oxide production rate

Introduction

Spontaneous vertebral artery dissection (sVAD) occurs via a non-traumatic tearing of the arterial wall and is the second leading cause of stroke in young and middle-aged adults (Schievink, 2001; Ferro et al., 2010). However, the pathogenesis of sVAD remains obscure (Schievink, 2001; Debette and Leys, 2009). Accumulating evidence suggests that vertebral artery hypoplasia (VAH) is a significant independent risk factor for sVAD, as found in our previous study (Zhou et al., 2015; Günther et al., 2016). Asymmetric hemodynamics resulting from VAH make it more likely to cause ischemic events (Giannopoulos et al., 2007; Hong et al., 2009). Hence, we hypothesized that sVAD would tend to develop in VAH with hemodynamic dysfunction.

However, the complexity of the hemodynamic microenvironment in the vertebrobasilar system and the lack of *in vivo* models of sVAD and VAH that evaluate detailed hemodynamics have made it difficult to explicitly verify this hypothesis (Wake-Buck et al., 2012). Although previous studies used ultrasound and magnetic resonance imaging (MRI) to acquire hemodynamic data of sVAD and VAH, the accuracy of these measures is controversial (Augst et al., 2003; Giannopoulos et al., 2007; Hori et al., 2020). Therefore, it is crucial to realistically assess hemodynamic parameters in sVAD with VAH arteries to investigate this hypothesis. Computational fluid dynamics (CFD) has been widely utilized to analyze *in vivo* hemodynamics of healthy and diseased arteries because this technique allows the observation of flow patterns and quantification of hemodynamic parameters via simulation of a constructive model of patient-specific imaging data (Biasetti et al., 2010; Samady and Jaber, 2022).

To quantify hemodynamic parameters and investigate the potential hemodynamic characteristics of sVAD with VAH arteries, we performed CFD to reconstruct three-dimensional (3D) models and analyze the numerical simulation of sVAD with VAH arteries based on CT angiography (CTA) data. We further compared these hemodynamic parameters to contralateral healthy VAs, with the aim of providing direct and reliable evidence of hemodynamic characteristics in sVAD with VAH arteries and establishing a solid foundation for further investigations into sVAD hemodynamics.

Abbreviations: sVAD, spontaneous vertebral artery dissection; VAH, vertebral artery hypoplasia; VAs, vertebral arteries; MRI, magnetic resonance imaging; CFD, computational fluid dynamics; 3D, three-dimensional; CTA, CT angiography; NIHSS, the National Institutes of Health Stroke Scale; mRS, the modified Rankin Scale; STL, stereolithography; WSS, wall shear stress; SST, shear stress transport; PISO, pressure-implicit splitting of operators; TAWSS, time-averaged wall shear stress; OSI, oscillatory shear index; ECAP, endothelial cell action potential; RRT, relative residence time; NO, nitric oxide; TAR_{NO}, time-averaged nitric oxide production rate; ANOVA, analysis of variance; LSD, least significant difference; SDs, standard deviations; IMT, intima media thickening; ROS, reactive oxygen species.

Methods

Participants

Between October 1, 2014, and July 31, 2019, we retrospectively enrolled patients who suffered posterior circulation infarcts due to an sVAD of the hypoplastic VA in the Neurology department of West China Hospital. The Ethical Review Committee of the West China Hospital of Sichuan University approved this research [2020(69)]. Since this study is a retrospective study collecting de-identified data, the requirement of obtaining informed consent was waived. The following inclusion criteria were used for patient selection: (1) diagnosis of sVAD and VAH using previously described criteria (Maruyama et al., 2012; Zhou et al., 2015); (2) posterior circulation infarcts attributed to sVAD diagnosis based on clinical and radiological data (Adams et al., 1993); (3) sVAD on the side of hypoplastic VA; and (4) source images of CTA (DICOM format) before treatment. The following exclusion criteria were used: (1) the presence of multiple dissections in cervical arteries; (2) the presence of nondissected aneurysms or nondissected stenosis in cervical arteries; (3) history of associated connective tissue or vascular disorders; (4) history of head or neck trauma; (5) cervical intracranial artery malformation; (6) cervical and intracranial artery atherosclerosis; (7) time of sVAD onset to hospitalization was longer than 2 months (Schievink, 2001); and (8) incomplete information (e.g., poor 3D models because of insufficient quality of CTA imaging). We recorded detailed demographic and clinical characteristics, including lesion morphological subtypes. Stroke severity was assessed with the National Institutes of Health Stroke Scale (NIHSS) score on admission. Clinical outcome was evaluated with the modified Rankin Scale (mRS) at 3-month during clinical follow-up by face-to-face interview or telephone.

Computational fluid dynamics

Thin-slice CTA images of the sVAD with VAH arteries were obtained, and 3D models before treatment were reconstructed based on these CTA images (DICOM format) using the commercially available software Mimics (version 20.0; Materialise, NV, Belgium) and Geomagic Studio software (Geomagic, Research Triangle Park,

NC, United States). The final reconstructed models covered the aortic arch from the initial basilar artery (posterior circulation). The model had one inlet (aortic ostium) and six outlets (cross-sections of main arteries in the considered region), as suggested previously (Jozwik and Obidowski, 2010). The inlet and outlets were cut orthogonally to the centerline and extended 10 times the vessel diameter to ensure that the boundary condition would not influence the flow field within the vessels. As previously described, velocity in the inlet is 1.44 m/s and all static pressures in all outlet cross-sections were equal to 13 kPa. The portion of the arteries included in the geometrical model was determined by the quality of the images. The walls of all vessels were assumed to be rigid and nondeformable with changes in the pressure of the blood to simulate the flow.

Reconstructed models were imported as a stereolithography (STL) format file into ANSYS ICEM (version 19.0; Fluent, Inc., Lebanon, NH, United States) for mesh generation. A mesh sensitivity analysis that compared pressure, mass flow, and wall shear stress (WSS) at coarse, middle and fine mesh was generated to obtain a relationship between discretization error and element size and an estimate for the required element size (Biasetti et al., 2010). The mesh sensitivity analysis did not yield any significant differences that could influence the results of the computations performed (Supplementary Table S1). To account for time-consuming transient simulations, a mid-size density (2.72×10^6 elements) was used. A mesh file was generated and exported.

Similar to a previous study (Jozwik and Obidowski, 2010), a constant density of blood equal to 1,055 kg/m^3 was assumed. Blood is mathematically modeled as an incompressible, laminar and nonNewtonian fluid. The modified Power Law model was used to express blood viscosity. Detailed calculations of the inlet and outlet conditions were performed using the same previously described method, which resulted in a stable CFD simulation (Jozwik and Obidowski, 2010). Due to the nonstationary nature of blood flow, turbulence is expected in many places of the system being modeled. To meet the needs of the simulation, a shear stress transport (SST) model was used as the turbulence model.

All CFD simulations were performed in ANSYS FLUENT (version 19.0; Fluent, Inc., Lebanon, NH, United States) using standard numeric techniques. The governing equations of blood flow are the continuity and Navier–Stokes equations, which are described as:

$$\nabla \bullet \vec{v} = 0 \tag{1}$$

$$\rho\left(\frac{\partial \vec{v}}{\partial \vec{t}} + \vec{v}\cdot\nabla\vec{v}\right) = -\nabla p + \nabla\cdot\left[\mu\left(\nabla\vec{v} + \left(\nabla\vec{v}\right)^T\right)\right] + f \tag{2}$$

where $\vec{v}$ and P represent the velocity and pressure vectors, respectively, and ρ (1,055 kg/m^3) and μ (0.0035 Pa·s) denote the density and dynamic viscosity of blood, respectively.

Pressure-implicit splitting of operators (PISO) for the pressure–velocity coupling and a second-order upwind scheme for the momentum spatial discretization were used to calculate the hemodynamic parameters. Five cardiac cycles were calculated to ensure periodicity and achieve stable solutions, with a time step of 0.0025 s, and the data obtained for the fifth cardiac cycle were used in subsequent analyses.

Moreover, slices at the upstream normal area of sVAD, the area of sVAD, and the downstream normal area of sVAD for each patient were obtained. For healthy VAs, three slices (upstream area, midstream area, and downstream area) corresponding to the contralateral sVAD were also acquired (Supplementary Figure S1).

Patterns of blood flow analysis and hemodynamic parameters

The patterns of blood flow included the instantaneous streamline and the pressure at peak systole (0.2 s) and late diastole (0.7 s). The maximum velocity and maximum pressure of different slices at peak systole were calculated. To better present a comparison of pulsatile and steady-state flows, the time-averaged blood flow for each VA was calculated as:

$$\varnothing_a = \frac{1}{T}\int_0^T \varnothing dt \tag{3}$$

$\varnothing$ is the scalar flow at each node of the computational grid.

We also analyzed the WSS-related indices. The average WSS of each vessel wall cell over a cardiac cycle was evaluated using the time-averaged wall shear stress (TAWSS), defined as:

$$\mathrm{TAWSS} = \frac{1}{\mathrm{T}}\int_0^{\mathrm{T}} \left|\mathrm{WSS}(\mathrm{s,t})\right| dt \tag{4}$$

where T is the cardiac cycle period, WSS is the instantaneous WSS vector, and s is the position on the vessel wall.

The cyclic departure of the WSS vector from its predominant axial alignment during the cardiac cycle is introduced by the oscillatory shear index (OSI), described as Ku et al. (1985):

$$\mathrm{OSI} = 0.5\left[1 - \left(\frac{\left|\int_0^T WSS(s,t)\cdot dt\right|}{\int_0^T \left|WSS(s,t)\right|\cdot dt}\right)\right] \tag{5}$$

where T is the cardiac cycle period, WSS is the instantaneous WSS vector, and s is the position on the vessel wall.

The degree of "thrombotic susceptibility" at the vessel wall is represented by the endothelial cell action potential (ECAP) and expressed as Kelsey et al. (2017):

$$\mathrm{ECAP} = \frac{OSI}{TWASS} \tag{6}$$

The relative residence time (RRT) is a hemodynamic indicator of the luminal surface areas experiencing low and oscillating WSS and defined as Zhang et al. (2015):

$$\mathrm{RRT} = \frac{1}{(1-2\cdot OSI)\cdot TWASS} \quad \frac{1}{\frac{1}{T}\left|\int_0^T WSS(s,t)\cdot dt\right|} \tag{7}$$

Time-averaged nitric oxide (NO) production rate (TAR_{NO}) reflects the NO production rate of the endothelium and can be calculated as Andrews et al. (2010) and Li et al. (2019):

$$TAR_{NO}=\frac{1}{t}\int_0^t R_{NO}(t)2.13+457.5\times\frac{1}{t}\int_0^t\left(\frac{|WSS(c,t)|}{|WSS(c,t)|+3.5}\right)\times dt \quad (8)$$

By considering a quantitative analysis, we evaluated the TAWSS, OSI, ECAP, RRT and TAR_{NO} using the area-averaged mean, as suggested previously (Zhang et al., 2015). All hemodynamic parameters were measured at the peak of the systolic phase. More details are provided in Supplementary material.

Statistical analysis

All statistical analyses were performed using IBM SPSS Statistics software (version 22; IBM Corp, Armonk, NY, United States). To analyze the velocity and pressure of different slices (upstream area, dissection area or midstream area, downstream area), two-way analysis of variance (ANOVA) [least significant difference (LSD)] followed by Bonferroni's *post-hoc* test and the Friedman test were used. Differences in hemodynamic parameters between the sVAD with VAH arteries and the contralateral healthy VAs were compared using the paired t-test or the Wilcoxon matched-pairs signed-rank test. Continuous variables are expressed as the means ± standard deviations (SDs) or medians (interquartile ranges), and categorical variables are described using the frequency and percent. For all statistical analyses, the significance level was set at $p<0.05$.

Results

Study population

Per the inclusion and exclusion criteria, 14 patients with sVAD of the hypoplastic VA (12 males, 2 females) were included in this study. Their demographic and clinical characteristics are illustrated in Table 1. The median age of all patients was 36 years (with a range between 21 and 51 years). Of the 14 patients, 10 presented with right sVAD with VAH, while 4 presented with left sVAD with VAH. Steno-occlusive sVAD (12/14) was more frequently observed in the present study, and aneurysmal dilatative sVAD was found in only two patients (neither of whom had rupture). The most frequent segments of sVAD were the V3 and V4 levels, and the most common general clinical features was vertigo and dizziness. The ischemic brain regions attributed to sVAD included the dorsolateral medullary, dorsal medullary and cerebellar hemispheres.

TABLE 1 Demographic and clinical characteristics of patients who diagnosed with sVAD with VAH.

Patients (*n* =14)	N (%)/median (IQR)
Gender	
Female	2 (14%)
Male	12 (86%)
Age (years)	36 (30–37)
Side of sVAD	
Right	10 (71%)
Left	4 (29%)
Segments of sVAD	
V1	1
V2	2
V3	5
V4	6
Subtypes of sVAD	
Steno-occlusion	12
Aneurysmal dilatation	2
Length of dissection (mm)	29.46 (19.09–32.78)
Clinical symptom	
Headache	6
Neck pain	2
Vertigo/dizziness	11
Dysarthria	3
Dysphagia	6
Nystagmus	2
Gait ataxia	6
Unilateral limb numbness	5
Unilateral limb paralysis	3
Brain infarct	
Dorsolateral medullary	10
Dorsal medullary	1
Cerebellar hemisphere	3
Onset to door time (day)	4 (3–7)
SBP at admission (mmHg)	131 (122–148)
DBP at admission (mmHg)	84 (79–92)
Risk factors	
Hypertension	1
Diabetes mellitus	2
Atrial fibrillation	0
Migraine	2
History of ischemic stroke	0
Hyperlipidemia	2
Current smoking	3
History of alcohol	2
Baseline NIHSS	2 (1–4)
mRS at 90days	
0	8
≥1	6

sVAD, spontaneous vertebral artery dissection; VAH, Vertebral Artery Hypoplasia; SBP, systolic blood pressure; DBP, diastole blood pressure; NIHSS, National Institutes of Health Stroke Scale; mRS, modified Rankin Scale.

Patterns of blood flow analysis

Two hemodynamic variables (pressure and velocity) that directly observed blood flow patterns, were obtained from CFD simulations. Figure 1 demonstrated velocity streamlines at peak systole. We observed that laminar flow occurred in most healthy VAs at peak systole. More disordered flow was observed in the dissection area in

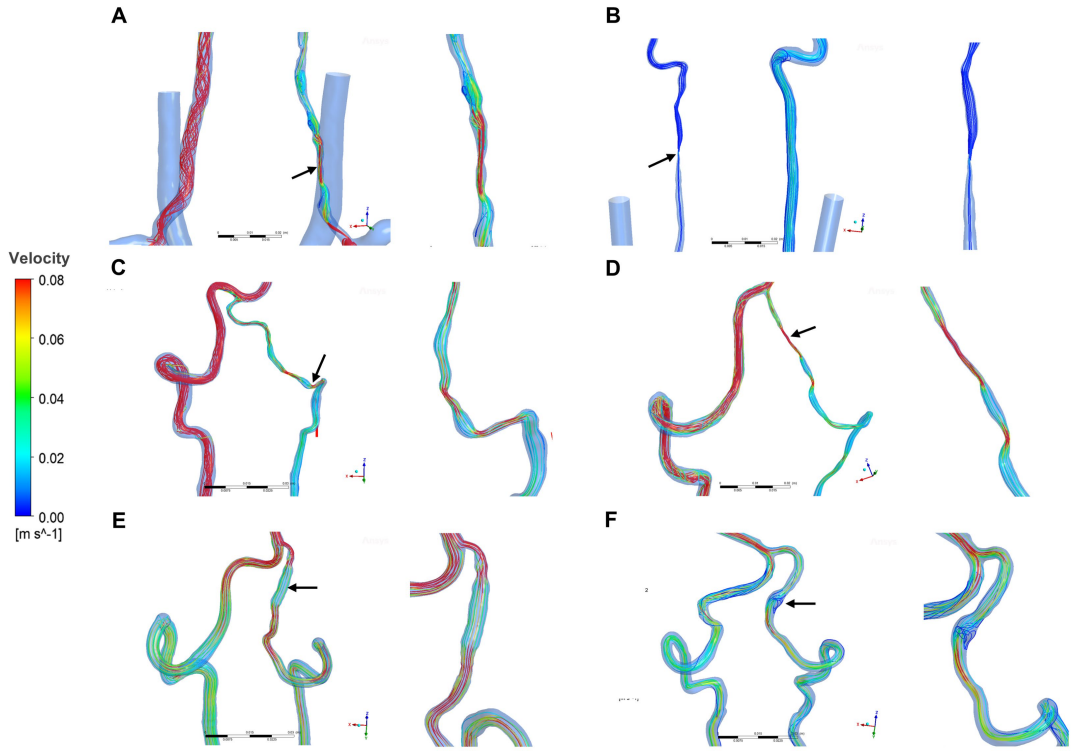

FIGURE 1
Velocity streamlines for sVAD with VAH arteries and contralateral normal VAs at peak systole. **(A–D)** Steno-occlusive sVAD with VAH arteries. **(E,F)** Aneurysmal dilatative sVAD with VAH artery. →: dissected region. sVAD, spontaneous vertebral artery dissection; VAH, vertebral artery hypoplasia; VAs, vertebral arteries.

TABLE 2 The upstream area, dissection area or midstream area, and downstream area of hemodynamic parameters in sVAD with VAH and contralateral normal VAs.

Slices	Steno-occlusive sVAD with VAH			Healthy VAs		
	Velocity (m/s)‡	Pressure (Pa)‡	WSS(Pa)‡	Velocity (m/s)#	Pressure (Pa)‡	WSS(Pa)‡
Upstream	0.449 ± 0.456	15273.458 ± 2194.785	4.100 ± 7.148	0.727 ± 0.469	15474.868 ± 2332.914	6.422 ± 5.828
Dissection area/ Midstream	0.910 ± 0.738	14913.067 ± 2117.591	11.667 ± 14.393	0.881 ± 0.578	15252.871 ± 2244.378	10.739 ± 8.699
Downstream	0.566 ± 0.646	14504.092 ± 1844.347	7.397 ± 9.186	0.825 ± 0.642	14859.277 ± 2101.296	12.021 ± 14.912
p value	<0.001***	<0.001***	<0.01**	0.502	0.017*	0.472

*$p < 0.05$; **$p < 0.01$; ***$p < 0.001$. #Two-way analysis of variance (ANOVA). ‡Friedman test.
Variables were expressed as $\bar{x} \pm s$.
VA, vertebral arteries; sVAD, spontaneous vertebral artery dissection; WSS, wall shear stress.

sVAD with VAH arteries (Figure 1). We also observed that normal slices of steno-occlusive sVAD with VAH arteries had slower blood flow velocity than the opposite slices of contralateral healthy (Figures 1A–D). Aneurysmal dilatative sVAD cases manifested slow blood flow velocity in the dissection region, but the velocity was not visibly different between sVAD with VAH artery and contralateral normal VA in those cases (Figures 1E,F). The mean maximum velocity values for the VAs with the upstream area, dissection/midstream area, and downstream area are listed in Table 2. Friedman test for multiple comparisons revealed significant differences in the maximum velocity of steno-occlusive sVAD with VAH arteries ($\chi^2 = 19.500$, $p < 0.001$) among the upstream normal area (0.449 m/s ± 0.456), dissection area (0.910 m/s ± 0.738), and downstream normal area (0.566 m/s ± 0.646), whereas maximum velocity between the 3 slices of healthy VAs was not statistically significant ($F = 0.711$, $p = 0.502$) (Table 2).

Figure 2 presents the pressure distribution superimposed with pressure contour map at peak systole and late diastole. As shown in Figure 2, pressure was not visibly different between steno-occlusive dissection region of sVAD and VAH artery and the midstream of the contralateral normal VA. Regarding the aneurysmal dilatation type, focal high pressure was observed in the aneurysmal dissection region of sVAD with VAH artery according to pressure contour map (Figure 2), but we did not perform statistical analyses due to the limited sample size. Moreover, whether for healthy VAs or sVAD with VAH arteries, the pressure from inlet to outlet showed a gradually dropping trend in healthy VAs and sVAD with VAH arteries.

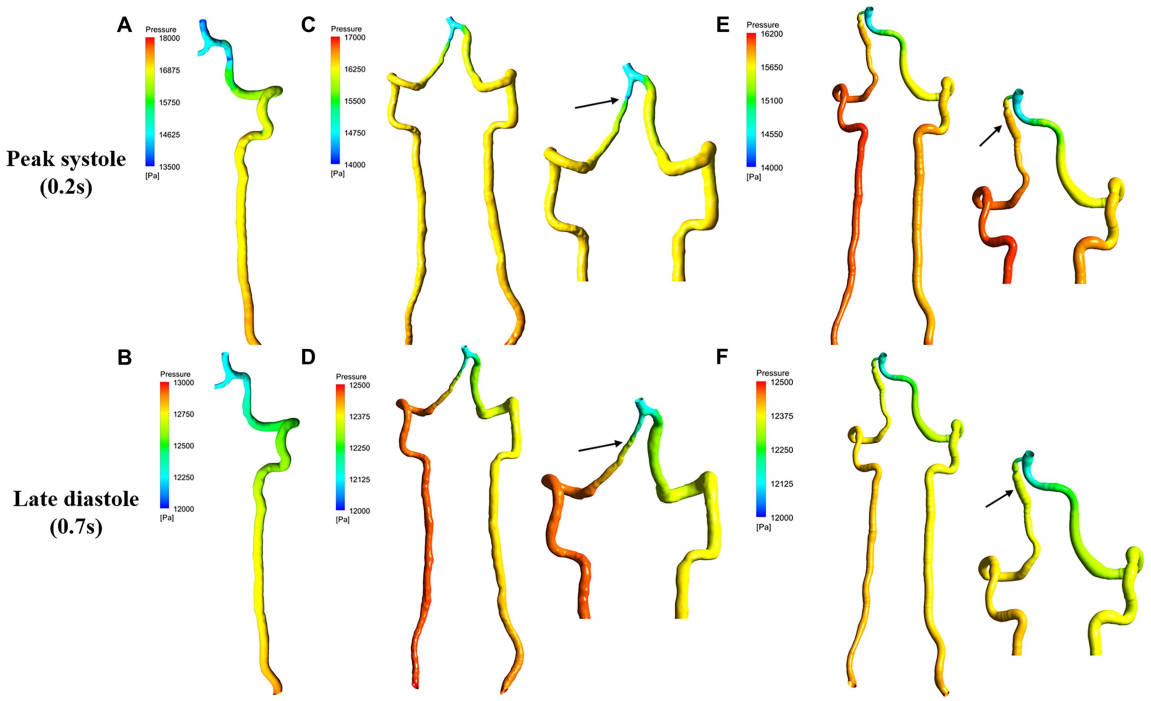

FIGURE 2
Pressure contour map for sVAD with VAH arteries and contralateral normal VAs at peak systole and late diastole. **(A,B)** Contralateral healthy VAs. **(C,D)** Steno-occlusive sVAD with VAH arteries. **(E,F)** Aneurysmal dilatative sVAD with VAH artery. →: dissected region. sVAD, spontaneous vertebral artery dissection; VAH, vertebral artery hypoplasia; VAs, vertebral arteries.

Friedman test also showed that the pressure dropping trend in the healthy VAs and steno-occlusive sVAD with VAH arteries were statistically significant ($\chi^2 = 8.167$, $p = 0.017$ and $\chi^2 = 17.167$, $p < 0.001$, respectively) (Table 2).

Hemodynamics characteristics

To assess the hemodynamic characteristics of sVAD with VAH arteries, time-averaged blood flow, TWASS, OSI, ECAP, RRT, and TAR_{NO} of each VA were solved. Figure 3 presents the distribution of TAWSS, OSI, ECAP, RRT, and TAR_{NO} on the vessel wall. TAWSS contour plots are shown in Figures 3A,B. Steno-occlusive sVAD patients exhibited local maxima of TAWSS in the dissection area (Figure 3A). For the two patients with aneurysmal dilatative sVAD, the dissection area manifested low TAWSS (Figure 3B). Other non-dissection areas of sVAD with VAH arteries had lower TAWSS than the counterparts of the contralateral healthy VAs regardless of the dissection subtype. The OSI contour plots (Figures 3C,D) showed that the local maxima of OSI were distributed in the dissection area in the steno-occlusive VAD model (Figure 3C) and aneurysmal dilatative VAD model (Figure 3D). Moreover, there was higher OSI on the sVAD with VAH artery regardless of dissection subtypes in comparison with contralateral healthy VA. Most of the walls of the sVAD with VAH artery showed a relatively high ECAP and high RRT (Figures 3E–H), and the distributions of high ECAP and high RRT were approximately same. As Figure 3I shown, the highest TAR_{NO} concentration was observed at dissection area in steno-occlusive subtype. In contrast, the local minimum TAR_{NO} concentration occurred at the dissection area in aneurysmal dilatation subtype (Figure 3J). In non-dissection area, both of steno-occlusive sVAD and aneurysm dilatative sVAD had lower TAR_{NO} concentration compared with the opposite healthy VAs.

The quantitative results of time-averaged blood flow, TAWSS, OSI, ECAP, RRT and TAR_{NO} are recorded in Table 3. All steno-occlusive sVAD cases showed strong statistically significant differences between all hemodynamic parameters between the sVAD artery and non-sVAD artery. Compared with contralateral healthy VAs, steno-occlusive sVAD with VAH arteries had a lower time-averaged blood flow ($0.499\,cm^3/s \pm 0.467$ vs. 2.268 ± 0.984, $t = -7.381$, $p < 0.001$), lower TAWSS ($1.115\,Pa \pm 0.589$ vs. 2.437 ± 0.970, $t = -4.287$, $p = 0.001$), higher OSI (0.248 ± 0.054 vs. 0.173 ± 0.038, $t = 3.382$, $p = 0.006$), higher ECAP ($0.328\,Pa^{-1} \pm 0.192$ vs. 0.094 ± 0.034, $t = 4.143$, $p = 0.002$), higher RRT ($3.519\,Pa^{-1} \pm 1.960$ vs. 1.044 ± 0.407, $t = 4.216$, $p = 0.001$) and deceased TAR_{NO} ($104.014\,nM/s \pm 28.308$ vs. 158.195 ± 18.082, $t = -6.021$, $p < 0.001$) according to statistical analyses. More details are provided in Supplementary material.

Discussion

The present study used CFD to reconstruct 28 high-quality 3D models of VA, display blood flow patterns, and quantify hemodynamic parameters of sVAD with VAH arteries, which allowed us to detect the occurrence of abnormal blood flow patterns, smaller time-averaged blood flow, lower TAWSS, higher OSI, higher ECAP, higher RRT and

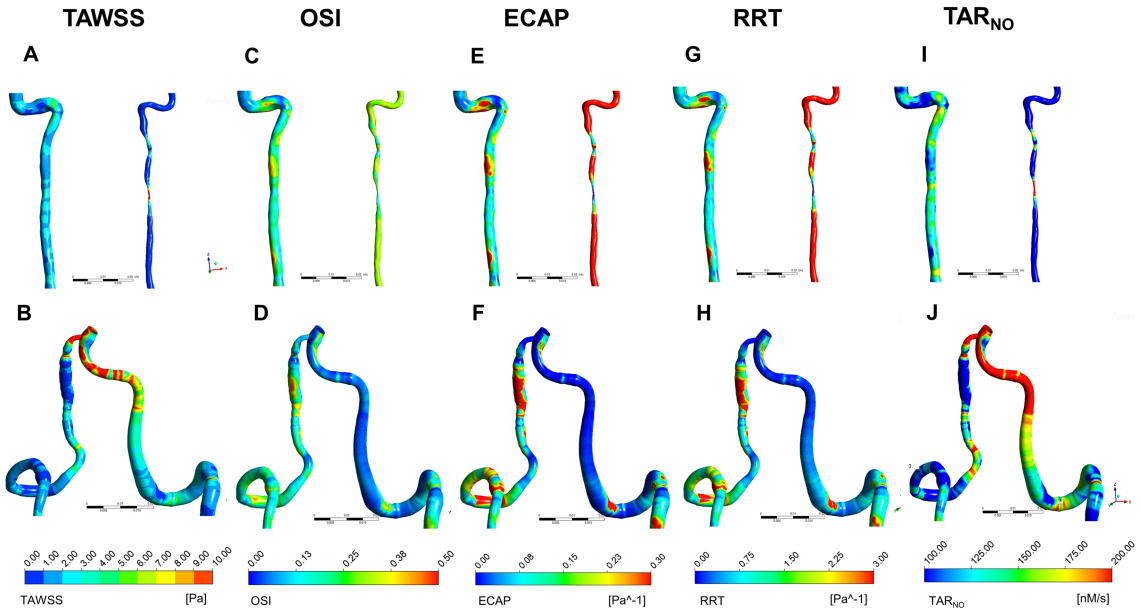

FIGURE 3
Distribution of TWASS, OSI, ECAP, RRT, and TAR_{NO} at peak systole for sVAD with VAH arteries and contralateral normal VAs. **(A,B)** Distribution of TWASS; **(C,D)** distribution of OSI; **(E,F)** distribution of ECAP; **(G,H)** distribution of RRT; **(I,J)** distribution of TAR_{NO}. **(A,C,E,G,I)** Steno-occlusive sVAD with VAH; **(B,D,F,H,J)** aneurysmal dilatative sVAD with VAH. →: dissected region. TWASS, time-averaged wall shear stress; OSI, oscillatory shear index; ECAP, endothelial cell action potential; RRT, relative residence time; TAR_{NO}, time-averaged nitric oxide production rate; sVAD, spontaneous vertebral artery dissection; VAH, vertebral artery hypoplasia; VAs, vertebral arteries.

TABLE 3 Comparisons of hemodynamic parameters between steno-occlusive sVAD with VAH and contralateral normal VAs.

Parameters	Steno-occlusive sVAD with VAH	Normal VAs	*t*	*p*-value
TWASS(Pa)	1.115 ± 0.589	2.437 ± 0.970	−4.287	0.001**
OSI†	0.248 ± 0.054	0.173 ± 0.038	3.382	0.006**
ECAP(Pa^{-1})	0.328 ± 0.192	0.094 ± 0.034	4.143	0.002**
RRT(Pa^{-1})	3.519 ± 1.960	1.044 ± 0.407	4.216	0.001**
TAR_{NO} (nM/s)	104.014 ± 28.308	158.195 ± 18.082	−6.021	<0.001***
Time-averaged blood flow (cm^3/s)	0.499 ± 0.467	2.268 ± 0.984	−7.381	<0.001***
Cross-sectional area (cm^2)	5.514 ± 2.465	13.294 ± 3.355	−14.185	<0.001***

**$p < 0.01$; ***$p < 0.001$. Variables were expressed as $\bar{x} \pm s$.
VA, vertebral arteries; sVAD, spontaneous vertebral artery dissection; VAH, vertebral artery hypoplasia; TWASS, time-averaged wall shear stress; OSI, oscillatory shear index; ECAP, endothelial cell action potential; RRT, Relative residence time; TAR_{NO}, time-averaged NO production rate.

decreased TAR_{NO} in steno-occlusive sVAD with VAH arteries. These results provided direct hemodynamic characteristics in sVAD with VAH arteries and supported the applicability of the CFD method in testing the hemodynamic hypothesis of sVAD. In contrast to prior studies (Giannopoulos et al., 2007; McNally et al., 2018), this study is one of the first biomechanical studies of the hemodynamic pathogenesis of sVAD to apply the CFD method.

First, we quantified blood flow velocity and pressure, that was different from other prior VAD hemodynamics studies (de Bray et al., 1997; Zhang et al., 2021). We detected that a focal increase in blood flow velocity at the dissected area compared to other nondissected areas in steno-occlusive sVAD with VAH arteries, which is consistent with a previous ultrasound study of stenosis VAD (de Bray et al., 1997). In contrast, aneurysmal dilatative sVAD with VAH arteries showed a decreased blood flow velocity at the dissection area based on the velocity streamlines rather than statistical analyses. Additionally, there was more pronounced disordered flow in sVAD with VAH arteries regardless of the dissection subtype. We also observed a slower blood flow velocity in nondissected areas of steno-occlusive sVAD with VAH arteries than in the counterparts of contralateral healthy VAs. This phenomenon may have occurred because hypoplastic VAs have a lower mean flow velocity, which was previously found using Transcranial Doppler (TCD) (Min and Lee, 2007) and sVAD on the same side as hypoplastic VAs in the present

study. We also found that dissected stenosis areas manifested low pressure due to a sudden narrowing of the inner diameter, and dissected aneurysmal dilation manifested high pressure based on the pressure contour map. However, there were no visibly differences in pressures between the dissected area of steno-occlusive sVAD with VAH arteries and the counterparts of contralateral healthy VAs. The small differences in pressure between the two groups were expected due to the limited sample size. Consequently, these pressure results of sVAD with VAH need further confirmation in a larger sample of patients to enable inter-patients comparisons and statistical analyses follow-up studies. Overall, our findings suggest that high velocity and focal low pressure occurred at the dissected stenosis region, while low velocity and focal high pressure occurred at the dissected aneurysm region. These results reveal the phenomena that different subtypes of sVAD possibly exhibited different blood flow patterns. Moreover, these observations also hint at an unstable hemodynamic microenvironment in sVAD with VAH arteries, and the unstable blood flow patterns may be a risk factor for vascular diseases (Biasetti et al., 2010; Sui et al., 2015). Hence, future investigations of sVAD hemodynamics should pay more attention to patient-specific blood flow patterns with morphologic and regional variation.

Furthermore, we detected a notably lower time-averaged blood flow in steno-occlusive sVAD with VAH arteries compared with the contralateral healthy VAs. This phenomenon represents the insufficient blood supply in steno-occlusive sVAD with VAH arteries, which may be due to the following reasons. Firstly, the definition of congenital VAH indicates that the diameter of sVAD with VAH arteries was smaller than that of the contralateral healthy VAs (Zhou et al., 2015). Secondly, a decreased blood flow velocity at the nondissected area in steno-occlusive sVAD with VAH arteries was observed. Poiseuille's fourth-power radius law indicates that liquid flow through a vessel is proportional to the fourth power of the radius (Wilkin, 1989), which resulted in a lower blood flow was detected in these subjects. Importantly, several studies demonstrated a correlation between blood flow and artery remodeling. For example, Langille and O'Donnell (1986) and Lee and Langille (1991) measured the blood flow through the vessel lumen of rabbits and suggested that long-term, flow-induced reductions in arterial diameter were due to a structural modification of the artery wall rather than just sustained contractive smooth muscle. Based on these previous findings, we speculate that congenital VAH and long-term blood flow reductions have a potentially positive feedback relationship, wherein long-term low blood flow may promote VA remodeling. If the inner diameter of hypoplastic VAs decreases further, it may affect blood flow, and if these regulative changes reach an unbalanced state, it may induce hemodynamic dysfunction of VAH triggered by other hemodynamic forces or nonhemodynamic risk factors. Although our speculation of the potential hemodynamic dysfunction mechanism of VAH needs further in-depth research to corroborate, it may explain the prior observation that VAH is prone to the development of cerebrovascular events.

Especially, our study using CFD analysis has offered new perspectives on the precise evaluation of WSS-related indices in sVAD with VAH arteries, which is an improvement compared to the conventional hemodynamic assessment methods used in prior studies (Augst et al., 2003; Giannopoulos et al., 2007; Hori et al., 2020). Below is an elaborated summary of our findings. Initially, our finding indicated that TAWSS decreased in steno-occlusive sVAD with VAH arteries. The reduction in blood flow within these steno-occlusive sVAD with VAH arteries is likely responsible for this finding. WSS is considered as a crucial hemodynamic parameter for predicting the risk of arterial dissection (Li et al., 2019; Xu et al., 2020), and its correlation with blood flow has been investigated intensively since 1991. Langille and O'Donnell (1986) were the first to reported that vascular remodeling of common carotid arteries in a rabbit external carotid ligation model reduced the diameter due to decreased blood flow, and they suggested that the adaptation of flow-induced remodeling restored WSS to control levels. Two cell-based studies substantially showed that the maintenance of WSS at normal physiological levels appeared to involve the development of intima media thickening (IMT) and artery remodeling, resulting in alterations in blood flow (Korshunov and Berk, 2003; Korshunov et al., 2006). More importantly, abnormal WSS has a negative effect on endothelial function because low WSS leads to a proinflammatory, procoagulant surface via activation of proinflammatory and procoagulant transcription factors (Boon and Horrevoets, 2009; Meng et al., 2014). Therefore, flow-induced WSS plays an important role in artery remodeling and endothelial function, both of which are related to vascular diseases (Cibis et al., 2014; Frösen et al., 2019). We hypothesized that prolonged low TAWSS may also be a key trigger in the hemodynamic pathogenesis hypothesis of sVAD. Although this hypothesis requires stronger evidence to support in the future, our study tentatively verified that steno-occlusive sVAD with VAH arteries had low TAWSS. Further hemodynamic studies of sVAD should pursue more detailed data about WSS at different stages and types of arterial dissection to explore risk predictors of sVAD.

We also observed a significant increase in OSI, ECAP and RRT in the dissection area regardless of sVAD subtypes. And the difference in OSI, ECAP and RRT values between steno-occlusive sVAD with VAH arteries and contralateral healthy VAs has showed significance after statistical analysis. One possible reason for our findings was that sVAD with VAH artery had more disturbed flow conditions than contralateral healthy VAs. Previous literatures have reported that high OSI areas were commonly detected around vortex flow, which could induce more reactive oxygen species (ROS) production from endothelial cells more than laminar shear (Hwang et al., 2003; Hohri et al., 2021), thereby contribute to vascular diseases, such as artery deformation and atherosclerosis (Xu et al., 2020; Chen et al., 2022). Additionally, our results revealed that sVAD with VAH arteries might have higher thrombotic susceptibility at the hemodynamic level owing to both of high ECAP and high RRT were indicators for the risk of thrombogenesis as previously described (Zhang et al., 2015; Ong et al., 2019), which supporting antithrombosis treatment as the main therapeutic intervention in patients with sVAD in clinical practice (Sugiyama et al., 2013; CADISS Trial Investigators et al., 2015). However, whether high ECAP and high RRT help create an unfavorable hemodynamic environment and somehow promote sVAD progression, or whether this unfavorable hemodynamic environment results from sVAD are still unknown.

In addition, decreased TAR_{NO} on sVAD with VAH arteries was detected in the present study. This finding is consistent with previous studies on atherosclerosis stenosis, suggesting that stenotic VAD

might have potential effects on inhibiting the NO production of endothelium (Liu et al., 2012). TAR_{NO} has been seen as an indicator of NO transport of endothelium in previous publications (Li et al., 2019). NO, as a key endothelium-divided substance, has diverse functions such as leucocyte adhesion, endothelial regeneration, and vascular relaxation (Busse et al., 1995; de Caterina et al., 1995; Napoli et al., 2006). Converging evidence has demonstrated that NO produced from endothelium is a signal in regulating vascular wall function and low NO concentration may contribute to restenosis and thrombosis (Knowles and Moncada, 1992; Busse et al., 1995; Liu et al., 2015). The finding of TAR_{NO} in the present study could offer valuable insight into sVAD hemodynamic pathogenesis, and whether such phenomena truly exist *in vivo* remains to be demonstrated in future research.

In brief, the strength of the current study is its demonstration of the potential of CFD as a valuable tool for investigating hemodynamic parameters in sVAD. Our study provides novel insights into the hemodynamics of sVAD with VAH arteries. In contrast to conventional hemodynamic assessment tools, CFD offers several advantages, including non-invasiveness, patient-specificity, high accuracy, and cost-effectiveness (Pontone and Rabbat, 2017). Numerous previous studies have utilized CFD to flexibly analyze the hemodynamics and construct personalized mathematical models of vascular diseases (Deyranlou et al., 2020; Jiang et al., 2022). In particularly, CFD could provide more precise and detailed information on flow patterns, such as WSS, which is often challenging to obtain through other imaging techniques. Moreover, with the advancement of artificial intelligence, CFD holds promise as a clinical tool for the future (Pontone and Rabbat, 2017; Randles et al., 2017).

There are some limitations that must be acknowledged in this study. First, the sample size was relatively small. This was due in part to the low prevalence of sVAD with VAH (Schievink, 2001), and also because the quantity of reconstructed high-quality 3D models was susceptible to the patients' images quality. Therefore, we ultimately obtained 28 high-quality 3D models of VA. Inherent selection bias was inevitable. Second, while the focus on hemodynamic characteristics of sVAD with VAH arteries is a strength of this study, interpretation of hemodynamic mechanism of sVAD attributed to VAH is limited by lack of data on images prior to sVAD occurs. Interestingly, some recent CFD studies used the variance and mean curvature calculation method to successfully recover the parent artery back to its pre-aneurysm state (Le et al., 2013). If this recovery method is utilized in future study, the hemodynamic hypothesis of sVAD attributed to VAH could be certified. Third, owing to only 2 cases exhibited aneurysmal dilatation in our study, the hemodynamic characteristics of aneurysmal sVAD were observed by contour plots rather than stratified analysis in order to assure the sufficient statistical power. The generalizability of these observations in aneurysmal dilatative sVAD with VAH arteries requires further confirmation.

Despite these limitations, this study suggest that abnormal flow patterns are present in the dissection area of sVAD with VAH arteries, and these hemodynamic dysfunctions might trigger the arterial wall to develop dissection. As far as we know, this study is a prime example for the application of CFD for quantification of hemodynamic characteristics in sVAD. These results may have implications for the importance of considering VAH in the management of sVAD, as well as for the understanding of its pathogenesis. Further studies are needed to confirm these findings and explore the possibility of hemodynamic characteristics as a diagnostic and prognostic measurement for sVAD with VAH arteries. In our view, the simplification of the relationship between the hemodynamic variables and sVAD occurrence may provide a convenient method to predict the risk of VAH developing sVAD, and more aggressive hemodynamic monitoring should be utilized in VAH patients if the sVAD hemodynamic pathogenesis hypothesis is confirmed in future studies.

Conclusion

In conclusion, this study has novelty at the methodological level and provides direct evidence of hemodynamic characteristics in sVAD with VAH arteries, thereby enhancing our understanding of the hemodynamic pathogenesis of sVAD attributed to VAH. However, further validation is needed to confirm the results, and more detailed hemodynamic conditions with different stages of sVAD are warranted in the future. Furthermore, noninvasive hemodynamic assessment might have the potential to serve as a monitoring tool for predicting sVAD risk and assist clinicians in formulating intervention strategies for VAH patients.

Data availability statement

The raw data supporting the conclusions of this article will be made available by the authors, without undue reservation.

Ethics statement

The studies involving human participants were reviewed and approved by the West China Hospital of Sichuan University Biomedical Research Ethics Committee. Written informed consent for participation was not required for this study in accordance with the national legislation and the institutional requirements.

Author contributions

JB: data collection, analysis and interpretation of data, and manuscript writing. XG: data collection and data analysis. WF: data analysis and data interpretation. YL: critical revision of the manuscript. YQ: data analysis. MZ: study design. JG and LH: study design, critical revision of the manuscript for important intellectual content, and study supervision. All authors contributed to manuscript revision, read, and approved the submitted version.

Funding

This work was supported by the Natural Science Foundation of China (Grant no. 81971162), Institute of Brain Science and Brain-Inspired Technology of West China Hospital, Sichuan University, China Postdoctoral Science Foundation (Grant no. 2020M673248 and 2021M692294), and Sichuan Science and Technology Program (Grant no. 2021YJ0437).

Conflict of interest

The authors declare that the research was conducted in the absence of any commercial or financial relationships that could be construed as a potential conflict of interest.

Publisher's note

All claims expressed in this article are solely those of the authors and do not necessarily represent those of their affiliated organizations, or those of the publisher, the editors and the reviewers. Any product that may be evaluated in this article, or claim that may be made by its manufacturer, is not guaranteed or endorsed by the publisher.

Supplementary material

The Supplementary material for this article can be found online at: https://www.frontiersin.org/articles/10.3389/fnins.2023.1179963/full#supplementary-material

References

Adams, H. P. Jr., Bendixen, B. H., Kappelle, L. J., Biller, J., Love, B. B., Gordon, D. L., et al. (1993). Classification of subtype of acute ischemic stroke. Definitions for use in a multicenter clinical trial. TOAST. Trial of org 10172 in acute stroke treatment. *Stroke* 24, 35–41. doi: 10.1161/01.STR.24.1.35

Andrews, A. M., Jaron, D., Buerk, D. G., Kirby, P. L., and Barbee, K. A. (2010). Direct, real-time measurement of shear stress-induced nitric oxide produced from endothelial cells *in vitro*. *Nitric Oxide* 23, 335–342. doi: 10.1016/j.niox.2010.08.003

Augst, A. D., Barratt, D. C., Hughes, A. D., Glor, F. P., Thom, S. A. M. G., and Xu, X. Y. (2003). Accuracy and reproducibility of CFD predicted wall shear stress using 3D ultrasound images. *J. Biomech. Eng.* 125, 218–222. doi: 10.1115/1.1553973

Biasetti, J., Gasser, T. C., Auer, M., Hedin, U., and Labruto, F. (2010). Hemodynamics of the normal aorta compared to fusiform and saccular abdominal aortic aneurysms with emphasis on a potential thrombus formation mechanism. *Ann. Biomed. Eng.* 38, 380–390. doi: 10.1007/s10439-009-9843-6

Boon, R. A., and Horrevoets, A. J. G. (2009). Key transcriptional regulators of the vasoprotective effects of shear stress. *Hamostaseologie* 29, 39–43. doi: 10.1055/s-0037-1616937

Busse, R., Fleming, I., and Schini, V. B. (1995). Nitric oxide formation in the vascular wall: regulation and functional implications. *Curr. Top. Microbiol. Immunol.* 196, 7–18. doi: 10.1007/978-3-642-79130-7_3

CADISS Trial InvestigatorsMarkus, H. S., Hayter, E., Levi, C., Feldman, A., Venables, G., et al. (2015). Antiplatelet treatment compared with anticoagulation treatment for cervical artery dissection (CADISS): a randomised trial. *Lancet Neurol.* 14, 361–367. doi: 10.1016/S1474-4422(15)70018-9

Chen, H., Su, T., Wang, Q., Zheng, Z., Li, H., and Li, J. (2022). Comparison of thrombosis risk in an abdominal aortic dissection aneurysm with a double false lumen using computational fluid dynamic simulation method. *Technol. Heal. Care* 31, 1003–1015. doi: 10.3233/THC-220481

Cibis, M., Potters, W. V., Gijsen, F. J. H., Marquering, H., vanBavel, E., van der Steen, A. F. W., et al. (2014). Wall shear stress calculations based on 3D cine phase contrast MRI and computational fluid dynamics: a comparison study in healthy carotid arteries. *NMR Biomed.* 27, 826–834. doi: 10.1002/nbm.3126

de Bray, J. M., Penisson-Besnier, I., Dubas, F., and Emile, J. (1997). Extracranial and intracranial vertebrobasilar dissections: diagnosis and prognosis. *J. Neurol. Neurosurg. Psychiatry* 63, 46–51. doi: 10.1136/jnnp.63.1.46

de Caterina, R., Libby, P., Peng, H. B., Thannickal, V. J., Rajavashisth, T. B., Gimbrone, M. A. Jr., et al. (1995). Nitric oxide decreases cytokine-induced endothelial activation. Nitric oxide selectively reduces endothelial expression of adhesion molecules and proinflammatory cytokines. *J. Clin. Invest.* 96, 60–68. doi: 10.1172/JCI118074

Debette, S., and Leys, D. (2009). Cervical-artery dissections: predisposing factors, diagnosis, and outcome. *Lancet Neurol.* 8, 668–678. doi: 10.1016/S1474-4422(09)70084-5

Deyranlou, A., Naish, J. H., Miller, C. A., Revell, A., and Keshmiri, A. (2020). Numerical study of atrial fibrillation effects on flow distribution in aortic circulation. *Ann. Biomed. Eng.* 48, 1291–1308. doi: 10.1007/s10439-020-02448-6

Ferro, J. M., Massaro, A. R., and Mas, J. L. (2010). Aetiological diagnosis of ischaemic stroke in young adults. *Lancet Neurol.* 9, 1085–1096. doi: 10.1016/S1474-4422(10)70251-9

Frösen, J., Cebral, J., Robertson, A. M., and Aoki, T. (2019). Flow-induced, inflammation-mediated arterial wall remodeling in the formation and progression of intracranial aneurysms. *Neurosurg. Focus* 47:E21. doi: 10.3171/2019.5.FOCUS19234

Giannopoulos, S., Kosmidou, M., Pelidou, S. H., Kyritsis, A. P., and Perren, F. (2007). Vertebral artery hypoplasia: a predisposing factor for posterior circulation stroke? *Neurology* 68, 1956–1957. doi: 10.1212/01.wnl.0000265359.83038.a8

Günther, A., Witte, O. W., Freesmeyer, M., and Drescher, R. (2016). Clinical presentation, magnetic resonance angiography, ultrasound findings, and stroke patterns in patients with vertebral artery dissection. *Eur. Neurol.* 76, 284–294. doi: 10.1159/000452303

Hohri, Y., Numata, S., Itatani, K., Kanda, K., Yamazaki, S., Inoue, T., et al. (2021). Prediction for future occurrence of type A aortic dissection using computational fluid dynamics. *Eur. J. Cardiothorac. Surg.* 60, 384–391. doi: 10.1093/ejcts/ezab094

Hong, J. M., Chung, C. S., Bang, O. Y., Yong, S. W., Joo, I. S., and Huh, K. (2009). Vertebral artery dominance contributes to basilar artery curvature and peri-vertebrobasilar junctional infarcts. *J. Neurol. Neurosurg. Psychiatry* 80, 1087–1092. doi: 10.1136/jnnp.2008.169805

Hori, S., Hori, E., Umemura, K., Shibata, T., Okamoto, S., Kubo, M., et al. (2020). Anatomical variations of vertebrobasilar artery are closely related to the occurrence of vertebral artery dissection—an MR angiography study. *J. Stroke Cerebrovasc. Dis.* 29:104636. doi: 10.1016/j.jstrokecerebrovasdis.2020.104636

Hwang, J., Saha, A., Boo, Y. C., Sorescu, G. P., McNally, J. S., Holland, S. M., et al. Oscillatory shear stress stimulates endothelial production of O_2-from p47 -dependent NAD(P)H oxidases, leading to monocyte adhesion. *J. Biol. Chem.* (2003). 278:47291–47298. doi: 10.1074/jbc.M305150200

Jiang, X., Cao, H., Zhang, Z., Li, T. Z. X., and Wu, P. (2022). A hemodynamic analysis of the thrombosis within occluded coronary arterial fistulas with terminal aneurysms using a blood stasis model. *Front. Physiol.* 13:906502. doi: 10.3389/fphys.2022.906502

Jozwik, K., and Obidowski, D. (2010). Numerical simulations of the blood flow through vertebral arteries. *J. Biomech.* 43, 177–185. doi: 10.1016/j.jbiomech.2009.09.026

Kelsey, L. J., Powell, J. T., Norman, P. E., Miller, K., and Doyle, B. J. (2017). A comparison of hemodynamic metrics and intraluminal thrombus burden in a common iliac artery aneurysm. *Int. J. Numer. Method Biomed. Eng.* 33, 1–21. doi: 10.1002/cnm.2821

Knowles, R. G., and Moncada, S. (1992). Nitric oxide as a signal in blood vessels. *Trends Biochem. Sci.* 17, 399–402. doi: 10.1016/0968-0004(92)90008-W

Korshunov, V. A., and Berk, B. C. (2003). Flow-induced vascular remodeling in the mouse: a model for carotid intima-media thickening. *Arterioscler. Thromb. Vasc. Biol.* 23, 2185–2191. doi: 10.1161/01.ATV.0000103120.06092.14

Korshunov, V. A., Mohan, A. M., Georger, M. A., and Berk, B. C. (2006). Axl, a receptor tyrosine kinase, mediates flow-induced vascular remodeling. *Circ. Res.* 98, 1446–1452. doi: 10.1161/01.RES.0000223322.16149.9a

Ku, D. N., Giddens, D. P., Zarins, C. K., and Glagov, S. (1985). Pulsatile flow and atherosclerosis in the human carotid bifurcation. Positive correlation between plaque location and low oscillating shear stress. *Arteriosclerosis* 5, 293–302. doi: 10.1161/01.ATV.5.3.293

Langille, B. L., and O'Donnell, F. (1986). Reductions in arterial diameter produced by chronic decreases in blood flow are endothelium-dependent. *Science* 231, 405–407. doi: 10.1126/science.3941904

Le, W. J., Zhu, Y. Q., Li, M. H., Yan, L., Tan, H.-Q., Xiao, S.-M., et al. (2013). New method for retrospective study of hemodynamic changes before and after aneurysm formation in patients with ruptured or unruptured aneurysms. *BMC Neurol.* 13:166. doi: 10.1186/1471-2377-13-166

Lee, R. D. B., and Langille, B. L. (1991). Arterial adaptations to altered blood flow. *Can. J. Physiol. Pharmacol.* 69, 978–983. doi: 10.1139/y91-147

Li, Z., Hu, L., Chen, C., Wang, Z., Zhou, Z., and Chen, Y. (2019). Hemodynamic performance of multilayer stents in the treatment of aneurysms with a branch attached. *Sci. Rep.* 9, 1–10. doi: 10.1038/s41598-019-46714-7

Liu, X., Fan, Y., Xu, X. Y., and Deng, X. (2012). Nitric oxide transport in an axisymmetric stenosis. *J. R. Soc. Med.* 9, 2468–2478. doi: 10.1098/rsif.2012.0224

Liu, X., Wang, M., Zhang, N., Fan, Z., Fan, Y., and Deng, X. (2015). Effects of endothelium, stent design and deployment on the nitric oxide transport in stented artery: a potential role in stent restenosis and thrombosis. *Med. Biol. Eng. Comput.* 53, 427–439. doi: 10.1007/s11517-015-1250-6

Maruyama, H., Nagoya, H., Kato, Y., Deguchi, I., Fukuoka, T., Ohe, Y., et al. (2012). Spontaneous cervicocephalic arterial dissection with headache and neck pain as the only symptom. *J. Headache Pain* 13, 247–253. doi: 10.1007/s10194-012-0420-2

McNally, J. S., Hinckley, P. J., Sakata, A., Eisenmenger, L. B., Kim, S. E., de Havenon, A. H., et al. (2018). Magnetic resonance imaging and clinical factors associated with ischemic stroke in patients suspected of cervical artery dissection. *Stroke* 49, 2337–2344. doi: 10.1161/STROKEAHA.118.021868

Meng, H., Tutino, V. M., Xiang, J., and Siddiqui, A. (2014). High WSS or low WSS? Complex interactions of hemodynamics with intracranial aneurysm initiation, growth, and rupture: toward a unifying hypothesis. *Am. J. Neuroradiol.* 35, 1254–1262. doi: 10.3174/ajnr.A3558

Min, J. H., and Lee, Y. S. (2007). Transcranial Doppler ultrasonographic evaluation of vertebral artery hypoplasia and aplasia. *J. Neurol. Sci.* 260, 183–187. doi: 10.1016/j.jns.2007.05.001

Napoli, C., de Nigris, F., Williams-Ignarro, S., Pignalosa, O., Sica, V., and Ignarro, L. J. Nitric oxide and atherosclerosis: an update. *Nitric Oxide* (2006). 15: 265–279. doi: 10.1016/j.niox.2006.03.011 1089-8611.

Ong, C. W., Xiong, F., Kabinejadian, F., Praveen Kumar, G., Cui, F. S., Chen, G., et al. (2019). Hemodynamic analysis of a novel stent graft design with slit perforations in thoracic aortic aneurysm. *J. Biomech.* 85, 210–217. doi: 10.1016/j.jbiomech.2019.01.019

Pontone, G., and Rabbat, M. G. (2017). The new era of computational fluid dynamics in CT angiography: far beyond the FFR number. *JACC Cardiovasc. Imaging* 10, 674–676. doi: 10.1016/j.jcmg.2016.08.001

Randles, A., Frakes, D. H., and Leopold, J. A. (2017). Computational fluid dynamics and additive manufacturing to diagnose and treat cardiovascular disease. *Trends Biotechnol.* 35, 1049–1061. doi: 10.1016/j.tibtech.2017.08.008

Samady, H., and Jaber, W. (2022). Harnessing vascular biology and fluid dynamics to risk stratify patients with acute coronary syndromes. *JACC Cardiovasc. Interv.* 15, 2049–2051. doi: 10.1016/j.jcin.2022.08.046

Schievink, W. I. (2001). Spontaneous dissection of the carotid and vertebral arteries. *N. Engl. J. Med.* 344, 898–906. doi: 10.1056/NEJM200103223441206

Sugiyama, S., Niizuma, K., Nakayama, T., Shimizu, H., Endo, H., Inoue, T., et al. (2013). Relative residence time prolongation in intracranial aneurysms: a possible association with atherosclerosis. *Neurosurgery* 73, 767–776. doi: 10.1227/NEU.0000000000000096

Sui, B., Gao, P., Lin, Y., Jing, L., Sun, S., and Qin, H. (2015). Hemodynamic parameters distribution of upstream, stenosis center, and downstream sides of plaques in carotid artery with different stenosis: a MRI and CFD study. *Acta Radiol.* 56, 347–354. doi: 10.1177/0284185114526713

Wake-Buck, A. K., Gatenby, J. C., and Gore, J. C. (2012). Hemodynamic characteristics of the vertebrobasilar system analyzed using MRI-based models. *PLoS One* 7:e51346. doi: 10.1371/journal.pone.0051346

Wilkin, J. K. (1989). Poiseuille, periodicity, and perfusion: rhythmic oscillatory vasomotion in the skin. *J. Invest. Dermatol.* 93, S113–S118. doi: 10.1038/jid.1989.20

Xu, L., Chen, X., Cui, M., Ren, C., Yu, H., Gao, W., et al. (2020). The improvement of the shear stress and oscillatory shear index of coronary arteries during enhanced external counterpulsation in patients with coronary heart disease. *PLoS One* 15, 1–15. doi: 10.1371/journal.pone.0230144

Zhang, P., Liu, X., Sun, A., Fan, Y., and Deng, X. (2015). Hemodynamic insight into overlapping bare-metal stents strategy in the treatment of aortic aneurysm. *J. Biomech.* 48, 2041–2046. doi: 10.1016/j.jbiomech.2015.03.028

Zhang, Y., Miao, C., Gu, Y., Jiang, S., and Xu, J. (2021). High-resolution magnetic resonance imaging (HR-MRI) imaging characteristics of vertebral artery dissection with negative MR routine scan and hypoperfusion in arterial spin labeling. *Med. Sci. Monit.* 27, e929445–e929441. doi: 10.12659/MSM.929445

Zhou, M., Zheng, H., Gong, S., Guo, J., Chen, N., Zhou, D., et al. (2015). Vertebral artery hypoplasia and vertebral artery dissection: a hospital-based cohort study. *Neurology* 84, 818–824. doi: 10.1212/WNL.0000000000001284

Frontiers in Neuroscience

Provides a holistic understanding of brain function from genes to behavior

Part of the most cited neuroscience journal series which explores the brain - from the new eras of causation and anatomical neurosciences to neuroeconomics and neuroenergetics.

Discover the latest Research Topics

See more →

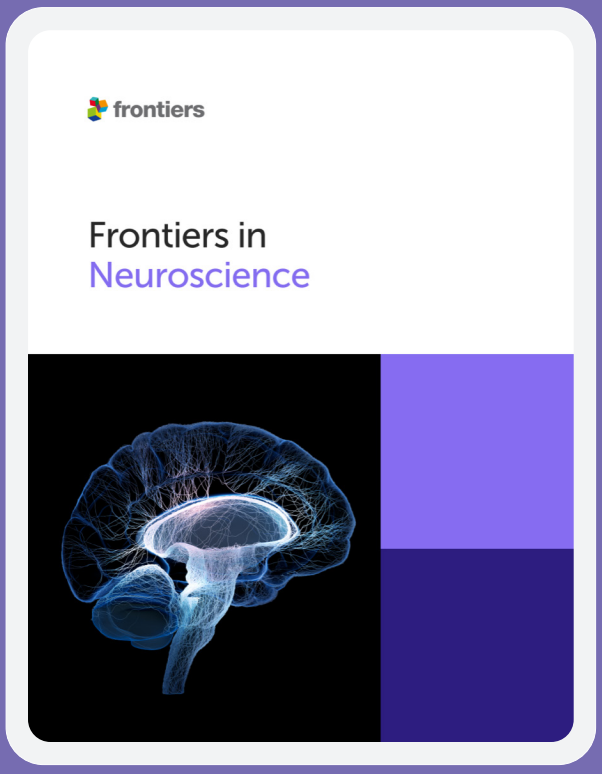

Frontiers

Avenue du Tribunal-Fédéral 34
1005 Lausanne, Switzerland
frontiersin.org

Contact us

+41 (0)21 510 17 00
frontiersin.org/about/contact